Western Graduate&PostdoctoralStudies

Western University
Scholarship@Western

Electronic Thesis and Dissertation Repository

8-15-2013 12:00 AM

Development of Novel Nanomaterials for Lithium-Air and Sodium-Air Batteries

Yongliang Li, *The University of Western Ontario*

Supervisor: Dr. Xueliang Sun, *The University of Western Ontario*

A thesis submitted in partial fulfillment of the requirements for the Doctor of Philosophy degree in Mechanical and Materials Engineering

© Yongliang Li 2013

Follow this and additional works at: https://ir.lib.uwo.ca/etd

Part of the Other Materials Science and Engineering Commons

Recommended Citation

Li, Yongliang, "Development of Novel Nanomaterials for Lithium-Air and Sodium-Air Batteries" (2013). *Electronic Thesis and Dissertation Repository*. 1407.
https://ir.lib.uwo.ca/etd/1407

This Dissertation/Thesis is brought to you for free and open access by Scholarship@Western. It has been accepted for inclusion in Electronic Thesis and Dissertation Repository by an authorized administrator of Scholarship@Western. For more information, please contact wlswadmin@uwo.ca.

DEVELOPMENT OF NOVEL NANOMATERIALS FOR LITHIUM-AIR AND SODIUM-AIR BATTERIES

(Thesis format: Integrated Article)

by

Yongliang Li

Graduate Program in Mechanical and Materials Engineering

A thesis submitted in partial fulfillment
of the requirements for the degree of
Doctor of Philosophy

The School of Graduate and Postdoctoral Studies
The University of Western Ontario
London, Ontario, Canada

© Yongliang Li 2013

Abstract

Lithium-air and sodium-air batteries are promising energy storage systems for future smart grids and electric vehicles due to their extremely high theoretical energy densities. However, electrode material development and architecture design for cathode as well as the battery cycleability are big challenges for these batteries. This research aims at developing various novel nanomaterials with desired morphology and structure as cathode materials for lithium-air and sodium-air batteries.

For lithium-air batteries, various carbon nanostructured cathodes were developed. They include: (1) Carbon black nanoparticles were treated under ammonia and carbon dioxide/hydrogen atmospheres and the surface area, porosity, defects, nitrogen-doping, and functional groups were modulated. These parameters for battery performance were investigated and it was found that the surface area of mesopores rather than others played an important role for the discharge capacity due to the passivation effect of discharge products. (2) One-dimensional (1D) nitrogen-doped carbon nanotubes (N-CNTs) electrode showed 50% higher of discharge capacity and better electrocatalytic activity for discharge product decomposition than pristine carbon nanotubes (CNTs) electrode. (3) Two-dimensional (2D) graphene nanosheets (GNSs) electrode delivered extremely high discharge capacity compared to porous carbon blacks due to the ideal porosity which increased the electrolyte wetting and oxygen diffusion, improving the efficiency of reactions. (4) Nitrogen-doped graphene nanosheets (N-GNSs) exhibited 1.5 times higher of electrocatalytic activity for oxygen reduction reaction than GNSs, further improved 40% of the discharge capacity. In addition, the morphology of discharge products was changed due to the defects and functional groups introduced by nitrogen doping. (5) The correlation between discharge product morphology and battery performance for sulphur-doped GNSs was studied and it was found that the discharge product contained structural defects such as oxygen and/or lithium vacancies resulting in different charge performance.

In terms of exploring catalysts which have potential for improving battery cycleability, a facile rapid microwave-assisted hydrothermal method was developed and it was shown that the morphology and crystallinity of MnO_2 were easily controlled by adjusting the reaction parameters.

For sodium-air battery cathode, it was also found that N-GNSs showed higher electrocatalytic activity for oxygen reduction reaction and oxygen evolution reaction, resulting in improving discharge and charge performance.

Keywords：

Nanomaterials, Porous carbon blacks, Nitrogen-doped carbon nanotubes, Graphene nanosheets, Nitrogen-doped graphene nanosheets, Sulphur-doped graphene nanosheets, Three-dimensional electrodes, Microwave-assisted hydrothermal method, Lithium-air batteries, Sodium-air batteries

Co-Authorship Statement

1.

Title: Challenges and Opportunities of Nanostructured Materials for Aprotic Rechargeable Lithium-Oxygen Batteries

Authors: Jiajun Wang, Yongliang Li, Xueliang Sun

The final version of this manuscript has been published in ***Nano Energy***, 2013, **2**, 443-467. All the authours contributed to designing, writing, and modifying the manuscript.

2.

Title: Carbon Black Cathodes for Lithium Oxygen Batteries: Influence of Porosity and Heteroatom-Doping

Authors: Yongliang Li, Xifei Li, Dongsheng Geng, Yongji Tang, Ruying Li, Jean-Pol Dodelet, Michel Lefèvre, Xueliang Sun

The final version of this manuscript has been accepted for publishing in ***Carbon***. Xifei Li and Dongsheng Geng conducted the measurement of surface area. Yongji Tang conducted the Raman characterization. Ruying Li provided access to the equipment. Dr. Jean-Pol Dodelet and Michel Lefefèvre provided the carbon black samples. All authors contributed editorial comments on the manuscript.

3.

Title: Nitrogen-Doped Carbon Nanotubes as Cathode for Lithium-Air Batteries

Authors: Yongliang Li, Jiajun Wang, Xifei Li, Jian Liu, Dongsheng Geng, Jinli Yang, Ruying Li, Xueliang Sun

The final version of this manuscript has been published in ***Electrochemistry Communications***, 2011, **13**, 668-672. Jiajun Wang conducted the Raman characterization. Xifei Li and Dongsheng Geng conducted the measurement of surface area. Jian Liu provided the nitrogen-doped nanobute samples. Jinli Yang contributed to the XRD measurement. Ruying Li conducted the TEM charaterization. All authors contributed editorial comments on the manuscript.

4.

Title: Superior Energy Capacity of Graphene Nanosheets for Nonaqueous Lithium-Oxygen Battery

Authors: Yongliang Li, Jiajun Wang, Xifei Li, Dongsheng Geng, Ruying Li, Xueliang Sun

The final version of this manuscript has been published in ***Chemical Communications***, 2011, **47**, 9438-9440. Jiajun Wang conducted the FTIR characterization. Xifei Li and Dongsheng Geng conducted the measurement of surface area. Ruying Li conducted the TEM charaterization. All authors contributed editorial comments on the manuscript.

5.

Title: Nitrogen-Doped Graphene Nanosheets as Cathode Materials with Excellent Electrocatalytic Activity for High Capacity Lithium-Oxygen Batteries

Authors: Yongliang Li, Jiajun Wang, Xifei Li, Dongsheng Geng, Mohammad Norouzi Banis, Ruying Li, Xueliang Sun

The final version of this manuscript has been published in ***Electrochemistry Communications***, 2012, **18**, 12-15. Xifei Li and Dongsheng Geng conducted the measurement of surface area. Jiajun Wang conducted the Raman characterization. Mohammad Norouzi Banis contributed to the XRD measurement. Ruying Li conducted the TEM charaterization. All authors contributed editorial comments on the manuscript.

6.

Title: Discharge Product Morphology and Increased Charge Performance of Lithium-Oxygen Batteries with Graphene Nanosheet Electrodes: The Effect of Sulphur Doping

Authors: Yongliang Li, Jiajun Wang, Xifei Li, Dongsheng Geng, Mohammad Norouzi Banis, Yongji Tang, Dongniu Wang, Ruying Li, Tsun-Kong Sham, Xueliang Sun

The final version of this manuscript has been published in ***Journal of Materials Chemistry***, 2012, **22**, 20170-20174. Xifei Li and Jiajun Wang conducted the Raman Characterization. Dongsheng Geng provided the samples. Mohammad Norouzi Banis contributed to the XRD measurement. Yongji Tang, Dongniu Wang, and Dr. Tsun-Kong Sham contributed to the XANES characterization. Ruying Li conducted the TEM charaterization. All authors contributed editorial comments on the manuscript.

7.

Title: Facile Controlled Synthesis and Growth Mechanisms of Flower-Like and Tubular MnO_2 Nanostructres by Microwave-Assisted Hydrothermal Method

Authors: Yongliang Li, Jiajun Wang, Yong Zhang, Mohammad Norouzi Banis, Jian Liu, Dongsheng Geng, Ruying Li, Xueliang Sun

The final version of this manuscript has been published in ***Journal of Colloid and Interface Science***, 2012, **369**, 123-128. Jiajun Wang conducted the Raman Characterization. Yongzhang conducted the HRTEM characterization. Mohammad Norouzi Banis contributed to the XRD measurement. Jian Liu contributed to the FTIR characterization. Ruying Li conducted the TEM charaterization. All authors contributed editorial comments on the manuscript.

8.

Title: Enhanced Performance of Sodium-Oxygen Batteries by Nitrogen-Doped Graphene Cathode Materials

Authors: Yongliang Li, Xifei Li, Hossein Yadegari, Yongji Tang, Biwei Xiao, Ruying Li, Xueliang Sun

The final version of this manuscript is to be submitted for publishing. Xifei Li and Yongji Tang conducted the Raman Characterization. Hossein Yadegari contributed to the EIS testing. Biwei Xiao contributed to the XRD measurement. All authors contributed editorial comments on the manuscript.

Two things awe me most, the starry sky above me and the moral law within me.

—— *Immanuel Kant*

To the people I love.

Acknowledgments

This Ph.D. work was carried on in Professor Andy Xueliang Sun's Nanomaterials and Energy Group at the University of Western Ontario (UWO). It is with great pleasure that I acknowledge every individual who has contributed to my research in the past four years.

I would like to express my deepest gratitude to my supervisor, Prof. Andy Xueliang Sun, who granted me the opportunity to work under his guidance. With his supervision, I have broadened my knowledge and improved my capabilities for research. Without his encouragement and support in various ways, this thesis could not have been possible. Not to mention his valuable advice, rigorous enthusiasm and unsurpassed knowledge will also benefit me for my life.

I am grateful to Mrs. Kathy Ruying Li, for providing me with understanding and support. She has taught me many techniques for synthesis and characterization of nanomaterials, and has given me lot of suggestions for overcomimg the problems I encountered. In addition, she always showed her kindness to my routine life, I will never forget her encouragement when I felt depressed and frustrated.

I wish to extend my appreciation to Dr. Jiajun Wang and Dr. Xifei Li for giving me lots of advice and suggestions for my research. The comprehensive help and fruitful discussions were very important on improving my experimental and writing skills.

Sincerely thanks to my advisory committee members Dr. Liying Jiang and Dr. Jun Yang, two professors of Mechanical and Materials Engineering (MME) at UWO for their valuable advices to my Ph.D. study. I would also like to thank the examiners of my thesis defence, Dr. Liying Jiang (a professor in MME at UWO), Dr. George K. Knopf (a professor in MME at UWO), Dr. Zhifeng Ding (a professor in Chemistry at UWO), and Dr. Xuhui Sun (a professor in College of Nano Science and Technology at

Soochow University, China) for their careful examination, insightful suggestions, comments, and discussions.

I gratefully acknowledge Professor Tsun-Kong Sham in the department of Chemistry at UWO and Professor Jean-Pol Dodelet in Institut national de la recherche scientifique (INRS), Canada for their valuable advice and discussions.

I would like to thank all my colleagues in Nanomaterials and Energy Group. They have created a friendly and professional environment and it was so much pleasure to work with them.

The research would not have been possible without the financial assistance from the Canada Research Chair (CRC) Program, Canada Foundation for Innovation (CFI), Ontario Early Researcher Award and the University of Western Ontario and I would express my acknowledgement to them.

Specially, I would like to express my sincere gratitude towards my parents and my brother. I love them so much, and I would not have made it this far without their understanding, support and encouragement.

Yongliang Li

June 12th, 2013

Table of Contents

Abstract ii

Co-Authorship Statement iv

Epigraph. viii

Dedication. ix

Acknowledgments x

Table of Contents xii

List of Tables xviii

List of Figures xix

List of Appendices xxvi

List of Abbreviations xxvii

Chapter 1 1

1 Introduction 1

1.1 Introduction to lithium-air batteries 2

1.2 Challenges of cathode for lithium-air batteries 7

1.3 The solutions with nanomaterials 8

1.3.1 Air electrode materials and structures 9

1.3.2 Catalysts 12

1.4 Introduction to sodium-air batteries 14

1.5 Thesis objectives 16

1.6 Thesis organization 19

References 21

Chapter 2 33

2 Experimental and Characterizations 33

2.1 Experimental 34

2.1.1 Synthesis of porous carbon blacks 34

2.1.2 Synthesis of nitrogen-doped carbon nanotubes (N-CNTs) 35

2.1.3 Synthesis of graphene nanosheets (GNSs), nitrogen-doped graphene nanosheets (N-GNSs), and sulphur-doped graphene nanosheets (S-GNSs) 36

2.1.4 Synthesis of manganese oxide (MnO_2) nanostructures 37

2.2 Characterizations 38

2.2.1 Physical characterizations 39

2.2.2 Electrochemical characterizations 44

References 47

Chapter 3 50

3 Carbon Black Cathodes for Lithium Oxygen Batteries: Influence of Porosity and Heteroatom-Doping 50

3.1 Introduction 51

3.2 Experimental 53

3.2.1 Sample preparation 53

3.2.2 Physical characterizations 54

3.2.3 Electrochemical measurements 54

3.3 Results and Discussion 55

3.4 Conclusions 66

Acknowledgements 66

References 67

Supporting Information 71

Chapter 4 80

4 Nitrogen-Doped Carbon Nanotubes as Novel Cathode for Lithium-Air Batteries 80

4.1 Introduction 81

4.2 Experimental 82

4.2.1 Materials synthesis 82

4.2.2 Physical characterizations 82

4.2.3 Electrochemical measurements 83

4.3 Results and Discussion 84

4.4 Conclusions 89

Acknowledgements 89

References 90

Chapter 5 93

5 Superior Energy Capacity of Graphene Nanosheets for Nonaqueous Lithium-Oxygen Battery 93

5.1 Introduction 94

5.2 Experimental 95

5.2.1 Material synthesis 95

5.2.2 Physical characterizations 95

5.2.3 Electrochemical characterizations 95

5.3 Results and Discussion 96

5.4 Conclusions 102

Acknowledgment 102

References 103

Supporting Information 107

Chapter 6 108

6 Nitrogen-Doped Graphene Nanosheets as Cathode Materials with Excellent Electrocatalytic Activity for High Capacity Lithium-Oxygen Batteries 108

6.1 Introduction 109

6.2 Experimental 110

6.2.1 Materials synthesis 110

6.2.2 Physical characterizations 110

6.2.3 Electrochemical measurements 110

6.3 Results and Discussion 111

6.4 Conclusions 117

Acknowledgements 117

References 118

Chapter 7 121

7 Discharge Product Morphology and Increased Charge Performance of Lithium-Oxygen Batteries with Graphene Nanosheet Electrodes: The Effect of Sulphur Doping 121

7.1 Introduction 122

7.2 Experimental 123

7.2.1 Materials synthesis 123

7.2.2 Physical characterizations 123

7.2.3 Electrochemical measurements 124

7.3 Results and Discussion 125

7.4 Conclusions 133

Acknowledgements 134

References 135

Supporting Information 140

Chapter 8 143

8 Facile Controlled Synthesis and Growth Mechanisms of Flower-Like and Tubular MnO_2 Nanostructres by Microwave-Assisted Hydrothermal Method 143

8.1 Introduction 144

8.2 Experimental 146

8.2.1 Materials synthesis 146

8.2.2 Physical characterizations 146

8.3 Results and Discussion 147

8.3.1 Structure and morphology characterization 147

8.3.2 Growth mechanisms of MnO_2 nanostructures 154

8.4 Conclusions 160

Acknowledgement 160

References 161

Chapter 9 167

9 Enhanced Performance of Sodium-Oxygen Batteries by Nitrogen-Doped Graphene Cathode Materials 167

9.1 Introduction 168

9.2 Experimental 169

9.2.1 Materials synthesis 169

9.2.2 Physical characterizations 169

9.2.3 Electrochemical measurements 170

9.3 Results and Discussion 171

9.4 Conclusions 181

Acknowledgements 181

References 182

Supporting Information 185

Chapter 10 186

10 Conclusions and Future Perspective 186

10.1 Conclusions 187

10.2 Future Perspective 190

Appendices 192

Curriculum Vitae 196

List of Tables

……Chapter 3……..……...

Table 3.1 Carbon mass based discharge capacity, surface-normalized discharge capacity and current, and the corresponding number of Li_2O_2 monolayers deposited on the surface of mesopores for carbon blacks with different mass losses.....59

Table SI-3.1 Carbon mass based discharge capacity, surface-normalized discharge capacity/current, and the corresponding number of Li_2O_2 monolayers on the surface of carbon blacks treated by CO_2 and CO_2/H_2 with different mass losses. 75

……Chapter 5……..……...

Table SI-5.1 Physical properties of GNSs, BP-2000, and Vulcan XC-72.....107

……Chapter 9……..……...

Table 9.1 Dependence of equivalent-circuit parameters for GNSs and N-GNSs electrodes. 175

List of Figures

……Chapter 1……..……...

Figure 1.1 The gravimetric energy densities (Wh kg^{-1}) for various types of rechargeable batteries compared to gasoline.....3

Figure 1.2 The schematic figure of an aprotic lithium-air battery and the oxygen electrode structure. 5

Figure 1.3 The general function principle of an alkali metal–oxygen battery. 15

Figure 1. 4 Electrochemical characterization of a, Na-O_2 and b, Li-O_2 cells. 16

……Chapter 2……..……...

Figure 2.1 Schematic diagram of FCCVD method for synthesis of N-CNTs. 35

Figure 2.2 A photo of an Anton Paar Synthos 3000 microwave synthesis system in our lab. 37

Figure 2.3 Characterization techniques in this research.....38

Figure 2.4 A photo of a Hitachi S-4800 SEM in our lab. 39

Figure 2.5 A photo of a Hitachi H-7000 TEM in our lab. 40

Figure 2.6 A photo of a Kratos Axis Ultra X-ray photoelectron spectrometer [15]. 41

Figure 2.7 A photo of a Bruker D8 Discover diffractometer [17]. 42

Figure 2.8 A photo of a HORIBA Scientific LabRAM HR Raman spectrometer in our lab. 43

Figure 2.9 A photo of an Autolab potentiostat/galvanostat (Model, PGSTAT-30, Ecochemie, Brinkman Instruments) with rotation control (MSR, Pine Instruments)...44

Figure 2.10 (a) A diagram illustration of swagelok type cells, (b) a photo of an Arbin BT-2000 battery test station. 46

……Chapter 3……..……...

Figure 3.1 SEM images and particle size distributions of carbon blacks with mass losses of (a, and b) 0%, (c, and d) 35%, and (e, and f) 75%. 55

Figure 3.2 (a) Total specific area (BET) and specific surface areas for micropores, mesopores, and macropores vs. mass loss during pyrolysis in NH_3, (b) discharge capacity (left Y axis), the specific area of micropores, mesopores, and macropores (right Y axis) vs. mass loss, (c) discharge capacity vs. the specific area for micropores, mesopores, and macropores and (d) the pore size distribution (PSD) curves for carbon blacks with various mass loss. 58

Figure 3.3 Estimated thickness of the discharge product on the surface (left Y axis) and pore size (right Y axis) of carbon blacks with different mass losses. 60

Figure 3.4 (a) Raman spectrum of the N330 carbon black, (b) Width at half maximum (fwhm) of D peak of carbon blacks vs. mass loss, and (c) The specific capacity vs. the fwhm. 62

Figure 3.5 (a) Nitrogen surface concentrations (left Y axis), and (b) oxygen surface concentrations (left Y axis), the specific area of the micropores (right Y axis) of the carbon blacks with different mass losses. 65

Figure SI-3.1 (a) Discharge capacity (left Y axis), total volume and specific volume for micropores and mesopores (right Y axis) vs. mass loss, (b) discharge capacity vs. the total volume and specific volume for mesopores for carbon blacks. 71

Figure SI-3.2 The discharge specific capacity vs. the average mesopore sizes of carbon blacks. 72

Figure SI-3.3 (a and b) Total specific area (BET) and specific surface areas for micropores, mesopores, and macropores vs. mass loss, (c and d) Discharge capacity (left Y axis), the specific area of micropoes, mesopores, and macropores (right Y axis) vs. mass loss during pyrolysis, and (e and f) discharge capacity vs. the specific area for micropores, mesopores, and macropores for carbon blacks treated by CO_2 (left column) and CO_2/H_2 (right column). 73

Figure SI-3.4 The pore size distribution (PSD) curves for carbon blacks treated by (a) CO_2 and (b) CO_2/H_2 with different mass losses. 74

Figure SI-3.5 Estimated thickness of the discharge product on the surface (left Y axis) and pore size (right Y axis) of carbon blacks treated by (a) CO_2 and (b) CO_2/H_2 with different mass losses. 76

Figure SI-3.6 Raman spectra of the carbon blacks with different mass losses during pyrolysis under NH_3. 77

Figure SI-3.7 Etching of carbon black by NH_3 as a function of time [21, 22]. 78

Figure SI-3.8 XPS survey spectra of the carbon blacks with different mass losses during pyrolysis under NH_3. 79

……Chapter 4……..……...

Figure 4.1 SEM and TEM images of CNTs (a, and b) and N-CNTs (c, and d)..... 84

Figure 4.2 (a) XRD patterns of the CNTs and N-CNTs, (b) Raman spectra of the CNTs and N-CNTs, (c) XPS survey spectrum of the N-CNTs, and (d) N_2 adsorption–desorption isotherms for the CNTs and N-CNTs. The inset of (a) is the XRD patterns in the range between 28° and 34°.....85

Figure 4.3 The voltage profiles of (a) CNTs and (b) N-CNTs electrodes cycled in a voltage range of 2.0~4.5 V at a current density of 75 mA g^{-1} in the first three cycles; CV curves of (c) CNTs and (d) N-CNTs electrodes at a scan rate of 0.2 mV s^{-1}; (e) Variation of Voltage on charging cells with CNTs and N-CNTs electrodes at a density of 75 mA g^{-1}. Cathode composition: CNTs or N-CNTs/Li_2O_2/binder (70/20/10); (f) Voltage profiles of N-CNTs electrodes at current densities of 75, 150, and 300 mA g^{-1}. 87

……Chapter 5……..……...

Figure 5.1 Discharge-charge performances of lithium-oxygen batteries with (a) GNSs, (b) BP-2000, and (c) Vulcan XC-72 cathodes at a current density of 75 mA g^{-1}. 97

Figure 5.2 SEM and TEM images of GNSs electrodes before (a, and b) and after (c, and d) discharge. 98

Figure 5.3 FTIR spectra of GNSs, BP-2000 and Vulcan XC-72. 99

Figure 5.4 (a) N_2 adsorption-desorption isotherms at 77 K and (b) pore size distribution (PSD) for GNSs, BP-2000 and Vulcan XC-72.....100

Figure 5.5 XRD pattern of GNSs electrode after discharge.....101

……Chapter 6……..……...

Figure 6.1 a, Voltage profiles of GNSs and N-GNSs electrodes at various current densities; b, CVs of GNSs and N-GNSs electrodes in O_2-saturated 0.1 mol dm^{-3} $LiPF_6$ in TEGDME solution at a scan rate of 5 mV s^{-1}, inset is the CVs in Ar-saturated solution; c, Rotating-disk voltamograms recorded for GNSs and N-GNSs electrodes for ORR at a rotating speed of 100 rpm in O_2-saturated 0.1 mol dm^{-3} $LiPF_6$ in TEGDME solution at a scan rate of 5 mV s^{-1}; d, Tafel-slops for the ORR on the GNSs and N-GNSs electrodes. 112

Figure 6.2 TEM images of a, GNSs and b, N-GNSs; c, N_2 adsorption–desorption isotherms at 77 K, inset is the pore size distribution; XPS d, survey, e, C1s, and f, O1s spectra of GNSs and N-GNSs, inset of d is N 1s spectra of two samples; g, Raman spectra of GNSs and N-GNSs. 114

Figure 6.3 SEM images of the fully discharged a, GNSs, b, N-GNSs electrodes and c, GNSs, d, N-GNSs electrodes discharged for 1 h; e, XRD patterns of pristine and discharged GNSs and N-GNSs electrodes. 116

……Chapter 7……..……...

Figure 7.1 (a) SEM image, (b) EDS mapping, (c) XPS spectroscopy, and (d) S K-edge XANES of sulphur-doped graphene. 125

Figure 7.2 Discharge/charge curves of (a) sulphur-doped and (b) pristine graphene electrodes at a current density of 75 mA g^{-1}. Inset of (b) is enlarged figure of the charge curve for 1st cycle. 127

Figure 7.3 SEM images of (a) sulphur-doped and (b) pristine graphene discharged electrodes. (c) XRD patterns, (d) XANES of discharge products of S-GNSs. 128

Figure 7.4 SEM images of discharged S-GNSs electrodes to (a) 2.6 V, (b) 2.4 V and (c) 2.2 V at a current density of 75 mA g^{-1}; (d) Mean diameters of the discharge products. 130

Figure 7.5 SEM images of discharge products at current density of (a) 150 mA g^{-1}, (b) 300 mA g^{-1}. Inset of (a) and (b) are the high-magnification images. 131

Figure 7.6 Schematic of discharge product nanostructures growth on S-GNSs electrodes. 132

Figure SI-7.1 SEM image of graphene nanosheets. 140

Figure SI-7.2 Raman spectroscopy of S-GNSs and GNSs. 141

Figure SI-7.3 SEM image (a) and XRD pattern (b) of the discharge product after 2nd discharge. 142

……Chapter 8……..……...

Figure 8.1 XRD patterns of the products prepared at (a) 100 °C, and (b) 140 °C in 25 min. 148

Figure 8.2 SEM images of the products prepared at (a, and b) 100 °C, and (c, and d) 140 °C in 25 min. The insets of a, and c are the lower magnification images. 149

Figure 8.3 TEM (a, and c) and HRTEM (b, and d) images of the products prepared at (a, and b) 100 °C, and (c, and d) 140 °C in 25 min. The insets of a, and c show the corresponding SAED patterns. 150

Figure 8.4 FT-IR spectra (A) and Raman scattering spectra (B) of the products prepared at (a) 100 °C, and (b) 140 °C in 25 min. 152

Figure 8.5 TEM images of the products prepared in (a) 5 min, (b, d, e, and f) 15 min, and (c) 25 min at a reaction temperature of 140 °C. 156

Figure 8.6 Schematic illustration of the formation stages of different shapes of the MnO_2 nanostructures. 157

Figure 8.7 SEM images of the product prepared at 180 °C in 25 min. 159

……Chapter 9……..……...

Figure 9.1 The voltage profiles of (a) GNSs and (b) N-GNSs electrodes at various current densities; CV curves of (c) GNSss and (d) N-GNSs electrodes at a scan rate of 2 mV s^{-1} in a voltage range of 1.8-3.6 V. 171

Figure 9.2 Charge/discharge performance of initial 3 cycles of (a) GNS and (b) N-GNSs electrodes at 75 mA g^{-1}. 173

Figure 9.3 Measured and calculated electrochemical impedance spectra of GNSs and N-GNSs electrodes after discharge at 75 mA g^{-1}. The inset is the equivalent circuit used for the analysis of the impedance plots. 174

Figure 9.4 SEM images of the fully discharged a, GNSs, b, N-GNSs electrodes and c, GNSs, d, N-GNSs electrodes discharged for 12 h; e, Raman spectra of pristine and discharged GNSs and N-GNSs electrodes. 177

Figure 9.5 SEM images of discharge products on N-GNSs electrodes at (a) 150, and (b) 300 mA g^{-1}. 179

Figure 9.6 Schematic of the growth of discharge product nanostructures on N-GNS electrodes. 180

Figure SI-9.1 Raman spectra of GNSs and N-GNSs. 185

List of Appendices

Appendix I: PERMISSION FROM ELSEVIER FOR PUBLISHED ARTICLE.....192

Appendix II: PERMISSION FROM ROYAL SOCIETY OF CHEMISTRY (RSC) FOR PUBLISHED ARTICLE.....195

List of Abbreviations

0D	zero dimensional
1D	one dimensional
2D	two dimensional
3D	three dimensional
AAO	anodized aluminum oxide
BET	Brunauer-Emmett-Teller
BJH	Barrett-Joyner-Halenda
CLS	Canadian Light Source
CNFs	carbon nanofibers
CNTs	carbon nanotubes
CV	cyclic voltammetry
CVD	chemical vapor deposition
DEGDME	diethylene glycol dimethyl ether
DFT	density functional theory
DOD	depth of discharge
EC	ethylene carbonate
EDS	energy-dispersive X-ray spectroscopy

EIS	electrochemical impedance spectroscopy
EVs	electric vehicles
Fwhm	width at half maximum
FESEM	field emission scanning electron microscopy
FCCVD	floating catalyst chemical vapor deposition
FGSs	functional graphene nanosheets
FT-IR	Fourier transform-infrared
FLY	fluorescence yield
GNSs	graphene nanosheets
HEVs	hybrid electric vehicles
HRTEM	high-resolution transmission electron microscope
I_D/I_G	Intensity ratio of D and G band
KB	Ketjen black
LIB	lithium-ion battery
MA-HM	microwave-assisted hydrothermal method
MCF-C	mesocellular carbon foam
MWNTs	multi-walled carbon nanotubes
MnO_2	manganese oxide
N-CNTs	nitrogen-doped carbon nanotubes

N-GNSs	nitrogen-doped graphene nanosheets
OER	oxygen evolution reaction
OMS-2	octahedral molecular sieves
ORR	oxygen reduction reaction
PC	propylene carbonate
PEM	proton exchange membrane
PHEVs	plug-in hybrid vehicles
PSD	pore size distribution
PTFE	polytetrafluoroethene
PVDF	poly(vinylidene fluoride)
RDE	rotating disk electrode
RS	Raman scattering
SAED	selected area electron diffraction
SEM	scanning electron microscope
S-GNSs	sulphur-doped graphene nanosheets
SS	stainless steel
SXRMB	soft X-ray microcharacterization beamline
TEM	transmission electron microscope
TEGDME	tetraethylene glycol dimethyl ether

VLS-PGM	variable line-spacing planar grating monochromator beamline
XANEs	X-ray absorption near edge structure
XPS	X-ray photoelectron spectroscopy
XRD	X-ray diffraction

Chapter 1

1 Introduction*

In this chapter, the recent development of lithium-air and sodium-air batteries is reviewed. The challenges of cathodes for these batteries are discussed and the solutions by nanomaterials and nanotechnology are suggested. In addition, the research objectives, and the thesis organization of this study are stated.

---

*A version of this chapter has been published in ***Nano Energy***, 2013, **2**, 443–467.

1.1 Introduction to lithium-air batteries

The demand for energy is putting pressure on fossil fuel reserves, which in turn is responsible for the climate change. It has been reported that oil consuming accounts for 40% of the total CO_2 emission and is a major cause of geopolitical instability. On one hand, due to the fluctuation of oil prices and the serious environmental issues, there has been substantial interest in renewable energy sources. On the other hand, since the majority of oil is used for automobile and light truck applications, a transition to an electrified road transportation system should be a societal goal of utmost importance. This is heralded by the advent of hybrid electric vehicles (HEVs), and will be accelerated by plug-in hybrid vehicles (PHEVs) and ultimately pure electric vehicles (EVs). Therefore, the development of novel energy storage and conversion systems is required for effective utilization of renewable energy sources in future smart grids and power delivery systems.

Rechargeable battery systems may provide a feasible route to achieve this objective. Various battery systems have been developed and been commercialized over the past few decades [1-6]. **Figure 1.1** shows a range of battery technologies available or currently under development and compares their respective energy densities to gasoline [7]. Among of them, the most successful rechargeable battery technology is lithium-ion battery (LIB), which was first commercialized in 1991 and is widely used in a variety of portable electronic equipments and devices [8-10].

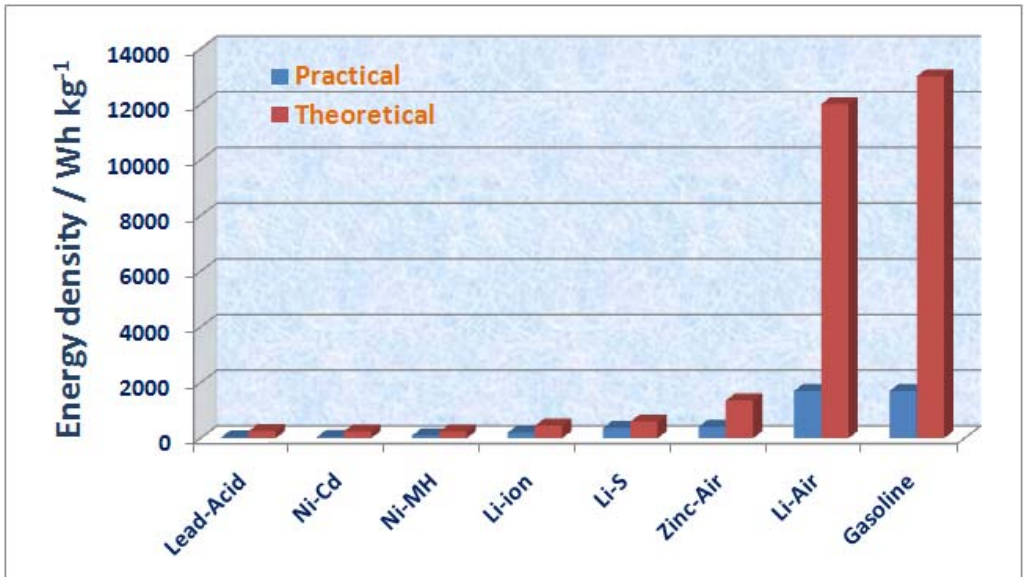

Figure 1.1 The gravimetric energy densities (Wh kg^{-1}) for various types of rechargeable batteries compared to gasoline.

However, the maximum energy density of current lithium-ion batteries is limited by the intercalation chemistry occurring within the electrode materials [11]. While it is known that the theoretical energy density of gasoline is 13000 Wh kg^{-1}, the energy density of lithium-ion batteries is usually less than 200 Wh kg^{-1} [7]. Considering the energy conversion efficiency of 12.6%, the practical energy density for automotive applications is 1700 Wh kg^{-1}, which is still much higher than lithium-ion batteries. There is no expectation that current or even future lithium-ion batteries will ever reach this target because of the intercalation reaction mechanism limit in lithium-ion battery system. A novel energy system must be considered.

Metal-air batteries (e.g. iron-air, aluminum-air, and zinc-air) have attracted much attention as a possible alternative due to their relatively high energy densities because the cathode of a metal-air battery utilizes oxygen from ambient air as reactant in the electrochemical reaction rather than storing heavier active materials as in other battery systems. Among them, zinc-air batteries have been studied for many years because

they have more advantages such as a flat discharge voltage plateau, high safety, low cost, and long shelf life [12-14]. However, the theoretical specific energy density of zinc-air batteries is only 1084 Wh kg^{-1} [15], which is still much lower than gasoline and cannot fulfill the requirements of many high-energy applications of electric vehicles.

Lithium is the lightest metal element and its theoretical energy density is approximately 11680 Wh kg^{-1} [7], nearly equivalent to gasoline. Therefore, many efforts have been devoted to lithium-air battery research [7, 16-18]. The concept of lithium-air chemistry was first introduced by Littauer and Tsai at Lockheed [19] in 1976, but it received little attention until a lithium-air battery system based on nonaqueous electrolyte was presented by Abraham et al. in 1996 and the rechargeability was explored by Bruce et al. in 2006 [20, 21]. These pioneer works have attracted worldwide attentions and triggered numerous research works into lithium-air field. However, current lithium-air battery (most of the current research on lithium-air batteries has focused on pure oxygen rather than air as air contains H_2O and CO_2 which interferes with the desired electrochemical behavior) still suffers from a relatively low practical energy density as compared to the theoretical one and internal combustion engine that uses gasoline. Numerous fundamental and systematic studies are required to mature this novel electrochemical energy system. Undoubtedly, lithium-air battery is a pivotal research area for next-generation power source and could bring electric vehicles to the mass market in the future.

Currently, there are four architectures of lithium-air batteries being pursued, which are categorized based on the applied electrolyte species (aprotic, aqueous, hybrid, and all solid-state electrolytes) [22-44]. The aprotic system is advantageous because it has been proved that the reduction product of Li_2O_2 can be reversed into the original reagents of the oxygen reduction reaction (ORR). This is aptly named the oxygen evolution reaction (OER) and signifies the recharge ability of the aprotic lithium-air battery. Because only the aprotic lithium-air battery has shown promise of electrical

rechargeability, this configuration has attracted the most effort worldwide to date compared to other electrolyte systems.

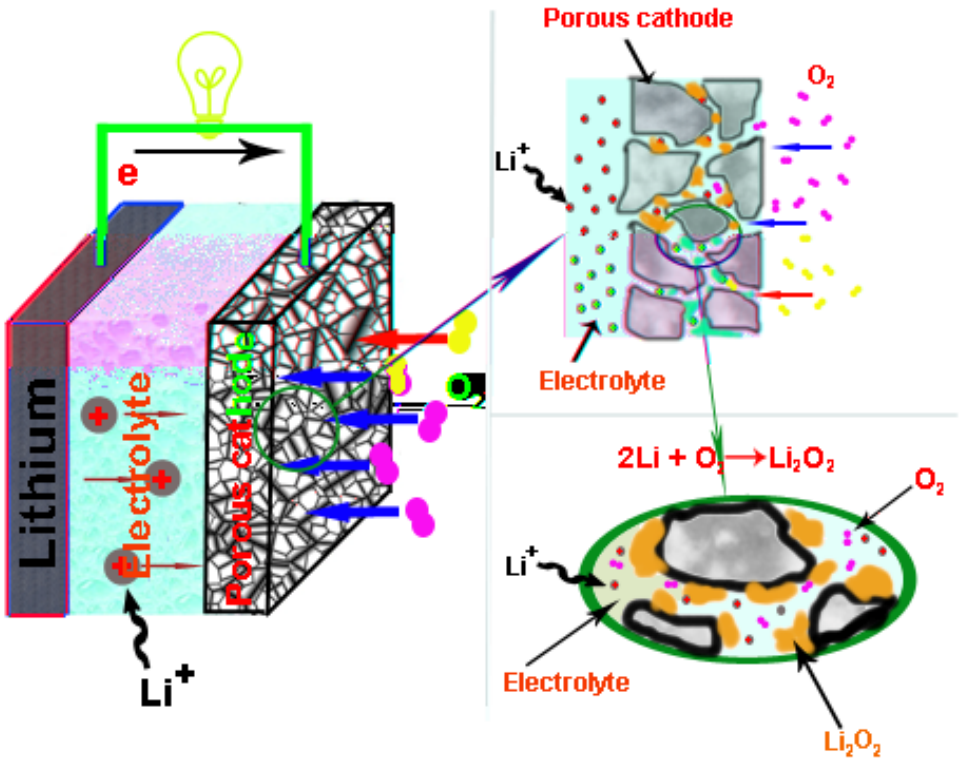

Figure 1.2 The schematic figure of an aprotic lithium-air battery and the oxygen electrode structure.

During the discharge of an aprotic lithium-air battery, an oxidation reaction occurs at the anode ($Li \rightarrow Li^+ + e^-$). The electrons flow through an external circuit and the lithium ions generated from this reaction react with oxygen to form Li_2O_2 (and possibly Li_2O) in the cathode. At the cathode, oxygen is reduced in either a two or four electron process as described by the following half cell reactions (**Figure 1.2**) [45, 46]:

$$O_2 + 2e^- + 2Li^+ \rightarrow Li_2O_2 \quad (3.10\ V) \qquad (1.1)$$

$$O_2 + 4e^- + 4Li^+ \rightarrow 2Li_2O \quad (2.90\ V) \qquad (1.2)$$

The reaction above is thought to be reversible at externally applied potentials, i.e., lithium metal is plated out on the anode, and O_2 is evolved or generated at the cathode. The potentials of reactions (1.1) and (1.2) are close, so both Li_2O_2 and Li_2O are the most abundant reduction products after the discharge process. However, based on the studies from Abraham et al. [20] and Bruce et al. [21] using Raman spectrometry, Li_2O_2 was identified as the dominant reduction product formed after discharge. Moreover, Li_2O_2 exhibits a better rechargeability than Li_2O since Li_2O is believed to be electrochemically irreversible. Despite the fact that both Li_2O_2 and Li_2O are bulk insulators, a recent study indicated that the stable surfaces of Li_2O_2 are half-metallic [47]. In contrast, the stable surfaces of Li_2O are insulating and non-magnetic. The distinct surface properties of these compounds may explain the observations of electrochemical reversibility for systems with Li_2O_2 as the discharge product, and the irreversibility of systems that discharge product is Li_2O.

Considering Li_2O_2 is more desirable for rechargeable aprotic lithium-air batteries, currently the net discharge/charge reactions in an aprotic lithium-air battery is the oxidation/reductions involving of lithium peroxide,

Discharge: $$2Li + O_2 \rightarrow Li_2O_2 \quad (1.3)$$

Charge: $$Li_2O_2 \rightarrow 2Li + O_2 \quad (1.4)$$

In the mechanism study, there are various different mechanisms proposed for O_2 reduction in Li^+ electrolytes over past years [48-53]. Recently, Bruce et al. applied spectroscopic methods to directly identify the reaction products and their intermediates. A possible mechanism has also been suggested in order to further elucidate the chemical reactions that occur at the cathode during discharge.

$$O_2 + e^- \rightarrow O_2^- \quad (1.5a)$$

$$O_2^- + Li^+ \rightarrow LiO_2 \quad (1.5b)$$

$$2LiO_2 \rightarrow Li_2O_2 + O_2 \quad (1.5c)$$

The O_2 is first reduced to O_2^- in the nonaqueous electrolyte in presence of Li^+ ions, and the produced O_2^- binds to Li^+ to form LiO_2 on the surface of the electrode. Here LiO_2 is unstable and disproportionates to the more stable Li_2O_2, as shown in reaction (1.5c). Therefore, Li_2O_2 is the final discharge product. Further, a charging process mechanism was also suggested by Bruce et al. [54]. During the charging process, oxidation occurs by direct decomposition according to the reaction

$$Li_2O_2 \rightarrow 2Li^+ + 2e^- + O_2 \qquad (1.6)$$

In other words, the pathways followed on reduction and oxidation are different. On charging, Li_2O_2 decomposes directly, in a one-step reaction to evolve O_2 and does not pass through LiO_2 as an intermediate.

1.2 Challenges of cathode for lithium-air batteries

The lithium-air battery may achieve a high practical specific energy as its theoretical specific energy is 11,431 Wh kg^{-1} based on lithium, assuming that Li_2O_2 is the product, starts with lithium (0.006941 Kg/mol) and the equilibrium potential is 2.96 V.

$$Spec.E = \frac{2.96V \times 96500C/mol}{3600C/Ah \times 0.006941Kg/mol} = 11,431Wh/Kg$$

Currently the specific energy of an aprotic lithium-air battery is lower than the theoretical one. The reason is the components of battery, including anodes, electrolytes (solvents and lithium salts), and cathodes cannot meet the requirements of practical applications. Furthermore, these components interplay each other, making the investigation of individual component more complicated. However, it has been shown that the battery performance is strongly determined by the cathode properties; therefore, our focus is primarily on the challenges of cathodes for the lithium-air batteries which are discussed below.

(I) One of the challenges for cathode is the limiting oxygen solubility and diffusion, accumulation of reaction products, and the lack of effective three-phase electrochemical interface, which are directly determined by air electrode materials and structures [55]. Because the discharge product, Li_2O_2, is not soluble in the organic electrolyte, it will deposit on the surface of the electrode. The channels of oxygen transportation will be blocked when the pores in the electrode are clogged, and the battery discharge is terminated. Therefore, developing of novel electrode materials and structures with optimum oxygen diffusion channels may relieve the pore clogging problems and improve the discharge performance.

(II) Another big challenge is the limited electrical efficiency which is due to the overpotential or polarization losses at the cathode during discharge and charge. A high potential is needed for charging (~ 4.5 V) the porous carbon electrode whereas the discharge potential is around 2.5 V; the big difference between these two values leads to a low round-trip efficiency. The improvement of this efficiency may be expected by applying effective catalysts. Although recent reports doubt the efficacy of electrocatalys is in the aprotic lithium-air batteries considering the electrolyte solvent decomposition [56], most reports indicate that by applying catalysts, which are both good for oxygen reduction reaction during discharge and oxygen evolution during charge, the round-trip efficiency will be dramatically increased, thus increasing the battery performance [57, 58].

1.3 The solutions with nanomaterials

Nanomaterials are defined as solid materials processing at least one of physical dimension on the order of nanometer scale which can be classified in terms of dimensionality into three categories: zero-dimensional (0D) nanomaterials which refer to the materials whose all three dimensions are limited to nanoscale (nanoparticles and

quantum dots), one-dimensional (1D) nanomaterials which have two dimensions in nanoscale (nanowires, nanorods and nanotubes), and two-dimensional (2D) nanomaterials which have only one nanoscale dimension (nanofilms) [59]. Since the properties of nanomaterials mainly depend on grain size and particle size distribution, chemical composition, and interfaces (grain boundaries, free surface, etc), they show unique physical and chemical properties compared to the bulk counterparts [60]. For example, the mechanical strength of nanomaterials is usually higher than that of bulk materials because of the reduced crystal defects and dislocations [61]; the thermal stability may change due to the large surface to volume ratio and surface energy [62]; the catalytic activity of nanocatalysts will increase because of the different surface structure and electronic properties [63].

Many nanomaterials have been widely studied for energy storage applications, such as solar cells, lithium-ion batteries, supercapacitors, etc [64] and it is believed that they are good candidates for cathode materials of lithium-air batteries. In order to develop the cathodes for aprotic lithium-air battery, intensive research efforts have been devoted to various aspects, including electrode materials, structures, and catalysts.

1.3.1 Air electrode materials and structures

1.3.1.1 Electrode materials

Various carbon materials have been applied as the air electrode materials for lithium-air batteries. Commercial carbon powders were studied as cathode materials for lithium-air batteries by Xiao et al. and the results indicated that the pore volume of carbon materials played an important role in determining the electrochemical performances of the lithium-air batteries [65, 66]. The large volume expansion in the Ketjen black (KB)-based electrode led to not only extra three-phase regions to facilitate the reaction in the electrode but also extra volume to hold the reaction product. Consequently, the battery using KB-based air electrode exhibited the highest specific capacity among all carbon powder samples.

Mesoporous carbon materials have been applied as cathode materials for lithium-air battery application. Xia et al. synthesized mesocellular carbon foam (MCF-C) with narrow pore size distribution (~ 30 nm) and the MCF-C delivered a discharge capacity of about 40% higher than that of Super P. Compared to commercial carbon powder; MCF-C has a hollow structure which possesses much larger mesopores, which is beneficial on accommodating discharge product [67]. Hall et al. prepared mesoporous carbon aerogels with tunable porosity by the polycondensation of resorcinol with formaldehyde [66]. The discharge capacity of the porous carbons showed that the appropriate pore volume and pore diameter are the key factors contributing to high discharge capacity.

1D carbon nanomaterials (nanotube, nanofibres) have been widely studied in various electrochemical energy systems such as fuel cells, supercapacitors, and batteries due to their superior properties [68]. These 1D carbon nanomaterials also showed good performance in lithium-air battery applications. For example, aligned carbon nanofibers (CNFs) electrodes were fabricated using atmospheric pressure chemical vapor deposition (CVD) on porous anodized aluminum oxide (AAO) substrates coated with thin layers of Ta and Fe [69]. It was found that the unique properties of the CNFs electrodes, including high electronic conductivity, high void volume, and an interconnected, well-developed pore structure played significant roles in determining the battery performance.

As the hottest carbon material currently, graphene nanosheets (GNSs) have also exhibited superior property in lithium-air batteries [70, 71]. The GNSs electrode increased the electrochemically accessible site and provided a large diffusion path for the oxygen which was due to their unique morphology and structure, therefore, significantly improving the discharge capacity. In addition, the edge sites of GNSs contained a large amount unsaturated carbon atoms which were very active to oxygen, improving activity for oxygen reduction reaction.

1.3.1.2 Structure design

In addition to optimizing of the air electrode composition which may affect the cathode porosity [72], more efforts should be devoted towards designing novel porous air electrodes.

Zhang et al. simulated and analyzed several air electrode designs including single pore system, dual pore system in two dimensions, and dual pore system with multiple time-release catalysts. Some important parameters including the porosity distribution, pore connectivity, the tortuosity of the pore system, and the catalyst spatial distribution were studied. The results indicated that the dual pore system offers advantages for improved oxygen transport into the inner regions of the air electrode. When coupled with multiple time-release catalysts, the system can substantially extend the duration at higher powers, and result in maximum utilization of air electrode materials [73]. Considering the requirement of porous structure and available void volume for discharge products, numerous efforts have been devoted to designing a novel porous air electrode with maximum void volume [74, 75]. Shao-Horn et al. developed all-carbon–nanofiber porous electrode with highly efficient utilization of carbon material and void volume for lithium-air batteries which was found to yield high gravimetric energies of four times higher than lithium-ion batteries [69]. A similar freestanding carbon nanotube/nanofiber mixed buckypaper was also devepoped and applied in lithium-air batteries [76].

The oxygen diffusion in air electrode also plays an important role in battery performance. Recently, a porous carbon microstructure based on GNSs was developed by Zhang et al [77]. The hierarchical arrangement of the functional graphene nanosheets (FGSs) aggregated into loosely packed, “broken egg” structures with large interconnected tunnels which can function as numerous arteries that continuously supply oxygen into the interior of the electrode during the discharge process. Therefore, the lithium-air battery with this novel electrode delivered an exceptionally high capacity.

Another strategy to enhance the accessible void volume and oxygen diffusion rate is to decrease the amount of additive carbon and binder. For example, a novel free-standing type cathode was designed by a simple chemical deposition method, and the new air electrode exhibited a noticeably higher specific capacity and improved cycle efficiency compared to the conventional carbon-supported electrode [78]. Without additional carbon and binders, this 3D electrode provided abundant catalytic sites, intimate electronic contact and open pore system for unrestricted access of the reactant oxygen molecules

1.3.2 Catalysts

1.3.2.1 Metal oxide nanomaterials

Transition metal oxides, including Fe_2O_3, Fe_3O_4, NiO, CuO, Co_3O_4, $CoFe_2O_4$ etc, have been employed as catalysts in lithium-air batteries by Bruce et al [79]. It was shown that Fe_2O_3 exhibited the highest initial discharge capacity, while Fe_3O_4, CuO and $CoFe_2O_4$ gave the best capacity retention. Co_3O_4 showed the best compromise between the discharge capacity and the retention [80, 81]. However, the reaction mechanism for these findings is still unclear and more detailed investigations are required.

Manganese oxides are the most intensively studied catalysts for lithium-air battery applications [82]. Bruce et al. compared several types of MnO_x, including α-MnO_2 nanowires, β-MnO_2 nanowires, bulk MnO_2 (α, β, γ, λ), and commercial Mn_2O_3 and Mn_3O_4 and it was found that α-MnO_2 nanowires were the most effective catalysts for rechargeable lithium-air batteries due to their crystal structure and high surface area. Zheng et al. prepared composite electrodes by mixing α-MnO_2 nanorods with carbon nanotubes or nanofibers and demonstrated that the charge capacity and cycleability of the battery were largely increased with the catalysts [83]. The reason is that the α-MnO_2 reacts with discharge product Li_2O to form Li_2MnO_3 during discharge, while the Li_2O could be electrochemically removed from Li_2MnO_3 during charge. Guan et al. synthesized α-MnO_2 nanoflakes coated on multi-walled carbon nanotubes (MWNTs)

and used this composite as cathode for lithium-air batteries [84]. The MnO_2/MWNTs cathode exhibits a low charge potential of 3.8 V, dramatically improved the energy efficiency and cyclic ability. The MnO_2 catalysts with different morphologies were also applied for lithium-air batteries [85-87].

1.3.2.2 Noble metal nanomaterials

An important breakthrough to improve the charging efficiency of lithium-air batteries was made by Shao-Horn et al. who reported that Au can enhance the ORR during discharge, and Pt can facilitate OER during charge [88-93]. They further demonstrated that the PtAu alloy particles can serve as bifunctional catalysts, leading to a high round-trip efficiency of 77%. The discharge voltage of electrode with PtAu/C is higher than that of Vulcan XC-72 carbon electrode, while the average charge voltage of PtAu/C is 3.6 V which is 900 mV lower than that of carbon (~ 4.5 V). This finding evoked ample research interests on noble catalysts for lithium-air batteries. For example, Tatsumi et al. investigated the catalysis of Pd, mixed Pd and several metal oxides or metals for cost reduction as well as the improvement of discharge performance [94, 95]. It was found that by adding MnO_2 to the electrode, the discharge plateau of the battery increases to 2.9 V, while the charge potential decreases to 3.6 V, leading to a high specific energy efficiency of 82%. However, similar to the research for fuel cells, noble metal catalyst may exhibit superior catalytic activity for ORR and OER, deserving further study to improve the electrochemical performance of lithium-air batteries. However, the high cost and limited source of noble metal have to be considered in future application.

1.3.2.3 Other nanomaterials

Transition metal N4-macrocycle complexes have long been known to be highly active for the catalytic reduction of oxygen. The heat-treated transition metal N4-macrocycle

complexes have been considered as an excellent catalyst for the oxygen reduction in lithium-air batteries [96]. In addition, conductive polymer and composites, transition metal nitrides, and perovskite-type oxides also exhibited good catalytic activity for oxygen reduction in lithium-air batteries [97-100].

1.4 Introduction to sodium-air batteries

Lithium-air batteries have been intensively studied for the past few years and they showed extremely high discharge capacity. And the batteries could be charged when electrocatalysts which facilitate the oxygen evolution reaction are applied in cathodes. Therefore, lithium-air batteries are expected to be the choice for powering future generations of HEVs, PHEVs, and EVs. However, the supply of lithium is not able to meet the requirement if the amount of EVs increases too quickly and would probably run out in the foreseeable future.

Sodium, an element with wide availability and low cost, is a very promising material for meeting the large scale grid energy storage needs. In addition, this material is the 4th most abundant element in the Earth, providing potential to be an alternative source to lithium [101, 102]. Recently sodium has been investigated to replace lithium in air battery system [103-108]. To use sodium instead of lithium also has other advantages, such as the reaction mechanism for sodium is very similar to lithium in the positive electrode, making it possible to replace the anode materials without changing the configuration of the system; the working potential of sodium is relatively lower than that of lithium, if the rechargeable sodium batteries could be developed, low voltages are suitable for charge process and therefore the electrolyte would become more stable in these systems.

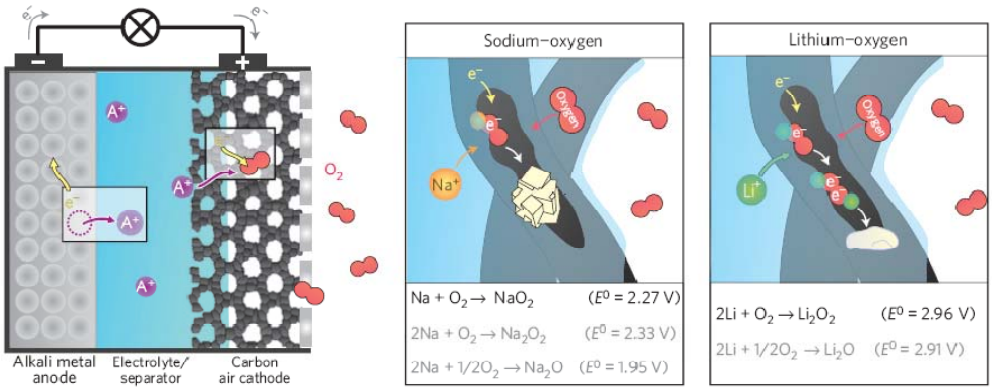

Figure 1.3 The general function principle of an alkali metal–oxygen battery.

As shown in **Figure 1.3**, the discharge products of sodium-air batteries are various, depending on discharge voltage [106]. And it is interesting to note that the formation of Na_2O_2 (E = 2.33 V) is thermodynamically favored than that of NaO_2 (E = 2.27 V), however, from the kinetically point of view, the formation of NaO_2 only requires on electron transfer which is relatively easier. Moreover, NaO_2 is considered to be an electronic conductor which may show different properties for charge process. The charge occurs at a voltage ~ 2.3 V at low current densities, which is close to the potential for decomposition of NaO_2 to form sodium and oxygen. The finding clearly indicates the formation and decomposition of NaO_2 is reversible.

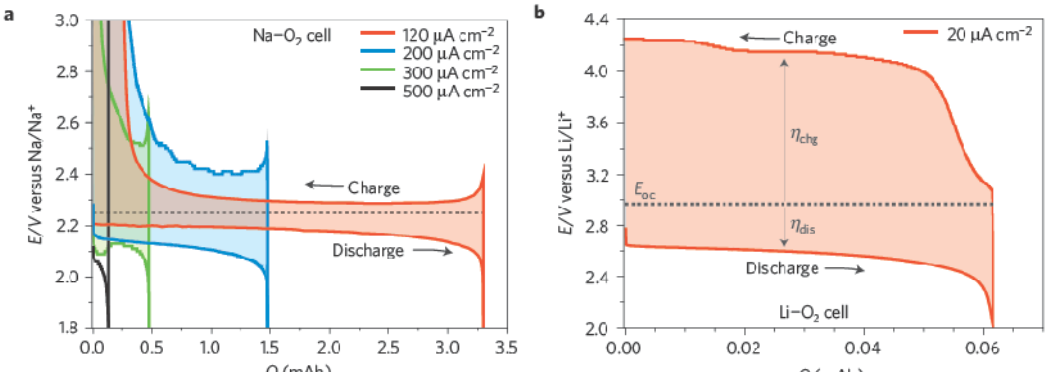

Figure 1. 4 Electrochemical characterization of a, Na-O_2 and b, Li-O_2 cells.

Figure 1.4 shows the discharge/charge curves of the Na-O_2 cells and an analogous Li-O_2 cell [106]. It can be seen that for the Li-O_2 cell, the discharge voltage plateau is about

2.6 V, corresponding to an overpotential of about 300 mV. While for charging, the voltage increased quickly to around 4.2V, showing a large overpotential. In contrast, the Na-O_2 cells show a very high round-trip efficiency.

Since the discharge products of sodium-air batteries are not soluble in the organic electrolyte but deposit on the electrode which is similar to lithium-air batteries, it is believed that the cathode materials and structures will also show significantly impacts for battery performance. For example, Fu et al. has suggested that sodium-air battery using GNSs as cathode showed not only higher discharge voltage plateau than that of carbon film electrode, but also better performance in the charge process, resulting in good cycleability [107]. Therefore, air electrode material development and electrode structure design are necessary for improving the sodium-air battery performance.

1.5 Thesis objectives

Lithium-air and sodium-air batteries are promising energy storage and conversion systems for future smart grids and automobile applications. However, the cathode development, including electrode materials and structure design is a big challenge for these systems and it is believed that nanomaterials and nanotechnology are one of the key solutions to address the challenges.

In this content, the author devoted to develop various nanomaterials as cathode materials for lithium-air and sodium-air batteries. The efforts were mainly focused on synthesis of several carbon-based nanomaterials, such as carbon nanoparticles, carbon nanotubes, and graphene nanosheets and the pristine and heteroatom-doped materials were employed as electrode materials as well as for structure design. Furthermore, a facile microwave-assisted hydrothermal method was developed for synthesizing various MnO_2 nanostructures which will be used as electrocatalysts for lithium-air and sodium-air batteries. The main research objectives are list below.

(1) To study the parameters of cathode made of porous carbon black powders and find out which of them determines the lithium-air battery performance. As described in the above section, several carbon blacks were employed as cathode materials in other research groups; however, it is still debatable about the influence of carbon black properties on the battery performance since different carbon blacks were used in previous work. In this research, carbon black were treated under different atmospheres and the several parameters, including porosity, nitrogen content, functional groups, defects, etc were controlled and the influence of these in carbon cathode were studied in detail.

(2) To design 3D electrodes with porous structure based on 1D CNTs and 2D GNSs, respectively. The interconnected opening structures in the electrodes provide ideal oxygen transportation channels as well as volume for accommodation of discharge products, increasing the battery performance. More importantly, the unsaturated carbon atoms at the edge of GNSs can increase activity for cathode reactions.

(3) To study the heteroatom-doping effects of carbon materials for battery performance. The carbon materials doped with other elements have shown superior activity for ORR or OER which makes these desired materials for lithium-air batteries. The finding will give a rational direction to modify other materials in this field.

(4) To investigate the morphological evolution of the discharge products of lithium-air batteries and the relationship between them ang the battery performance by designing the cathode materials. The structure, composition, and electronic properties of the discharge products of lithium-air batteries could affect the battery performance. However, there are less supported experimental results, therefore, it is necessary to get a further insight into the reaction mechanisms.

(5) To develop a facile method for synthesizing nanomaterials which can be applied as electrocatalysts for lithium-air batteries. The experimental parameters, such as the reaction time, temperature, etc. have significant effect on the morphology of the products. Through adjusting the above mentioned parameters, nanomaterials with different morphology and crystallinities can be obtained.

(6) To design 3D electrode with GNSs for sodium-air batteries. The porous electrode is also believed to be critical for sodium-air batteries since the discharge product will deposit in the electrode which is similar to lithium-air batteries. However, because of the different properties of sodium (radius, activity, etc), it is necessary to study the influence of cathode material and structures design.

1.6 Thesis organization

This thesis is consisted of ten chapters and fulfills the requirements on "Integrated-Article" form as outlined in the *Thesis Regulation Guide* by the School of Graduate and Postdoctoral Studie of the University of Western Ontario. It includes the following arrangement.

Chapter 1 gives an introduction to lithium-air and sodium-air batteries. In this section, the working principle, the challenges of the cathodes and the solutions by nanomaterials and nanotechnology are highlighted. Besides these, the research objectives and the thesis organization of this study are also clearly stated.

Chapter 2 describes the experimental procedures, including methods for materials synthesis and characterization techniques used to study the as-prepared materials.

Chapter 3 presents a detail study about the correlation between lithium-air battery performance and parameters of carbon black cathode, such as porosity, surface area, defects, heteroatom-doping, and functional groups. In this study, carbon blacks were treated under different atmospheres and all the parameters were controlled.

Chapter 4 reports a novel electrode based on 1D N-CNTs for lithium-air batteries. The CNT electrode provides not only increased electrical connectivity and mechanical integrity, but also interconnected channels for oxygen transportation. More importantly, it is found that the heteroatom-doping of nitrogen to CNTs significantly increased the battery performance which is due to the active sites introduced after doping.

Chapter 5 studies another novel electrode made of 2D GNSs for lithium-air batteries. The unique structures of GNSs form an ideal 3D three-phase electrochemical area and the diffusion channels for the electrolyte and oxygen, which increase the efficiency of the catalyst reactions. In addition, the active sites at the edge sites significantly contribute to the superior electrocatalytic activity towards ORR.

Chapter 6 describes the nitrogen-doping effects to GNSs electrode for lithium-air batteries. The changes of properties after doping elements to graphene framework and the influence of them to battery performance were studied and it is found that the defects and functional groups introduced played important roles in improving the performance.

Chapter 7 investigates the morphology and properties of discharge products of lithium-air batteries and the related charge performance. The composition, phase, and morphology evolution were studied and a growth mechanism was proposed. This study clearly shows that it is very important to select or design optimal growth of discharge products by substrate controlling, therefore, tailoring Li_2O_2 properties to battery performance.

Chapter 8 explores a facile rapid procedure to fabricate MnO_2 nanostructures by a microwave-assisted hydrothermal method. MnO_2 nanostructures with different morphology and crystallographic forms were selectively obtained by controlling the reaction parameters, such as temperature, reaction time, etc. The growth mechanism was studied and discussed in detail based on detailed observations in different growth stages. This study showed that this synthetic route is a promising way for synthesizing nanomaterials which can be used as electrocatalysts for lithium-air batteries.

Chapter 9 demonstrates that the nitrogen-doping effects to GNSs electrode also have influence for sodium-air battery performance. Several parameters, such as the cycleability, electrochemical impedance and discharge products of the battery were studied and it clearly gave a direction for developing cathode materials and structures for the sodium battery system.

Chapter 10 summarizes the results and contributions of the thesis work. In addition, some personal opinions and suggestions for future work are given by the author.

References

[1] F. Cheng, J. Liang, Z. Tao, J. Chen, Functional materials for rechargeable batteries, *Adv. Mater.*, 2011, **23**, 1695–1715.

[2] G. May, N. Maleschitz, H. Diermaier, T. Haeupl, The optimisation of grid designs for valve–regulated lead/acid batteries for hybrid electric vehicle applications, *J. Power Sources*, 2010, **195**, 4520–4524.

[3] B. Knosp, C. Jordy, P. Blanchard, T. Berlureau, Evaluation of $Zr(Ni,Mn)_2$ laves phase alloys as negative active material for Ni-MH electric vehicle batteries, *J. Electrochem. Soc.*, 1998, **145**, 1478–1482.

[4] X. Ji, K. Lee, L. Nazar, A highly ordered nanostructured carbon-sulphur cathode for lithium-sulphur batteries, *Nat. Mater.*, 2009, **8**, 500–506.

[5] X. Ji, S. Evers, R. Black, L. Nazar,Stabilizing lithium-sulphur cathodes using polysulphide reservoirs, *Nat. Commun.*, 2011, **2**, 325.

[6] A. Arico, P. Bruce, B. Scrosati, J. Tarascon, W. Schalkwijk, Nanostructured materials for advanced energy conversion and storage devices, *Nat. Mater.*, 2005, **4**, 366–377.

[7] G. Girishkumar, B. McCloskey, A. Luntz, S. Swanson, W. Wilcke, Lithium-air battery: Promise and challenges, *J. Phys. Chem. Lett.*, 2010, **1**, 2193–2203.

[8] J. Tarascon, M. Armand, Issues and challenges facing rechargeable lithium batteries, *Nature*, 2001, **414**, 359–367.

[9] M. Whittingham, Lithium batteries and cathode materials, *Chem. Rev.*, 2004, **104**, 4271–4301.

[10] P. Bruce, B. Scrosati, J. Tarascon, Nanomaterials for rechargeable lithium batteries, *Angew. Chem. Int. Ed.*, 2008, **47**, 2930–2946.

[11] J. Goodenough, Y. Kim, Challenges for rechargeable Li batteries, *Chem. Mater.*, 2010, **22**, 587–603.

[12] E. Deiss, F. Holzer, O. Haas, Modeling of an electrically rechargeable alkaline Zn-air battery, *Electrochim. Acta*, 2002, **47**, 3995–4010.

[13] J. Goldstein, I. Brown, B. Koretz, New developments in the Electric Fuel Ltd. zinc/air system, *J. Power Sources*, 1999, **80**, 171–179.

[14] X. Zhang, Fibrous zinc anodes for high power batteries, *J. Power Sources*, 2006, **163**, 591–597.

[15] J. Lee, S. Kim, R. Cao, N. Choi, M. Liu, K. Lee, J. Cho, Metal-air batteries with high energy density: Li-air versus Zn-air, *Adv. Energy Mater.*, 2011, **1**, 34–50.

[16] P. Bruce, S. Freunberger, L. Hardwick, J. Tarascon, Li-O_2 and Li-S batteries with high energy storage, *Nat. Mater.*, 2012, **11**, 19–29.

[17] P. Bruce, L. Hardwick, K. Abraham, Lithium-air and lithium-sulfur batteries, *MRS Bull.*, 2011, **36**, 506–512.

[18] A. Kraytsberg, Y. Ein-Eli, Review on Li-air batteries: Opportunities, limitations and perspective, *J. Power Sources*, 2011, **196**, 886–893.

[19] E. Littauer, K. Tsai, Anodic behavior of lithium in aqueous electrolytes I. Transient passivation, *J. Electrochem. Soc.*, 1976, **123**, 771–776.

[20] K. Abraham, Z. Jiang, A polymer electrolyte-based rechargeable lithium/oxygen battery, *J. Electrochem. Soc.*, 1996, **143**, 1–5.

[21] T. Ogasawara, A. Debart, M. Holzapfel, P. Novak, P. Bruce, Rechargeable Li_2O_2 electrode for lithium batteries, *J. Am. Chem. Soc.*, 2006, **128**, 1390–1393.

[22] J. Read, Characterization of the lithium/oxygen organic electrolyte battery, *J. Electrochem. Soc.*, 2002, **149**, A1190–A1195.

[23] T. Zhang, N. Imanishi, Y. Takeda, O. Yamamoto, Aqueous lithium/air rechargeable batteries, *Chem. Lett.*, 2011, **40**, 668–673.

[24] S. Visco, E. Nimon, B. Katz, L. Jonghe, M. Chu, Books of Abstract, The 12th International Meeting on Lithium Batteries, Nara, Japan, Jun. 27–Jul. 2, 2004; Abstract #53.

[25] S. Visco, E. Nimon, B. Katz, L. Jonghe, M. Chu, Books of Abstract, The Electrochemical Society Meeting, Cancun, Mexico, Oct. 29–Nov. 3, 2006; Abstract #0389.

[26] S. Visco, Y. Nimon, B. Katz, Ionically conductive composites for protection of active metal anodes, U. S. Patent, 2007, US 7,282,302, B2,

[27] T. Zhang, N. Imanishi, S. Hasegawa, A. Hirano, J. Xie, Y. Takeda, O. Yamamoto, N. Sammes, Li/polymer electrolyte/water stable lithium-conducting glass ceramics composite for lithium-air secondary batteries with an aqueous electrolyte, *J. Electrochem. Soc.*, 2008, **155**, A965–A969.

[28] T. Zhang, N. Imanishi, S. Hasegawa, A. Hirano, J. Xie, Y. Takeda, O. Yamamoto, N. Sammes, Water-stable lithium anode with the three-layer construction for aqueous lithium-air secondary batteries, *Electrochem. Solid-State Lett.*, 2009, **12**, A132–A135.

[29] N. Imanishi, S. Hasegawa, T. Zhang, A. Hirano, Y. Takeda, O. Yamamoto, Lithium anode for lithium-air secondary batteries, *J. Power Sources*, 2008, **185**, 1392–1397.

[30] S. Hasegawa, N. Imanishi, T. Zhang, J. Xie, A. Hirano, Y. Takeda, O. Yamamoto, Study on lithium/air secondary batteries-Stability of NASICON-type lithium ion conducting glass-ceramics with water, *J. Power Sources*, 2009, **189**, 371–377.

[31] Y. Shimonishi, T. Zhang, P. Johnson, N. Imanishi, A. Hirano, Y. Takeda, O. Yamamoto, N. Sammes, A study on lithium/air secondary batteries-Stability of NASICON-type glass ceramics in acid solutions, *J. Power Sources*, 2010, **195**, 6187–6191.

[32] T. Zhang, N. Imanishi, Y. Shimonishi, A. Hirano, J. Xie, Y. Takeda, O. Yamamoto, N. Sammes, Stability of a water-stable lithium metal anode for a lithium-air battery with acetic acid-water solutions, *J. Electrochem. Soc.*, 2010, **157**, A214–A218.

[33] L. Li, S. Zhao, A. Manthiram, A dual-electrolyte rechargeable Li-air battery with phosphate buffer catholyte, *Electrochem. Commun.*, 2012, **14**, 78–81.

[34] E. Yoo, H. Zhou, Li-air rechargeable battery based on metal-free graphene nanosheet catalysts, *ACS Nano*, 2011, **5**, 3020–3026.

[35] Y. Wang, P. He, H. Zhou, A lithium-air capacitor-battery based on a hybrid electrolyte, *Energy Environ. Sci.*, 2011, **4**, 4994–4999.

[36] Y. Wang, H. Zhou, A lithium-air fuel cell using copper to catalyze oxygen-reduction based on copper-corrosion mechanism, *Chem. Commun.*, 2010, **46**, 6305–6307.

[37] P. He, Y. Wang, H. Zhou, The effect of alkalinity and temperature on the performance of lithium-air fuel cell with hybrid electrolytes, *J. Power Sources*, 2011, **196**, 5611–5616.

[38] P. He, Y. Wang, H. Zhou, A Li-air fuel cell with recycle aqueous electrolyte for improved stability, *Electrochem. Commun.*, 2010, **12**, 1686–1689.

[39] Y. Wang, H. Zhou, A lithium-air battery with a potential to continuously reduce O_2 from air for delivering energy, *J. Power Sources*, 2010, **195**, 358–361.

[40] J. Zheng, R. Liang, M. Hendrickson, E. Plichta, Theoretical energy density of Li-air batteries, *J. Electrochem. Soc.*, 2008, **155**, A432–A437.

[41] P. He, Y. Wang, H. Zhou, Titanium nitride catalyst cathode in a Li-air fuel cell with an acidic aqueous solution, *Chem. Commun.*, 2011, **47**, 10701–10703.

[42] B. Kumar, J. Kumar, R. Leese, J. Fellner, S. Rodrigues, K. Abraham, A solid-state, rechargeable, long cycle life lithium-air battery, *J. Electrochem. Soc.*, 2010, **157**, A50–A54.

[43] B. Kumar, J. Kumar, Cathodes for solid-state lithium-oxygen cells: Roles of NASICON glass-ceramics, *J. Electrochem. Soc.*, 2010, **157**, A611–A616.

[44] E. Yoo, J. Nakamura, H. Zhou, N-doped graphene nanosheets for Li-air fuel cells under acidic conditions, *Energy Environ. Sci.*, 2012, **5**, 6928–6932.

[45] M. Chase, Jr., NIST-JANAF Thermochemical Tables, 4th ed., *J. Phys. Chem. Ref. Data, Monograph*, 1998, **9**.

[46] S. Zhang, D. Foster, J. Read, Discharge characteristic of a non-aqueous electrolyte Li/O_2 battery, *J. Power Sources*, 2010, **195**, 1235–1240.

[47] M. Radin, J. Rodriguez, F. Tian, D. Siegel, Lithium peroxide surfaces are metallic, while lithium oxide surfaces are not, *J. Am. Chem. Soc.*, 2012, **134**, 1093–1103.

[48] T. Fujinaga, S. Sakura, Polarographic investigation of dissolved-oxygen in non-aqueous solvent, *Bull. Chem. Soc. Jpn.*, 1974, **47**, 2781–2786.

[49] D. Sawyer, G. Chlericato, C. Angelis, E. Nanni, T. Tsuchiya, Effects of media and electrode materials on the electrochemical reduction of dioxygen, *Anal. Chem.*, 1982, **54**, 1720–1724.

[50] D. Aurbach, M. Daroux, P. Faguy, E. Yeager, The electrochemistry of noble metal electrodes in aprotic organic solvents containing lithium salts, *J Electroanal. Chem*, 1991, **297**, 225–244.

[51] Y. Lu, H. Gasteiger, E. Crumlin, R. McGuire, Y. Shao-Horn, Electrocatalytic activity studies of select metal surfaces and implications in Li-air batteries, *J. Electrochem. Soc.*, 2010, **157**, A1016–A1025.

[52] C. Laoire, S. Mukerjee, K. Abraham, E. Plichta, M. Hendrickson, Elucidating the mechanism of oxygen reduction for lithium-air battery applications, *J. Phys. Chem. C*, 2009, **113**, 20127–20134.

[53] C. Laoire, S. Mukerjee, K. Abraham, E. Plichta, M. Hendrickson, Influence of nonaqueous solvents on the electrochemistry of oxygen in the rechargeable lithium-air battery, *J. Phys. Chem. C*, 2010, **114**, 9178–9186.

[54] S. Freunberger, Y. Chen, N. Drewett, L. Hardwick, F. Bard, P. Bruce, The lithium-oxygen battery with ether-based electrolytes, *Angew. Chem. Int. Ed.*, 2011, **50**, 8609–8613.

[55] C. Tran, X. Yang, D. Qu, Investigation of the gas-diffusion-electrode used as lithium/air cathode in non-aqueous electrolyte and the importance of carbon material porosity, *J. Power Sources*, 2010, **195**, 2057–2063.

[56] B. McCloskey, R. Scheffler, A. Speidel, D. Bethune, R. Shelby, A. Luntz, On the efficacy of electrocatalysis in nonaqueous Li-O_2 batteries, *J. Am. Chem. Soc.*, 2011, **133**, 18038–18041.

[57] X. Ren, S. Zhang, D. Tran, J. Read, Oxygen reduction reaction catalyst on lithium/air battery discharge performance, *J. Mater. Chem.*, 2011, **21**, 10118–10125.

[58] Y. Lu, H. Gasteiger, M. Parent, V. Chiloyan, Y. Shao-Horn, The influence of catalysts on discharge and charge voltages of rechargeable Li-oxygen batteries, *Electrochem. Solid-State Lett.*, 2010, **13**, A69–A72.

[59] G. Cao, Nanostructures & nanomaterials synthesis, properties & applications. Imperial College Press, 2004.

[60] H. Nalwa, Handbook of nanostructured materials and nanotechnology. Academic Press, San Diego, 2000.

[61] Z. Wang, Transmission electron microscopy of shape-controlled nanocrystals and their assemblies, *J. Phys. Chem. B*, 2000, **104**, 1153–1175.

[62] C. Zhong, J. Luo, B. Fang, B. Wanjala, P. Njoki, R. Loukrakpam, J. Yin, Nanostructured catalysts in fuel cells, *Nanotechnology*, 2010, **21**, 062001.

[63] X. Xie, W. Shen, Morphology control of cobalt oxide nanocrystals for promoting their catalytic performance, *Nanoscale*, 2009, **1**, 50–60.

[64] X. Chen, C. Li, M. Gratzel, R. Kostechi, S. Mao, Nanomaterials for renewable energy production and storage, *Chem. Soc. Rev.,* 2012, **41**, 7909–7937.

[65] Y. Yang, Q. Sun, Y. Li, H. Li, Z. Fu, Nanostructured diamond like carbon thin film electrodes for lithium air batteries, *J. Electrochem. Soc.*, 2011, **158**, B1211–B1216.

[66] M. Mirzaeian, P. Hall, Preparation of controlled porosity carbon aerogels for energy storage in rechargeable lithium oxygen batteries, *Electrochim. Acta*, 2009, **54**, 7444–7451.

[67] X. Yang, P. He, Y. Xia, Preparation of mesocellular carbon foam and its application for lithium/oxygen battery, *Electrochem. Commun.*, 2009, **11**, 1127–1130.

[68] Q. Zhang, E. Uchaker, S. Candelaria, G. Cao, Nanomaterials for energy conversion and storage, *Chem. Soc. Rev.*, 2013, **42**, 3127–3171.

[69] R. Mitchell, B. Gallant, C. Thompson, Y. Shao-Horn, All-carbon-nanofiber electrodes for high-energy rechargeable Li-O_2 batteries, *Energy Environ. Sci.*, 2011, **4**, 2952–2958.

[70] B. Sun, B. Wang, D. Su, L. Xiao, H. Ahn, G. Wang, Graphene nanosheets as cathode catalysts for lithium-air batteries with an enhanced electrochemical performance, *Carbon*, 2012, **50**, 727–733.

[71] Y. Wang, H. Zhou, To draw an air electrode of a Li-air battery by pencil, *Energy Environ. Sci.*, 2011, **4**, 1704–1707.

[72] S. Younesi, S. Urbonaite, F. Bjorefors, K. Edstrom, Influence of the cathode porosity on the discharge performance of the lithium-oxygen battery, *J. Power Sources*, 2011, **196**, 9835–9838.

[73] R. Williford, J. Zhang, Air electrode design for sustained high power operation of Li/air batteries, *J. Power Sources*, 2009, **194**, 1164–1170.

[74] Y. Lu, D. Kwabi, K. Yao, J. Harding, J. Zhou, L. Zuin, Y. Shao-Horn, The discharge rate capability of rechargeable Li-O_2 batteries, *Energy Environ. Sci.*, 2011, **4**, 2999–3007.

[75] G. Shitta-Bey, M. Mirzaeian, P. Halla, The electrochemical performance of phenol-formaldehyde based activated carbon electrodes for lithium/oxygen batteries, *J. Electrochem.Soc.*, 2012, **159**, A315–A320.

[76] G. Zhang, J. Zheng, R. Liang, C. Zhang, B. Wang, M. Hendrickson, E. Plichta, Lithium-air batteries using SWNT/CNF buckypapers as air electrodes, *J. Electrochem. Soc.*, 2010, **157**, A953–A956.

[77] J. Xiao, D. Mei, X. Li, W. Xu, D. Wang, G. Graff, W. Bennett, Z. Nie, L. Saraf, I. Aksay, J. Liu, J. Zhang, Hierarchically porous graphene as a lithium-air battery electrode, *Nano Lett.*, 2011, **11**, 5071–5078.

[78] Y. Cui, Z. Wen, Y. Liu, A free-standing-type design for cathodes of rechargeable Li-O_2 batteries, *Energy Environ. Sci.*, 2011, **4**, 4727–4734.

[79] A. Debart, J. Bao, G. Armstrong, P. Bruce, An O_2 cathode for rechargeable lithium batteries: the effect of a catalyst, *J. Power Sources*, 2007, **174**, 1177–1182.

[80] T. Yoon, Y. Park, Carbon nanotube/Co_3O_4 composite for air electrode of lithium-air battery, *Nanoscale Res. Lett.*, 2012, **7**, 1–4.

[81] Y. Cui, Z. Wen, S. Sun, Y. Lu, J. Jin, Mesoporous Co_3O_4 with different porosities as catalysts for the lithium-oxygen cell, *Solid State Ionics*, 2012, **225**, 598–603.

[82] A. Debart, A. Paterson, J. Bao, P. Bruce, α-MnO_2 nanowires: A catalyst for the O_2 electrode in rechargeable lithium batteries, *Angew. Chem. Int. Ed.*, 2008, **47**, 4597–4600.

[83] G. Zhang, J. Zheng, R. Liang, C. Zhang, B. Wang, M. Au, M. Hendrickson, E. Plichta, α-MnO_2/carbon nanotube/carbon nanofiber composite catalytic air electrodes for rechargeable lithium-air batteries, *J. Electrochem. Soc.*, 2011, **158**, A822–A827.

[84] J. Li, N. Wang, Y. Zhao, Y. Ding, L. Guan, MnO_2nanoflakes coated on multi-walled carbon nanotubes for rechargeable lithium-air batteries, *Electrochem. Commun.*, 2011, **13**, 698–700.

[85] H. Cheng, K. Scott, Carbon-supported manganese oxide nanocatalysts for rechargeable lithium-air batteries, *J. Power Sources*, 2010, **195**, 1370–1374.

[86] S. Ida, A. Thapa, Y. Hidaka, Y. Okamoto, M. Matsuka, H. Hagiwara, T. Ishihara, Manganese oxide with a card-house-like structure reassembled from nanosheets for rechargeable Li-air battery, *J. Power Sources*, 2012, **203**, 159–164.

[87] L. Jin, L. Xu, C. Morein, C. Chen, M. Lai, S. Dharmarathna, A. Dobley, S. Suib, Titanium containing γ-MnO_2 (TM) hollow spheres: One-step synthesis and catalytic

activities in Li/air batteries and oxidative chemical reactions, *Adv. Funct. Mater.*, 2010, **20**, 3373–3382.

[88] P. Andrei, J. Zheng, M. Hendrickson, E. Plichta, Some possible approaches for improving the energy density of Li-air batteries, *J. Electrochem. Soc.*, 2010, **157**, A1287–A1295.

[89] G. Dathar, W. Shelton, Y. Xu, Trends in the catalytic activity of transition metals for the oxygen reduction reaction by lithium, *J. Phys. Chem. Lett.*, 2012, **3**, 891–895.

[90] Y. Lu, H. Gasteiger, E. Crumlin, R. McGuire, Y. Shao-Horn, Electrocatalytic activity studies of select metal surfaces and implications in Li-air batteries, *J. Electrochem. Soc.*, 2010, **157**, A1016–A1025.

[91] Y. Lu, H. Gasteiger, M. Parent, V. Chiloyan, Y. Shao-Horn, The influence of catalysts on discharge and charge voltages of rechargeable Li-oxygen batteries, *Electrochem. Solid-State Lett.*, 2010, **13**, A69–A72.

[92] Y. Xu, W. Shelton, O_2 reduction by lithium on Au(111) and Pt(111), *J. Chem. Phys.*, 2010, **133**, 024703.

[93] J. Chen, J. Hummelshoj, K. Thygesen, J. Myrdal, J. Norskov, T. Vegge, The role of transition metal interfaces on the electronic transport in lithium-air batteries, *Catal. Today*, 2011, **165**, 2–9.

[94] A. Thapa, K. Saimen, T. Ishihara, Pd/MnO_2 air electrode catalyst for rechargeable lithium/air battery, *Electrochem Solid-State Lett.*, 2010, **13**, A165–A167.

[95] A. Thapa, T. Ishihara, Mesoporous α-MnO_2/Pd catalyst air electrode for rechargeable lithium-air battery, *J. Power Sources*, 2011, **196**, 7016–7020.

[96] S. Zhang, D. Foster, J. Read, Heat-treated metal phthalocyanine complex as an oxygen reduction catalyst for non-aqueous electrolyte Li/air batteries, *Electrochim. Acta*, 2011, **56**, 4544–4548.

[97] S. Lee, S. Zhu, C. Milleville, C. Lee, P. Chen, K. Takeuchi, E. Takeuchi, A. Marschilok, The influence of catalysts on discharge and charge voltages of rechargeable Li-oxygen batteries, *Electrochem. Solid-State Lett.*, 2010, **13**, A162–A164.

[98] A. Marschilok, S. Zhu, C. Milleville, S. Lee, E. Takeuchi, K. Takeuchi, Electrodes for nonaqueous oxygen reduction based upon conductive polymer-silver composites, *J. Electrochem. Soc.*, 2011, **158**, A223–A226.

[99] S. Dong, X. Chen, K. Zhang, L. Gu, L. Zhang, X. Zhou, L. Li, Z. Liu, P. Han, H. Xu, J. Yao, C. Zhang, X. Zhang, C. Shang, G. Cui, L. Chen, Molybdenum nitride based hybrid cathode for rechargeable lithium-O_2 batteries, *Chem. Commun.*, 2011, **47**, 11291–11293.

[100] Z. Fu, X. Lin, T. Huang, A. Yu, Nano-sized $La_{0.8}Sr_{0.2}MnO_3$ as oxygen reduction catalyst in nonaqueous Li/O_2 batteries, *J. Solid State Electrochem.*, 2012, **16**, 1447–1452.

[101] X. Lu, G. Xia, J. Lemmon, Z. Yang, Advanced materials for sodium-beta alumina batteries: Status, challenges and perspectives, *J. Power Sources*, 2010, **195**, 2431–2442.

[102] S. Kim, D. Seo, X. Ma, G. Ceder, K. Kang, Electrode materials for rechargeable sodium-ion batteries: Potential alternatives to current lithium-ion batteries, *Adv. Energy Mater.*, 2012, **2**, 710–721.

[103] E. Peled, D. Golodnitsky, H. Mazor, M. Goor, S. Avshalomov, Parameter analysis of a practical lithium- and sodium-air electric vehicle battery, *J. Power Sources*, 2011, **196**, 6835–6840.

[104] Q. Sun, Y. Yang, Z. Fu, Electrochemical properties of room temperature sodium-air batteries with non-aqueous electrolyte, *Electrochem.Commoun.*, 2012, **16**, 22–25.

[105] S. Das, S. Xu, L. Archer, Carbon dioxide assist for non-aqueous sodium-oxygen batteries, *Electrochem. Commoun.*, 2013, **27**, 59–62.

[106] P. Hartmann, C. bender, M. Vracar, A. Durr, A. Garsuch, J. Janek, P. Adelhelm, A rechargeable room-temperature sodium superoxide (NaO_2) battery, *Nat. Mater.*, 2013, **12**, 228–232.

[107] W. Liu, Q. Sun, Y. Yang, J. Xie, Z. Fu, An enhanced electrochemical performance of a sodium-air battery with graphene nanosheets as air electrode catalysts, *Chem. Commun.*, 2013, **49**, 1951–1953.

[108] J. Kim, H. Lim, H. Gwon, K. Kang, Sodium-oxygen batteries with alkyl-carbonate and ether based electrolytes, *Phys. Chem. Chem. Phys.*, 2013, **15**, 3623–3629.

Chapter 2

2 Experimental and Characterizations

In this chapter, the methods for material synthesis and characterization techniques are described.

2.1 Experimental

2.1.1 Synthesis of porous carbon blacks

The synthesis of carbon blacks with different porosity have been widely reported [1-4]. Commercial N330 furnace carbon black (from Sid Richardson Carbon Corporation) was used as the starting material. It was heat-treated under NH_3 or CO_2 (with or without H_2) atmospheres. The percentage of mass that was lost during the heat-treatment, W, was calculated as follows:

$$W = \frac{initial\ mass - final\ mass}{initial\ mass} \times 100 \qquad (2.1)$$

2.1.1.1 Samples treated by NH_3

Typically, 500 mg of carbon black powder was spread in a fused silica boat and then the boat was introduced in a fused silica tube (5 cm diameter). Ar was purged into the tube for 30 min. Then the tube was place in an oven and NH_3 was introduced into the tube when the temperature of the oven reached to 1050 ^{o}C. Based on the desired mass losses (10, 35, 54, 75, 85%), different pyrolysis time was applied for the heat-treatment. It is to note that for the 75 and 85% mass losses, the samples were made with several pyrolysis to obtain around 150-200 mg of final powder.

2.1.1.2 Samples treated by CO_2 (with or without H_2)

Typically, 500 mg of carbon black was spread in a fused silica boat and then the boat was introduced in a fused silica tube (5 cm diameter). Ar was purged into the tube for 30 min. Then the tube was place in an oven and CO_2 was introduced into the tube when the temperature of the oven reached to 1050 ^{o}C. Based on desired mass losses (13, 35, 50, 75%), different pyrolysis time was applied for the heat-treatment. For the

75% mass loss, the sample was again made with several pyrolysis to obtain around 150-200 mg of final powder. These samples were further pyrolysed under H_2 at 950 ^oC to remove oxygen. It is possible that some oxygen was introduced in the sample by simple contact with air after pyrolysis.

2.1.2 Synthesis of nitrogen-doped carbon nanotubes (N-CNTs)

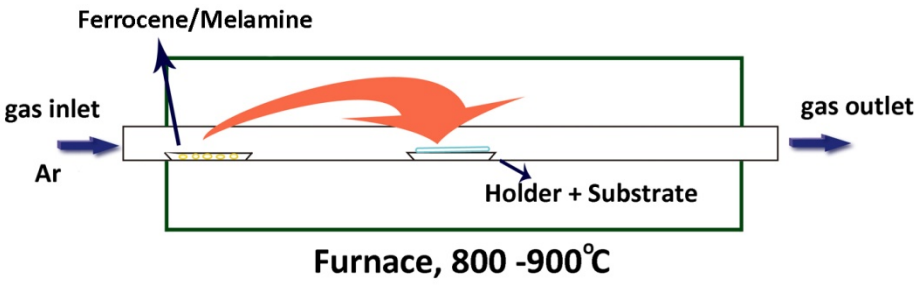

Figure 2.1 Schematic diagram of FCCVD method for synthesis of N-CNTs.

The nitrogen-doped carbon nanotubes (N-CNTs) were synthesized by a floating catalyst chemical vapor deposition (FCCVD) method [5], as shown in **Figure 2.1**. The experiment was carried out in a tube furnace (Lindberg/Blue, Mini-Mite Tube Furnace, Model: TF55035A) system. Typically, 100 mg of ferrocene (Sigma-Aldrich, 98%) and 1000 mg of melamine were placed at the entrance of the furnace in a quartz tube. As the system reached to the target temperature (800-900 ^oC), the vapor of ferrocene with melamine was carried by Ar flow of 320 sccm into the high temperature region where the substrate was placed. The furnace was turned off after 30 min and cooled down to room temperature. The as-prepared N-CNTs were collected from the substrate.

2.1.3 Synthesis of graphene nanosheets (GNSs), nitrogen-doped graphene nanosheets (N-GNSs), and sulphur-doped graphene nanosheets (S-GNSs)

Graphene nanosheets (GNSs) were prepared by the oxidation of graphite powder using the modified Hummers' method [6, 7]. All the chemicals used in this experiment were of analytical grade from Sigma-Aldrich Company and used without further purification. In a typical process, 1 g of graphite powder (325 mesh), 0.75 g of $NaNO_3$ and 4.5 g of $KMnO_4$ were added to 37.5 ml of concentrated H_2SO_4 and stirred for 2 h in an ice water bath. Then the mixture was stirred for five days at room temperature. 100 mL of 5 wt. % H_2SO_4 and 3 g of 30 wt. % H_2O_2 were added into the above mixture in sequence under stirring with interval of 1 h. After stirring for 2 h, the sample was filtered and washed until the pH=7. The as-received sample was dried in a vacuum oven at 60 ^oC and heated at 1050 ^oC for 30 s under Ar to produce GNSs.

Nitrogen-doped graphene nanosheets (N-GNSs) were synthesized by heat-treated GNSs under NH_3 atmosphere [8, 9]. Typically, 100 mg of GNSs was put on a quartz boat and placed in the middle of the furnace (high temperature region). When the temperature was reached to 900 ^oC, a mixture of Ar and NH_3 (with a ratio of 9:1) flow of 200 sccm was introduced. The furnace was turned off after 10 min and cooled down to room temperature. N-GNSs samples were collected from the boat.

To prepare sulphur-doped graphene nanosheets (S-GNSs), 50 mg of graphene nanosheets were dispersed into acetone with 800 mg of p-toluenesulfonic acid (Alfa Aesar, 97%). Then the slurry was stirred at room temperature until the solvent was totally evaporated. And the resulting product was dried at 100 ^oC over night and finally was calcined at 900 ^oC in Ar flow of 200 sccm for 1 hour [10, 11].

2.1.4 Synthesis of manganese oxide (MnO_2) nanostructures

Figure 2.2 A photo of an Anton Paar Synthos 3000 microwave synthesis system in our lab.

Synthesis of manganese oxides using microwave-assisted hydrothermal method is performed in a Synthos 3000 microwave synthesis system (Anton Paar), as shown in **Figure 2.2**. In a typical synthesis, 1.5 mmol of $KMnO_4$ was added to 20 ml deionized water to form a homogeneous solution. 0.5 ml of HCl (37 wt. %) was then added dropwise into the solution under magnetic stirring. After stirring for 20 min, the obtained solution was transferred to a 100 ml Teflon-lined ceramic-walled vessel. The autoclave was sealed and heated to different reaction temperatures (100, 140, and 180 ºC) with the same holding time of 25 min in an Anton Paar Synthos 3000 microwave synthesis system. After the autoclave was cooled down to room temperature, the

sample was collected by centrifugation and washed with deionized water and absolute ethanol several times to remove the impurities, and dried in air at 80 ºC for 12 h.

2.2 Characterizations

The structure, composition, bonding environment, etc have been identified by a variety of microscopy and spectroscopy techniques, including scanning electron microscope (SEM), transmission electron microscope (TEM), X-ray photoelectron spectroscopy (XPS), X-ray diffraction (XRD), and Raman spectroscopy; and the electrochemical activity and performance of the as-prepared samples were characterized by cyclic voltammetry (CV), and full battery testing (**Figure 2.3**).

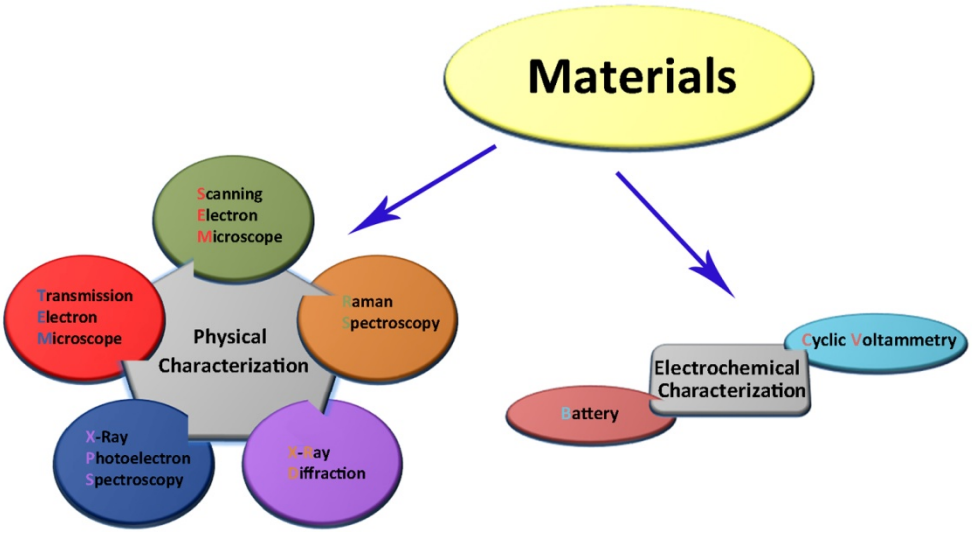

Figure 2.3 Characterization techniques in this research.

2.2.1 Physical characterizations

The morphology of solid state materials can be observed by a scanning electron microscope (SEM) [12]. It is a powerful instrument to study the surface of nanostructures and produce high-resolution images for the details. The as-prepared samples were examined by SEM (Hitachi S-4800) operated at 5kV. The instrument is shown in **Figure 2.4**.

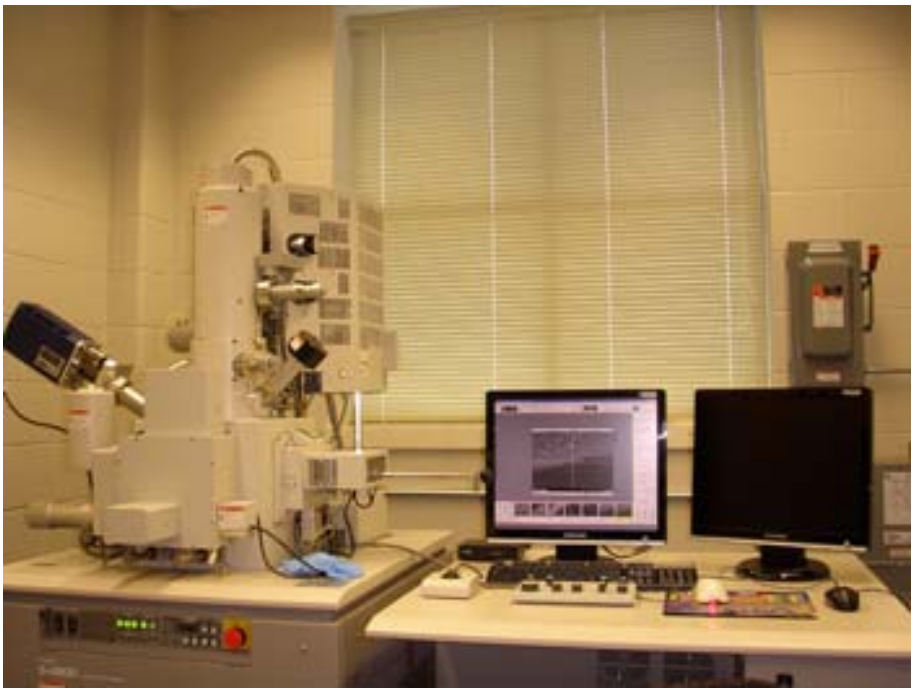

Figure 2.4 A photo of a Hitachi S-4800 SEM in our lab.

Transmission electron microscopy (TEM) is a technique to study the structural information of nanomaterials [13]. During the operating, electrons will pass through the samples which are thin enough. Compared to SEM, the TEM can observe the information much deeper in the materials and by using high-resolution TEM (HRTEM), the lattice information as well as the diffraction patterns can be obtained. The regular TEM images were obtained by Hitachi H-7000, as shown in **Figure 2.5**; while the HRTEM images were obtained by JEOL JEM-2100, operating at 200 kV.

Figure 2.5 A photo of a Hitachi H-7000 TEM in our lab.

X-ray photoelectron spectroscopy (XPS) is a spectroscopic technique to determine the surface chemistry, such as elemental composition, chemical states, and electronic state, etc. This technique is very surface sensitive since it can only measure the kinetic energy and number of electrons which escape from the top 1 to 10 nm of the material [14]. The XPS analysis was carried out by a Kratos Axis Ultra X-ray photoelectron spectrometer with Al Kα as the X-ray source at a base pressure of 2×10^{-9} mbar, as shown in **Figure 2.6**.

Figure 2.6 A photo of a Kratos Axis Ultra X-ray photoelectron spectrometer [15].

X-ray diffraction (XRD) is a technique which reveals detailed information about the crystal structure, chemical composition and physical properties of materials [16]. The XRD patterns were recorded on a Bruker D8 Discover diffractometer employing a Co-Kα source, as shown in **Figure 2.7**.

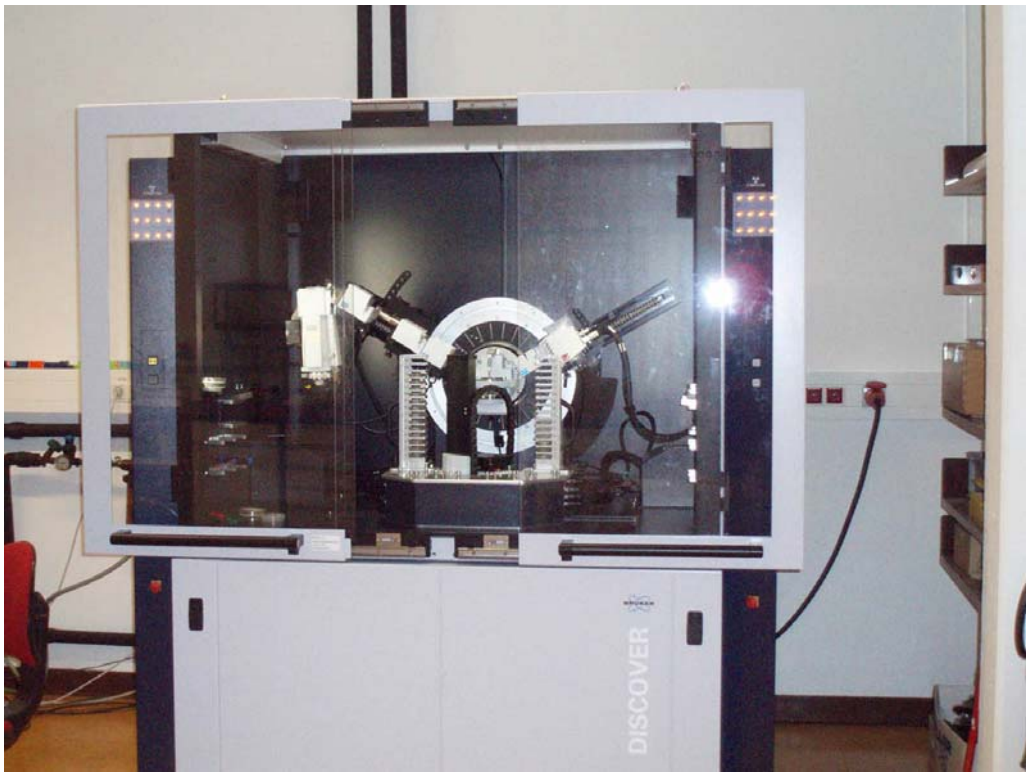

Figure 2.7 A photo of a Bruker D8 Discover diffractometer [17].

Raman spectroscopy is a spectroscopic technique used to obtain the vibrational, rotational information of chemical bonds in materials by determining the photon energy shift which is caused by the interaction between the laser light and the molecular vibrations [18]. Raman scattering spectra were recorded on a HORIBA Scientific LabRAM HR Raman spectrometer system equipped with a 532.4 nm laser, as shown in **Figure 2.8**. Typically, the ratio between peaks at ~ 1345 cm^{-1} (D band) and ~ 1570 cm^{-1} (G band) is used to evaluate the disorder in the carbon materials [19].

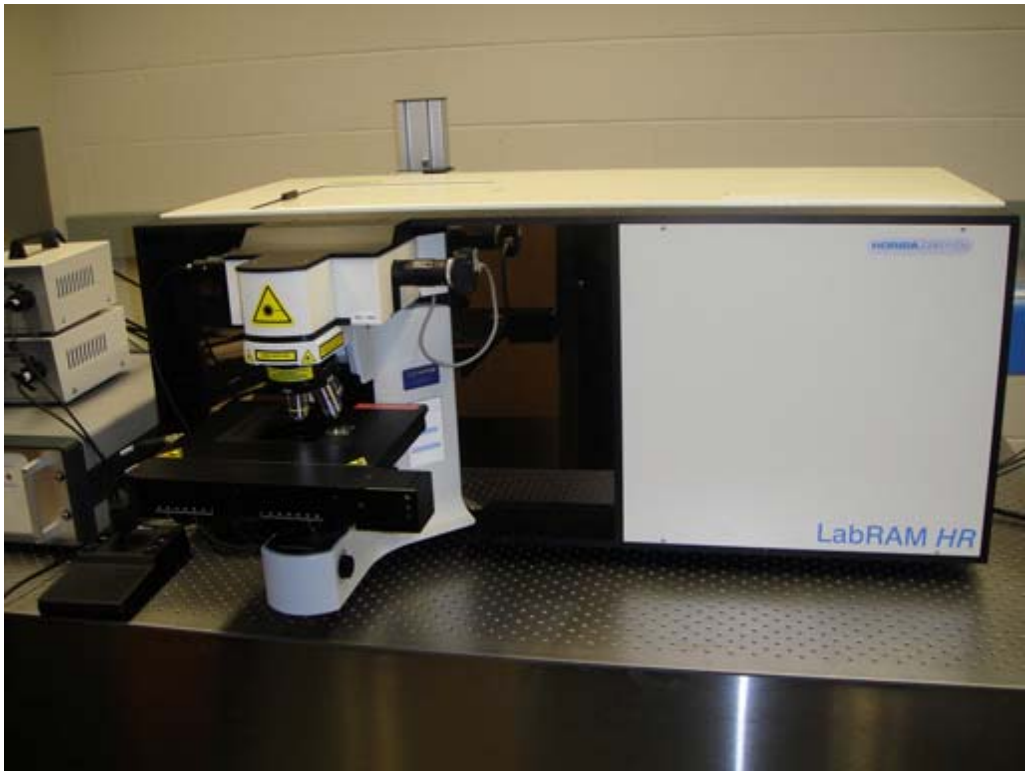

Figure 2.8 A photo of a HORIBA Scientific LabRAM HR Raman spectrometer in our lab.

2.2.2 Electrochemical characterizations

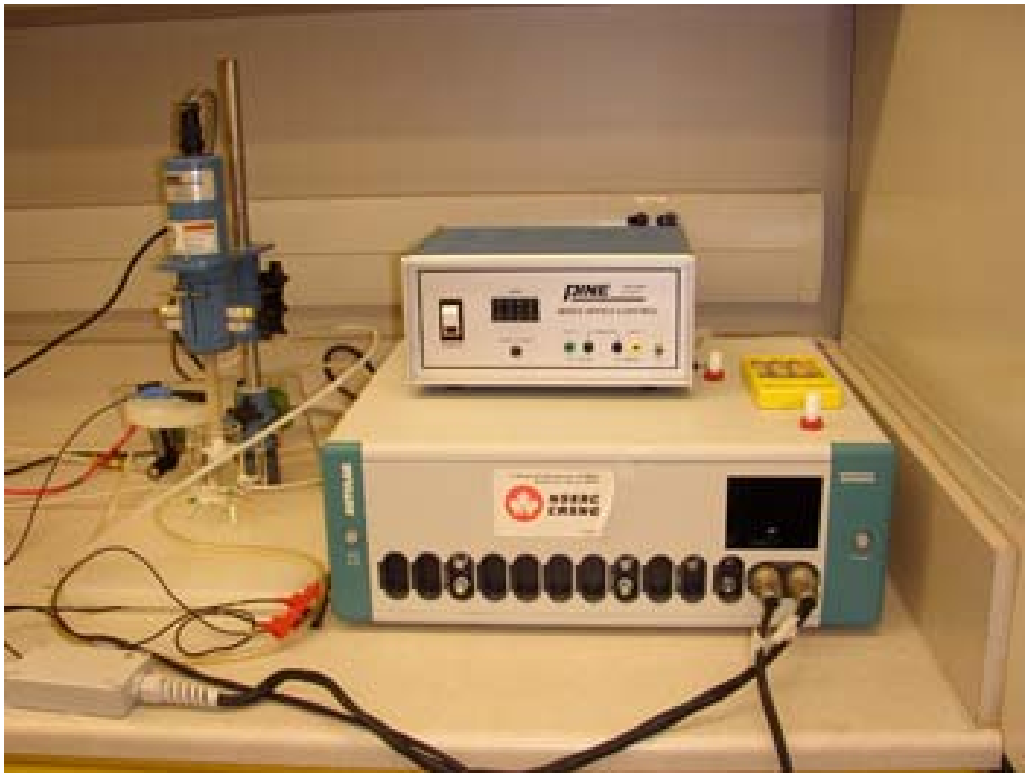

Figure 2.9 A photo of an Autolab potentiostat/galvanostat (Model, PGSTAT-30, Ecochemie, Brinkman Instruments) with rotation control (MSR, Pine Instruments).

The electrocatlytic activity is measured by cyclic voltammetry (CV) tests conducting in a three-electrode cell. A platinum wire was used as the counter electrode. A silver wire immersed into 0.1 mol dm^{-3} $AgNO_3$ in tetraethylene glycol dimethyl ether (TEGDME) solution, connected to the main solution by a glass frit, was used as reference electrode. A glass carbon disk (0.196 cm^2, Pine Inc.) covered with catalyst thin film was used as the working electrode. Typically, 2 mg of GNSs or N-GNSs, 2 mg of Polytetrafluoroethene (PTFE) (Sigma-Aldrich, 60 wt.%) were suspended in a 30 vol. % 2-propanol (Sigma-Aldrich) solution in deionized water and ultrasonically

blended for 30 min. 10 μL of the suspension was dropped on the disk electrode and dried at 80 °C in vacuum for 1 h. CV curves were recorded by scanning the disk potential from 3.5 to 2.0 V (0.1 mol dm^{-3} $LiPF_6$ in TEGDME solution) at a scan rate of 5 mV s^{-1} using an Autolab Potentiostat/Galvanostat (PGSTAT-30, Eco Chemie, Brinkmann Instruments) at room temperature (25 °C) (**Figure 2.9**).

Swagelok type cells were used to test the battery performance [20]. Typically, GNSs or N-GNSs and Poly(vinylidene fluoride) (PVDF) (Alfa Aesar) with a weight ratio of 9:1 were casted onto a separator (Celgard 3500) as cathode. The electrodes were cut to 3/8 inch in diameter and the loadings of GNSs or N-GNSs were ~ 0.3 mg. The electrolyte was 1 mol dm^{-3} $LiPF_6$ dissolved in TEGDME solution. The discharge/charge characteristics were performed using an Arbin BT-2000 battery station in a voltage range of 2.0-4.5 V in a 1 atm oxygen atmosphere at room temperature (25 °C) (**Figure 2.10**). Electrochemical impedance spectroscopic (EIS) analysis was conducted to study the electrode polarization. Electrochemical impedance spectra were recorded in the frequency range of 0.01-10^5 Hz using a VMP3 Potentiostat (BioLogic Science Instruments). The resulted spectra were fitted by ZView software.

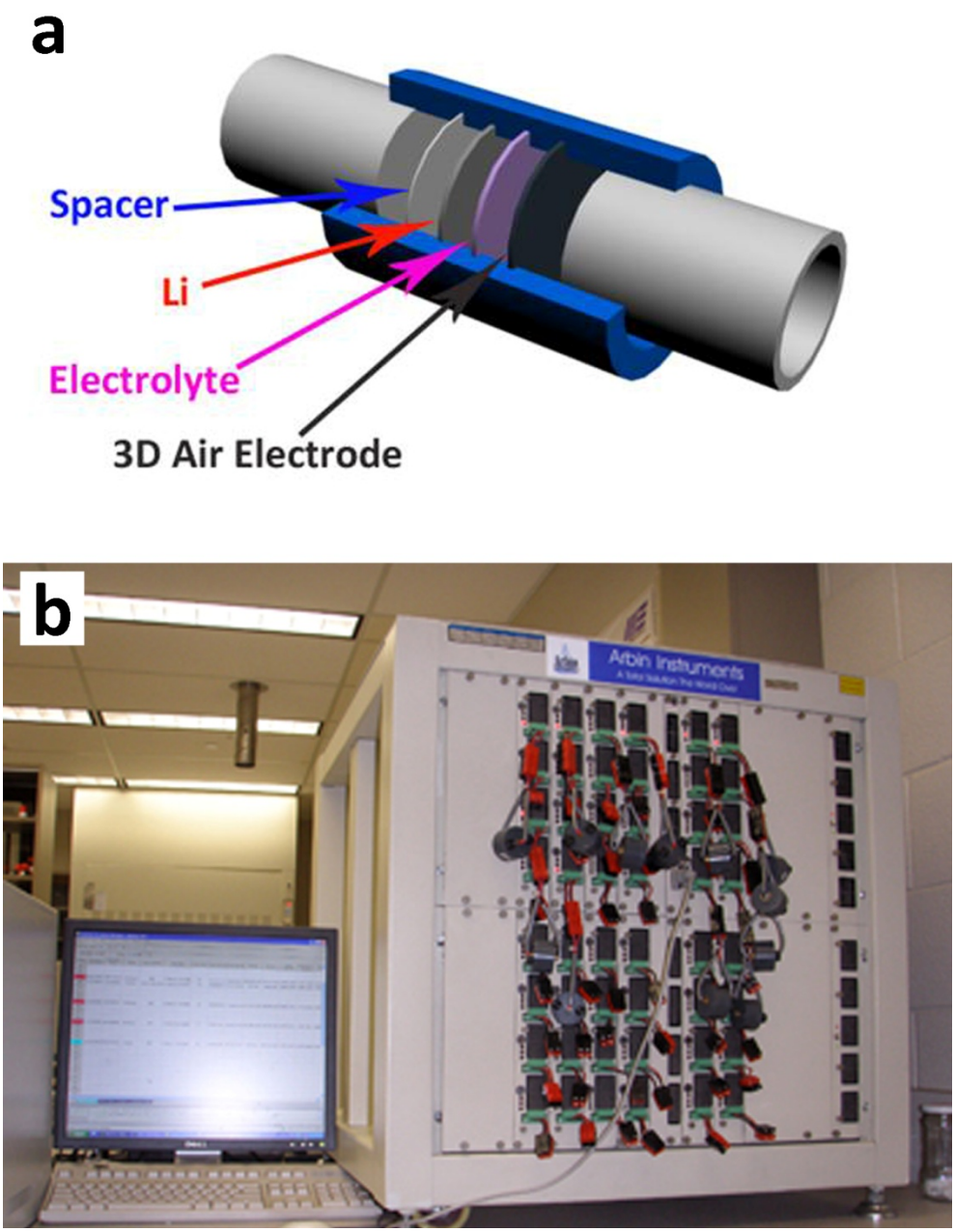

Figure 2.10 (a) A diagram illustration of swagelok type cells, (b) a photo of an Arbin BT-2000 battery test station.

References

[1] H. Meng, N. Larouche, M. Lefèvre, F. Jaouen, B. Stansfield, J.-P. Dodelet, Iron porphyrin-based cathode catalysts for polymer electrolyte membrane fuel cells: Effect of NH_3 and Ar mixtures as pyrolysis gases on catalytic activity and stability, *Electrochim. Acta*, 2010, **55**, 6450–6461.

[2] S. Ruggeri, J.-P. Dodelet, Influence of structural properties of pristine carbon blacks on activity of Fe/N/C cathode catalysts for PEFCs, *J. Electrochem. Soc.*, 2007, **154**, B761–B769.

[3] F. Jaouen, J.-P. Dodelet, Non-noble electrocatalysts for O_2 reduction: How does heat treatment affect their activity and structure? Part I. Model for carbon black gasification by NH_3: Parametric calibration and electrochemical validation, *J. Phys. Chem. C*, 2007, **111**, 5963–5970.

[4] F. Jaouen, A. Serventi, M. Lefèvre, J.-P. Dodelet, P. Bertrand, Non-noble electrocatalysts for O_2 reduction: How does heat treatment affect their activity and structure? Part II. Structural changes observed by electron microscopy, Raman, and mass spectroscopy, *J. Phys. Chem. C*, 2007, **111**, 5971–5976.

[5] H. Liu, Y. Zhang, R. Li, X. Sun, D. Désilets, H. Abou-Rachid, Structural and morphological control, nitrogen incorporation and stability of aligned nitrogen-doped carbon nanotubes, *Carbon*, 2010, **48**, 1498–1507.

[6] W. Hummers Jr., R. Offeman, Preparation of graphitic oxide, *J. Am. Chem. Soc.*, 1958, **80**, 1339–1339.

[7] A. Geim, Graphene: Status and prospects, *Science*, 2009, **324**, 1530–1534.

[8] D. Geng, Y. Chen, Y. Chen, Y. Li, R. Li, X. Sun, S. Ye, S. Knights, High oxygen-reduction activity and durability of nitrogen-doped graphene, *Energy Environ. Sci.*, 2011, **4**, 760–764.

[9] D. Geng, S. Yang, Y. Zhang, J. Yang, J. Liu, R. Li, T.-K. Sham, X. Sun, S. Ye, S. Knights, Nitrogen doping effects on the structure of graphene, *Appl. Surf. Sci.*, 2011, **257**, 9193–9198.

[10] H. Schniepp, J.-L. Li, M. McAllister, H. Sai, M. Herrera-Alonso, D. Adamson, R. Prud'homme, R. Car, D. saville, I. Aksay, Functionalized single graphene sheets derived from splitting graphite oxide, *J. Phys. Chem. B*, 2006, **110**, 8535–8539.

[11] X. Li, D. Geng, Y. Zhang, X. Meng, R. Li, X. Sun, Superior cycle stability of nitrogen-doped graphene nanosheets as anode for lithium ion batteries, *Electrochem. Commun.*, 2011, **13**, 822–825.

[12] G. Goldstein, D. Newbury, P. Echlin, D. Joy, C. Fiori, E. Lifshin, Scanning electron microscopy and X-ray microanalysis, Plenum Press, New York, 1981.

[13] B. Fultz, J. Howe, Transmission electron microscopy and diffractometry of materials, Springer-Verlag Berlin Heidelberg, 2008.

[14] C. Corcorana, H. Tavassola, M. Rigsbya, P. Bagusb, A. Wieckowskia, Application of XPS to study electrocatalysts for fuel cells, *J. Power Sources*, 2010, **195**, 7856–7879.

[15] http://www.surfacesciencewestern.com

[16] J. Skakle, Applications of X-ray powder diffraction in materials chemistry, *Chem. Rec.*, 2005, **5**, 252–262.

[17] http://camcor.uoregon.edu

[18] M. Banholzer, J. Millstone, L. Qin, C. Mirkin, Rationally designed nanostructures for surface-enhanced Raman spectroscopy, *Chem. Soc. Rev.*, 2008, **37**, 885–897.

[19] J. Huang, W. Chen, C. Lee, Y. Chang, Role of amorphous carbon nanowires in reducing the turn-on field of carbon films prepared by microwave-heated CVD, *Diamond Relat. Mater.*, 2004, **13**, 1012–1016.

[20] S. Beattie, D. Manolescu, S. Blair, High-capacity lithium-air cathodes, *J. Electrochem. Soc.*, 2009, **156**, A44–A47.

Chapter 3

3 Carbon Black Cathodes for Lithium Oxygen Batteries: Influence of Porosity and Heteroatom-Doping*

The key component of lithium-air batteries is the porous cathode in which the reactions take place during discharge and charge processes. The discharge product deposits on the surface of the carbon cathode, causing pore blocking and volume reducing, which limits oxygen access to the inner part of electrode, hence terminate the discharge reactions. Therefore, the air electrode structure is an essential factor for determining the discharge performance. Carbon black powders have been widely used as cathode materials due to their abundance and low price, however, the detailed influence of the material structure on the performance is not very clear.

In this chapter, commercial carbon black was treated under different atmospheres and the resultant samples were employed as cathode materials for lithium-oxygen batteries. The advantages of the carbon cathode designed in this study are that all structural and surface parameters of the carbon electrode are obtained from only one kind of carbon black by using various treatments. It was demonstrated that the porosity changed tremendously as the treating time increases. The parameters that influenced the battery performance were identified And it was found that the specific surface area of mesopores was the main factor determining the battery performance, while nitrogen- or oxygen-bearing functionalities, introduced during heat-treatment or by contact with air after pyrolysis, have little or no influence on the battery performance.

---

*A version of this chapter has been accepted for publishing in ***Carbon***.

3.1 Introduction

Lithium oxygen battery is one of the most promising energy storage candidates for meeting the future demands of the electric vehicles (EVs) or hybrid electric vehicles (HEVs) [1,2]. However, the challenges for this battery system, such as the rate capability, cycle life, power performance, etc. should be overcome before lithium oxygen batteries can be used in practical applications [3]. It is reported that during discharge process of the battery, the product, Li_2O_2, deposits on the surface of the electrodes and eventually blocks the path ways for electrolyte and oxygen transportation, terminating the discharge process. Therefore, the electrodes are directly determining the battery performance.

To date, carbon materials are still the most studied cathode materials for lithium oxygen batteries, and efforts have been made to increase the oxygen solubility and diffusion, to decrease the accumulation of reaction products, and to create effective three-phase electrochemical interface of these materials [4-8]. For example, one-dimensional carbon materials (CNTs, CNFs) have been reported to exhibit good performance because they could form an interconnected porous electrode with high void volume [9, 10]. Graphene nanosheets, a two-dimensional material showed significantly improvement for the battery performance due to its unique morphology and structures [11-13]. It was also reported that heteroatom-doping to carbon nanotubes and graphene nanosheets further increased the battery performance because of the active sites introduced into the pristine samples [14-16]. Due to abundance and low cost, carbon black has also been extensively studied as a cathode in lithium oxygen batteries. For example, several carbon black powders have been studied by Xiao et al. [4] and the results suggested that the pore volume and the pore size affect the battery performance. Hall et al. [8] also suggested that electrode made of carbon aerogel with appropriate pore volume and pore diameter delivered high discharge capacity. The findings indicated that the limited discharge capacity was associated to pore clogging as claimed by others [17]. However, recently Luntz et al. [18, 19]

reported that the electrical passivation caused by the formation of discharge product layer on the electrode was the limiting factor by using the electrochemical experiments and modeling. They found that even a very thin layer (4-5 nm) of the insulated film of Li_2O_2 was sufficient to terminate the discharge reaction due to the increased electrical resistance at the electrode/electrolyte interface, then preventing further O_2 reduction. This would imply that the specific capacity should be related to the effective carbon surface area, accessible to the electrolyte and oxygen.

In the present paper, various carbons all derived from the same starting commercial pristine carbon black (N330) were obtained by treating this carbon black in different treating atmospheres and for different times. The resulting carbons have been used as cathode in lithium oxygen batteries, revealing that the discharge capacity is proportional to the specific surface area of mesopores in these carbon electrodes. For the first time, the influence of various parameters resulting from the heat-treatment of the same starting carbon black, such as the content of disorganized carbon and heteroatom-doping effects, is studied in detail as well on the performance of the lithium oxygen battery.

3.2 Experimental

3.2.1 Sample preparation

Commercial N330 furnace carbon black (from Sid Richardson Carbon Corporation) was used as the starting material. It was heat-treated under NH_3 or CO_2 (with or without H_2) atmospheres. The percentage of mass that was lost during the heat-treatment, W, was calculated as follows:

$$W = \frac{initial\ mass - final\ mass}{initial\ mass} \times 100 \qquad (3.1)$$

3.2.1.1 Samples treated by NH_3

500 mg of carbon black powder spread in a fused silica boat was pyrolysed in a fused silica reactor under NH_3 at 1050 ^{o}C until the desired mass losses (10, 35, 54, 75, and 85%) were obtained. For the 75 and 85% mass losses, the samples were made with several pyrolysis to obtain around 150-200 mg of final powder.

3.2.1.2 Samples treated by CO_2 (with or without H_2)

500 mg of carbon black spread in a fused silica boat was pyrolysed in a fused silica reactor under CO_2 at 1050 ^{o}C until the desired mass losses (13, 35, 50, and 75%) were obtained. For the 75% mass loss, the sample was again made with several pyrolysis to obtain around 150-200 mg of final powder. These samples were further pyrolysed under H_2 at 950 ^{o}C to remove oxygen. It is possible that some oxygen was introduced in the sample by simple contact with air after pyrolysis.

3.2.2 Physical characterizations

The morphologies of the samples were characterized by Hitachi S-4800 field-emission scanning electron microscope (SEM) operated at 5.0 kV. N_2 adsorption/desorption isotherms were obtained using a Folio Micromeritics TriStar II Surface Area and Pore Size Analyser. The nitrogen and oxygen contents of the carbon materials were determined by Kratos Axis Ultra Alα X-ray photoelectron spectroscopy (XPS). Raman scattering spectra were recorded on a HORIBA Scientific LabRAM HR Raman spectrometer system equipped with a 532.4 nm laser.

3.2.3 Electrochemical measurements

Cathodes were prepared by casting a mixture of carbon materials and poly(vinylidene fluoride) (PVDF) (Alfa Aesar) with a weight ratio of 9:1 onto a separator (Celgard3500). The electrodes were 3/8 inch in diameter and the loadings were ~ 0.3 mg. Swagelok type cells composed of lithium foil anode, Celgard 3500 separator, different cathodes and a stainless steel mesh as current collector were used to carry out the electrochemical measurements. The electrolyte was 1 mol $LiCF_3SO_3$ dissolved in tetraethylene glycol dimethyl ether (TEGDME). The discharge/charge characteristics were performed by using an Arbin BT-2000 battery station in a 1 atm oxygen atmosphere at room temperature (25 °C).

3.3 Results and Discussion

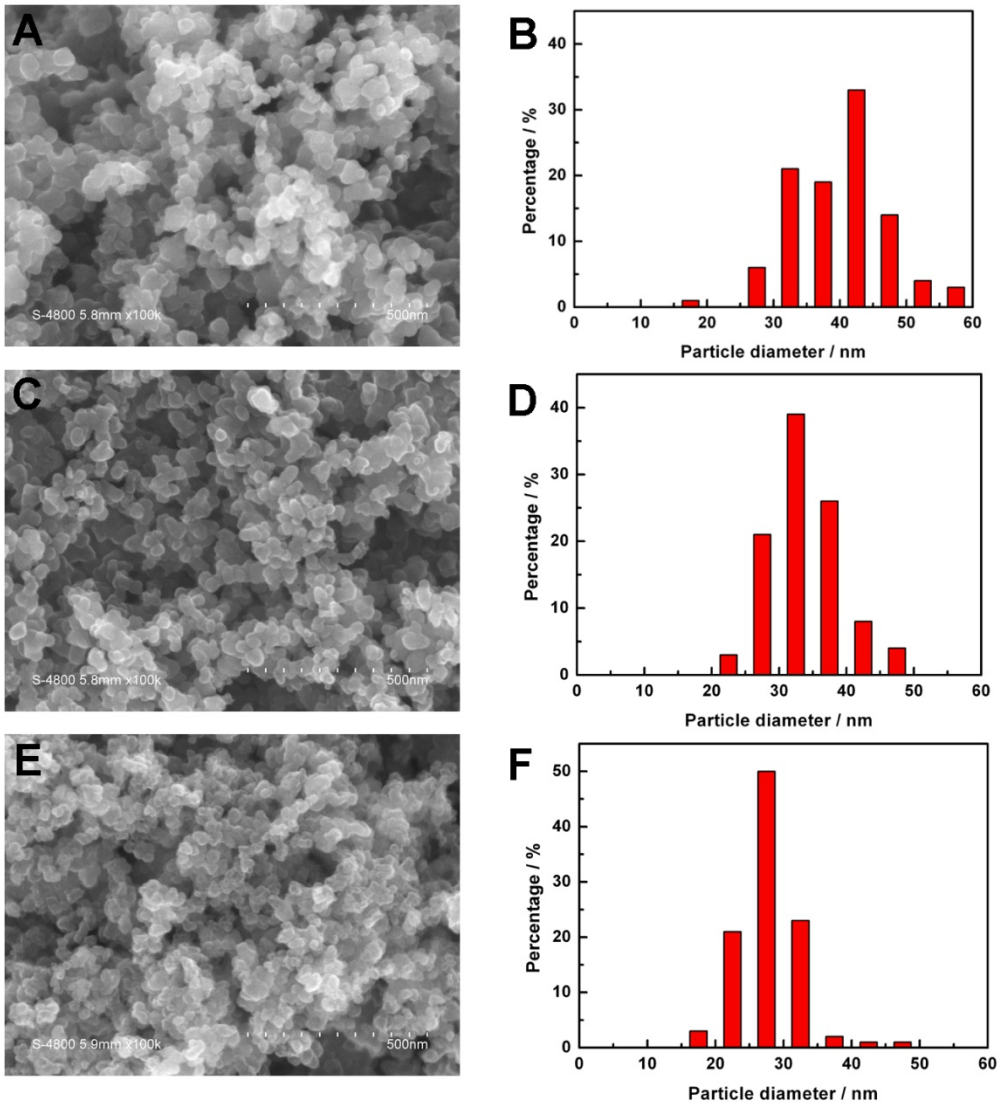

Figure 3.1 SEM images and particle size distributions of carbon blacks with mass losses of (a, and b) 0%, (c, and d) 35%, and (e, and f) 75%.

The morphology and the distribution of particle sizes of some of the samples resulting from the heat-treatment of N330 in NH_3 are shown in **Figure 3.1**. The distribution of

particle sizes of the carbon black was obtained from the analysis of SEM micrographs based on about 300 particles. It can be seen that the shape of the particles is kept almost the same, even after a loss of 75% of the pristine N330 carbon mass. However, the particle size is decreasing after the heat treatment. Several large particles (> 40 nm) are observed at 0% mass loss but their number decreases at 75% mass loss, while the mean diameter of the maximum number of particles shifted from an initial value of 40-45 nm, at 0% mass loss, to 25-30 nm after 75% mass loss.

It is known that NH_3 etches the carbon black at 1050 ^{o}C according to the following reactions [20]:

$$C + NH_3 \rightarrow HCN + H_2 \qquad (3.2)$$

$$C + H_2 \rightarrow CH_4 \qquad (3.3)$$

The gasification reactions of carbon blacks results in decreasing particle sizes and the occurrence of porosity leading to an increasing specific surface area of the remaining carbon black. The total specific surface area, and the specific surface areas of micro-, and meso-pores of the samples have been measured as a function of mass loss. These results are presented in **Figure 3.2a**. It can be seen that the Brunauer-Emmett-Teller (BET) surface area and the mesopore surface areas of the samples both steadily increase as the mass loss increases. This behavior is different from that of the specific surface area of the micropores, which first increases, reaches a maximum, and then decreases as the mass loss increases. A formation mechanism of the porosity in carbon blacks has been well described by Jaouen et al [21, 22].According to these authors, the surface area of the pristine carbon black is only that of the outer spheres of the carbon particles with almost no pores; then, as gasification of carbon proceeds according to equations 2 and 3, disordered carbon is removed from the outer surface and some edge surface is created. As more disordered carbon is removed from the particle, the micropores become larger in size and deeper in length leading to the formation of mesopores. The surface area of mesopores increases as the treating time increases. It

has been reported that the catalytic activity of Fe/N/C catalysts used for oxygen reduction reaction at the cathode of proton exchange membrane (PEM) fuel cells is related to the microporosity of their carbon black support, since their most active sites are hosted in these micropores [23, 24]. However, in our case, it can be seen in **Figure 3.2b** (right Y axis) that, for lithium oxygen batteries, only the specific surface area of mesopores vs. mass loss curve well matches the behavior of the discharge specific capacity vs. mass loss curve (**Figure 3.2b**, left Y axis). This indicates that the surface area of mesopores plays the major role in determining the battery discharge performance.The correlation between discharge capacity and specific surface areas is further illustrated in **Figure 3.2c**, where it is indeed shown that the discharge capacity only increases nearly linearly with an increase of the surface area of the mesopores.

Figure 3.2d shows the pore size distribution (PSD) curves of carbon blacks with different mass losses. As can be seen, for the pristine carbon black, only the pores centered at size of ~ 30 nm are present. They probably are voids between the carbon black particles. Even when the mass loss increases to 35%, the volume of pores having sizes between 2 and 4 nm only slightly increases, while the volume of pores having sizes centered at ~ 30 nm remains almost the same. It has been reported that the discharge product, Li_2O_2, would not deposit in micropores because the electrolyte could not have access to them [7]. Therefore, the discharge product would deposit on the surface of the voids between carbon particles. When the mass loss reaches 54%, not only a peak at ~ 3.5 nm appears in **Figure 3.2d**, but also the volume of the pore sizes in the range of 10-50 nm increases, as a result to the enlargement of micropores. As the pyrolysis time increases, the pore volume peaks at a pore size of ~ 3.8 nm, indicating that this is the main pore size in such carbon black when the mass loss is 75%. As expected, the volume of the pore with sizes of 10-50 nm continues to increase in these conditions. When the mass loss increases from 75% to 85%, the volume of pore size at ~ 4 nm does not increase anymore, but the volume of pore sizes from 10-50 nm increases a lot. This should be beneficial for discharge product accommodation.

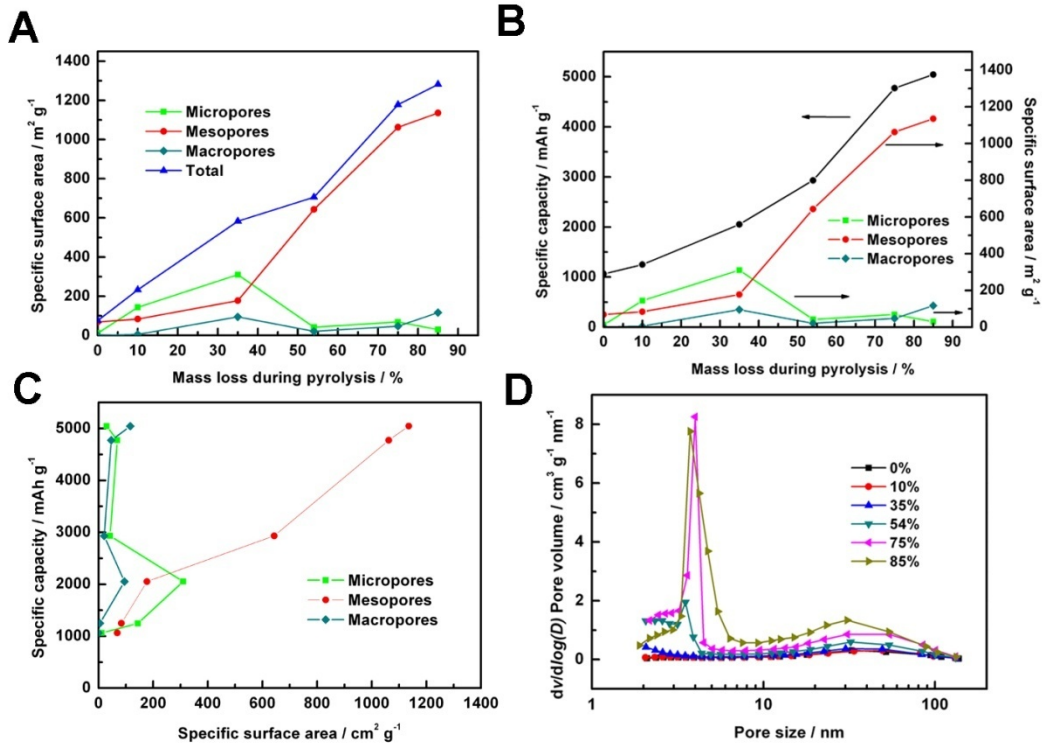

Figure 3.2 (a) Total specific area (BET) and specific surface areas for micropores, mesopores, and macropores vs. mass loss during pyrolysis in NH_3, (b) discharge capacity (left Y axis), the specific area of micropores, mesopores, and macropores (right Y axis) vs. mass loss, (c) discharge capacity vs. the specific area for micropores, mesopores, and macropores and (d) the pore size distribution (PSD) curves for carbon blacks with various mass loss.

However, it can be seen in **Figure SI-3.1** that the discharge capacity only slightly increases (~ 6%), while the volume of mesopores increases by more than 50%. From this observation, one may suggest that the very large increase in the volume of mesopores, when mass loss increases from 75 to 85%, is not more effective for accommodating discharge product deposition (**Figure SI-3.1**). While some of the pores are clogged as discharge product forms, passivation is the main issue for the cathode due to the low electrical conductivity of Li_2O_2. In order to study the effect of

effective surface area towards to discharge capacity, it is necessary to estimate the coverage of carbon surface by Li_2O_2 after battery discharge.

Table 3.1 Carbon mass based discharge capacity, surface-normalized discharge capacity and current, and the corresponding number of Li_2O_2 monolayers deposited on the surface of mesopores for carbon blacks with different mass losses.

Mass loss / %	Discharge capacity / mAh g^{-1}	Surface-normalized discharge capacity / μC cm^{-2}	Number of monolayers	Surface-normalized current / μA cm^{-2}
0	1062	5577	21.5	0.328
10	1248	5349	20.6	0.268
35	2051	4158	16.0	0.127
54	2931	1641	6.3	0.035
75	4773	1617	6.2	0.021
85	5045	1600	6.2	0.020

The discharge capacity based on carbon mass can be expressed to the surface-normalized discharge capacity based on the specific area of the mesopores. Knowing that 260 μC cm^{-2}_{carbon} is the estimated normalized discharge necessary to obtain the deposition of 1 monolayer of Li_2O_2, the number of monolayers of discharge products can be estimated for our carbons [25]. It is shown in **Table 3.1**, the sample with 10% mass loss has a surface-normalized discharge capacity very similar to that of pristine carbon (~ 5500 μC cm^{-2}). As the mass loss increases to 35%, the capacity decreases to 4158 μC cm^{-2} and the thickness of discharge product decreases from ~ 7 nm to ~ 5 nm accordingly [26]. The reason for the decreasing thickness of discharge products on carbon samples may be due to the different cathodic polarization of the carbon surface caused by the various surface-normalized currents (last column

in **Table 3.1**) [27]. It is important to note that when the mass loss ≥ 54%, the capacity values drop to 1600-1650 μC cm^{-2} for these samples; these values suggest that about 6 monolayers of Li_2O_2 are formed on the carbon surface, corresponding to a ~ 2 nm thick layer. It is expected that only a thin layer of product can stop the discharge reaction, which supports the hypothesis proposed by Luntz et al [6]. As can be seen from **Figure 3.3**, the estimated thickness of discharge product on carbon surface is smaller than the average pore size of each sample, suggesting that a too large pore size in the mesoporous range leads to a less efficient use of mesopore volumes, which is consistent with our observations described above. **Figure SI-3.2** shows the curve of discharge specific capacity vs. mesopore size. One can see that when the pore size is about 3.5 nm, the capacity is maximum, indicating that it is the desired pore size considering the passivation.

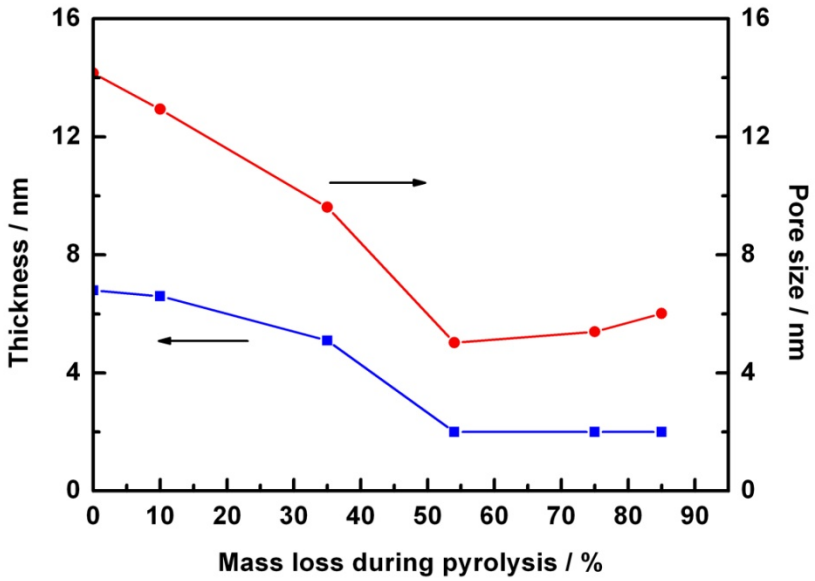

Figure 3.3 Estimated thickness of the discharge product on the surface (left Y axis) and pore size (right Y axis) of carbon blacks with different mass losses.

So far, we have shown that the specific surface area of carbon black mesopores is an important factor determining the lithium oxygen battery performance. These

mesopores were obtained by pyrolysing N330 in NH_3 at 1050 °C. Now, it will be shown that similar results are also obtained when the porosity in N330 is generated by pyrolysing at 1050 °C the same carbon black in CO_2 (or CO_2 + H_2; to remove at least partially the oxygen-bearing functionalities introduced by the pyrolysis under CO_2). Indeed, as seen in **Figure SI-3.3**, both groups of samples show that the specific surface areas of mesopores are also proportional to the discharge capacities. The pore size distribution curves are shown in **Figure SI-3.4** and it can be seen that all the curves steadly shift upwards for pore volumes in the small and large pore diameter regions. However, the amount of pores of which size at ~ 3.8 nm is relatively less in the carbon blacks refer to the pores in the diameter range of 10-50 nm. From **Table SI-3.1**, similar results about the deposit of discharge products as a thin film are also demonstrated for the carbon blacks treated by CO_2 with/without H_2, and the thickness of discharge products is very similar to that of the carbon samples treated by NH_3, especially at the mass losses > 40% (**Figure SI-3.5**).

Raman spectroscopy is a powerful technique to identify the structure of carbon blacks. **Figure SI-3.6** shows the Raman spectra of the NH_3-treated samples. Each spectrum was deconvoluted into five peaks as suggested by Sadezky et al [28]. The D band (~ 1365 cm^{-1}) and G band (~ 1590 cm^{-1}) correspond to disordered and graphitic carbon phase, respectively. The peaks at about 1190, 1530, and 1620 cm^{-1} are associated with the sp^3 carbon, amorphous carbon, and another band accounting for structural disorder, respectively. The width at half maximum (fwhm) of the D band, W_D, in the Raman spectroscopy of the carbon black indicates the degree of structural disorder in the samples [29].

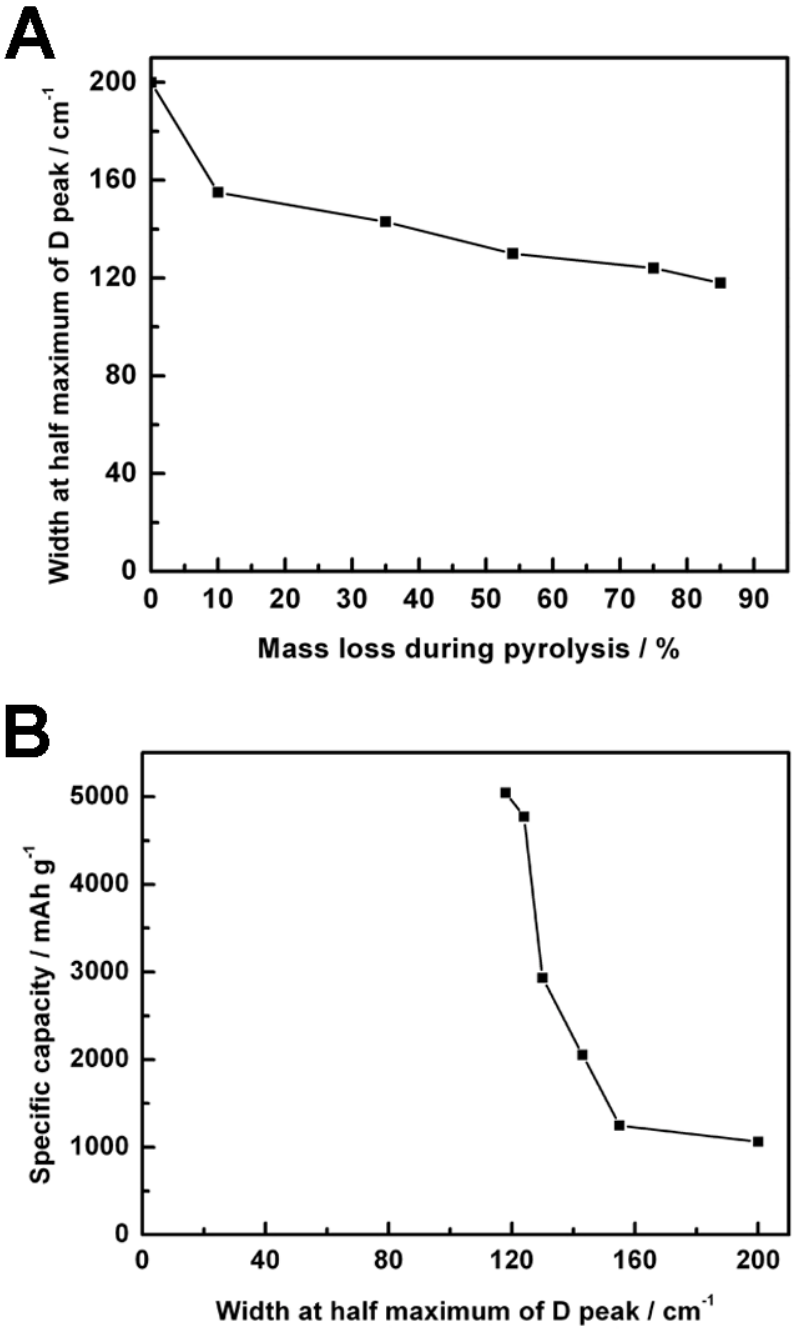

Figure 3.4 (a) Raman spectrum of the N330 carbon black, (b) Width at half maximum (fwhm) of D peak of carbon blacks vs. mass loss, and (c) The specific capacity vs. the fwhm.

As can be seen from **Figure 3.4a**, W_D decreases from 200 to 118 cm^{-1} as the mass loss increases from 0 to 85%. The constant decrease of the W_D clearly indicates the decrease of the amount of disordered carbon phase in the samples. **Figure 3.4b** depicts the discharge specific capacity vs. W_D; it is obviously that the capacity increases as the amount of disordered carbon phase decreases in the carbon black. This finding is interesting because in our previous study about graphene nanosheets, the electrode made of nitrogen doped graphene nanosheets which have more defects delivered higher discharge capacity than pristine sample [12, 13, 15]. In this study, we believe that the different behaviour comes from the nature of the carbon black and graphene nanosheets.

A model for heat treatment of carbon blacks under NH_3 has been proposed by Jaouen et al [21, 22] and is shown in **Figure SI-3.7**. The pristine carbon black particle has no pores and consists of disordered carbon and graphitic crystallites. Both disordered carbon and graphitic crystallite edges contribute to the D band in the Raman spectrum. At the beginning of the heat treatment, NH_3 only reacts with the outer surface of the disordered carbon, and it will take time t_c to remove all the disordered carbon from shell 1, thus micropores are created. However, as the heat treatment continues, NH_3 reacts not only with the disordered carbon on shell 2, but also with the edges of the graphitic crystallites on shell 1. It was found that, at 950 °C, NH_3 reacts about ten times faster with disordered carbon than with graphitic crystallites. As carbon black reaction with NH_3 proceeds, the microporous surface area increases therefore rapidly, but the obtained micropores become larger at a slower rate. It is important to notice that, at certain time, the outmost graphitic crystallite layer will vanish, leading to a decrease in the particle diameter, and the micropores in that layer will vanish as well. From the calculations made with this model, it is predicted that, in a carbon black like N330, the surface area of micropores will increase from 0 to 30-35% mass loss, and then decrease (from mass loss > 40%). The prediction matches very well our experimental results as shown in **Figure 3.2a**. Due to the decreased amount of disordered carbon and graphitic crystallite edges, W_D will continue to decrease as the treating time increases.

This work also enabled us to study the correlation (if any) between the nitrogen content of the carbon pyrolysed in NH_3 and the battery performance since nitrogen doping into the carbon framework and the occurrence of N-bearing functional groups has already been reputed to have a favorable influence on the performance of lithium oxygen batteries [14-16]. **Figure SI-3.8** shows the XPS survey spectra of the carbon blacks as the mass loss increased. As can be seen, nitrogen atoms were successfully doped into carbon blacks and the presence of oxygen may also be noticed at various amounts after the heat-treatments in NH_3 (**Figure 3.5**). It is obvious that nitrogen content also follows the same trend as the microporosity vs. mass loss, that is it increases from 0 to 30-35% mass loss, and then decrease for mass loss > 40%. Most of the nitrogen atoms are therefore located in the micropores. As these micropores have little influence on the performance of lithium oxygen batteries, the nitrogen doped sites are therefore not effective for improving battery performance (**Figure 3.5a**).

Experimental results and density functional theory (DFT) calculations have shown that oxygen-containing functional groups on graphene electrode play an important role for battery performance [13]. However, it can be seen in **Figure 3.5b** that the oxygen-bearing functional groups here also have no influence on the battery performance. The maximum of the oxygen surface concentration occurs at 54% mass loss, out of phase with the development of the microporous surface area, and simply decreases for mass losses larger than 54%, while the specific capacity of the carbon material continues to rise with the development of the mesoporous surface area.

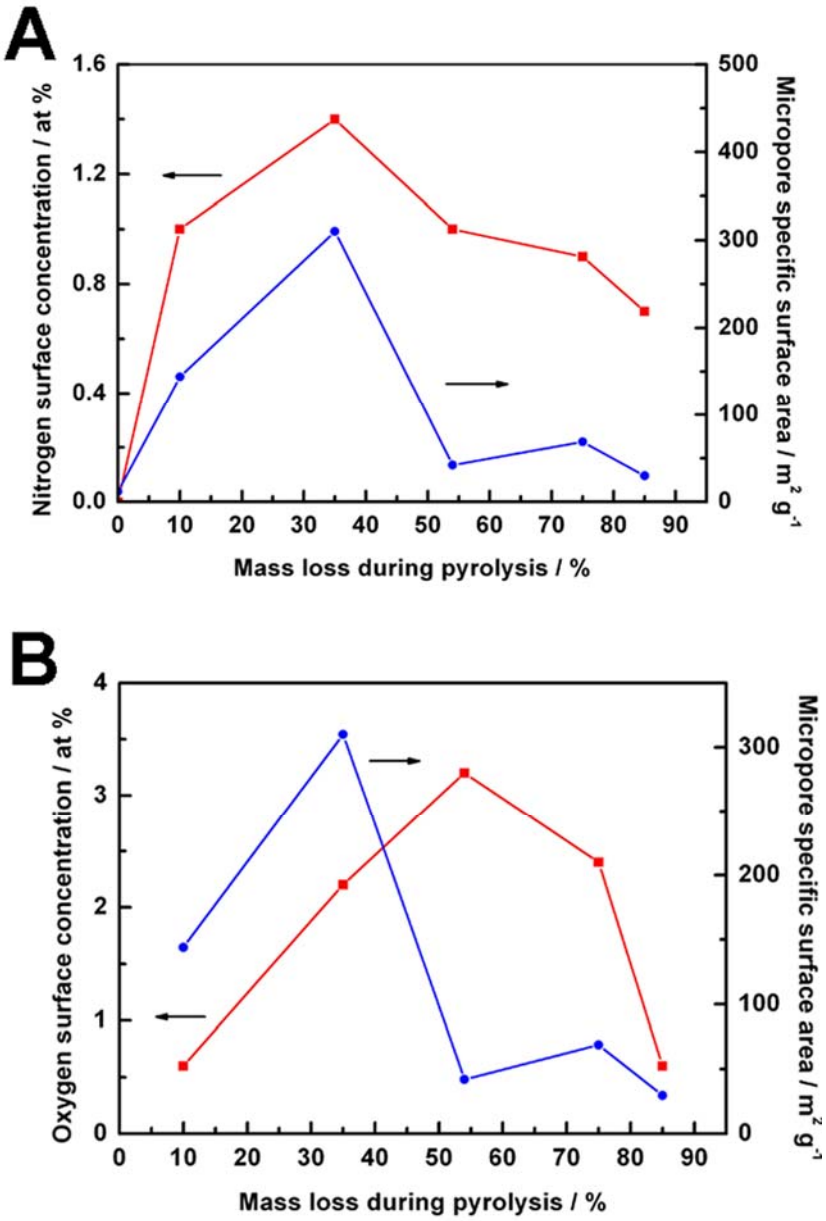

Figure 3.5 (a) Nitrogen surface concentrations (left Y axis), and (b) oxygen surface concentrations (left Y axis), the specific area of the micropores (right Y axis) of the carbon blacks with different mass losses.

3.4 Conclusions

In summary, commercial carbon black (N330) was treated under various atmospheres (NH_3, CO_2 and CO_2/H_2). The total and mesopore surface areas increased as the treating time increased while the micropore surface area only increased until the mass loss reached 35% and then decreased. It is suggested that the surface area of mesopores plays an important role for the discharge capacity of lithium oxygen batteries due to the passivation effect of discharge product film on the carbon surface. Nitrogen and oxygen-containing functional groups introduced by the gas treatments or by contact of the pyrolysed product with air, have very little or no influence on the performance of these carbon materials in lithium oxygen batteries. However, too large pore size in the mesoporous range leads to a less efficient use of mesopore volumesand the the desired pore size is about 3.5 nm considering the passivation effect. These findings established a correlation between the structure of carbon black and battery discharge capacity, which provides new insights into further designing or optimizing electrode materials for lithium oxygen batteries.

Acknowledgements

This research was supported by Natural Sciences and Engineering Research Council of Canada, Canada Research Chair Program, Canada Foundation for Innovation, Ontario Early Researcher Award and the University of Western Ontario.

References

[1] K.Abraham, Z. Jiang, A polymer electrolyte–based rechargeable lithium/oxygen battery, *J. Electrochem. Soc.*, 1996, **143**, 1–5.

[2] G. Girishkumar, B. McCloskey, A. Luntz, S. Swanson, W. Wilcke, Lithium-air battery: Promise and challenges, *J. Phys. Chem. Lett.*, 2010, **1**, 2193–2203.

[3] Y. Lu, D. Kwabi, K. Yao, J. Harding, J. Zhou, L. Zuin, Y. Shao-Horn, The discharge rate capability of rechargeable Li-O_2 batteries, *Energy Environ. Sci.*, 2011, **8**, 2999–3007.

[4] J. Xiao, D. Wang, W. Xu, D. Wang, R. Williford, J. Liu, J. Zhang, Optimization of air electrode for Li/air batteries, *J. Electrochem. Soc.*, 2010, **157**, A487–A492.

[5] R. Williford, J. Zhang, Air electrode design for sustained high power operation of Li/air batteries, *J. Power Sources*, 2009, **194**, 1164–1170.

[6] X. Yang, P. He, Y. Xia, Preparation of mesocellular carbon foam and its application for lithium/oxygen battery, *Electrochem. Commun.*, 2009, **11**, 1127–1130.

[7] S. Zhang, D. Foster, J. Read, Discharge characteristic of a non-aqueous electrolyte Li/O_2 battery, *J. Power Sources*, 2010, **195**, 1235–1140.

[8] M. Mirzaeian, P. Hall, Preparation of controlled porosity carbon aerogels for energy storage in rechargeable lithium oxygen batteries, *Electrochim. Acta*, 2009, **54**, 7444–7751.

[9] R. Mitchell, B. Gallant, C. Thompson, Y. Shao-Horn, All-carbon-nanofiberelectrodes for high-energy rechargeable Li-O_2 batteries, *Energy Environ. Sci.*, 2011, **8**, 2952–2958.

[10] G. Zhang, J. Zheng, R. Liang, C. Zhang, B. Wang, M. Hendrickson, E. Plichta, Lithium-air batteries using SWNT/CNF buckypapers as air electrodes, *J. Electrochem. Soc.*, 2010, **157**, A953–A956.

[11] Y. Li, J. Wang, X. Li, D. Geng, R. Li, X. Sun, Superior energy capacity of graphene nanosheets for a nonaqueous lithium-oxygen battery, *Chem. Comm.*, 2011, **33**, 9438–9440.

[12] E. Yoo, H. Zhou, Li-air rechargeable battery based on metal-free graphene nanosheet catalysts, *ACS Nano*, 2011, **5**, 3020–3026.

[13] J. Xiao, D. Mei, X. Li, W. Xu, D. Wang, G. Graff, W. Bennett, Z. Nie, L. Saraf, I. Aksay, J. Liu, J. Zhang, Hierarchically porous graphene as a lithium-air battery electrode, *Nano Lett.*, 2011, **11**, 5071–5078.

[14] Y. Wang, H. Zhou, To draw an air electrode of a Li-air battery by pencil, *Energy Environ. Sci.*, 2011, **5**,1704–1707.

[15] Y. Li, J. Wang, X. Li, D. Geng, M. Banis, R. Li, X. Sun, Nitrogen-doped graphene nanosheets as cathode materials with excellent electrocatalytic activity for high capacity lithium-oxygen batteries, *Electrochem. Commun.*, 2012, **18**, 12–15.

[16] Y. Li, J. Wang, X. Li, D. Geng, M. Banis, Y. Tang, D. Wang, R. Li, T. Sham, X. Sun, Discharge product morphology and increased charge performance of lithium-oxygen batteries with graphene nanosheet electrodes: The effect of sulphur doping, *J. Mater. Chem.*, 2012, **38**, 20170–20174.

[17] J. Read, Characterization of the lithium/oxygen organic electrolyte battery, *J. Electrochem. Soc.*, 2002, **149**, A1190–A1195.

[18] V. Viswanathan, K. Thygesen, J. Hummelshøj, J. Nørskov, G.Girishkumar, B. McCloskey, A. Luntz, Electrical conductivity in Li_2O_2 and its role in determining capacity limitations in non-aqueous Li-O_2 batteries, *J. Chem. Phys.*, 2011, **135**, 214704.

[19] P. Albertus, G. Girishkumar, B. McCloskey, R. SànchezCarrera, B. Kozinsky, J. Christensen, A. Luntz, Identifying capacity limitations in the Li/oxygen battery using experiments and modeling, *J. Electrochem. Soc.*, 2011, **158**, A343–A351.

[20] P. Given, Coal Science, Washington DC: *American Chemical Society*, 1966.

[21] F. Jaouen, J. Dodelet, Non-noble electrocatalysts for O_2 reduction: How does heat treatment affect their activity and structure? Part I. Model for carbon black gasification by NH_3: Parametric calibration and electrochemical validation, *J. Phys. Chem. C*, 2007, **111**, 5963–5970.

[22] F. Jaouen, A. Serventi, M.Lefèvre, J. Dodelet, P. Bertrand, Non-noble electrocatalysts for O_2 reduction: How does heat treatment affect their activity and structure? Part II. Structural changes observed by electron microscopy, raman, and mass spectroscopy, *J. Phys. Chem. C*, 2007, **111**, 5971–5976.

[23] M. Lefèvre, J. Dodelet, Fe-based electrocatalysts made with microporous pristine carbon black supports for the reduction of oxygen in PEM fuel cells, *Electrochim. Acta*, 2008, **53**, 8269–8276.

[24] F. Charreteur, F. Jaouen, J. Dodelet, Iron porphyrin-based cathode catalysts for PEM fuel cells: Influence of pyrolysis gas on activity and stability, *Electrochim. Acta*, 2009, **54**, 6622–6630.

[25] S. Meini, M. Piana, N. Tsiouvaras, A. Garsuch, H. Gasteiger, The effect of water on the discharge capacity of a non–-atalyzed carbon cathode for Li-O_2 batteries, *Electrochem. Solid–State Lett.*, 2012, **15**, A45–A48.

[26] S. Meini, M. Piana, H. Beyer, J. Schwämmlein, H. Gasteiger, Effect of carbon surface area on first discharge capacity of Li-O_2 cathodes and cycle-life behavior in ether-based electrolytes, *J. Electrochem. Soc.*, 2012, **159**, A2135–A2142.

[27] R. Black, S. Oh, J. Lee, T. Yim, B. Adams, L. Nazar, Screening for superoxide reactivity in Li-O_2 batteries: Effect on Li_2O_2/LiOH crystallization, *J. Am. Chem. Soc.*, 2012, **134**, 2902–2095.

[28] A. Sadezky, H. Muckenhuber, H. Grothe, R. Niessner, U. PöSchl, Raman microspectroscopy of soot and related carbonaceous materials: Spectral analysis and structural information, *Carbon*, 2005, **43**, 1731–1742.

[29] F. Charreteur, F. Jaouen, S. Ruggeri, J. Dodelet, Fe/N/C non-precious catalysts for PEM fuel cells: Influence of the structural parameters of pristine commercial carbon blacks on their activity for oxygen reduction, *Electrochim. Acta*, 2008, **53**, 2925–2938.

Supporting Information

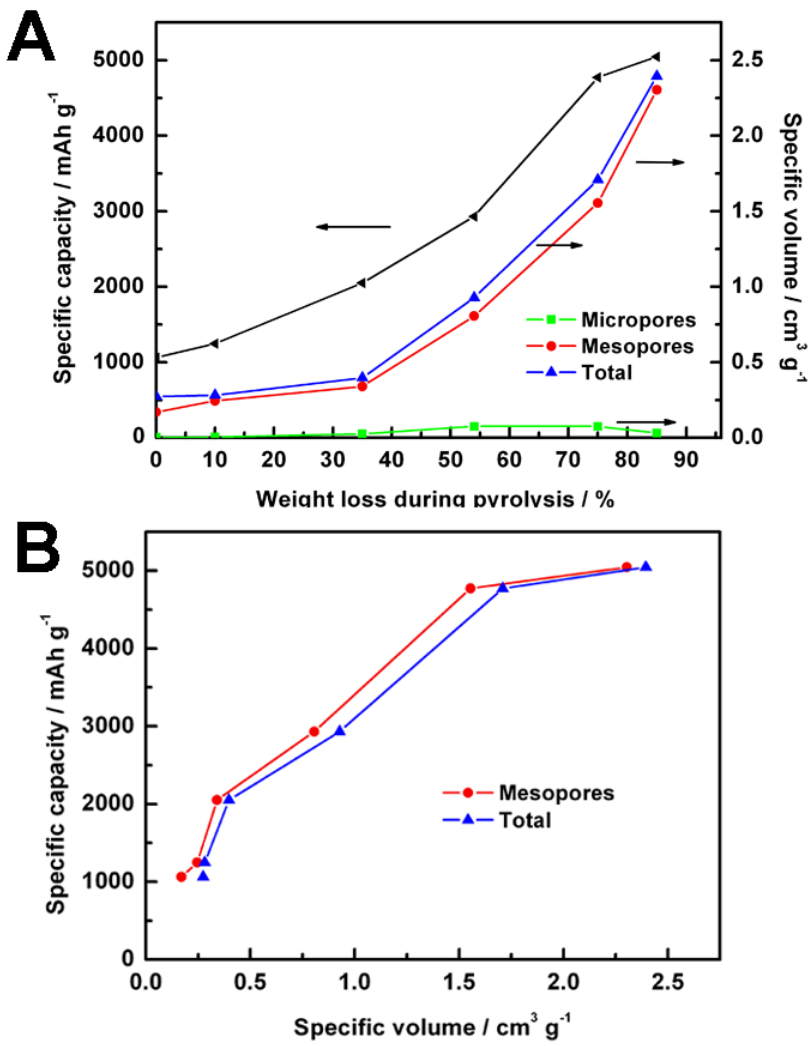

Figure SI-3.1 (a) Discharge capacity (left Y axis), total volume and specific volume for micropores and mesopores (right Y axis) vs. mass loss, (b) discharge capacity vs. the total volume and specific volume for mesopores for carbon blacks.

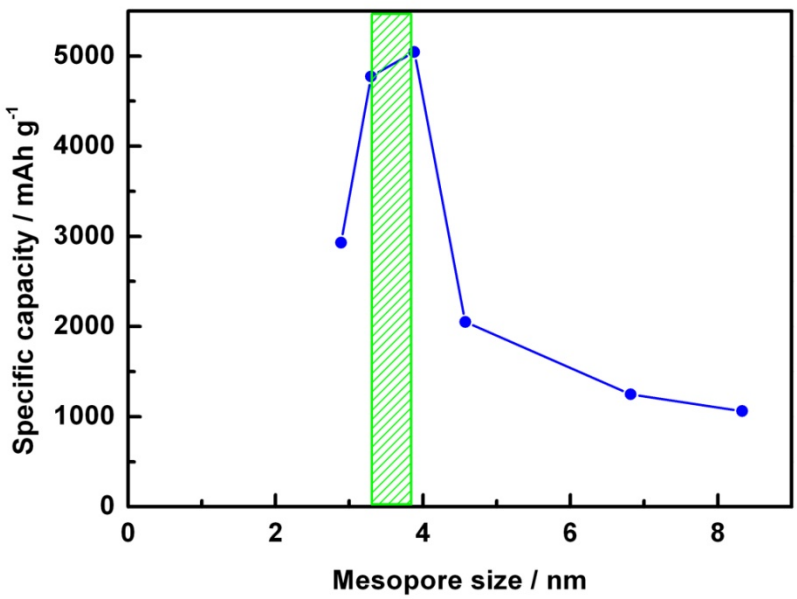

Figure SI-3.2 The discharge specific capacity vs. the average mesopore sizes of carbon blacks.

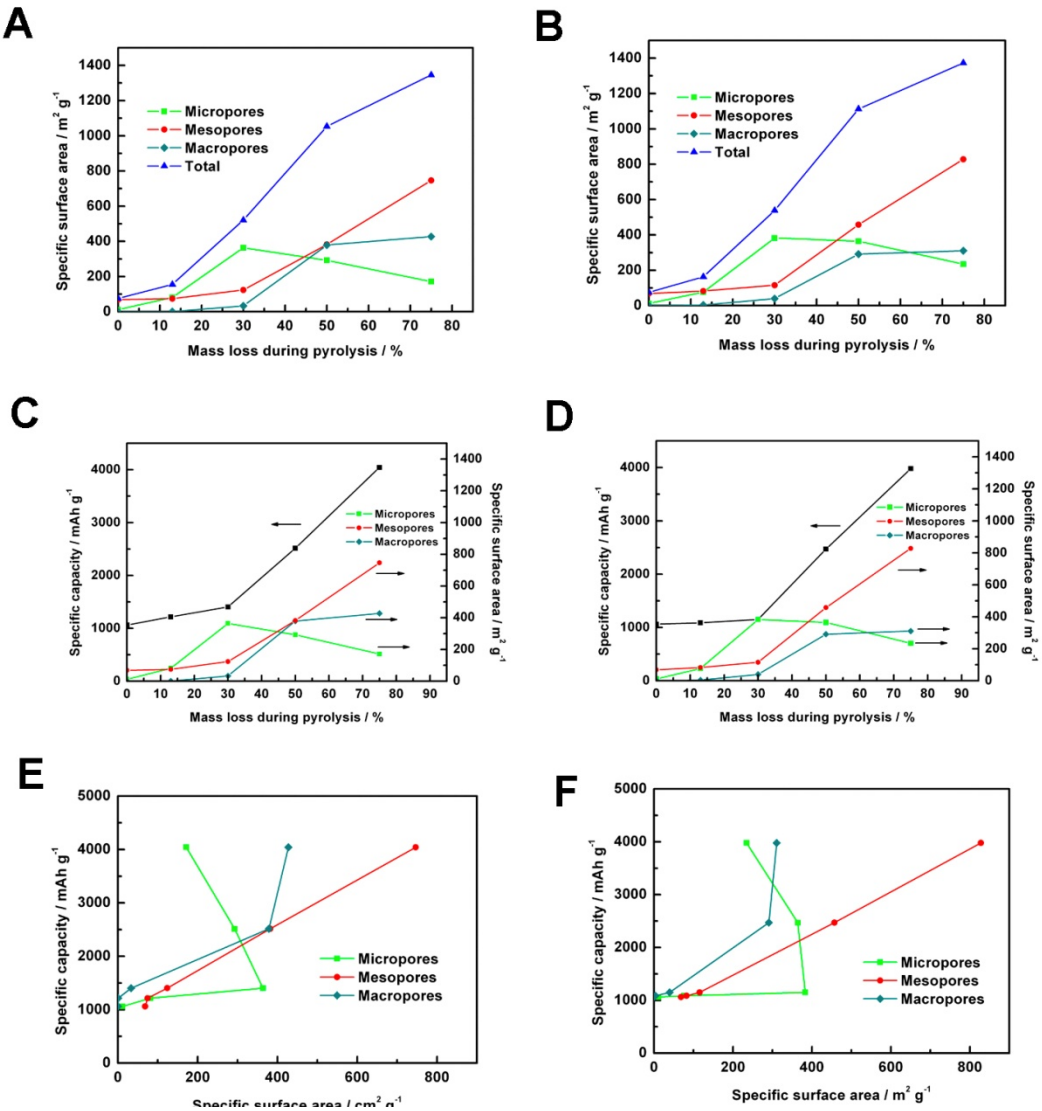

Figure SI-3.3 (a and b) Total specific area (BET) and specific surface areas for micropores, mesopores, and macropores vs. mass loss, (c and d) Discharge capacity (left Y axis), the specific area of micropoes, mesopores, and macropores (right Y axis) vs. mass loss during pyrolysis, and (e and f) discharge capacity vs. the specific area for micropores, mesopores, and macropores for carbon blacks treated by CO_2 (left column) and CO_2/H_2 (right column).

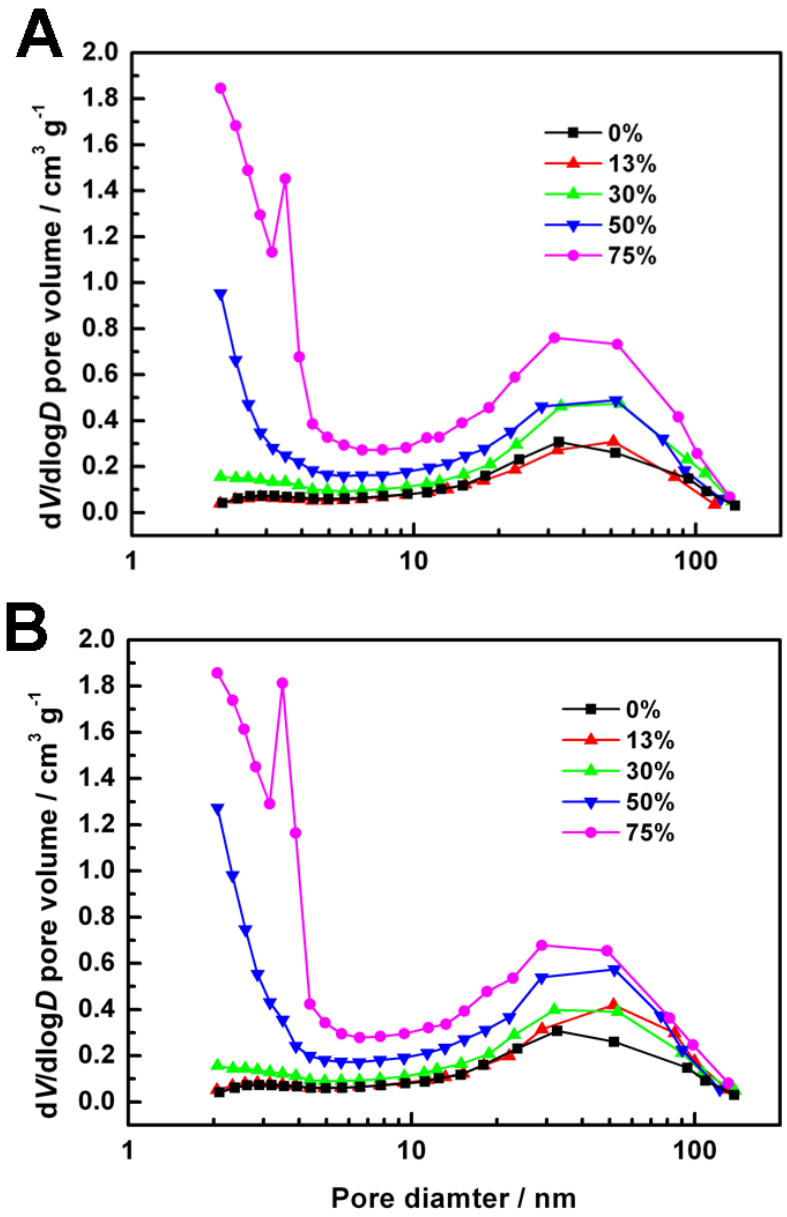

Figure SI-3.4 The pore size distribution (PSD) curves for carbon blacks treated by (a) CO_2 and (b) CO_2/H_2 with different mass losses.

Table SI-3.1 Carbon mass based discharge capacity, surface-normalized discharge capacity/current, and the corresponding number of Li_2O_2 monolayers on the surface of carbon blacks treated by CO_2 and CO_2/H_2 with different mass losses.

	CO_2			CO_2/H_2		
Mass loss / %	Surface-normalized discharge capacity / $\mu C\ cm^{-2}$	Number of monolayers	Surface-ormalized current / $\mu A\ cm^{-2}$	Surface-normalized discharge capacity / $\mu C\ cm^{-2}$	Number of monolayers	Surface-normalized current / $\mu A\ cm^{-2}$
0	5577	21.5	0.328	5577	21.5	0.328
13	5511	21.2	0.284	4735	19.2	0.272
30	4085	16.8	0.194	3577	12.9	0.182
50	2208	8.5	0.055	1945	7.5	0.049
75	1949	7.5	0.030	1731	6.7	0.027

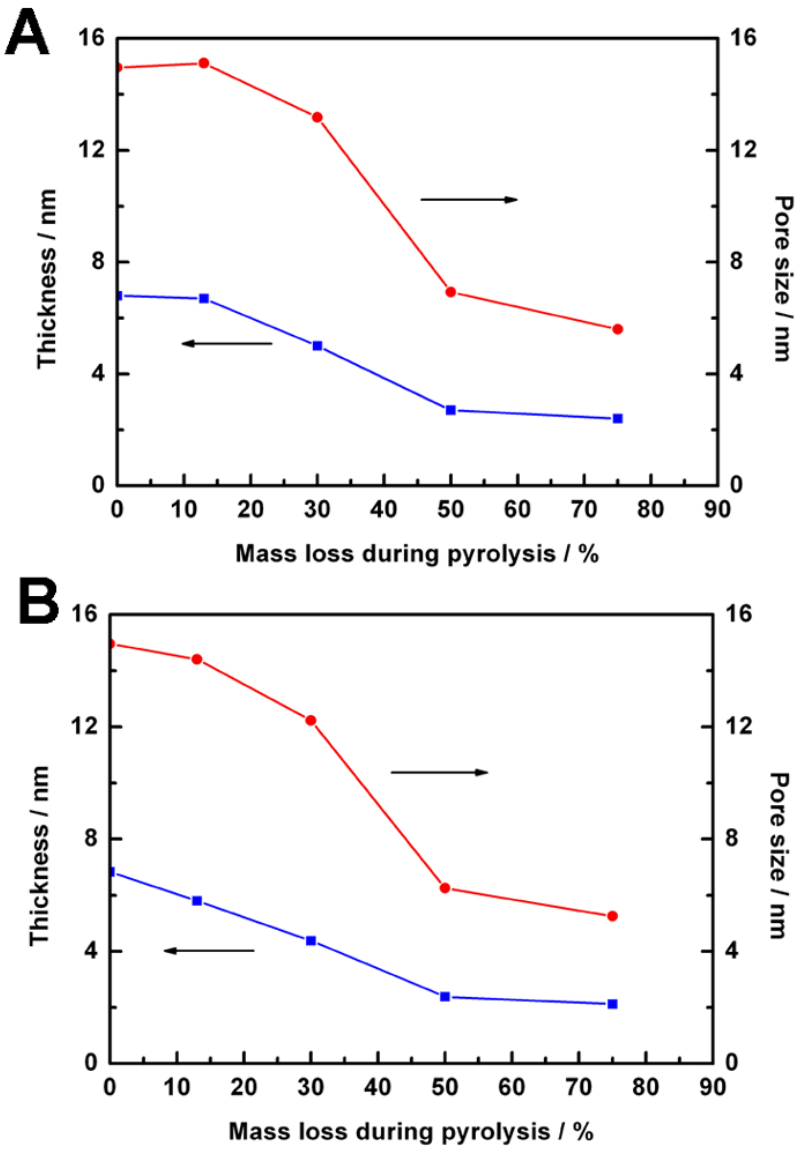

Figure SI-3.5 Estimated thickness of the discharge product on the surface (left Y axis) and pore size (right Y axis) of carbon blacks treated by (a) CO_2 and (b) CO_2/H_2 with different mass losses.

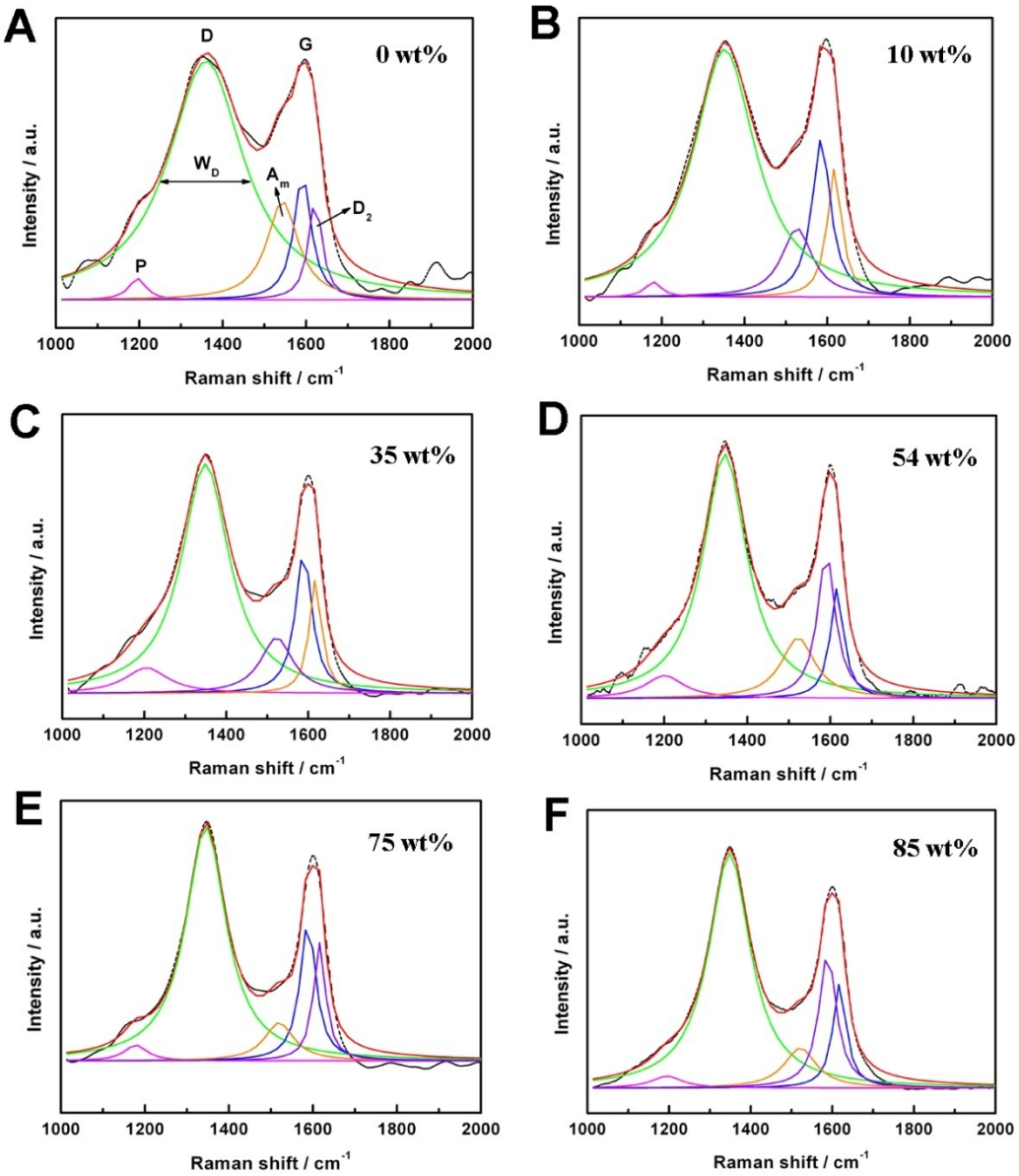

Figure SI-3.6 Raman spectra of the carbon blacks with different mass losses during pyrolysis under NH_3.

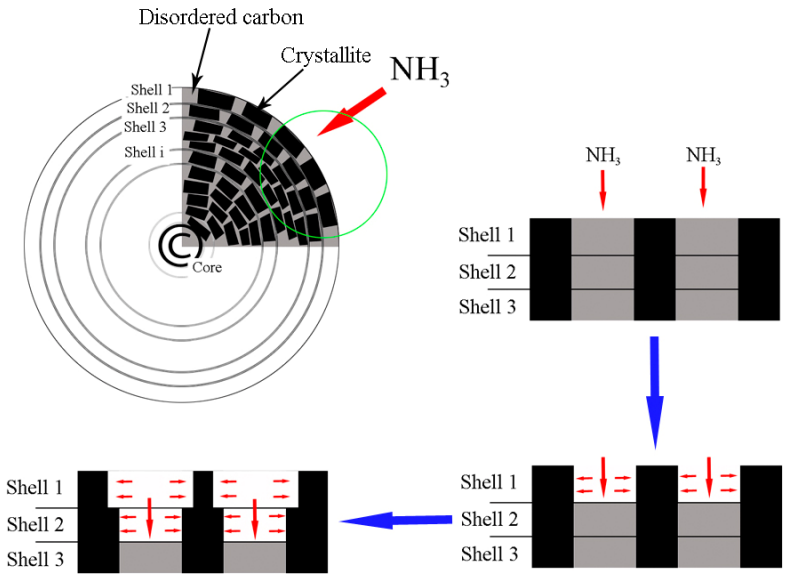

Figure SI-3.7 Etching of carbon black by NH_3 as a function of time [21, 22].

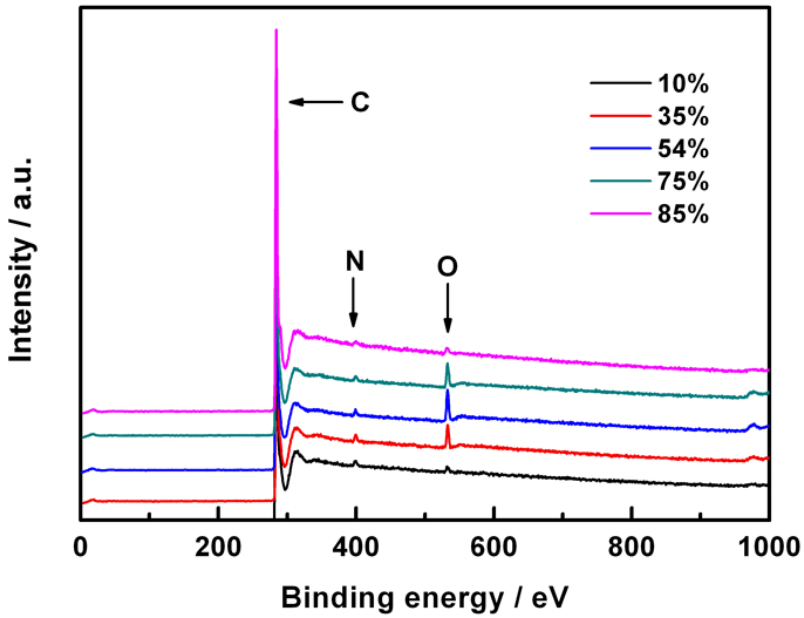

Figure SI-3.8 XPS survey spectra of the carbon blacks with different mass losses during pyrolysis under NH_3.

Chapter 4

4 Nitrogen-Doped Carbon Nanotubes as Novel Cathode for Lithium-Air Batteries*

As reported, the structure of the air electrode is a critical factor in determining the discharge performance. Compared to conventional carbon blacks, one-dimensional (1D) carbon nanotubes (CNTs) possess unique physical and chemical properties, including higher electrical conductivity, surface area and mechanical properties which are suitable for lithium-air battery. More importantly, it is found that the electrocatalytic activity for oxygen reduction reaction (ORR) of the CNTs was significantly increased after nitrogen doping. Since the discharge of lithium-air battery also involved the ORR, it is interesting to employ nitrogen-doped carbon nanotubes (N-CNTs) as cathode materials in this system which not only tailor the porosity of the electrode, but also catalyze the cathode reaction, increasing the battery performance.

In this chapter, N-CNTs were synthesized by a floating catalyst chemical vapor deposition (FCCVD) method. Various techniques including FESEM, TEM, XRD, XPS and Raman spectroscopy revealed the morphology and structure of CNTs and N-CNTs as well as confirmed the existence of incorporated nitrogen (10.2 at. %) in N-CNTs. In comparison to CNTs, N-CNTs were investigated as cathode material for lithium-air batteries and exhibited a specific discharge capacity of 866 mAh g^{-1}, which was about 1.5 times as that of CNTs. Our results indicated that the N-CNTs electrode showed high electrocatalytic activities for the cathode reaction therefore improved the lithium air battery performance.

---

*A version of this chapter has been published in ***Electrochemistry Communications***, 2011, **13**, 668-672.

4.1 Introduction

Lithium-air batteries have been attracting much attention due to its extremely high theoretical specific energy [1]. The cathode active material, oxygen, is not stored in the batteries, but can be absorbed from the environment during discharge, making these systems serious contenders to meet the rapid growing requirements of the hybrid electric vehicles (HEVs) and electric vehicles (EVs) [2]. Many work indicated that the battery performance strongly depends on the carbon cathode [3-5]. For example, Xiao et al. found that the surface area and mesopore volume of carbon powder significantly affected the discharge capacity [6]. Mirzaeian et al. found that the battery performance depended on the morphology of the carbon as well [7]. Therefore it is important to develop new carbon-based electrodes to improve the kinetics of the air cathode thus enhance the battery performance.

Recently, nitrogen-doped carbon powder as cathode material in lithium-air batteries showed improvement to the discharge capacity because of the high surface area, porosity and electrocatalytic activity [8]. This is because the doped heteroatoms are available to tailor the chemical and electronic nature of carbon based materials [9-11]. Recent works have shown that the N-CNTs exhibit excellent electrocatalytic activity for oxygen reduction reaction (ORR) in aqueous electrolyte [12-15]. Zhang et al. reported that battery made with carbon nanotube/nanofiber mixed buckypapers cathode delivered a high discharge capacity [16]. However, to our best knowledge, no research on N-CNTs as cathode for lithium air batteries was reported.

In this work, for the first time, we reported to employ N-CNTs as a novel cathode for lithium-air batteries. It was demonstrated that nitrogen-doping into carbon nanotubes not only increased the discharge capacity but also enhanced the reversibility in the charge/discharge process. This finding is opening a rational and promising direction in developing carbon electrode for lithium-air batteries.

4.2 Experimental

4.2.1 Materials synthesis

CNTs with diameters of 40-60 nm were purchased from Shenzhen Nanotech., China. N-CNTs were prepared in our group by a floating catalyst chemical vapor deposition (FCCVD) method, as described before [11]. Imidazole was used as carbon and nitrogen source, and ferrocene as catalyst precursor. At 850 ^{o}C, ferrocene decomposed into iron as the catalyst for carbon nanotube growth and the nitrogen atoms incorporated into the graphite layers to yield N-CNTs.

4.2.2 Physical characterizations

The morphologies and structures of CNTs and N-CNTs were characterized by a Hitachi S-4800 field emission scanning electron microscopy (FESEM) and a Hitachi H-7000 transmission electron microscopy (TEM). Powder X-ray diffraction (XRD) patterns were recorded by Rigaku RU-200BVH diffractometer employing a Co-Kα source (λ=1.7892 Å). Raman scattering spectra were recorded on a HORIBA Scientific LabRAM HR Raman spectrometer system equipped with a 532.4 nm laser. N_2 adsorption/desorption isotherms were obtained using a Folio Micromeritics TriStar II Surface Area and Pore Size Analyser. The nitrogen content in N-CNTs was determined by a Kratos Axis Ultra X-ray photoelectron spectrometer with Al Kα as the X-ray source.

4.2.3 Electrochemical measurements

Cathode was prepared by casting a mixture of CNTs (or N-CNTs), and PVDF (Alfa Aesar) with a weight ratio of 9:1 onto a separator (Celgard C3500). The electrode is 3/8 inch in diameter and the carbon loadings were 0.5 ± 0.1 mg. The electrolyte was 1 mol $LiPF_6$ (Sigma Aldrich, 99.99%) dissolved in propylene carbonate (PC) (Sigma Aldrich, anhydrous, 99.7%)/ethylene carbonate (EC) (Alfa Aesar, anhydrous, 99%) (1:1 weight ratio).

Swagelok cells composed of lithium foil, Celgard 3500 separator, different cathodes and a stainless steel (SS) mesh as current collector were assembled in an argon-filled glove box (MBraun Inc.) with the moisture and oxygen concentration < 1 ppm. The cells were gastight except for the SS mesh window that exposed to a 1 atm O_2 atmosphere. The discharge/charge characteristics were performed by using an Arbin BT-2000 battery station in a voltage range of 2.0-4.5 V. Cyclic voltammetry measurements were carried out by using a CHI 600c electrochemical work station at a scan rate of 0.2 mV s^{-1} in a voltage range of 2.0-4.5 V at room temperature.

To study the catalytic activity of CNTs and N-CNTs on the charge decomposition of Li_2O_2, the cathode was constructed by using the method previously reported [17]. The cathode was made by casting a mixture of CNTs or N-CNTs, Li_2O_2 (Alfa Aesar), and PVDF at a weight ratio of 7:2:1 onto a Celgard separator. The electrodes were incorporated into Swagelok cells and charged at a current density of 75 mA g^{-1} (of carbon) at room temperature.

4.3 Results and Discussion

Figure 4.1 shows SEM and TEM images of CNTs and N-CNTs. Both samples have uniform distributions in diameters (**Figure 4.1a and 4.1c**). As shown in **Figure 4.1b** and **4.1d**, the diameter of CNTs is about 40-50 nm, while 50-60 nm for N-CNTs. The typical bamboo-like structure in N-CNTs indicates that nitrogen atoms were introduced into the carbon network [11].

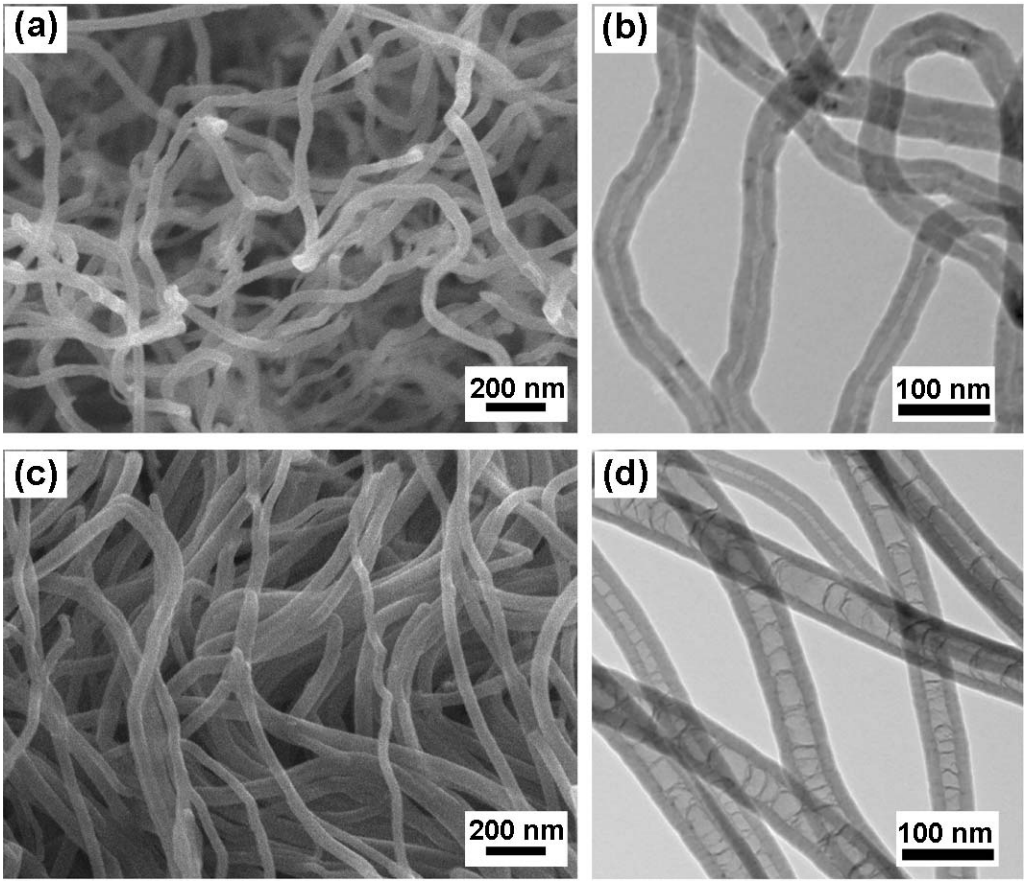

Figure 4.1 SEM and TEM images of CNTs (a, and b) and N-CNTs (c, and d).

XRD patterns of CNTs and N-CNTs are shown in **Figure 4.2a**. The diffraction peaks at around 30° and 52° are corresponding to the (002) and (100) facets of hexagonal graphitic carbon, respectively. However, the diffraction peaks of N-CNTs slightly shifted to lower 2θ values than those of CNTs, which is due to the distortion in the graphene layers resulting from the incorporation of nitrogen [18].

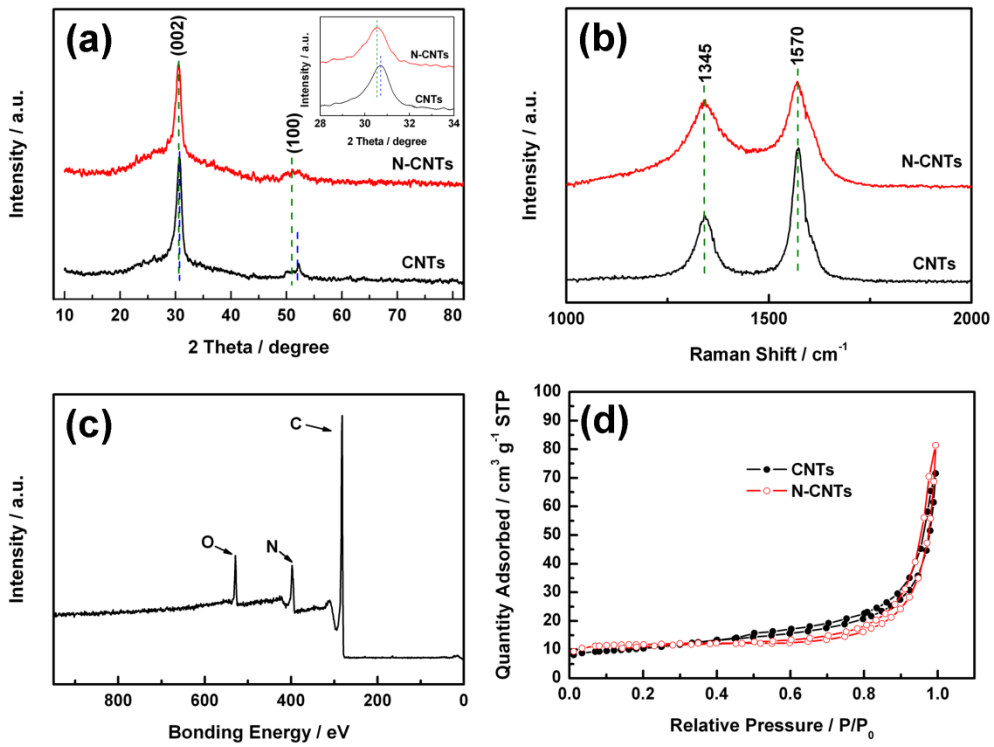

Figure 4.2 (a) XRD patterns of the CNTs and N-CNTs, (b) Raman spectra of the CNTs and N-CNTs, (c) XPS survey spectrum of the N-CNTs, and (d) N_2 adsorption–desorption isotherms for the CNTs and N-CNTs. The inset of (a) is the XRD patterns in the range between 28° and 34°.

Figure 4.2b shows the Raman spectra of CNTs and N-CNTs. Both samples exhibit two obvious peaks at ~ 1345 and ~ 1570 cm^{-1}, corresponding to the D and G bands, respectively. The D band denotes the disordered graphite structure, whereas the G band indicates the presence of crystalline graphitic carbon. The intensity ratio of D and

G band (I_D/I_G) is used to evaluate the disorder in the materials [19]. The I_D/I_G ratios of CNTs and N-CNTs are 0.53 and 0.85, respectively. The higher I_D/I_G ratio implies more defects in N-CNTs.

The XPS survey spectrum is shown in **Figure 4.2c**. Three strong peaks at 282, 398, and 529 eV are attributed to C1s, N1s and O1s, respectively. The atomic concentration of N can be estimated by the peak area ratio between N and C+N [20]. Therefore, *ca.* 10.2% nitrogen was introduced to the graphene layers in the as-prepared N-CNTs.

The N_2 adsorption–desorption isotherms for the CNTs and N-CNTs are shown in **Figure 4.2d**. Both samples are found to yield type-I isotherm, which indicates the presence of micropores and mesopores [21]. The BET surface area and average pore volume for CNTs are 44.95 m^2 g^{-1} and 0.081 cm^3 g^{-1} while for N-CNTs are 40.92 m^2 g^{-1} and 0.073 cm^3 g^{-1}, respectively, which is due to the different diameters. But both samples have similar pore size, ~ 7.3 nm.

As shown in **Figure 4.3a** and **4.3b**, the N-CNTs deliver an initial discharge capacity of 866 mAh g^{-1}, while 590 mAh g^{-1} for CNTs. Clearly, N-CNTs show a capacity about 1.5 times higher than that of the CNTs, although N-CNTs have lower BET surface area and pore volume [6]. The high specific capacity is resulting from the electrocatalytic activity of N–CNTs itself which facilitates the cathode reactions during discharge [8].

The discharge average voltage plateau of N-CNTs is ~ 2.52 V, which is higher than that of CNTs, ~ 2.41 V. The difference of ~ 0.1 V voltage between the N-CNTs and CNTs electrode remains through the whole discharge process, indicating a higher ORR activity on the N-CNTs electrode. To further compare the catalytic activity of the electrodes, cyclic voltammogram measurements were conducted. It can be seen from the CV curves in **Figure 4.3c** and **4.3d** that the onset voltage and peak voltage of N-CNTs are ~ 2.95 V and ~ 2.26 V, while for CNTs are ~ 2.83 V and ~ 2.14 V, respectively, which is consistent with the results in **Figure 4.3a** and **4.3b**.

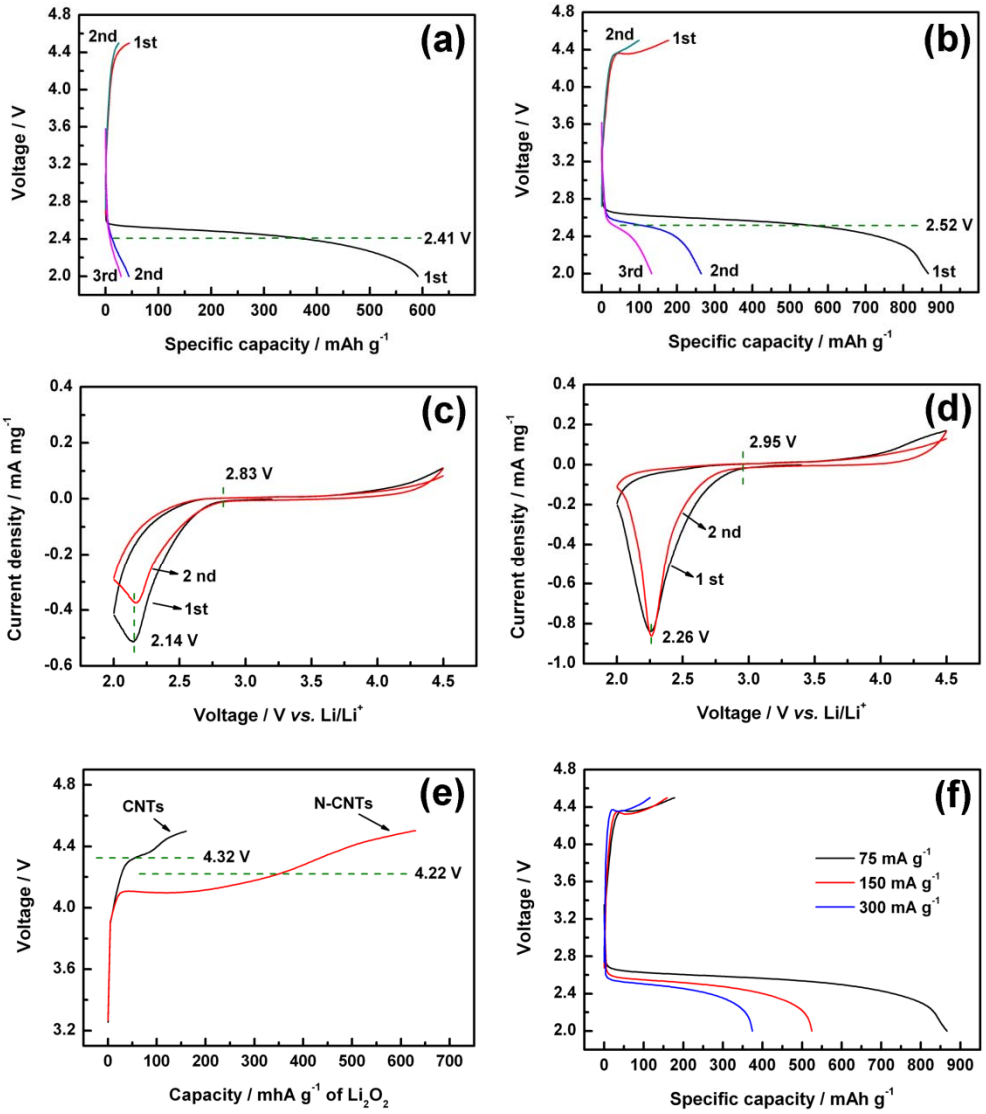

Figure 4.3 The voltage profiles of (a) CNTs and (b) N-CNTs electrodes cycled in a voltage range of 2.0~4.5 V at a current density of 75 mA g^{-1} in the first three cycles; CV curves of (c) CNTs and (d) N-CNTs electrodes at a scan rate of 0.2 mV s^{-1}; (e) Variation of Voltage on charging cells with CNTs and N-CNTs electrodes at a density of 75 mA g^{-1}. Cathode composition: CNTs or N-CNTs/Li_2O_2/binder (70/20/10); (f) Voltage profiles of N-CNTs electrodes at current densities of 75, 150, and 300 mA g^{-1}.

It is noticed that the discharge capacities of the second and the third cycle of N-CNTs are 264 and 133 mAh g^{-1}, respectively, whereas the capacity of CNTs electrode drops dramatically to less than 45 mAh g^{-1} in the second and the third cycle, therefore CNTs cathode showed limited reversibility (**Figure 4.3a** and **4.3b**). In order to compare the reversibility of CNTs and N-CNTs, their charge behavior for the electrochemical decomposition of the discharge product, Li_2O_2, was shown in **Figure 4.3e**. The N-CNTs have lower average charging plateau voltage (4.22 V) and higher capacity (630 mAh g^{-1} of Li_2O_2) than that of CNTs. These results reveal that the N-CNTs are more efficient for Li_2O_2 decomposition, indicating a high catalytic activity in the charge process. The discharge capacities of N-CNTs electrode at different current densities is shown in **Figure 4.3f**. With the increase of the current density, the discharge capacity decreases, 866, 525, and 374 mAh g^{-1} at current density of 75, 150, and 300 mA g^{-1}, respectively. This is because the electrochemical polarization becomes much more significant at high current densities [22].

The role of nitrogen doping in the carbon nanotubes for the electrocatalytic activities in lithium-air batteries is not clear now, and the understanding about the catalytic behavior of N-CNTs for ORR in nonaqueous electrolyte is scarce to date. Maybe the doped-nitrogen with lone electron pair could provide additional negative charges which enhance the interaction between carbon structures and foreign molecules and increase the conductivity, thus improves the electrode reaction for lithium air batteries [14-15, 23-24]. The related work is carrying out in our group to understand the doping effect.

4.4 Conclusions

The electrochemical performance of CNTs and N-CNTs electrodes were studied in lithium-air battery. The N-CNTs electrode has a specific discharge capacity of 866 mAh g^{-1}, which is about 1.5 times as that of CNTs. It was demonstrated the N-CNTs have much better electrocatalytic activity for Li_2O_2 decomposition, therefore improve the reversibility for lithium air batteries. The performance improvement of N-CNTs results from heteroatom nitrogen doping. The detailed fundamental mechanism is under study.

Acknowledgements

This research was supported by Natural Sciences and Engineering Research Council of Canada, Canada Research Chair Program, Canada Foundation for Innovation, Ontario Early Researcher Award and the University of Western Ontario.

References

[1] K. Abraham, Z. Jiang, A polymer electrolyte–based rechargeable lithium/oxygen battery, *J. Electrochem. Soc.*, 1996, **143**, 1–5.

[2] G. Girishkumar, B. McCloskey, A. Luntz, S. Swanson, W. Wilcke, Lithium-air battery: Promise and challenges, *J. Phys. Chem. Lett.*, 2010, **1**, 2193–2203.

[3] A. Débart, J. Bao, G. Armstrong, P. Bruce, An O_2 cathode for rechargeable lithium batteries: the effect of a catalyst, *J. Power Sources*, 2007, **174**, 1177–1182.

[4] J. Read, Characterization of the lithium/oxygen organic electrolyte battery, *J. Electrochem. Soc.*, 2002, **149**, A1190–A1195.

[5] Y. Lu, H. Gasteiger, M. Parent, V. Chiloyan, Y. Shao-Horn, The influence of catalysts on discharge and charge voltages of rechargeable Li-oxygen batteries, *Electrochem. Solid-State Lett.*, 2010,**13**, A69–A72.

[6] J. Xiao, D. Wang, W. Xu, D. Wang, R. Williford, J. Liu, J. Zhang, Optimization of air electrode for Li/air batteries, *J. Electrochem. Soc.*, 2010, **157**, A487–A492.

[7] M. Mirzaeian, P. Hall, Preparation of controlled porosity carbon aerogels for energy storage in rechargeable lithium oxygen batteries, *Electrochim. Acta*, 2009, **54**, 7444–7451.

[8] P. Kichambare, J. Kumar, S. Rodrigues, B. Kumar, Electrochemical performance of highly mesoporous nitrogen doped carbon cathode in lithium-oxygen batteries, *J. Power Sources*, 2011, **196**, 3310–3316.

[9] D. Geng, H. Liu, Y. Chen, R. Li, X. Sun, S. Ye, S. Knights, Non-noble metal oxygen reduction electrocatalystsbased on carbon nanotubes with controlled nitrogen contents, *J. Power Sources*, 2010, **196**, 1795–1801.

[10] Y. Chen, J. Wang, H. Liu, M. Banis, R. Li, X. Sun, T. Sham, S. Ye, S. Knights, Nitrogen doping effects on carbon nanotubes and the origin of the enhanced electrocatalyticactivity of supported Pt for proton exchange membrane fuel cells, *J. Phys. Chem. C*, 2011, **115**, 3769–3776.

[11] H. Liu, Y. Zhang, R. Li, X. Sun, S. Desilets, H. Abou-Rachid, M. Jaidann, L.-S. Lussier, Structural and morphological control, nitrogen incorporation and stability of aligned nitrogen-doped carbon nanotubes, *Carbon*, 2010, **48**, 1498–1507.

[12] K. Gong, F. Du, Z. Xia, M. Durstock, L. Dai, Nitrogen-doped carbon nanotube arrays with high electrocatalyticactivity for oxygen reduction, *Science*, 2009, **323**, 760–764.

[13] W. Xiong, F. Du, Y. Liu, A. Perez, Jr., M. Supp, T. Ramakrishnan, L. Dai, L. Jiang, 3-D carbon nanotube structures used as high performance catalyst for oxygen reduction reaction, *J. Am. Chem. Soc.*, 2010, **132**, 15839–15841.

[14] M. Saha, R. Li, X. Sun, S. Ye, S. Knights, 3-D composite electrodes of Pt supported nitrogen-doped carbon nanotubes grown on carbon paper for high performance PEM fuel cells, *Electrochem. Commun.*, 2009, **11**, 438–441.

[15] Y. Chen, J. Wang, H. Liu, R. Li, X. Sun, S. Ye, S. Knights, Enhanced stability of Pt electrocatalysts by nitrogen doping in CNTs for PEM fuel cells, *Electrochem. Commun.*, 2009, **11**, 2071–2076.

[16] G. Zhang, J. Zheng, R. Liang, C. Zhang, B. Wang, M. Hendrickson, E. Plichta, Lithium-air batteries using SWNT/CNF buckypapers as air electrodes, *J. Electrochem. Soc.*, 2010, **157**, A953–A956.

[17] V. Giordani, S. Freunberger, P. Bruce, J.-M. Tarascon, D. Larcher, H_2O_2 decomposition reaction as selecting tool for catalysts in Li-O_2 cells, *Electrochem. Solid-State Lett.*, 2010,**13**, A180–A183.

[18] S. Lim, S. Yoon, I. Mochida, D. Jung, Direct synthesis and structural analysis of nitrogen-doped carbon nanofibers, *Langmuir*, 2009, **25**, 8268–8273.

[19] J. Huang, W. Chen, C. Lee, Y. Chang, Role of amorphous carbon nanowires in reducing the turn-on field of carbon films prepared by microwave-heated CVD, *Diamond Relat. Mater.*, 2004, **13**, 1012–1016.

[20] M. Nath, B.Satishkumar, A. Govindaraj, C.Vinod, C. Rao, Production of bundles of aligned carbon and carbon-nitrogen nanotubes by the pyrolysis of precursors on silica-supported iron and cobalt catalysts, *Chem. Phys. Lett.*, 2000, **322**, 333–340.

[21] Y. Fang, D. Gu, Y. Zou, Z. Wu, F. Li, R. Che, Y. Deng, B. Tu, D. Zhao, A low-concentration hydrothermal synthesis of biocompatible ordered mesoporous carbon nanospheres with tunable and uniform size, *Angew. Chem. Int. Ed.*, 2010, **49**, 7987–7991.

[22] S. Zhang, D. Foster, J. Read, Discharge characteristic of a non-aqueous electrolyte Li/O_2 battery, *J. Power Sources*, 2010, **195**, 1235–1240.

[23] P. Ayala, R. Arenal, M. Rümmeli, A. Rubio, T. Pichler, The doping of carbon nanotubes with nitrogen and their potential applications, *Carbon*, 2010, **48**, 575–586.

[24] Y. Tang, B. Allen, D. Kauffman, A. Star, Electrocatalytic activity of nitrogen-doped carbon nanotube cups, *J. Am. Chem. Soc.*, 2009, **131**, 13200–13201.

Chapter 5

5 Superior Energy Capacity of Graphene Nanosheets for Nonaqueous Lithium-Oxygen Battery*

The discharge product, Li_2O_2, of lithium-air batteries is insoluble in the organic electrolyte, but deposits on the surface of carbon cathode. When the porous structure is clogged by Li_2O_2, the transportation of oxygen is limited, affecting the battery performance. It is important to design high surface area matrix with proper porous structures having effective three-dimensional (3D) three-phase (solid, liquid, and gas) interface which is ideal for the electrochemical reactions in the cathode.

Graphene nanosheets (GNSs) have attracted many interests due to its excellent mechanical, electrical, thermal and optical properties. More importantly, this two-dimensional (2D) material is a candidate for constructing and optimizing air electrode structure and properties, including porosity which is for oxygen diffusion as well as the catalytic activity for cathode reactions.

In this chapter, GNSs were synthesized by a modified Hummers' method and the as-prepared sample was used as cathode materials in lithium-oxygen battery. It was demonstrated that the GNSs electrode delivered an extremely high discharge capacity in comparison to carbon powders, which was attributed to its unique morphology and structure.

---

*Aversion of this chapter has been published in ***Chemical Communications***, 2011, **47**, 9438–9440.

5.1 Introduction

Nonaqueous lithium-oxygen/air battery is one of the most promising energy storage systems for hybrid electric vehicles (HEVs) and electric vehicles (EVs) because of its extremely high theoretical energy density [1-4]. The porosity of the air electrode plays an important role in the lithium-air battery performance because the insoluble products are deposited in the electrode, which block O_2 from diffusing to the reaction sites [5-9]. Recent work also showed that the oxygen reduction reaction (ORR) in the carbon electrode significantly affected its performance [10-15]. Therefore, it is important to develop new carbon electrodes to improve the kinetics and enhance the energy capacity.

Graphene nanosheets (GNSs) have attracted great attention for energy storage applications [16-19]. Especially, they have been widely used as catalyst supports or non-noble catalysts for fuel cells [20-23]. Recently, Zhou et al. examined the GNSs as air electrodes in lithium-air batteries with hybrid electrolyte and found that GNSs showed good electrocatalytic activity for ORR in aqueous electrolyte, resulting in high performance [24]. They also developed an idea of applying a graphene-like thin film on a ceramic state electrolyte in a lithium-air battery [25]. However, to our best knowledge, no research on GNSs as cathode for nonaqueous lithium-oxygen batteries has been reported.

Herein, for the first time, we employed GNSs as cathode active materials in nonaqueous lithium-oxygen batteries and found that GNSs delivered an extremely high discharge capacity.

5.2 Experimental

5.2.1 Material synthesis

Graphene nanosheets (GNSs) were prepared by the oxidation of graphite powder using the modified Hummers' method. Typically, graphite powder (1 g), sodium nitrate (0.75 g) and potassium permanganate (4.5 g) were added to concentrated sulphuric acid (37.5 mL) and stirred for 2 h in an ice water bath. Then the mixture was stirred for five days at room temperature. 100 mL of 5 wt% H_2SO_4 and 3 g of 30 wt% H_2O_2 were added into the above mixture in sequence under stirring with interval of 1 h. After stirring for 2 h, the sample was filtered and washed until the pH=7. The as-received sample was dried and heated at 1050 ^{o}C for 30 s under Ar to produce GNSs.

5.2.2 Physical characterizations

The morphology and structure of GNSs were characterized by a Hitachi S-4800 field emission scanning electron microscopy (SEM) and a Hitachi H-7000 transmission electron microscopy (TEM). N_2 adsorption/desorption isotherms were obtained using a Folio Micromeritics TriStar II Surface Area and Pore Size Analyser. The XRD pattern was recorded by a Bruker-AXS D8 Discover diffractometer employing a Co-Kα source (λ=1.7892 Å).

5.2.3 Electrochemical characterizations

Cathode was prepared by casting a mixture of carbon materials (GNSs, BP-2000, or Vulcan XC-72), and PVDF (Alfa Aesar) with a weight ratio of 9:1 onto a separator (Celgard 3500). The electrode is 7/16 inch in diameter and the loadings were 0.3 mg. Swagelok type cells composed of lithium foil anode, Celgard 3500 separator, different cathodes and a stainless steel (SS) mesh as current collector were used to carry out the

electrochemical measurements. The electrolyte was 1 mol $LiPF_6$ dissolved in propylene carbonate (PC)/ethylene carbonate (EC) (1:1 weight ratio). The discharge/charge characteristics were performed by using an Arbin BT-2000 battery station in a voltage range of 2.0-4.5 V in a 1 atm oxygen atmosphere at room temperature (25 °C).

5.3 Results and Discussion

Figure 5.1 shows the discharge/charge curves of the lithium-oxygen batteries with GNSs, BP-2000 and Vulcan XC-72 as cathodes at a current density of 75 mA g^{-1}. The discharge capacities of the BP-2000 and Vulcan XC-72 electrodes are 1909.1 and 1053.8 mAh g^{-1}, respectively. The GNSs electrode delivers a capacity of 8705.9 mAh g^{-1}, which is the highest capacity of any carbon-based materials in lithium-oxygen batteries ever reported so far. Moreover, it also shows a higher average discharge plateau and charge capacity than BP-2000 and Vulcan XC-72 electrodes, indicating a higher catalytic activity for cathode reactions [11, 12].

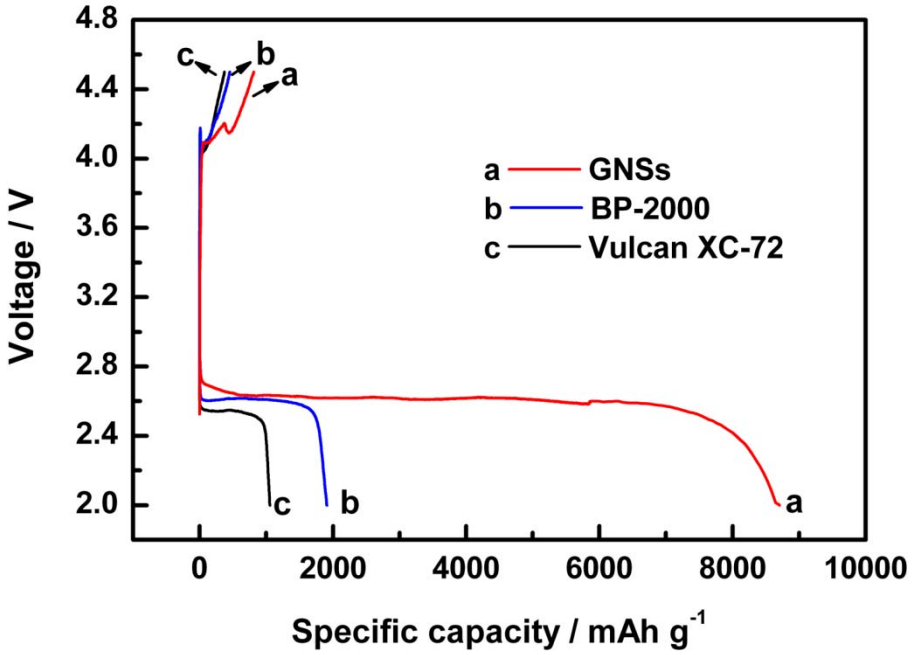

Figure 5.1 Discharge-charge performances of lithium-oxygen batteries with (a) GNSs, (b) BP-2000, and (c) Vulcan XC-72 cathodes at a current density of 75 mA g^{-1}.

The SEM and TEM images of GNSs electrode before and after discharge are shown in **Figure 5.2**. As shown in **Figure 5.2a** and **5.2b**, the GNSs have a curly morphology with a thin, wrinkled structure. These unique structures provide ideal porosity which is suitable for the electrolyte wetting and the O_2 diffusion, thus improving the efficiency of the catalyst reactions. The electrode with these structures not only increases the electrochemically accessible site, but also provides a large diffusion path for the O_2 mass transfer, therefore, improving the discharge capacity dramatically.

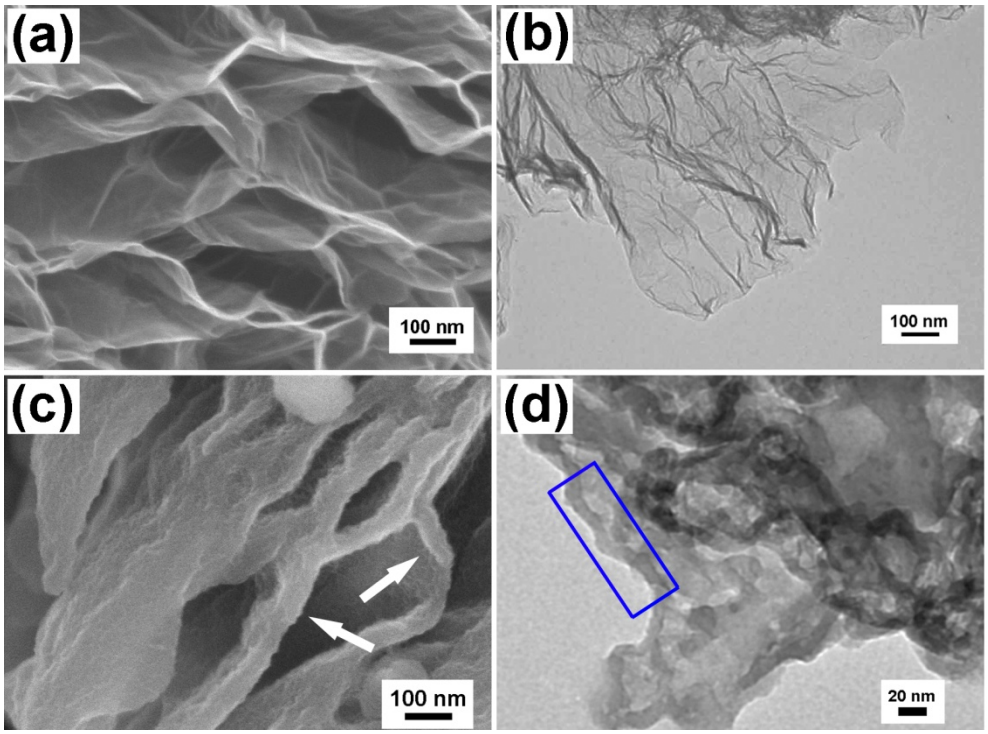

Figure 5.2 SEM and TEM images of GNSs electrodes before (a, and b) and after (c, and d) discharge.

After discharge, the products deposit on the both sides of the GNSs (**Figure 5.2c**), and it is important to note that at the edges of the GNSs, a relatively darker/thicker colour is observed (marked by arrows), suggesting more products on the edge sites as indicated by the square in **Figure 5.2d**.

Figure 5.3 shows the FTIR spectra of the GNSs, BP-2000 and Vulcan XC-72. It can be seen that in comparison to the other two carbon materials, GNSs show an extra band at 1120 cm^{-1}, which corresponds to the C-O stretching vibrations [26]. This is because the edge sites of the GNSs contain a large amount of unsaturated carbon atoms which are highly active to react with oxygen and form oxygen-containing groups. Therefore, the presence of the unsaturated carbon atoms results in high activity for ORR [27, 28].

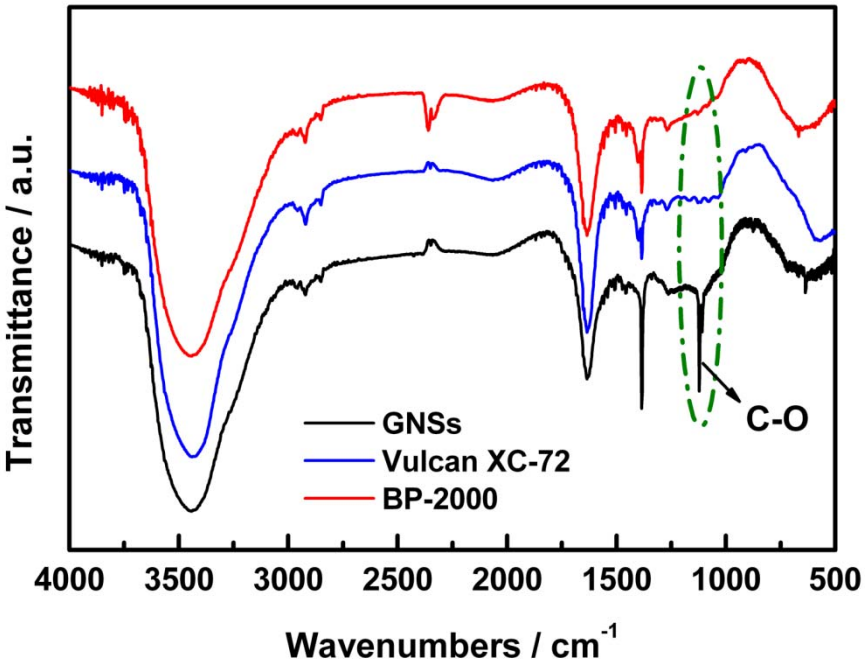

Figure 5.3 FTIR spectra of GNSs, BP-2000 and Vulcan XC-72.

Several works have reported that the surface area, pore size and mesopore volume of carbon materials significantly affected the specific capacity of lithium-air batteries [6, 7]. These effects are also investigated in this work.

Figure 5.4a shows the N_2 absorption-desorption isotherms at 77 K for GNSs, BP-2000 and Vulcan XC-72. All samples are found to yield type-I isotherm at low P/P_0, indicating the presence of micropores [29]. For GNSs, the hysteresis loop, in the P/P_0 range of ~ 0.4-1.0 is indicative of mesoporosity in addition to the presence of microporosity [30]. The hysteresis loop for mesopores shifts to a higher P/P_0 range (~ 0.8-1.0) for BP-2000 and Vulcan XC-72, which is associated with the presence of a narrower range of mesopores, with larger diameters.

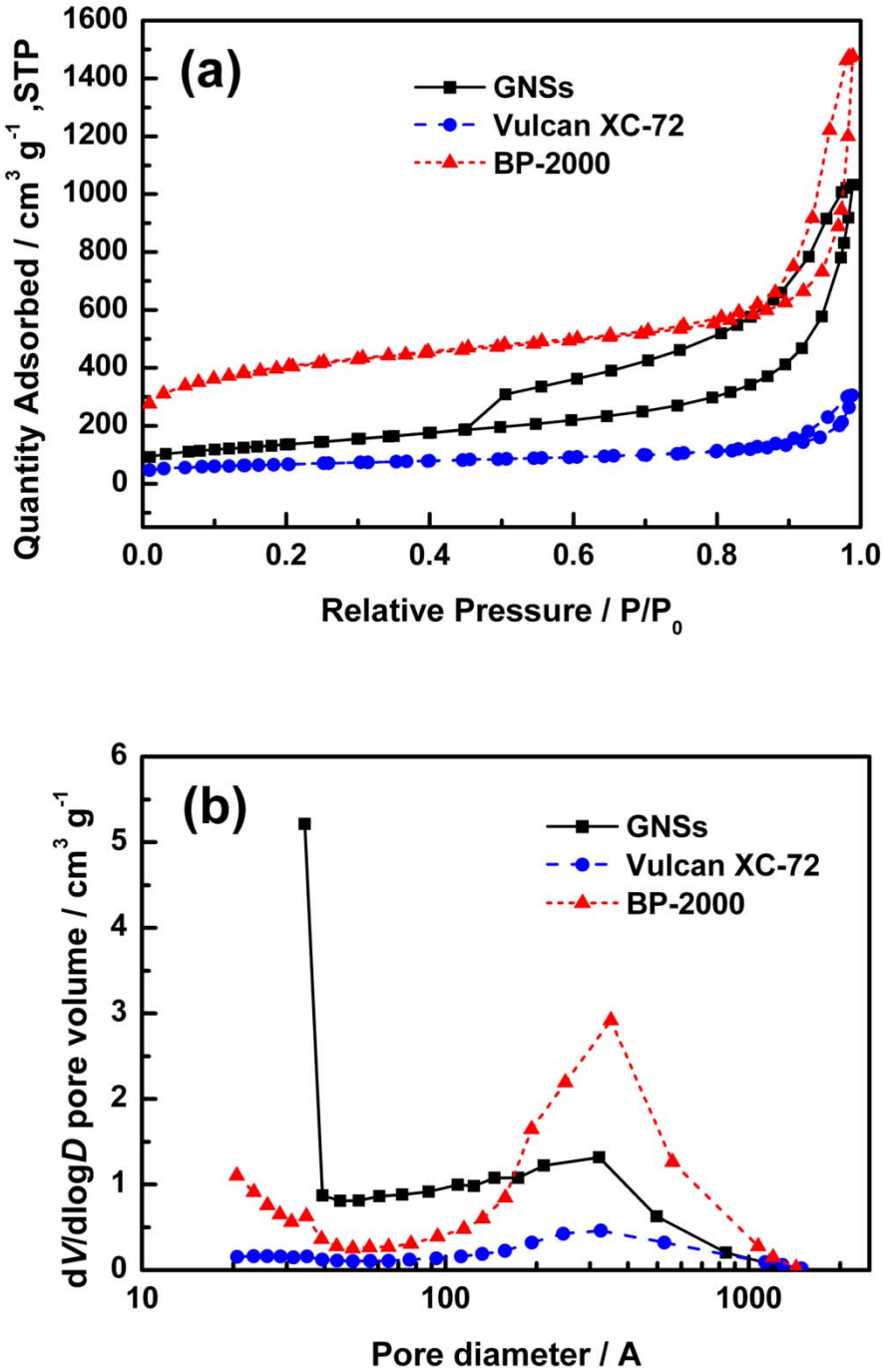

Figure 5.4 (a) N_2 adsorption-desorption isotherms at 77 K and (b) pore size distribution (PSD) for GNSs, BP-2000 and Vulcan XC-72.

The pore size distribution (PSD) obtained using the Barrett-Joyner-Halenda (BJH) method for the three carbon materials are shown in **Figure 5.4b**. In the mesopore size range (2-50 nm), the GNSs show a wide distribution of pore sizes and much higher pore volume at the pore size range from 2-20 nm, while at large pore size range (20-50 nm), BP-2000 possesses large pore volume. Vulcan XC-72 possesses small pore volume, compared to GNS and BP-2000.

GNSs have similar mesopore volume but smaller surface area compared to BP-2000 (**Table SI-5.1**), while the discharge capacity is much higher. Therefore, the pore size of GNSs plays a more important role in its superior performance, in addition to its novel structure. GNSs possess wide PSD in the mesopore range, forming suitable diffusion channels for the electrolyte and O_2, which is an ideal 3-dimentional (3D), 3-phase electrochemical area [31].

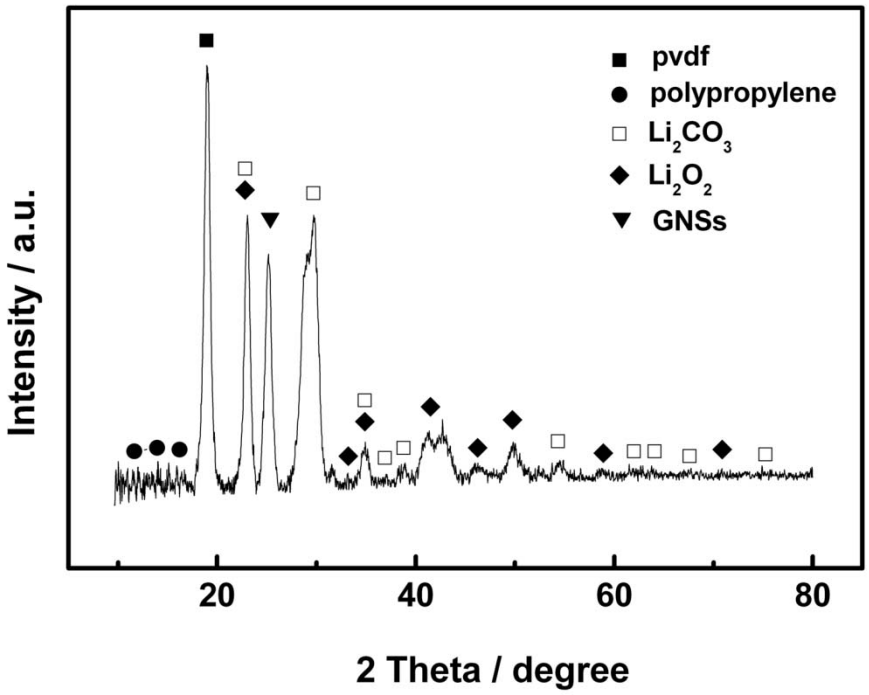

Figure 5.5 XRD pattern of GNSs electrode after discharge.

Figure 5.5 shows the XRD pattern of the GNSs electrode after discharge. The dominant discharge product is Li_2CO_3 and a small amount of Li_2O_2 is also present. Xiao and Zhang et al. and Bruce et al. have reported that for carbon-based electrode, the formation of Li_2CO_3, along with a small amount of Li_2O_2 was because the intermediate product of the reaction between Li and O_2 may in turn react with the carbonate solvent in the PC/EC-based electrolyte [32, 33].

5.4 Conclusions

In summary, graphene nanosheets were employed as the cathode materials for lithium-oxygen batteries, and for the first time, were demonstrated to show an excellent electrochemical performance with a discharge capacity of 8705.9 mAh g^{-1}. The unique structures of GNSs form an ideal 3D 3-phase electrochemical area and the diffusion channels for the electrolyte and O_2, which increase the efficiency of the catalyst reaction. In addition, the active sites at the edge sites significantly contribute to the superior electrocatalytic activity towards ORR. Although the detailed mechanism for the oxygen reduction reaction on GNSs in nonaqueous electrolyte is unclear, it has revealed that GNSs can deliver an extremely high discharge capacity, showing promising applications in lithium-oxygen batteries.

Acknowledgment

This research was supported by Natural Sciences and Engineering Research Council of Canada, Canada Research Chair Program, Canada Foundation for Innovation, Ontario Early Researcher Award and the University of Western Ontario.

References

[1] K. Abraham, Z. Jiang, A polymer electrolyte-based rechargeable lithium/oxygen battery, *J. Electrochem. Soc.*, 1996, **143**, 1–5.

[2] M. Armand, J.-M. Tarascon, Building better batteries, *Nature*, 2008, **451**, 652–657.

[3] T. Zhang, N. Imanishi, Y. Shimonishi, A. Hirano, Y. Takeda, O. Yamamoto, N. Sammes, A novel high energy density rechargeable lithium/air battery, *Chem. Commun.*, 2010, **46**, 1661–1663.

[4] K. Takechi, T. Shiga, T. Asaoka, A Li-O_2/CO_2 battery, *Chem. Commun.*, 2011, **47**, 3463–3465.

[5] J. Xiao, D. Wang, W. Xu, D. Wang, R. Williford, J. Liu, J.-G. Zhang, Optimization of air electrode for Li/air batteries, *J. Electrochem. Soc.*, 2010, **157**, A487–A492.

[6] R. Williford, J.-G. Zhang, Air electrode design for sustained high power operation of Li/air batteries, *J. Power Sources*, 2009, **194**, 1164–1170.

[7] X. Yang, P. He, Y. Xia, Preparation of mesocellular carbon foam and its application for lithium/oxygen battery, *Electrochem. Commun.*, 2009, **11**, 1127–1130.

[8] S. Zhang, D. Foster, J. Read, Discharge characteristic of a non-aqueous electrolyte Li/O_2 battery, *J. Power Sources*, 2010, **195**, 1235–1240.

[9] M. Mirzaeian, P. Hall, Preparation of controlled porosity carbon aerogels for energy storage in rechargeable lithium oxygen batteries, *Electrochim. Acta*, 2009, **54**, 7444–7451.

[10] R. Padbury, X. Zhang, Lithium-oxygen batteries—Limiting factors that affect performance, *J. Power Sources*, 2011, **196**, 4436–4444.

[11] Y. Lu, H. Gasteiger, Y. Shao-Horn, Method development to evaluate the oxygen reduction activity of high-surface-area catalysts for Li-air batteries, *Electrochem. Solid State Lett.*, 2011, **14**, A70–A74.

[12] A. Débart, A. Paterson, J. Bao, P. Bruce, α-MnO_2 nanowires: acatalyst for the O_2 electrode in rechargeable lithium batteries, *Angew. Chem. Int. Ed.*, 2008, **47**, 4521–4524.

[13] H. Cheng, K. Scott, Carbon-supported manganese oxide nanocatalysts for rechargeable lithium-air batteries, *J. Power Sources*, 2010, **195**, 1370–1374.

[14] P. Kichambare, J. Kumar, S. Rodrigues, B. Kumar, Electrochemical performance of highly mesoporous nitrogen doped carbon cathode in lithium-oxygen batteries, *J. Power Sources*, 2011, **196**, 3310–3316.

[15] Y. Li, J. Wang, X. Li, D. Geng, J. Yang, R. Li, X. Sun, Nitrogen-doped carbon nanotubes as cathode for lithium-air batteries, *Electrochem. Commun.*, 2011, **13**, 668–672.

[16] J. Choi, J. Jin, I. Jung, J. Kim, H. Kim, S. Son, $SnSe_2$ nanoplate-graphene composites as anode materials for lithium ion batteries, *Chem. Commun.*, 2011, **47**, 5241–5243.

[17] H. Wang, C. Zhang, Z. Liu, L. Wang, P. Han, H. Xu, K. Zhang, S. Dong, J. Yao, G. Cui, Nitrogen-doped graphene nanosheets with excellent lithium storage properties, *J. Mater. Chem.*, 2011, **21**, 5430–5434.

[18] K. Chang, W. Chen, In situ synthesis of MoS_2/graphene nanosheet composites with extraordinarily high electrochemical performance for lithium ion batteries, *Chem. Commun.*, 2011, **47**, 4252–4254.

[19] Q. Yue, K. Zhang, X. Chen, L. Wang, J. Zhao, J. Liu, J. Jia, Generation of OH radicals in oxygen reduction reaction at Pt-Co nanoparticles supported on graphene in alkaline solutions, *Chem. Commun.*, 2010, **46**, 3369–3371.

[20] Y. Zhou, J. Chen, F. Wang, Z. Sheng, X. Xia, A facile approach to the synthesis of highly electroactive Pt nanoparticles on graphene as an anode catalyst for direct methanol fuel cells, *Chem. Commun.*, 2010, **46**, 5951–5953.

[21] Y. Shao, S. Zhang, M. Engelhard, G. Li, G. Shao, Y. Wang, J. Liu, I. Aksay, Y. Lin, Nitrogen-doped graphene and its electrochemical applications, *J. Mater. Chem.*, 2010, **20**, 7491–7496.

[22] D. Geng, Y. Chen, Y. Chen, Y. Li, R. Li, X. Sun, S. Ye, S. Knights, High oxygen-reduction activity and durability of nitrogen-doped graphene, *Energy Environ. Sci.*, 2011, **4**, 760–764.

[23] L. Qu, Y. Liu, J. Baek, L. Dai, Nitrogen-doped graphene as efficient metal-free electrocatalyst for oxygen reduction in fuel cells, *ACS Nano*, 2010, **4**, 1321–1326.

[24] E. Yoo, H. Zhou, Li-air rechargeable battery based on metal-free graphene nanosheet catalysts, *ACS Nano*, 2011, **5**, 3020–3026.

[25] Y. Wang, H. Zhou, To draw an air electrode of a Li-air battery by pencil, *Energy Environ. Sci.*, 2011, **4**, 1704–1707.

[26] S. Stankovich, R. Piner, S. Nguyen, R. Ruoff, Synthesis and exfoliation of isocyanate-treated graphene oxide nanoplatelets, *Carbon*, 2006, **44**, 3342–3347.

[27] E. Yeager, Dioxygen electrocatalysis: mechanisms in relation to catalyst structure, *J. Mol. Catal.*, 1986, **38**, 5–25.

[28] C. Banks, T. Davies, G. Wildgoose, R. Compton, Electrocatalysis at graphite and carbon nanotube modified electrodes: edge-plane sites and tube ends are the reactive sites, *Chem. Commun.*, 2005, **7**, 829–841.

[29] M. Kruk, M. Jaroniec, K. Gadkaree, Nitrogen adsorption studies of novel synthetic active carbons, *J. Colloid Interface Sci.*, 1997, **192**, 250–256.

[30] Y. Fang, D. Gu, Y. Zou, Z. Wu, F. Li, R. Che, Y. Deng, B. Tu, D. Zhao, A low-concentration hydrothermal synthesis of biocompatible ordered mesoporous carbon nanospheres with tunable and uniform size, *Angew. Chem. Int. Ed.*, 2010, **49**, 7987–7991.

[31] C. Tran, X. Yang, D. Qu, Investigation of the gas-diffusion-electrode used as lithium/air cathode in non-aqueous electrolyte and the importance of carbon material porosity, *J. Power Sources*, 2010, **195**, 2057–2063.

[32] J. Xiao, J. Hua, D. Wang, D. Hu, W. Xu, G. Graff, Z. Nie, J. Liu, J.-G. Zhang, Investigation of the rechargeability of Li-O_2 batteries in non-aqueous electrolyte, *J. Power Sources*, 2011, **196**, 5674–5678.

[33] S. Freunberger, Y. Chen, Z. Peng, J. Griffin, L. Hardwick, F. Bardé, P. Novák, P. Bruce, Reactions in the rechargeable lithium-O_2 battery with alkyl carbonate electrolytes, *J. Am. Chem. Soc.*, 2011, **133**, 8040–8047.

Supporting Information

Table SI-5.1 Physical properties of GNSs, BP-2000, and Vulcan XC-72.

	GNSs	BP-2000	Vulcan XC-72
Surface area / m^2 g^{-1}	524.99	1401.00	232.79
Mesopore volume / cm^3 g^{-1}	1.1729	1.1139	0.2739

Chapter 6

6 Nitrogen-Doped Graphene Nanosheets as Cathode Materials with Excellent Electrocatalytic Activity for High Capacity Lithium-Oxygen Batteries*

Graphene nanosheets (GNSs) have shown much higher discharge capacity compared to carbon black powders due to their unique physical and chemical properties. The cathode of lithium-oxygen battery made of these GNSs has three-dimensional three-phase electrochemical area and diffusion channels for the electrolyte and oxygen, which increase the efficiency of the cathode reactions. More importantly, the active sites of the GNSs also contribute to the superior electrocatalytic activity for oxygen reduction reaction during discharge. It is reported that the properties of GNSs can be tailored by heteroatom doping other elements to the graphene frameworks. Therefore, it is interesting to study the doping effect of GNSs for lithium-oxygen battery performance.

In this chapter, nitrogen-doped graphenenanosheets (N-GNSs) were synthesized and employed as cathode materials for nonaqueous lithium-oxygen batteries and the battery delivered a discharge capacity of 11660 mAh g^{-1}, which was about 40% higher than that of the pristine GNSs electrode. Furthermore, the electrocatalytic activity of N-GNSs for oxygen reduction in the nonaqueous electrolyte was 2.5 times as that of GNSs. The excellent electrochemical performance of N-GNSs was attributed to the defects and functional groups as active sites introduced by nitrogen doping.

---

*Aversion of this chapter has been published in ***Electrochemistry Communications***, 2012, **18**, 12-15.

6.1 Introduction

Nonaqueous lithium-oxygen/air batteries have great potential for electric vehicles (EVs) and hybrid electric vehicles (HEVs) [1, 2]. The cathode active material, oxygen, is not stored in the battery but can be absorbed from the environment, leading to an extremely high energy density. However, the reaction products are not soluble in the nonaqueous electrolyte but deposit in the carbon electrode and eventually block the oxygen diffusion channels; therefore, it is a critical challenge to develop an optimum carbon cathode with appropriate surface area, porosity and morphology [3-5].

Graphene nanosheets (GNSs) have been reported as ideal cathode materials for lithium-oxygen batteries because of their unique morphology and structure. The GNSs electrode can provide not only ideal diffusion channels for electrolyte and oxygen, but also active sites for oxygen reduction reaction (ORR), therefore, improve the battery performance [6-8]. Chemical doping with nitrogen atoms to GNSs can modify the electronic property, provide more active sites, and enhance the interaction between carbon structure and other molecules, thus improves the performance in various applications, such as fuel cells, lithium-ion batteries, supercapacitors, etc [9-11].

In this study, nitrogen-doped graphene nanosheets (N-GNSs) were applied as cathode materials for lithium-oxygen batteries. They show excellent electrocatalytic activity for oxygen reduction, therefore, increasing about 40% of the discharge capacity compared to graphene nanosheets (GNSs). This finding not only shows that N-GNSs are promising electrode materials, but also gives a rational direction to modify other carbon materials for application in lithium-oxygen batteries.

6.2 Experimental

6.2.1 Materials synthesis

GNSs were prepared by the oxidation of graphite powder using the modified Hummers' method, and N-GNSs were prepared by post heating the GNSs under high purity ammonia mixed with Ar at 900 ^{o}C for 5 mins [10, 11].

6.2.2 Physical characterizations

The morphology of the discharge products of GNSs and N-GNSs electrodes were characterized by a Hitachi S-4800 field emission scanning electron microscopy (FESEM). The morphology of GNSs and N-GNSs were characterized by a Hitachi H-7000 transmission electron microscopy (TEM). The XRD patterns were recorded by a Bruker-AXS D8 Discover diffractometer employing a Co-Kα source (λ=1.7892 Å). The XPS spectra were tested by a Kratos Axis Ultra X-ray photoelectron spectrometer with Al Kα as the X-ray source. Raman scattering spectra were recorded on a HORIBA Scientific LabRAM HR Raman spectrometer system equipped with a 532.4 nm laser. N_2 adsorption/desorption isotherms were obtained using a Folio Micromeritics TriStar II Surface Area and Pore Size Analyser.

6.2.3 Electrochemical measurements

Swagelok type cells were used to test the battery performance. GNSs or N-GNSs and PVDF (Alfa Aesar) with a weight ratio of 9:1 were casted onto a separator (Celgard 3500) as cathode. The electrodes were cut to 3/8 inch in diameter and the loadings of GNSs or N-GNSs were ~ 0.3 mg. The electrolyte was 1 mol dm^{-3} $LiPF_6$ dissolved in tetraethylene glycol dimethyl ether (TEGDME). The discharge/charge characteristics

were performed by using an Arbin BT-2000 battery station in a voltage range of 2.0-4.5 V in a 1 atm oxygen atmosphere at room temperature (25 °C).

The cyclic voltammetry (CV) tests were conducted in a three-electrode cell. A platinum wire was used as the counter electrode. A silver wire immersed into 0.1 mol dm^{-3} $AgNO_3$ in TEGDME solution, connected to the main solution by a glass frit, was used as reference electrode. A glass carbon disk (0.196 cm^2, Pine Inc.) covered with catalyst thin film was used as the working electrode. 2 mg of GNSs or N-GNSs, 2 mg of PTFE (60 wt.%, Sigma-Aldrich) were suspended in a 30 vol.% 2-propanol (Sigma-Aldrich) solution in deionized water and ultrasonically blended for 30 min. 10 μL of the suspension was dropped on the disk electrode and dried at 80 °C in vacuum for 1 h. CV curves were recorded by scanning the disk potential from 3.5 to 2.0 V (0.1 mol dm^{-3} $LiPF_6$ in TEGDME solution) at a scan rate of 5 mV s^{-1} by using an AutolabPotentiostat/Galvanostat (PGSTAT-30, Eco Chemie, Brinkmann Instruments) at room temperature (25 °C).

6.3 Results and Discussion

Figure 6.1a shows the initial discharge curves of GNSs and N-GNSs electrodes in nonaqueous lithium-oxygen batteries at various current densities. The discharge capacity of GNSs electrode is 8530 mAh g^{-1} at a current density of 75 mA g^{-1}, while 11660mAh g^{-1} for N-GNSs, which is about 40% higher than that of GNSs. With the current densities increase, the discharge capacities of both samples decrease, which are 5333 and 3090mhA g^{-1} for GNSs and 6640 and 3960mAh g^{-1} for N-GNSs at current densities of 150 and 300 mA g^{-1}, respectively. Clearly, the N-GNSs electrode exhibits higher discharge capacity than GNSs electrode. Furthermore, N-GNSs electrode also shows higher average discharge plateau than GNSs electrode at various discharge

current densities, indicating a higher catalytic activity of N-GNSs for cathode reaction which may due to the higher binding energy of oxygen after nitrogen doping [12, 13].

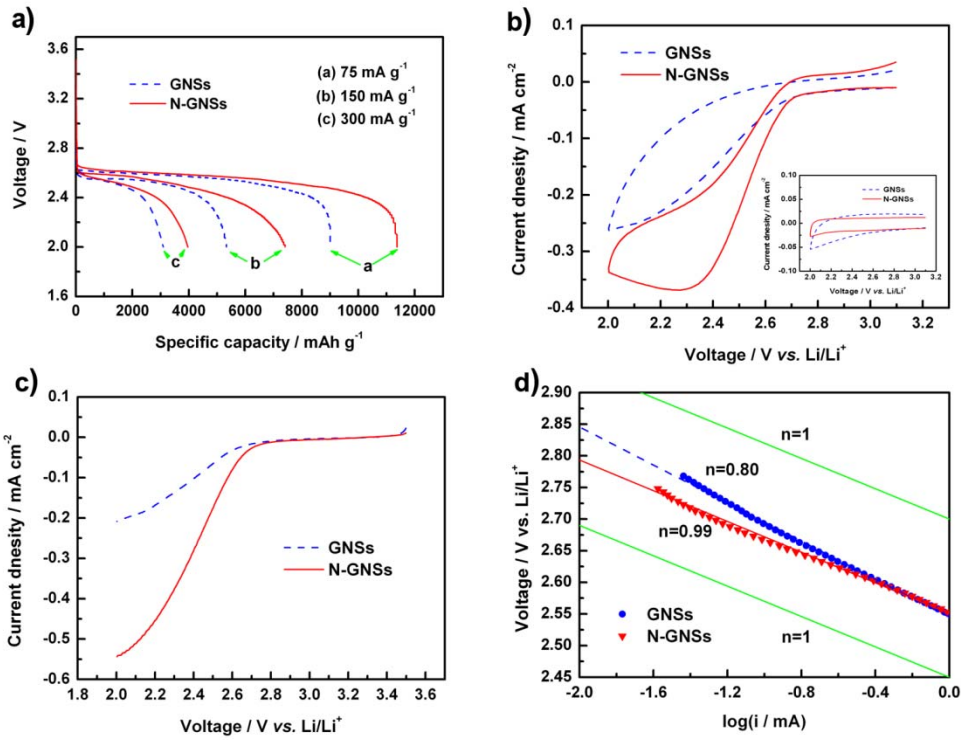

Figure 6.1 a, Voltage profiles of GNSs and N-GNSs electrodes at various current densities; b, CVs of GNSs and N-GNSs electrodes in O_2-saturated 0.1 mol dm^{-3} $LiPF_6$ in TEGDME solution at a scan rate of 5 mV s^{-1}, inset is the CVs in Ar-saturated solution; c, Rotating-disk voltamograms recorded for GNSs and N-GNSs electrodes for ORR at a rotating speed of 100 rpm in O_2-saturated 0.1 mol dm^{-3} $LiPF_6$ in TEGDME solution at a scan rate of 5 mV s^{-1}; d, Tafel-slops for the ORR on the GNSs and N-GNSs electrodes.

The cyclic voltammogram (CV) curves of GNSs and N-GNSs in 0.1 mol dm^{-3} $LiPF_6$ in TEGDME solution saturated with Ar or O_2 at a scan rate of 5 mV s^{-1} are shown in **Figure 6.1b**. Featureless voltammetric currents were observed in the Ar-saturated solution (inset of **Figure 6.1b**). As shown in **Figure 6.1b**, the onset potential of ORR

for GNSs is at 2.76 V and no reduction peak is observed. While for N-GNSs, the onset potential of ORR shifted positively to around 2.8 V and a great and well-defined enhanced reduction peak at 2.29 V presents, indicating a superior electrocatalytic activity of N-GNSs for ORR.

To further investigate the ORR performance, rotating disk electrode (RDE) voltammetry measurements were carried out (**Figure 6.1c**). The onset potential of ORR for GNSs is at 2.79 V, whereas for N-GNSs is at 2.84 V. It should be noted that there is no well-defined diffusion limiting current plateau for both samples which is similar to other non-noble catalysts especially pure carbon for ORR, however, the current density of N-GNSs at 2 V is about 2.5 times as that of GNSs [14-16]. Furthermore, according to the Tafel-slops of the two samples shown in **Figure 6.1d**, the numbers of electron transferred in ORR are 0.99 for N-GNSs and 0.80 for GNSs, respectively [17]. These results suggest that N-GNSs have higher catalytic activity for ORR in a nonaqueous solution than GNSs.

As shown in **Figure 6.2a** and **6.2b**, the structure and morphology of N-GNSs and GNSs show no obvious difference by observing the TEM images. N-GNSs and GNSs show the same micro/meso- porosity and pore size distribution (**Figure 6.2c** and inset). **Figure 6.2d** shows XPS survey spectra for GNSs and N-GNSs, as expected, nitrogen was introduced into GNSs and the content is about 2.8 at %. Based on the high resolution N1s spectra, three N peaks were observed at BE = 389.1 eV (pyridinic-N), 399.9 eV (pyrrolic-N) and 401.5 eV (graphitic-N) for N-GNSs (inset of **Figure 6.2d**). Recent studies reported that nitrogen-doped carbon powder and carbon nanotubes showed higher discharge capacities for lithium-air batteries than the pristine counterparts [18,19].

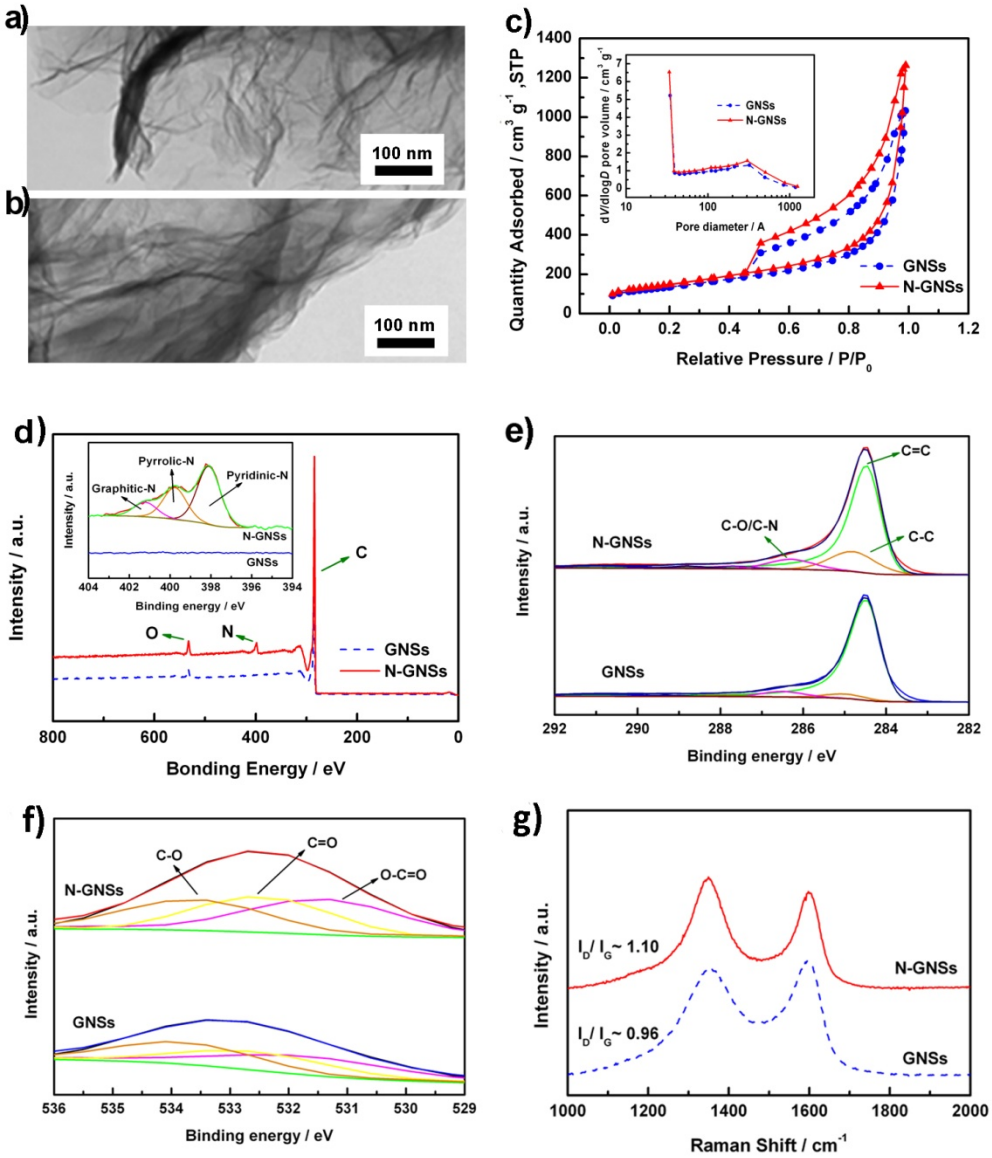

Figure 6.2 TEM images of a, GNSs and b, N-GNSs; c, N_2 adsorption–desorption isotherms at 77 K, inset is the pore size distribution; XPS d, survey, e, C1s, and f, O1s spectra of GNSs and N-GNSs, inset of d is N 1s spectra of two samples; g, Raman spectra of GNSs and N-GNSs.

The process for incorporation of nitrogen into graphene also creates structural defects on GNSs, which increases the amount of unsaturated carbon atoms (**Figure 6.2e**); and these atoms are very active to react with oxygen and form oxygen-containing groups, which can catalyze the ORR [20]. From **Figure 6.2f**, it can be seen that oxygen content increase after nitrogen doping, and present in the form of C-O bonds, carbonyls (C=O), and carboxylates (O=C-O) [21]. The Raman spectra of GNSs and N-GNSs are shown in **Figure 6.2g**. Two peaks observed at ~ 1350 and ~ 1595 cm^{-1} are corresponding to D and G bands, respectively. The intensity ratio of D to G bands of GNSs and N-GNSs are 0.96 and 1.10, respectively, confirming that there are more defects after nitrogen doping [22]. It is believed that there are more defects and functional groups after nitrogen doping, and the carbon atoms adjacent to nitrogen dopants possess higher positive charge density, resulting in an enhanced adsorption of oxygen and reactive intermediates that enhances the ORR [23].

The morphologies of discharge products for GNSs and N-GNSs electrodes are shown in **Figure 6.3a** and **6.3b**, respectively. It can be seen that the morphologies of the products on the two surfaces are significantly different. The diameter of the particles is about 600~1000 nm for GNSs and 200~500 nm for N-GNSs. Recent study by Density Functional Theory (DFT) calculations have shown that the discharge products most likely prefer to nucleate and grow around the defective sites with functional groups on GNSs [8]. To confirm it by experiment, the electrodes were discharged for 1 h and the SEM images of the products are shown in **Figure 6.3c** and **6.3d**. On GNSs, the product particle size is distributed from 20 to 45 nm, whereas on N-GNSs, a smaller size from 5 to 20 nm is observed. Moreover, the distribution of the product is more uniform on N-GNSs, while the product particles aggregated into large clusters on GNSs and some surfaces are free of coverage. These observations suggest that the presence of the homogeneously distributed nitrogen species resulting in more active sites (defects and functional groups) of N-GNSs provide more nucleation sites and thus promotes a higher dispersion.

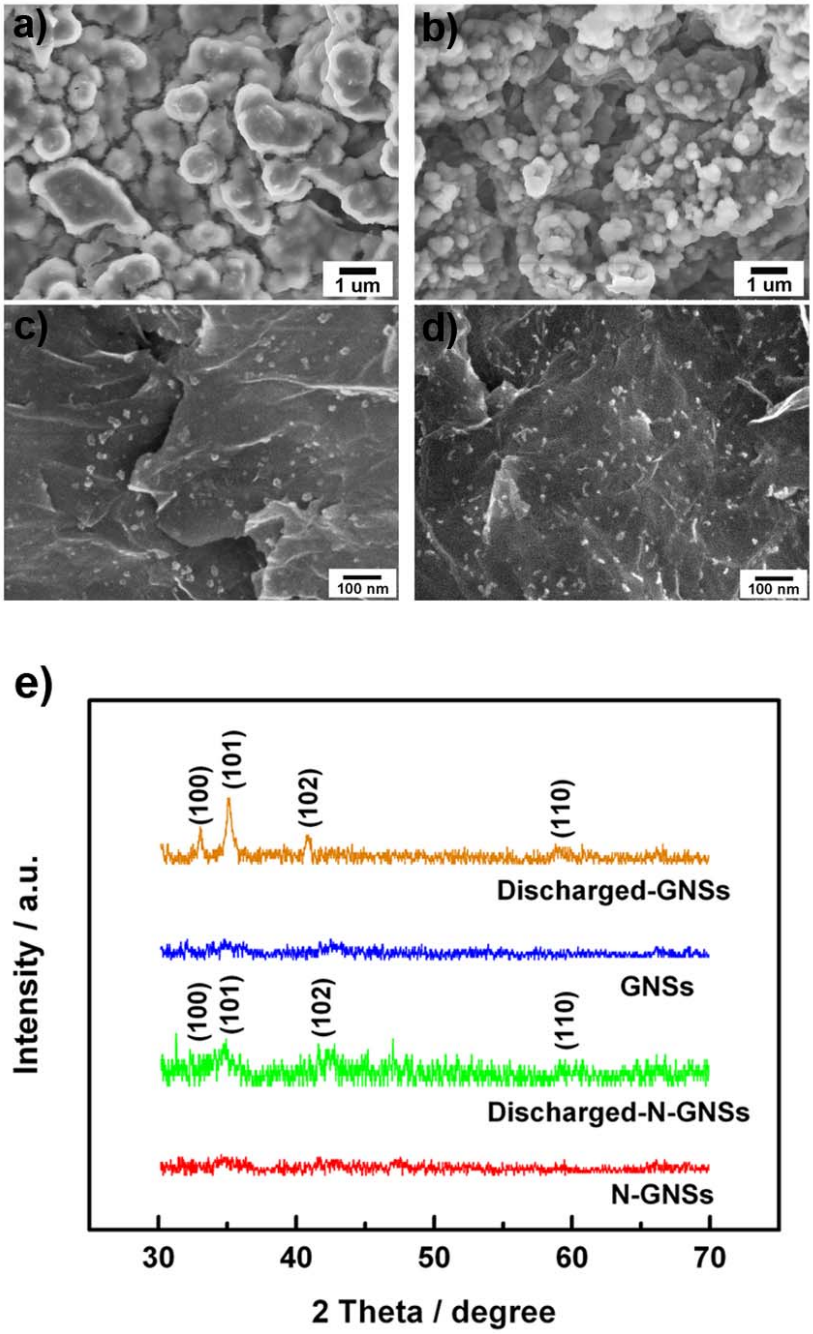

Figure 6.3 SEM images of the fully discharged a, GNSs, b, N-GNSs electrodes and c, GNSs, d, N-GNSs electrodes discharged for 1 h; e, XRD patterns of pristine and discharged GNSs and N-GNSs electrodes.

Recently, there are some discussions about the decomposition of the carbonatesolvent based electrolytes during discharge and charge in the lithium-oxygen batteries [24, 25]. To minimize this contribution, ether-based electrolyte has been used in this study. The GNSs and N-GNSs electrodes before and after discharged were examined by XRD and the patterns are shown in **Figure 6.3e**. The additional peaks of both electrodes after discharge were assigned to Li_2O_2, whereas neither Li_2O nor Li_2CO_3 was detected, and the results are consistent with the formation of Li_2O_2 by other groups [26]. It is important to note that the peaks of the products of N-GNSs electrodes were broader than those of GNSs electrodes, which may due to the smaller crystallite sizes of Li_2O_2, consistent with the SEM results discussed above.

6.4 Conclusions

It was demonstrated that the performance improvement of N-GNSs as cathode materials for lithium-oxygen batteries was due to the defects and functional groups introduced by doping nitrogen into the framework of GNSs. More importantly, for the first time, we showed that the catalytic activity for ORR of N-GNSs in a nonaqueous electrolyte is much higher than that of GNSs. This finding gives a rational direction to modify other carbon materials for application in lithium-oxygen batteries.

Acknowledgements

This research was supported by Natural Sciences and Engineering Research Council of Canada, Canada Research Chair Program, Canada Foundation for Innovation, Ontario Early Researcher Award and the University of Western Ontario.

References

[1] K. Abraham, Z. Jiang, A polymer electrolyte-based rechargeable lithium/oxygen battery, *J. Electrochem. Soc.*, 1996, **143**, 1–5.

[2] G. Girishkumar, B. McCloskey, A. Luntz, S. Swanson, W. Wilcke, Lithium-air battery: Promise and challenges, *J. Phys. Chem. Lett.*, 2010, **1**, 2193–2203.

[3] R. Williford, J. Zhang, Air electrode design for sustained high power operation of Li/air batteries, *J. Power Sources*, 2009, **194**, 1164–1170.

[4] C. Tran, X. Yang, D. Qu, Investigation of the gas-diffusion-electrode used as lithium/air cathode in non-aqueous electrolyte and the importance of carbon material porosity, *J. Power Sources*, 2010, **195**, 2057–2063.

[5] R. Mitchell, B. Gallant, C. Thompson, Y. Shao-Horn, All–carbon–nanofiber electrodes for high–energy rechargeable Li-O_2 batteries, *Energy Environ. Sci.*, 2011, **8**, 2952–2958.

[6] Y. Li, J. Wang, X. Li, D. Geng, R. Li, X. Sun, Superior energy capacity of graphene nanosheets for a nonaqueous lithium-oxygen battery, *Chem. Commoun.*, 2011, **33**, 9438–9440.

[7] E. Yoo, H. Zhou, Li-air rechargeable battery based on metal-free graphene nanosheet catalysts, *ACS Nano*, 2011, **5**, 3020–3026.

[8] J. Xiao, D. Mei, X. Li, W. Xu, D. Wang, G. Graff, W. Bennett, Z. Nie, L. Saraf, I. Aksay, J. Liu, J. Zhang, Hierarchically porous graphene as a lithium-air battery electrode, *Nano Lett.*, 2011, **11**, 5071–5078.

[9] L. Qu, Y. Liu, J. Baek, L. Dai, Nitrogen-doped graphene as efficient metal-free electrocatalyst for oxygen reduction in fuel cells, *ACS Nano*, 2010, **4**, 1321–1326.

[10] X. Li, D. Geng, Y. Zhang, X. Meng, R. Li, X. Sun, Superior cycle stability of nitrogen-doped graphene nanosheets as anode for lithium ion batteries, *Electrochem. Commun.*, 2011, **13**, 822–825.

[11] D. Geng, S. Yang, Y. Zhang, J. Yang, J. Liu, R. Li, T.-K. Sham, X. Sun, S. Ye, S. Knights, Nitrogen doping effects on the structure of graphene, *Appl. Surf. Sci.*, 2011, **257**, 9193–9198.

[12] Y. Lu, H. Gasteiger, Y. Shao-Horn, Method development to evaluate the oxygen reduction activity of high-surface-area catalysts for Li-air batteries, *Electrochem. Solid–State Lett.*, 2011, **14**, A70–A74.

[13] Y.-C. Lu, H. Gasteiger, Y. Shao-Horn, Catalytic activity trends of oxygen reduction reaction for nonaqueous Li-air batteries, *J. Am. Chem. Soc.*, 2011, **133**, 19048–19051.

[14] S. Ye, A. Vijh, Non-noble metal-carbonized aerogel composites as electrocatalysts for the oxygen reduction reaction, *Electrochem. Commun.*, 2003, **5**, 272–275.

[15] S. Wang, D. Yu, L. Dai, Polyelectrolyte functionalizedcarbon nanotubes as efficient metal-free electrocatalysts for oxygen reduction, *J. Am. Chem. Soc.*, 2011, **133**, 5182–5185.

[16] Y. Zheng, Y. Jiao, J. Chen, J. Liu, J. Liang, A. Du, W. Zhang, Z. Zhu, S. Smith, M. Jaroniec, G. Lu, S. Qiao, Nanoporous graphitic-C_3N_4@carbon metal-free electrocatalysts for highly efficient oxygen reduction, *J. Am. Chem. Soc.*, 2011, **133**, 20116–20119.

[17] Y. Lu, H. Gasteiger, E. Crumlin, R. Jr. McGuire, Y. Shao-Horn, Electrocatalytic activity studies of select metal surfaces and implications in Li-air batteries, *J. Electrochem. Soc.*, 2010, **157**, A1016–A1025.

[18] P. Kichambare, J. Kumar, S. Rodrigues, B. Kumar, Electrochemical performance of highly mesoporous nitrogen doped carbon cathode in lithium-oxygen batteries, *J. Power Sources*, 2011, **196**, 3310–3316.

[19] Y. Li, J. Wang, X. Li, D. Geng, J. Yang, R. Li, X. Sun, Nitrogen-doped carbon nanotubes as cathode for lithium-air batteries, *Electrochem. Commun.*, 2011, **13**, 668–672.

[20] E. Yeager, Dioxygen electrocatalysis: mechanisms in relation to catalyst structure, *J. Mol. Catal.*, 1986, **38**, 5–25.

[21] Y. Wang, Y. Shao, D. W. Matson, J. Li, Y. Lin, Nitrogen-doped graphene and its application in electrochemical biosensing, *ACS Nano*, 2010, **4**, 1790–1798.

[22] D. Deng, X. Pan, L. Yu, Y. Cui, Y. Jiang, J. Qi, W. Li, Q. Fu, X. Ma, Q. Xue, G. Sun, X. Bao, Toward N-doped graphene via solvothermal synthesis, *Chem. Mater.*, 2011, **23**, 1188–1193.

[23] C. Rao, C. R. Cabrera, Y. Ishikawa, In search of the active site in nitrogen-doped carbon nanotube electrodes for the oxygen reduction reaction, *J. Phys. Chem. Lett.*, 2010, **1**, 2622–2627.

[24] J. Xiao, J. Hua, D. Wang, D. Hu, W. Xu, G. Graff, Z. Nie, J. Liu, J.-G. Zhang, Investigation of the rechargeability of Li-O_2 batteries in non-aqueous electrolyte, *J. Power Sources*, 2011, **196**, 5674–5678.

[25] S. Freunberger, Y. Chen, Z. Peng, J. Griffin, L. Hardwick, F. Bardé, P. Novák, P. Bruce, Reactions in the rechargeable lithium-O_2 battery with alkyl carbonate electrolytes, *J. Am. Chem. Soc.*, 2011, **133**, 8040–8047.

[26] Z. Peng, S. Freunberger, L. Hardwick, Y. Chen, V. Giordani, F. Bardé, P. Novák, D. Graham, J.-M. Tarascon, P. Bruce, Oxygen reactions in a non-aqueous Li^+ electrolyte, *Angew. Chem. Int. Ed.*, 2011, **50**, 6351–6355.

Chapter 7

7 Discharge Product Morphology and Increased Charge Performance of Lithium-Oxygen Batteries with Graphene Nanosheet Electrodes: The Effect of Sulphur Doping*

Nitrogen-doped graphene nanosheets show not only better catalytic activity for the cathode reaction, but also increased discharge capacity of lithium-oxygen batteries, which is due to more active sites, resulting from defects and functional groups introduced into the graphene framework. Therefore, heteroatom doping is an effective way to improve the battery performance. Recently, sulphur has been successfully doped into graphene and the as-prepared sample even showed better catalytic activity for oxygen reduction reaction than commercial Pt catalyst.

In this chapter, Sulphur-doped graphene nanosheets (S-GNSs) were fabricated and the influence of the material on the discharge performance as well as product formation of lithium-oxygen batteries was demonstrated. The growth and distribution of the discharge products were studied and a mechanism was proposed. This will have significant implication for cathode catalysts and rechargeable battery performance.

---

*A version of this chapter has been published in ***Journal of Materials Chemistry***, 2012, **22**, 7537-7543.

7.1 Introduction

Nonaqueous lithium-oxygen batteries have received much attention as a promising energy storage system beyond lithium-ion batteries (LIBs) for electric vehicles (EVs) due to their extremely high specific energy densities which could be 5-10 times higher than those of LIBs [1, 2]. However, one critical challenge for practical application of lithium-oxygen batteries is to develop optimal porous cathode since the insoluble product, lithium peroxide (Li_2O_2), deposits in and eventually will clog the electrode pores which limit the discharge capacity [3-6]. Another challenge is the poor rate capability and significant polarization of cell voltage which is also due to the formation of Li_2O_2. Recent studies reported that the structure, composition, and electronic properties of the discharge products, Li_2O_2, of lithium-oxygen batteries could dramatically affect the battery performance. For example, Nanda et al. found that the distribution of lithium products in lithium-oxygen cathodes significantly affected the rechargeability of the batteries [7]. Luntz et al. suggested that sudden death occurred was arisen from limited charge transport through the growth of Li_2O_2 film [8]. Seriani et al. proposed that the particle size of lithium oxides had an impact on the porous electrodes [9]. Siegel et al. found that the surface electronic structure of small Li_2O_2 particles was dramatically different from the bulk insulator due to the lithium vacancies [10]. Ceder et al. further demonstrated that the electronic conduction was likely to be controlled by vacancy diffusion in Li_2O_2 [11].

Toward the goal of tailoring Li_2O_2 properties to battery performance, it is very important to select or design optimal growth of Li_2O_2 via substrate control. In our previous report, we had found that nitrogen-doped graphene showed significant influence not only on battery performance but also on the nucleation and growth of discharge products, which is that smaller and more uniform particles were obtained [12]. Therefore, it is interesting to investigate the properties of other heteroatom doped graphene. Recently, Huang et al. reported sulphur-doped graphene as an electrocatalyst for oxygen reduction reaction (ORR) and found that the sample

exhibited excellent catalytic activity, long-term stability, and high methanol tolerance [13]. However, to our best knowledge, sulphur-doped graphene has rarely been employed in the nonaqueous lithium-oxygen battery system. Herein, we successfully fabricated sulphur-doped graphene and demonstrate its influence on Li_2O_2 formation. The experimental results not only give a further insight into the reaction mechanism but also provide a rational direction to modify cathode material properties for lithium-oxygen batteries. This will also have significant implication for catalysts performance at cathode.

7.2 Experimental

7.2.1 Materials synthesis

Graphene nanosheets (GNSs) were prepared by the oxidation of graphite powder using the modified Hummers' method, and sulphur-doped graphene nanosheets (S-GNSs) was subsequently obtained using the following procedure: 0.05 g of graphene was dispersed into acetone with 0.8 g of p-toluenesulfonic acid (Alfa Aesar). Then the slurry was stirred at room temperature until the solvent was totally evaporated. And the resulting product was dried at 100 ^{o}C over night and finally was calcined at 900 ^{o}C in Ar for 1 hour [14-17].

7.2.2 Physical characterizations

The morphology of GNSs, S-GNSs and the discharge products were characterized by a Hitachi S-4800 FESEM. XRD patterns were recorded by a Bruker-AXS D8 Discover diffractometer (Co-Kα source). XPS spectra were tested by a Kratos Axis Ultra X-ray photoelectron spectrometer (Al Kα source). Raman scattering (RS) spectra were recorded on a HORIBA Scientific LabRAM HR Raman spectrometer system equipped

with a 532.4 nm laser. The S K-edge X-ray Absorption Near Edge Structure (XANES) spectra were obtained on the Soft X-ray Microcharacterization Beamline (SXRMB, $\Delta E/E$: 10^{-4}) while the Li K-edge spectra were obtained on the Variable Line-Spacing Planar Grating Monochromator beamline (VLS-PGM, $\Delta E/E$: 10^{-5}) at the Canadian Light Source (CLS). Reference samples, sulphur, Li_2O_2 and Li_2CO_3 were purchased from Sigma-Aldrich without further purification. Spectra were recorded in fluorescence yield mode (FLY).

7.2.3 Electrochemical measurements

Swagelok type cells were used to test the battery performance. GNSs or S-GNSs and Polyvinylidene fluoride (PVDF) (Alfa Aesar, 98.5%) with a weight ratio of 9:1 were casted onto a separator (Celgard 3500) and cut to 3/8 inch in diameter as cathode and the material loadings were ~ 0.3 mg. 1 mol dm^{-3} $LiPF_6$/Tetraethylene glycol dimethyl ether (TEGDME) was used as electrolyte. The discharge/charge characteristics were measured using an Arbin BT-2000 battery station in the voltage range of 2.0-4.5 V in a 1 atm oxygen atmosphere at 25 °C.

7.3 Results and Discussion

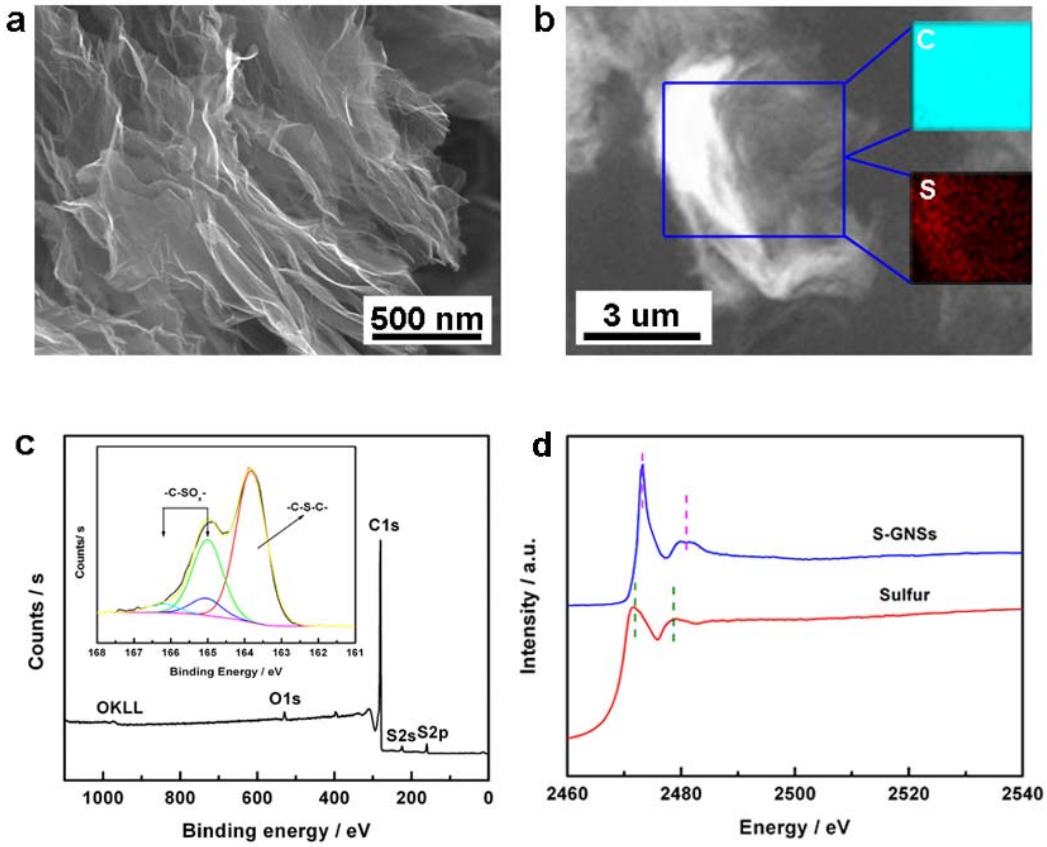

Figure 7.1 (a) SEM image, (b) EDS mapping, (c) XPS spectroscopy, and (d) S K-edge XANES of sulphur-doped graphene.

Figure 7.1a shows the SEM image of S-GNSs. It can be seen that it features a curly morphology with a thin, wrinkled structure which is similar to pristine graphene (Supporting Information, **Figure SI-7.1**). The elemental composition was analyzed by EDX mapping (**Figure 7.1b**). The presence of sulphur is confirmed and the sulphur distribution in the graphene is relatively uniform, suggesting that sulphur atoms are not only in plane but also at the edge of GNSs. XPS further confirms that sulphur is

successfully doped into to graphene, and the sulphur percentage is about 1.9 at % (**Figure 7.1c**). The high-resolution S 2p peak is shown in the inset of **Figure 7.1c**. As can be seen, covalent C-S bonds were doped in two forms. One is –C–S–C– (163.8 eV), and the other is –C–SO_x– (x=2–4, 165.0–166.5 eV), such as sulfate or sulfonate [13, 18, 19]. The synchrotron-based XANES spectroscopy is a molecular-scale technique that yields local electronic and structural information on the element of interest [20, 21]. The sulphur doping is supported by S K-edge XANES as shown in Fig. 1d, the intense peak at 2473.2 eV can be assigned to a transition of S 1s to a S-C final state of p character while the broad peak between 2480 - 2482 eV could be a mixture of sulphur of valences 4^+ (sulfone), 5^+ (sulfonate) [24]. Based on the XPS and XANES results, we can conclude that sulphur was doped into the framework of graphene, although the exact position of substitutional sulphur requires further study.

The Raman spectra of sulphur-doped and pristine graphene are shown in Supporting Information, **Figure SI-7.2**. Both samples display two peaks at ~ 1353 and 1598 cm^{-1}, which correspond to the D band and G band, respectively. It is well accepted that higher disorder (more defects) leads to a higher intensity ratio between D band and G band [25-28]. For S-GNSs, the I_D/I_G ratio increases to about 1.06 from a value of around 0.96 for pristine graphene. In addition, the spectra also exhibit a broadening of the D band for the S-GNSs, implying an enhanced defect density. In our previous effort on heteroatom-doped graphene for lithium-oxygen batteries, we found that the discharge capacity dramatically increased resulting from the introduction of defective sites (defects or functional groups) after nitrogen doping [12]. However, as can be seen from **Figure 7.2a** and **7.2b**, the initial discharge capacity of S-GNSs electrode is about 4300 mAh g^{-1}, which is lower than that of the pristine graphene electrode (~ 8700 mhA g^{-1}). However, it is noted that the initial charge capacity of the S-GNSs electrode is about 4100 mAh g^{-1}, while it is only about 170 mAh g^{-1} for the pristine graphene electrode. Moreover, the discharge capacities in the second cycle of the sulphur-doped and pristine graphene electrodes are 3500 and 220 mAh g^{-1}, respectively.

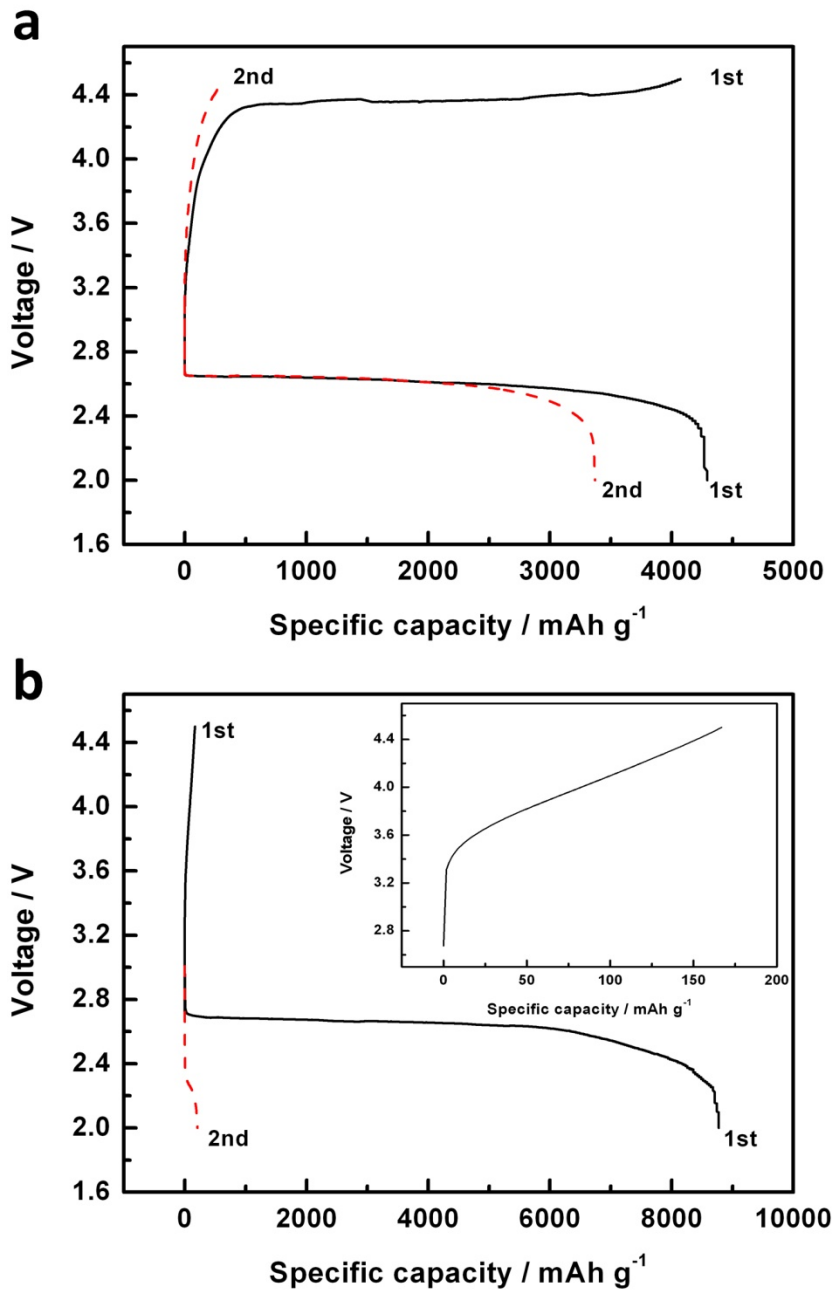

Figure 7.2 Discharge/charge curves of (a) sulphur-doped and (b) pristine graphene electrodes at a current density of 75 mA g^{-1}. Inset of (b) is enlarged figure of the charge curve for 1st cycle.

It is reported by Shao-Horn's group that the catalytic activity of the catalysts towards oxygen reduction reaction resulting in affecting the discharge performance for lithium-oxygen batteries, was related to oxygen adsorption energy [29]. But the first-principle calculations showed that the oxygen adsorption energy was not increased by doping sulphur to graphene [30]. Therefore, the discharge capacity of S-GNSs for lithium-oxygen batteries could not be improved based on the merely increased adsorption ability for oxygen; the reason that it shows lower discharge capacity but higher charge capacity will be further discussed below.

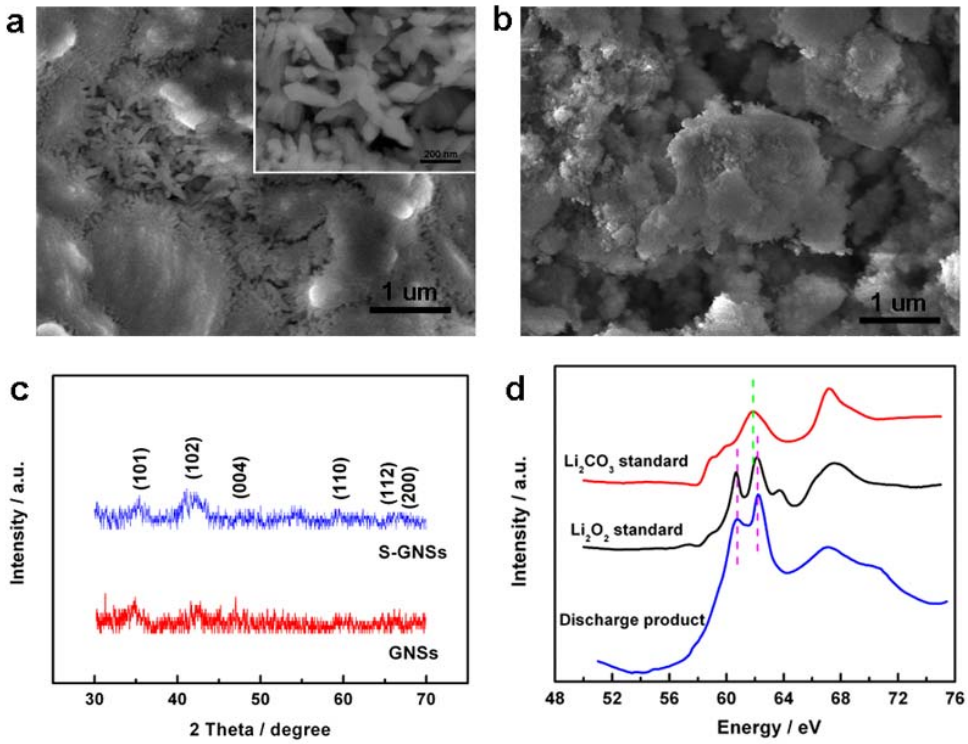

Figure 7.3 SEM images of (a) sulphur-doped and (b) pristine graphene discharged electrodes. (c) XRD patterns, (d) XANES of discharge products of S-GNSs.

Figure 7.3a and **7.3b** show the SEM morphologies of the discharge products for sulphur-doped and pristine graphene electrodes, respectively. It can be seen that the discharge products were deposited on the entire porous electrodes for both samples, but the morphology are significantly different. Irregular-shape particles formed on the pristine graphene electrode while interestingly, nanorods with a diameter about 100 nm grew on the S-GNSs electrode. The discharge products of two electrodes were examined by XRD and the patterns are shown in **Figure 7.3c**. It is interesting to find that the XRD peaks can be assigned to Li_2O_2, although the morphology of the discharge product on S-GNSs is different. In our previous report, we found that the discharge product on pristine and nitrogen-doped graphene were Li_2O_2, which are consistent with the results obtained by other groups [12]. The discharge product on S-GNSs is better crystallized than that on pristine graphene, suggesting that the dismustase reaction and nucleation of Li_2O_2 are promoted due to the strong interaction between carbon and the intermediate products after sulphur doping [31].

The Li K-edge XANES of discharge product for GNSs, S-GNSs electrodes and reference materials, such as standard Li_2CO_3 and Li_2O_2, are shown in **Figure 7.3d**. As can be seen, two major peaks at ~ 60.8 and ~ 62.2 eV were presented for both GNSs and S-GNSs samples; it matches well with standard Li_2O_2 material, while an addition peak at ~ 63.7 eV was observed for the reference. However, it is much different from that of Li_2CO_3 (only one peak at ~ 61.8 eV). It is reported that the Li^+ local environment in the Li_2O_2 of discharged pure carbon powder and Au/C electrodes is different from the standard bulk materials which is due to the presence of structural defects such as oxygen and/or lithium vacancies [31]. The broadening of the doublet is consistent with this notion (increasing disorder compared with the reference). The SEM image of the discharge products after 2nd discharge is shown in Supporting Information, **Figure SI-7.3a**. As can be seen, nanorod-shaped structure still appears, however, the diameter of the nanorods is smaller compared to the products form after 1st discharge. It can be seen from the XRD pattern that in addition to Li_2O_2, Li_2CO_3 also presents, indicating the side reactions of electrolyte during discharge/charge cycle (Supporting Information, **Figure SI-7.3b**) [32-34]. The decreased charge capacity in

the 2nd cycle is due to the Li_2CO_3 formation which increases the polarization in the electrode (higher charging voltage is needed to decompose Li_2CO_3) [35].

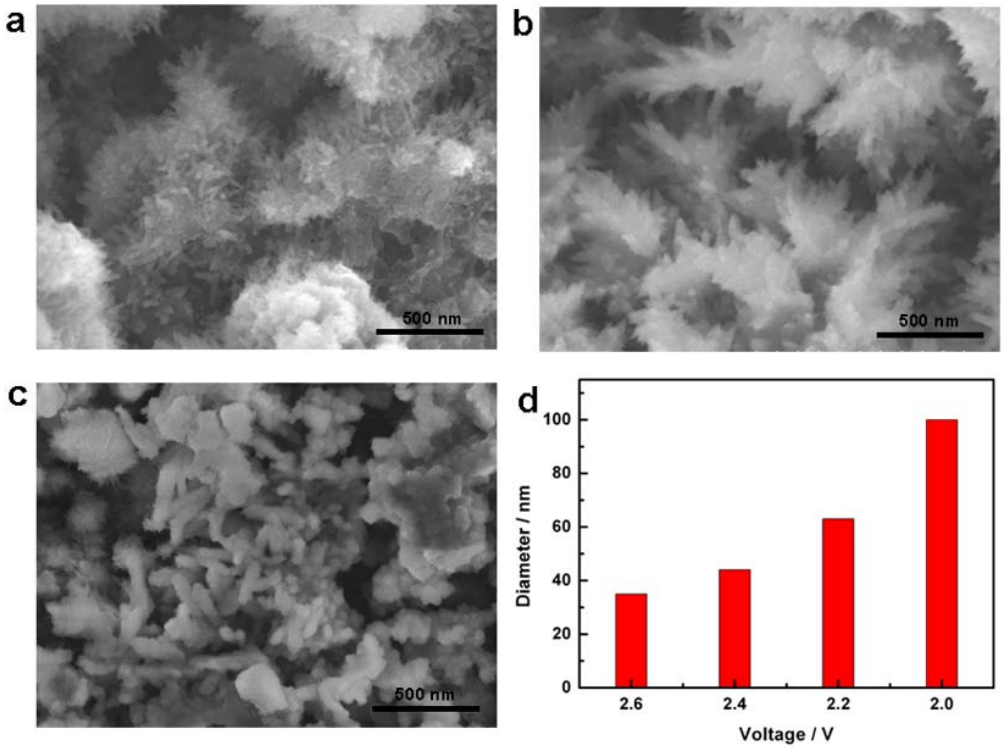

Figure 7.4 SEM images of discharged S-GNSs electrodes to (a) 2.6 V, (b) 2.4 V and (c) 2.2 V at a current density of 75 mA g^{-1}; (d) Mean diameters of the discharge products.

Several works have demonstrated that sulphur can be the catalyst for nanostrutural formation or determine the morphology, such as cementite [36], ZnO [37], SnO_2 [38], however, there is no literature on lithium oxides nanostructural formation. It is reported that S-doped graphene can become semiconductor compared to pristine one, resulting in an increased electrode polarization in the battery [18, 39]. This will diminish the binding of the generated O^{2-} to the substrate during discharge, therefore, enhance the diffusion of the superoxide molecules away from the electrode surface, and favour the disproportional peroxide formation, leading to a nanorod-shape

structure growth [32, 33]. However, the exact role of sulphur for the nanorod growth will need further study. The discharge current density is the same for the sulphur-doped and pristine graphene; the particle-shape discharge product would have a higher packing density on the deposition surface compared to nanowires/nanorods [40]. Therefore, the amount of the discharge product on the S-GNSs is less than that on pristine one, indicating a lower discharge capacity as well. However, the dense layer of Li_2O_2 on pristine graphene significantly affects the charge transport through the Li_2O_2-electrolyte interface, thus the charge performance. In contrast, for S-GNSs, the randomly distributed Li_2O_2nanorods will provide sufficient tunnelling holes that support the electrochemical reaction during charge process, leading an increased charge performance [8].

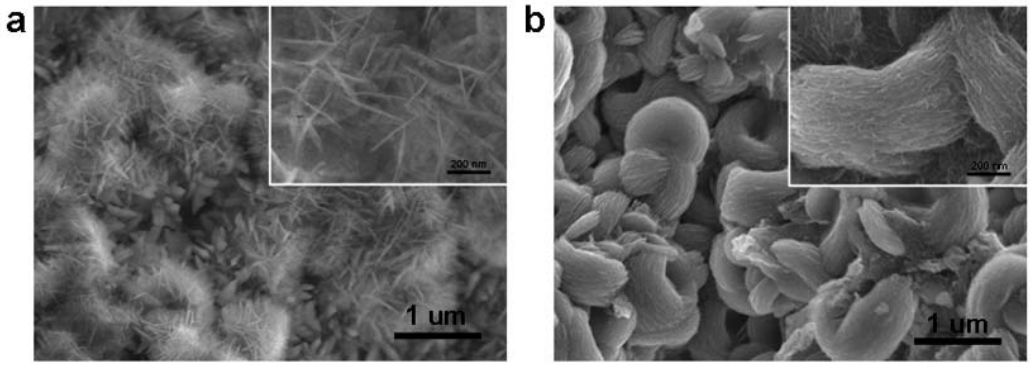

Figure 7.5 SEM images of discharge products at current density of (a) 150 mA g^{-1}, (b) 300 mA g^{-1}. Inset of (a) and (b) are the high-magnification images.

The growth of the Li_2O_2 nanorods were observed by controlling the discharge depth of the batteries while keeping the discharge current density at 75 mA g^{-1}. **Figure 7.4a**, **7.4b** and **7.4c** show the SEM images of the discharged electrodes. It can be seen that at 2.6 V, nanorods were already grown on most of the surface of the electrode and the diameter is around 35 nm. As the discharge voltage were decreased, the electrode surface were all cover with the nanorods and the diameters increased to ~ 45,~ 75 and ~ 100 nm at 2.4, 2.2 and 2 V, respectively (**Figure 7.4d**). However, the morphology of

the discharge product changes when higher current densities were applied. As shown in **Figure 7.5a**, in addition to the nanorods on the electrode surface, nanosheets with a thickness of ~ 10 nm were formed on the nanorods at 150 mA g^{-1}. Donut-shape particles on the order of ~ 1 um were found instead of nanorods or nanosheets at 300 mA g^{-1} (**Figure 7.5b**). These toroidal particles were composed of aggregated nanosheet-structures; these toroids were also found by other groups but the formation and structural evolution have not been observed before [33,34].

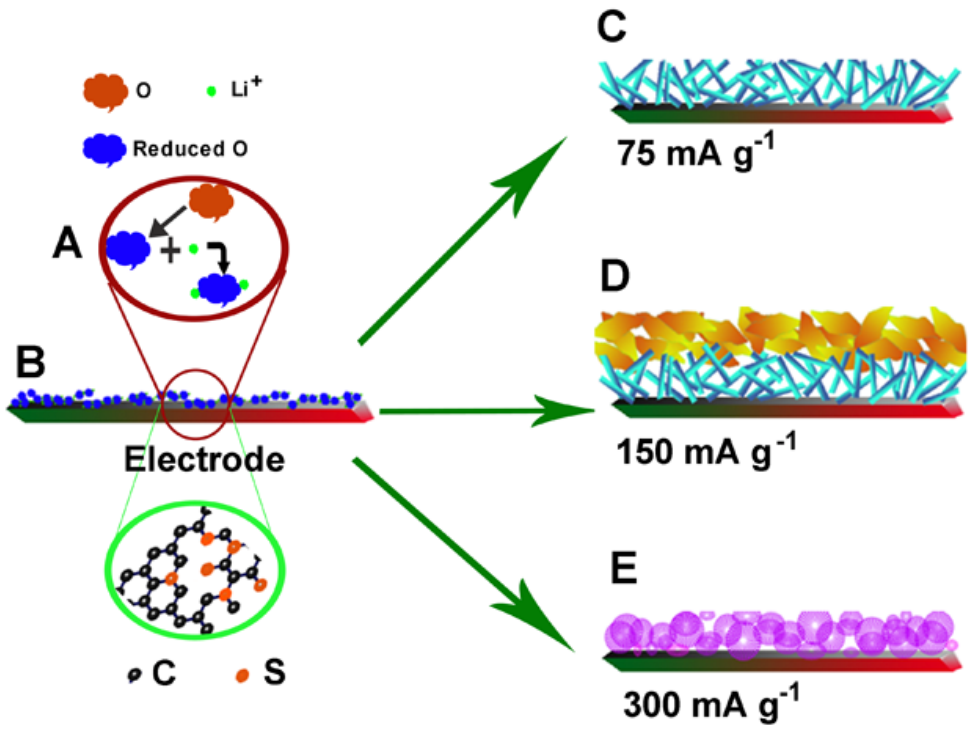

Figure 7.6 Schematic of discharge product nanostructures growth on S-GNSs electrodes.

From our study by employing S-GNSs electrode, the growth mechanism of the discharge product can be proposed based on the experimental results. **Figure 7.6** shows the schematic of the growth mechanism. Initially, O_2 is reduced to O^{2-} and combined with Li^+ to form LiO_2 (**Figure 7.6A**). Then elongated nanocrystallites of Li_2O_2 form on the carbon surface (**Figure 7.6B**). Depending on the discharge current density, different morphologies are obtained. At a current density of 75 mA g^{-1}, only Li_2O_2 nanorods were formed (**Figure 7.6C**). As the current density increases to 150 mA g^{-1}, the cathodic polarization increases which enhances the diffusion of the superoxide molecules away from the electrode surface, and peroxide forms along certain facet of Li_2O_2 crystal, thus nanosheets were observed on nanorods (**Figure 7.6D**). If a current density of 300 mA g^{-1} was applied, the cathodic polarization increases even more, instead of formation of nanrods, only nanosheets will form and give rise to the toroid aggregates for Li_2O_2 (**Figure 7.6E**). Nazar et al. suggested that Li_2O_2 favoured growth on the sites that the superoxide is generated in order to shorten the O^{2-} diffusion path which may support our hypothesis [33, 34]. However, in the real system, the growth is surely more complicated and further studies are needed to verify the hypothesis.

7.4 Conclusions

In summary, we have employed S-GNSs as cathode materials for lithium-oxygen batteries and found that the morphology of the discharge product, Li_2O_2, were significantly different from the pristine graphene, and therefore the discharge and charge properties of the batteries. The formation of Li_2O_2 nanorods during discharge and thus the charge properties are considered to be due to sulphur-doping, however, the role that sulphur played is not clearly at current stage and further study is needed.

It is also demonstrated, for the first time, the detailed morphological evolution of Li_2O_2 as a function of the discharge depth and current density. This study gives a rational direction for selecting and designing cathode materials (including catalysts) to tailor the morphology of Li_2O_2, thus improving the performance of lithium-oxygen batteries.

Acknowledgements

This research was supported by Natural Sciences and Engineering Research Council of Canada, Canada Research Chair Program, Canada Foundation for Innovation, Ontario Early Researcher Award and the University of Western Ontario.

References

[1] K. Abraham, Z. Jiang, A polymer electrolyte-based rechargeable lithium/oxygen battery, *J. Electrochem. Soc.*, 1996, **143**, 1–5.

[2] M. Armand, J.-M.Tarascon, Building better batteries, *Nature*, 2008, **451**, 652–657.

[3] J. Xiao, D. Wang, W. Xu, D. Wang, R. Williford, J. Liu, J.-G. Zhang, Optimization of air electrode for Li/air batteries, *J. Electrochem. Soc.*, 2010, **157**, A487–A492.

[4] Y. Li, J. Wang, X. Li, D. Geng, J. Yang, R. Li, X. Sun, Nitrogen-doped carbon nanotubes as cathode for lithium-air batteries, *Electrochem. Commun.*, 2011, **13**, 668–672.

[5] S. Zhang, D. Foster, J. Read, Discharge characteristic of a non-aqueous electrolyte Li/O_2 battery, *J. Power Sources*, 2010, **195**, 1235–1140.

[6] Y. Li, J. Wang, X. Li, D. Geng, R. Li, X. Sun, Superior energy capacity of graphene nanosheets for a nonaqueous lithium-oxygen battery, *Chem. Commun.*, 2011, **33**, 9438–9440.

[7] J. Nanda, H. Bilheux, S. Voisin, G. M. Veith, R. Archibald, L. Walker, S. Allu, N. Dudney, S. Pannala, Anomalous discharge product distribution in lithium-air cathodes, *J. Phys. Chem. C*, 2012, **116**, 8401–8408.

[8] V. Viswanathan, K. Thygesen, J. Hummelshøj, J. Nørskov, G. Girishkumar, B. McCloskey, A. Luntz, Electrical conductivity in Li_2O_2 and its role in determining capacity limitations in non-aqueous Li-O_2 batteries, *J. Chem. Phys.*, 2011,**135**, 214704.

[9] N. Seriani, Ab initio thermodynamics of lithium oxides: from bulk phases to nanoparticles, *Nanotechnology*, 2009, **20**, 445703.

[10] M.Radin, J. Rodriguez, F. Tian, D. Siegel, Lithium peroxide surfaces are metallic, while lithium oxide surfaces are not, *J. Am. Chem. Soc.*, 2012, **134**, 1093–1103.

[11] S. Ong, Y. Mo, G. Ceder, Low hole polaron migration barrier in lithium peroxide, *Phys. Rev. B*, 2012, **85**, 081105.

[12] Y. Li, J. Wang, X. Li, D. Geng, M. Banis, R. Li, X. Sun, Nitrogen-doped graphene nanosheets as cathode materials with excellent electrocatalytic activity for high capacity lithium-oxygen batteries, *Electrochem. Commun.*, 2012, **18**, 12–15.

[13] Z. Yang, Z. Yao, G. Li, G. Fang, H. Nie, Z. Liu, X. Zhou, X. Chen, S. Huang, Sulfur-doped graphene as an efficient metal-free cathode catalyst for oxygen reduction, *ACS Nano*, 2012, **6**, 205–211.

[14] D. Geng, Y. Chen, Y. Chen, Y. Li, R. Li, X. Sun, S. Ye, S. Knights, High oxygen-reduction activity and durability of nitrogen-doped graphene, *Energy Environ. Sci.*, 2011, **4**, 760–764.

[15] D. Geng, S. Yang, Y. Zhang, J. Yang, J. Liu, R. Li, T.-K. Sham, X. Sun, S. Ye, S. Knights, Nitrogen doping effects on the structure of graphene, *Appl. Surf. Sci.*,2011, **257**, 9193–9198.

[16] H. Schniepp, J.-L. Li, M. McAllister, H. Sai, M. Herrera-Alonso, D. Adamson, R. Prud'homme, R. Car, D. saville, I. Aksay, Functionalized single graphene sheets derived from splitting graphite oxide, *J. Phys. Chem. B*, 2006, **110**, 8535–8539.

[17] X. Li, D. Geng, Y. Zhang, X. Meng, R. Li, X. Sun, Superior cycle stability of nitrogen-doped graphene nanosheets as anode for lithium ion batteries, *Electrochem. Commun.*, 2011, **13**, 822–825.

[18] P. Denis, R. Faccio, A. Mombru, Is it possible to dope single-walled carbon nanotubes and graphene with sulfur? *Chem. Phys. Chem.*, 2009, **10**, 715–722.

[19] S. Glenis, A. Nelson, M. Labes, Sulfur doped graphite prepared via arc discharge of carbon rods in the presence of thiophenes, *J. Appl. Phys.*, 1999, **86**, 4464.

[20] S. Yang, D. Wang, G. Liang, Y. Yiu, J. Wang, L. Liu, X. Sun, T.-K. Sham, Soft X-ray XANES studies of various phases related to $LiFePO_4$ based cathode materials, *Energy Environ. Sci.*, 2012, **5**, 7007–7016.

[21] D. Wang, J. Yang, X. Li, J. Wang, R. Li, M. Cai, T. K. Sham, X. Sun, Observation of surface/defect states of SnO_2 nanowires on different substrates from X-ray excited optical luminescence, *Cryst. Growth Des.*, 2012, **12**, 397–402.

[22] G. George, M. Gorbaty, Sulfur K-edge X-ray absorption-spectroscopy of petroleum as phaltenes and models, *J. Am. Chem. Soc.*, 1989, **111**, 3182–3186.

[23] T. Smith, J. DeWitt, B. Hedman, K. Hodgson, Sulfur and chlorine K-edge X-ray absorption spectroscopic studies of photographic materials, *J. Am. Chem. Soc.*, 1994, **116**, 3836–3847.

[24] P. Frank, S. George, E. Anxolabéhère-Mallart, B. Hedman, K. Hodgson, A systematic resolution of sulfur in reticulated vitreous carbon using X-ray absorption spectroscopy, *Inorg. Chem.*, 2006, **45**, 9864–9876.

[25] Y. Shao, S. Zhang, M. Engelhard, G. Li, G. Shao, Y. Wang, J. Liu, I. Aksay, Y. Lin, Nitrogen-doped graphene and its electrochemical applications, *J. Mater. Chem.*, 2010, **20**, 7491–7496.

[26] D. Deng, X. Pan, L. Yu, Y. Cui, Y. Jiang, J. Qi, W. Li, Q. Fu, X. Ma, Q. Xue, G. Sun, X. Bao, Toward N-doped graphene via solvothermal synthesis, *Chem. Mater.*, 2011, **23**, 1188–1193.

[27] Z. Wu, W. Ren, L. Gao, J. Zhao, Z. Chen, B. Liu, D. Tang, B. Yu, C. Jiang, H. Chen, Synthesis of graphene sheets with high electrical conductivity and good thermal stability by hydrogen arc discharge exfoliation, *ACS Nano*, 2009, **3**, 411–417.

[28] H. Wang, C. Zhang, Z. Liu, L. Wang, P. Han, H. Xu, K. Zhang, S. Dong, J. Yao, G. Cui, Nitrogen-doped graphene nanosheets with excellent lithium storage properties, *J. Mater. Chem.*, 2011, **21**, 5430–5434.

[29] Y.-C. Lu, H. Gasteiger, Y. Shao-Horn, Catalytic activity trends of oxygen reduction reaction for nonaqueous Li-air batteries, *J. Am. Chem. Soc.*, 2011, **133**, 19048–19051.

[30] J. Dai, J. Yuan, P. Giannozzi, Gas adsorption on graphene doped with B, N, Al, and S: A theoretical study, *Appl. Phys. Lett.*, 2009, **95**, 232105.

[31] Y. Lu, D. Kwabi, K. Yao, J. Harding, J. Zhou, L.Zuin, Y. Shao-Horn, The discharge rate capability of rechargeable Li-O_2 batteries, *Energy Environ. Sci.*, 2011, **8**, 2999–3007.

[32] S. Freunberger, Y. Chen, N. Drewett, L. Hardwick, F. Bardé, P. Bruce, The lithium-oxygen battery with ether-based electrolytes, *Angew. Chem. Int. Ed.*, 2011, **50**, 8609–8613.

[33] R. Black, S. Oh, J. Lee, T. Yim, B. Adams, L. Nazar, Screening for superoxide reactivity in Li-O_2 batteries: Effect on Li_2O_2/LiOH crystallization, *J. Am. Chem. Soc.*, 2012, **134**, 2902–2095.

[34] R. Mitchell, B. Gallant, C. Thompson, Y. Shao-Horn, All-carbon-nanofiber electrodes for high-energy rechargeable Li-O_2 batteries, *Energy Environ. Sci.*, 2011, **8**, 2952–2958.

[35] A. Thapa, K. Saimen, T. Ishihara, Pd/MnO_2 air electrode catalyst for rechargeable lithium/air battery, *Electrochem. Solid-State Lett.*, 2010, **13**, A165–A167.

[36] J. Hucińska, Cementite transformation in low carbon steel under the influence of sulphur, *Mater. Corros.*, 2004, **55**, 292–297.

[37] G. Ambrožič, I. Djerdj, S. Škapin, M. Žigon, Z. C. Orel, The double role of p-toluenesulfonic acid in the formation of ZnO particles with different morphologies, *Cryst. Eng. Comm.*, 2010, **12**, 1862–1868.

[38] S. Monredon, A. Cellot, F. Ribot, C. Sanchez, L. Armelao, L. Gueneau, L. Delattre, Synthesis and characterization of crystalline tin oxide nanoparticles, *J. Mater. Chem.*, 2002, **12**, 2396–2400.

[39] P. Kulkarni, L. Porter, F. Koeck, Y.-J. Tang, R. Nemanich, Electrical and photoelectrical characterization of undoped and S-doped nanocrystalline diamond films, *J Appl. Phys.*, 2008, **103**, 084905.

[40] G. Cao, Y. Wang, Nanostructures and Nanomaterials: Synthesis, Properties and Applications, World Scientific Publishing, Hackensack, New York, 2011.

Supporting Information

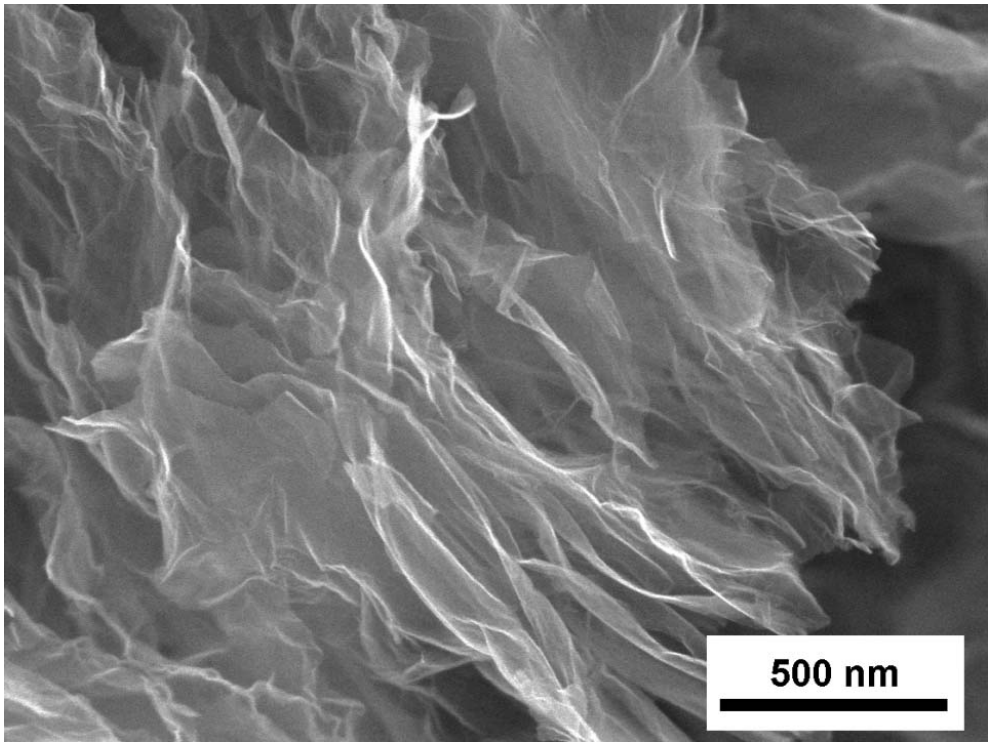

Figure SI-7.1 SEM image of graphene nanosheets.

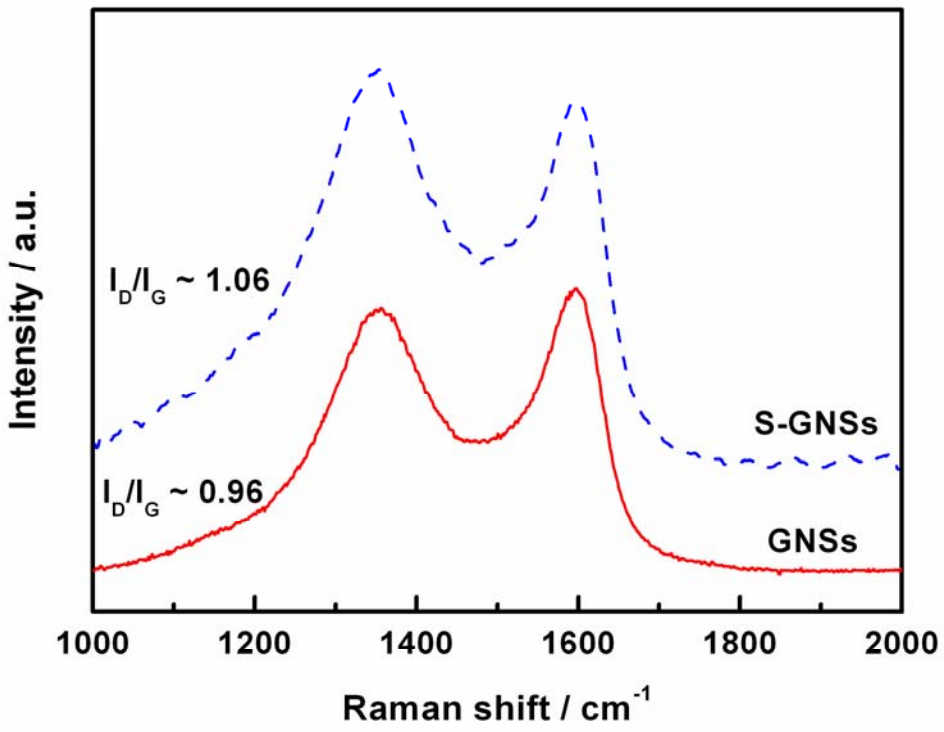

Figure SI-7.2 Raman spectroscopy of S-GNSs and GNSs.

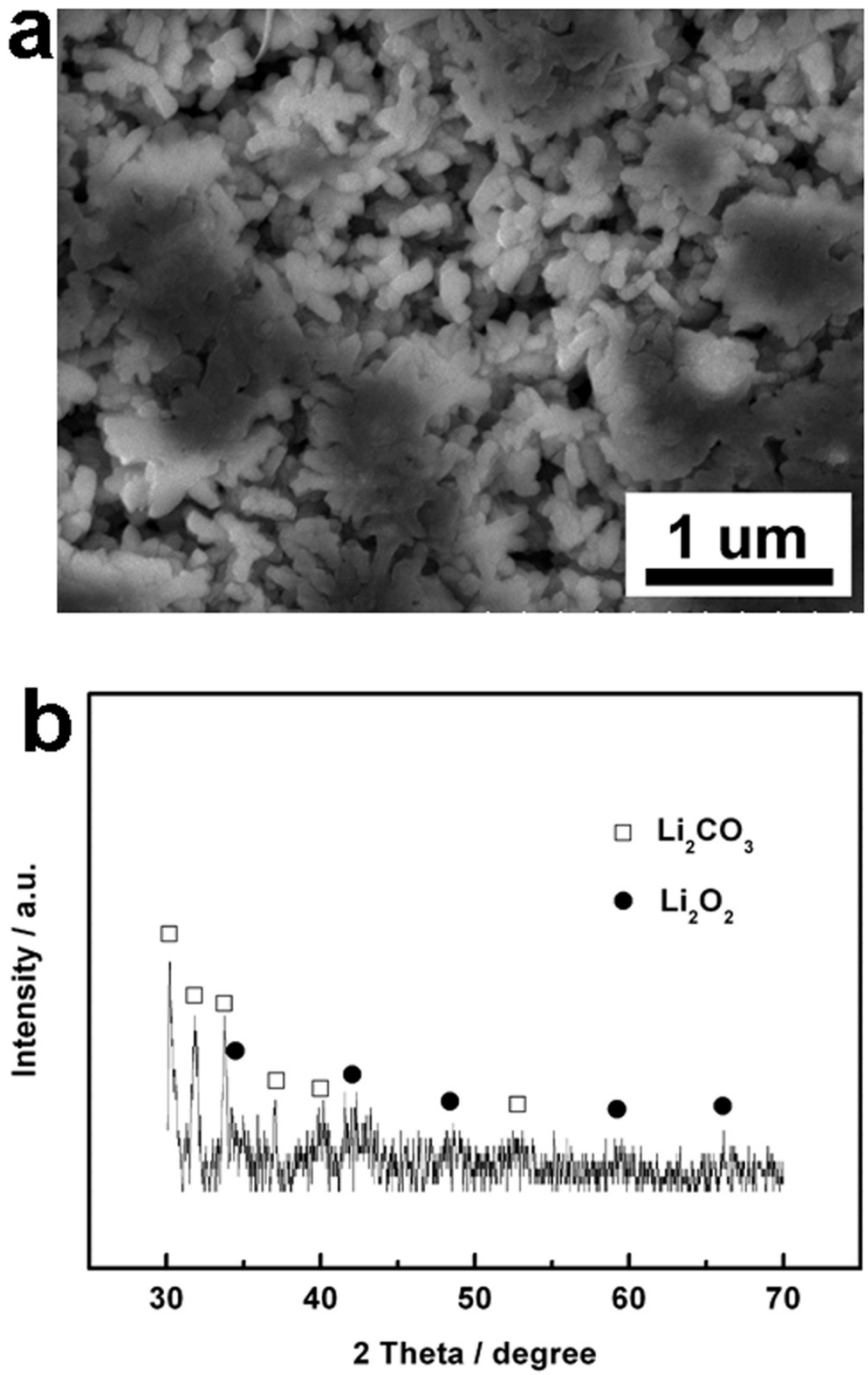

Figure SI-7.3 SEM image (a) and XRD pattern (b) of the discharge product after 2nd discharge.

Chapter 8

8 Facile Controlled Synthesis and Growth Mechanisms of Flower-Like and Tubular MnO_2 Nanostructres by Microwave-Assisted Hydrothermal Method*

The cycle performance is another critical issue for the practice application of lithium-oxygen batteries. Metal oxides, such as MnO_2, Co_3O_4, Fe_2O_3, etc have been proved to be good catalysts for charge process, improving the battery cycle performance. However, the conventional methods to synthesize metal oxides often need high temperatures, complex procedures, etc. Therefore, it is necessary to develop a facile way for material synthesis, especially for mass production.

In this chapter, birnessite flower-like and α-type tubular MnO_2 nanostructures were selectively synthesized through simple decomposition of $KMnO_4$ under hydrochloric acid condition by controlling reaction temperature using a microwave-assisted hydrothermal method. The as-prepared samples were characterized in detail by various techniques including XRD, FESEM, TEM, HRTEM, FTIR, and Raman spectroscopy. While the growth of flower-like birnessite-MnO_2 might follow a widely accepted Ostwald ripening process, we proposed a formation mechanism of the nanotubular α-MnO_2 based on our evidence, which was assembly of nanorods through an "oriented attachment" process.

---

*A version of this chapter has been published in ***Journal of Colloid and Interface Science***, 2012, **369**, 123-128.

8.1 Introduction

Synthesis of nanostructured materials with controlled shape, architecture and size is of importance to ensure their property performance in various device applications, such as optics, magnetism, mechanics, and electronics [1]. Among various synthesis approaches, solution-based wet chemical methods feature the virtue of multiplex routes and high output, templates, surfactants and complexing species have been applied to control size and structure of the products [2-4]. However, these methods usually imply complex and costly procedures, which are not versatile or environmental friendly.

Recently, microwave irradiation has been increasingly applied to replace conventional heating methods in material synthesis and sample digestion since it provides a selective, fast and homogenous heat which significantly reduces processing time and cost [5-7]. Combining the microwave irradiation with wet chemical methods such as hydrothermal or solvothermal techniques, required temperature and pressure for nanostructure growth can be rapidly achieved, which leads to enhanced kinetics of crystallization and promotes the formation of new phase of product [8]. In this case, nanomaterials with novel structures and architectures are expected to be generated. Up to now, different kinds of nanomaterials have been synthesized via a microwave-assisted route, including NiO [9], ZnO [10], Fe_3O_4 [11], WO_3 [12], Co_3O_4 [13], etc.

Manganese dioxide (MnO_2) nanostructures exhibit distinctive physical and chemical properties and have wide applications in molecular/ion sieves [14], catalysts [15], sensors [16], and energy storage [17]. It is known that the properties of nanostructured MnO_2 highly depend on the crystal structure, dimension and morphology [18]. Various MnO_2 nanostructures such as nanoparticles [19], nanorods/nanofibers [20], nanowires [21], and nanotubes [22] have been prepared by sol-gel [23], precipitation [24], reflux [25], thermal deposition [26], and hydrothermal [27] techniques. As a direct and one-step wet chemical route, hydrothermal method has been prevalently employed in

synthesizing MnO_2 nanostructures. For example, Wang et al. reported a selected-control low-temperature hydrothermal method of synthesizing 1D MnO_2 nanostructures through the oxidation of Mn^{2+} by $S_2O_8^{2-}$, MnO_4^- or ClO^- [28-29]. Cheng et al. synthesized 2D hexagram-like and dendrite-like hierarchical MnO_2 nanostructures by decomposition of $Mn(NO_3)_2$ solution with or without nitric acid [17]. Yu et al. obtained 3D urchin shaped and clewlike MnO_2 nanostructures in the presence of Al^{3+} or Fe^{3+} under hydrothermal condition [30]. However, these conventional hydrothermal methods require prolonged reaction time for more than twelve hours, even for several days. Recently, microwave-assisted hydrothermal method (MA-HM) was employed to synthesize octahedral molecular sieves (OMS-2) nanomaterials, and the samples possess better catalytic activity for cinnamyl alcohol oxidation than their conventional counterparts [31]. But to the best of our knowledge, synthesis of MnO_2 nanotubes by MA-HM has not been reported previously.

Herein, we demonstrate a facile rapid procedure to fabricate MnO_2 nanostructures through decomposition of $KMnO_4$ under hydrochloric acid condition by MA-HM. 3D hierarchical nanostructures and 1D nanotubes of MnO_2 with different crystallographic forms were selectively obtained by controlling the reaction parameters. The growth mechanism was studied and discussed in detail based on detailed observations in different growth stages. This synthetic route requires no templates, catalysts, or organic reagents which promises large-scale production of nanostructured MnO_2 with controlled structure and size.

8.2 Experimental

8.2.1 Materials synthesis

All the chemicals used in this experiment were of analytical grade from Sigma-Aldrich Company and used without further purification. In a typical synthesis, 1.5 mmol of $KMnO_4$ was added to 20 ml deionized water to form a homogeneous solution. 0.5 ml of HCl (37 wt. %) was then added dropwise into the solution under magnetic stirring. After stirring for 20 min, the obtained solution was transferred to a 100 ml Teflon-lined ceramic-walled vessel. The autoclave was sealed and heated to different reaction temperatures (100,140, and 180 ºC) with the same holding time of 25 min in an Anton Paar Synthos 3000 microwave synthesis system. After the autoclave was cooled down to room temperature, the sample was collected by centrifugation and washed with deionized water and absolute ethanol several times to remove the impurities, and dried in air at 80 ºC for 12 h.

8.2.2 Physical characterizations

The powder X-ray diffraction (XRD) patterns were recorded by a Inel multi purpose diffractometer system with Cu Kα radiation (λ = 1.54060 Å) operated at 30 kV and 20 mA. The morphology of the synthesized samples was determined by a Hitachi S-4800 field emission scanning electron microscope (FESEM) operated at 5 kV. Transmission electron microscopy (TEM) images were taken by a Philips CM 10 microscope operated at 80 kV. High-resolution transmission electron microscopy (HRTEM) and selected area electron diffraction (SAED) were characterized by a JEOL 2010 FEG microscope operated at 200 kV. Fourier transform-infrared (FT-IR) measurements were carried out by the KBr method using a Nicolet 6700 FT-IR spectrometer. FT-IR spectra were recorded in the transmittance mode over the range of 400–4000 cm^{-1} by averaging 16 scans at a resolution of 4 cm^{-1}. Raman scattering (RS)

spectra were collected on a HORIBA Scientific LabRAM HR Raman spectrometer system equipped with a 532 nm laser. A laser energy filter value of 2 was applied, which prevents decomposition of the samples. The spectra were taken between 100 and 1000 cm^{-1} in a backscattering configuration at room temperature.

8.3 Results and Discussion

8.3.1 Structure and morphology characterization

The phase purity and crystal structure of MnO_2 was examined by XRD. Different crystal structures can be achieved by controlling the reaction temperatures. As shown in **Figure 8.1a**, all the diffraction peaks of the XRD pattern for the sample prepared at 100 °C can be indexed to the birnessite-type MnO_2 (JCPDS No. 80-1098), which has a lamellar structure and the interlayer distance of MnO_6 octahedra layers is 0.73 nm. The broaden peaks with low intensity observed in XRD pattern suggest that the sample is in poor crystalline state with a short-range crystal form. In particular, the relative intensities of the (001) planes are lower than those in the standard JCPDS data, which suggests that the layers of MnO_6 octahedra are not perfectly oriented [32]. In contrast, the sample prepared at 140 °C (**Figure 8.1b**) can be attributed to the tetragonal phase α-MnO_2 (JCPDS No. 44-0141) and the XRD pattern with sharp and intense peaks indicates a good crystallinity for the α-MnO_2.

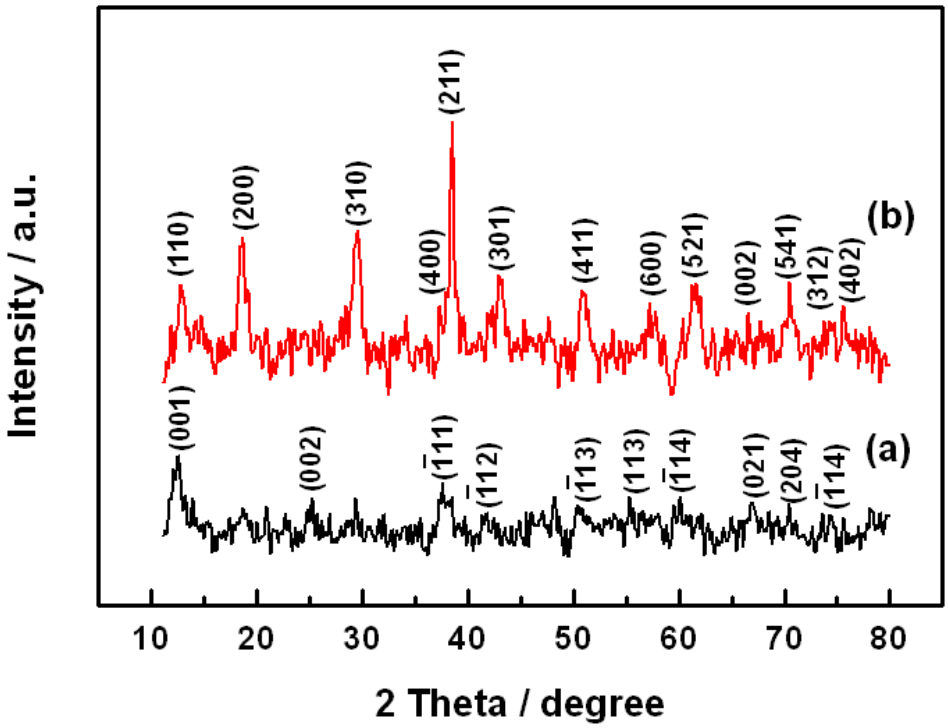

Figure 8.1 XRD patterns of the products prepared at (a) 100 °C, and (b) 140 °C in 25 min.

MnO_2 with different crystal structures exhibited significantly different morphologies. **Figure 8.2** shows the SEM images of birnessite-type and α-MnO_2. As shown in **Figure 8.2a**, the birnessite-type MnO_2 sample is composed of uniform flower-like microsphere nanostructures with a diameter of 200-400 nm. The high-magnification images reveal that the microsphere consists of crumpled nanosheets about 10 nm in thickness (**Figure 8.2b**). By comparison, the α-MnO_2 shows typical fibrous shape nanostructures with a length of 2-6 μm (**Figure 8.2c**). The images at higher magnification (**Figure 8.2d**) reveal that they have tubular structures and the diameter is about 100 nm.

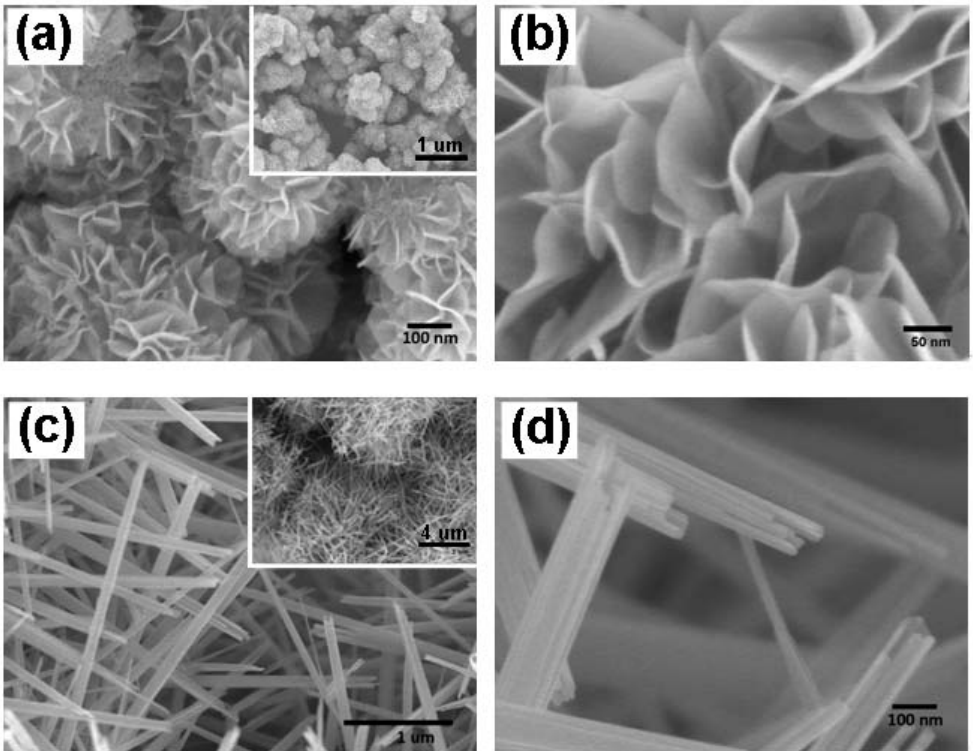

Figure 8.2 SEM images of the products prepared at (a, and b) 100 °C, and (c, and d) 140 °C in 25 min. The insets of a, and c are the lower magnification images.

The interior structure of the flower-like microsphere nanostrctures was further characterized by TEM and HRTEM. **Figure 8.3a** shows core-corona architecture of the birnessite-type MnO_2 which is similar to the previous report [33]. From the TEM image, it can be seen clearly that the nanosheets in the corona are grown perpendicularly/parallel from the core. The selected area electron diffraction (SAED) pattern (inset in **Figure 8.3a**) of a typical microsphere indicates that it is polycrystalline.

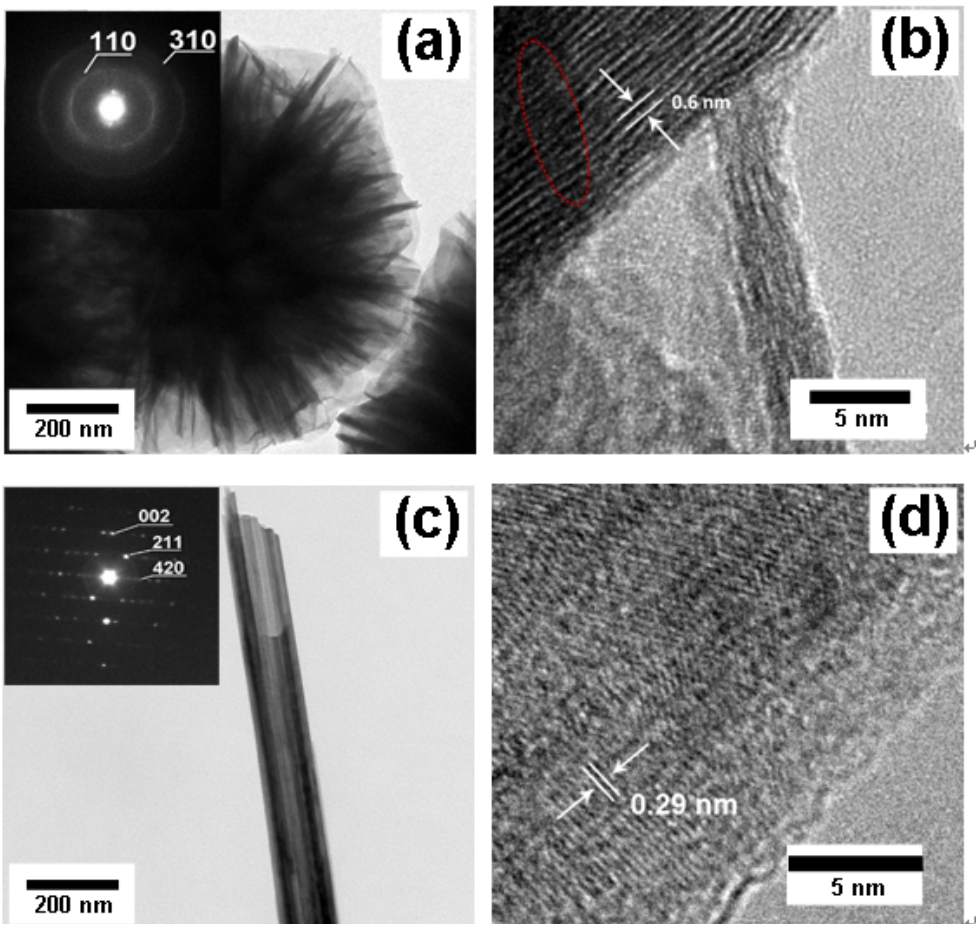

Figure 8.3 TEM (a, and c) and HRTEM (b, and d) images of the products prepared at (a, and b) 100 °C, and (c, and d) 140 °C in 25 min. The insets of a, and c show the corresponding SAED patterns.

The HRTEM image (**Figure 8.3b**) indicates that the corona is composed of thin sheets crystallized in the birnessite structure with a *d*-spacing about 0.6 nm. The distance is lower than the *d* spacing between the (001) planes (0.73 nm), which is due to the dehydrating under the electron beam. It is noticed that the distance between nanosheets are not even and there are some dislocations along the nanosheet direction (Red dash circle in **Figure 8.3b**), indicating the poor orientation of the (001) planes, which agrees with the XRD result.

Figure 8.3c and **8.3d** show the TEM and HRTEM images of the α-MnO_2 nanotube structures. As shown in **Figure 8.3c**, the α-MnO_2 nanotubes have relatively uniform outer diameters ranging between 80 and 100 nm and the wall thickness is about 20 nm. The SAED pattern (inset in **Figure 8.3c**) reveals the single-crystalline nature of the α-MnO_2 nanotubes. The lattice fringes in **Figure 8.3d** shows the interplanar distances perpendicularly to the rod axis is 0.29 nm, which agrees with the *d* value of (001) planes of α-MnO_2. Therefore, the nanotubes grow along the [001] direction. The TEM and HRTEM results are consistent with XRD data, confirming the mono-phase and good crystallinity of the α-MnO_2 nanotubes.

Fourier transform-infrared (FT-IR) and Raman scattering (RS) spectroscopy have been proved to be useful alternatives and/or supplements to X-ray diffraction for structural characterizations of materials [34]. Because they are sensitive to crystalline disorders as well as different local structural properties, FT-IR and RS spectroscopy can yield more complete and reliable description of materials, and further confirm our samples.

The FT-IR spectra of the samples are shown in **Figure 8.4A**. From the spectra results of as-prepared samples, it can be observed that a broadband appears at around 3442 cm^{-1} for both samples, which is caused by the absorbent of interlayer hydrates and some hydroxyl groups not from hydrates but those directly bound to the interlayer metal ions. And the bands at 1635 and 1385 cm^{-1} represent the vibration due to interaction of Mn with surrounding species, such as OH, O, H^+ and K^+. The water molecules or cations intercalated into the MnO_2 interlayer or tunnels were introduced during the synthesis to build/maintain the structures [35]. It has been reported that in hydrous MnO_2 samples, the peaks appear at 1620 and 1280 cm^{-1} [36]. The high frequency shift in our case reveals the strongly bonded nature [37].

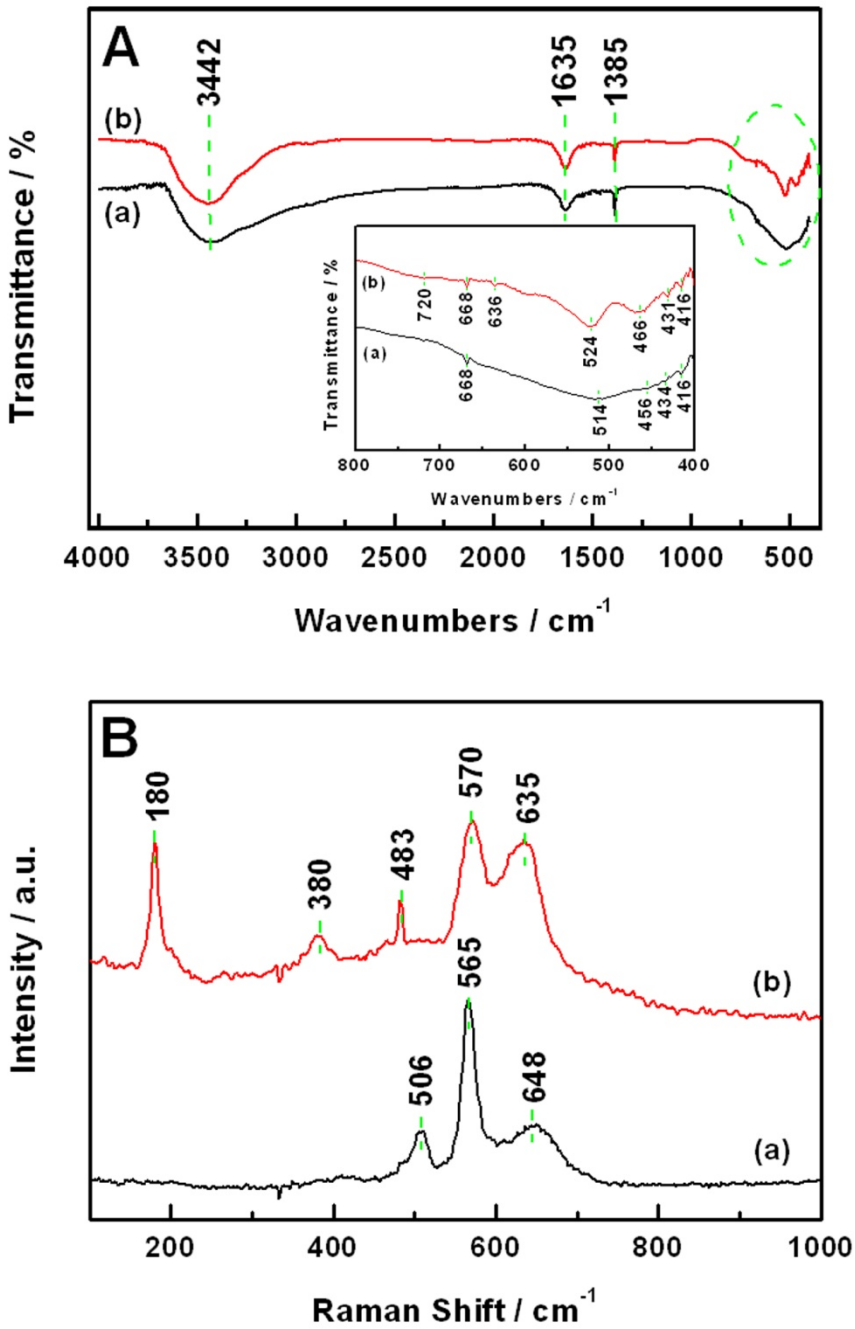

Figure 8.4 FT-IR spectra (A) and Raman scattering spectra (B) of the products prepared at (a) 100 °C, and (b) 140 °C in 25 min.

The FT-IR spectra results in the region of 800 to 400 cm^{-1} reveal information about MnO_6 octahedra (inset in **Figure 8.4A**). A major difference between the two kinds of samples has been witnessed in this region. For birnessite-type MnO_2, a broadband is present at 514 cm^{-1} while four weak bands are recorded at 668, 456, 434 and 416 cm^{-1}, respectively. The results are different from that of literatures, viz. the band at 635, 583, 513, 477 and 423 cm^{-1}, respectively [38]. Especially, the band at 423 cm^{-1} indicates the crystalline order of the birnessite compound [34]. The distortion of MnO_6 octahedra is due to the constitutional water in the sample [37]. Obvious differences can be observed for α-MnO_2. Two dominant bands at 524 and 466 cm^{-1} and five weak bands at 720, 668, 636, 431 and 416 cm^{-1} are recorded, which are similar to those previously reported for α-MnO_2 materials [39].

Figure 8.4B shows the Raman spectra of birnessite-type and α-MnO_2. Three main contributions at 506, 565 and 648 cm^{-1} are detected for the birnessite-type MnO_2. The Raman band at 648 cm^{-1} can be viewed as the symmetric ν_2(Mn-O) stretching vibration of MnO_6 groups and the band at 565 cm^{-1} is attributed to the ν_3(Mn-O) stretching vibration in the basal plane of MnO_6 sheets [40]. The ν_3(Mn-O) stretching frequency presents a shift of 10 cm^{-1} towards the low-frequency side, which is attributed to the defect chemistry and the local disorder of the as-prepared birnessite structure [34]. The Raman spectrum of α-MnO_2 nanotubes has several contributions at 180, 380, 483, 570 and 635 cm^{-1}. The low-frequency Raman band at 180 cm^{-1} is assigned to an external vibration that due to the translational motion of the MnO_6 octahedra while the Raman band at 380 cm^{-1} is caused by the Mn-O bending vibrations. It is emphasized that the relative intensities of two high-frequency Raman bands at 570 and 635 cm^{-1} are correlated to the nature of the tunnel species [39]. Hence, the spectrum reflects the good crystallinity of the α-MnO_2, which is agreement with the structural studies reported above.

8.3.2 Growth mechanisms of MnO_2 nanostructures

The formation mechanism of the flower-like MnO_2 microspheres has been widely accepted in the previous report for hydrothermal method [41]. We believe that the microwave-assisted hydrothermal method has a similar mechanism. In brief, firstly, large amount of nuclei form rapidly in a short time and then self-assembly to form amorphous spheres. During the hydrothermal process, an Ostwald ripening process is carried out, in which smaller particles dissolve while the bigger ones grow into sheet-like particles with a lamellar structure. Finally, the sheet-like particles tend to curl and assembly to form a core-corona hierarchical structure.

By contrast, several models have been suggested in terms of the formation of metal or metal oxide nanotubes in a solution based process. Meng et al. proposed a curving followed by seaming of molecular layers mechanism for the tube-formation process of materials with layered structure [42]. Mo et al. suggested a template-roll-growth and template-twist-join-growth mechanism for the formation of Te nanotubes [43]. Wang et al. proposed a rolling mechanism for the conversion from MnO_2 nanosheets to nanotubes [28]. Luo et al. proposed a tip/end-etching process for the formation of MnO_2 nanotubes [44]. However, no evidence is shown to support these hypotheses in our system.

The reaction in our process could be described as follows:

Half reaction:

$$2Cl^- \rightarrow Cl_2 + 2e^- \qquad (E^0 = -1.3595V) \tag{8.1}$$

$$MnO_4^- + 4H^+ + 3e^- \rightarrow MnO_2 + 2H_2O \qquad (E^0 = +1.695V) \tag{8.2}$$

Overall reaction:

$$2MnO_4^- + 8H^+ + 6Cl^- \Leftrightarrow 2MnO_2 + 3Cl_2 + 4H_2O \tag{8.3}$$

To understand the formation of the α-MnO_2 nanotubes, the reaction under different periods of time were investigated. **Figure 8.5** shows the TEM images of three samples taken at different stages of the reaction. When the reaction proceeded for 5 min, some microspheres with core-corona architecture were produced with a diameter about 1 μm, and the thickness of nanosheets is about 10 nm (**Figure 8.5a**). After 10 min, the microspheres tended to collapse and some fibrous structures formed. From **Figure 8.5b**, it can be seen that three different types of fibrous structures formed: nanorod with a diameter about 20 nm (**Figure 8.5d**); bundle-like tube with a diameter about 50 nm (**Figure 8.5e**); and nanotube with a diameter about 80 nm (**Figure 8.5f**). As shown in **Figure 8.5e**, the bundle-like tube consists of nanorods about 16 nm in diameter, which is consistent to the diameter of the single nanorod in **Figure 8.5d**. **Figure 8.5f** shows that the nanotube has smooth surface but an uneven end, and the wall thickness is about 20 nm. When the reaction time was prolonged to 25 min, the nanotubes with a diameter of 80-100 nm formed in majority (> 85%) (**Figure 8.5c**).

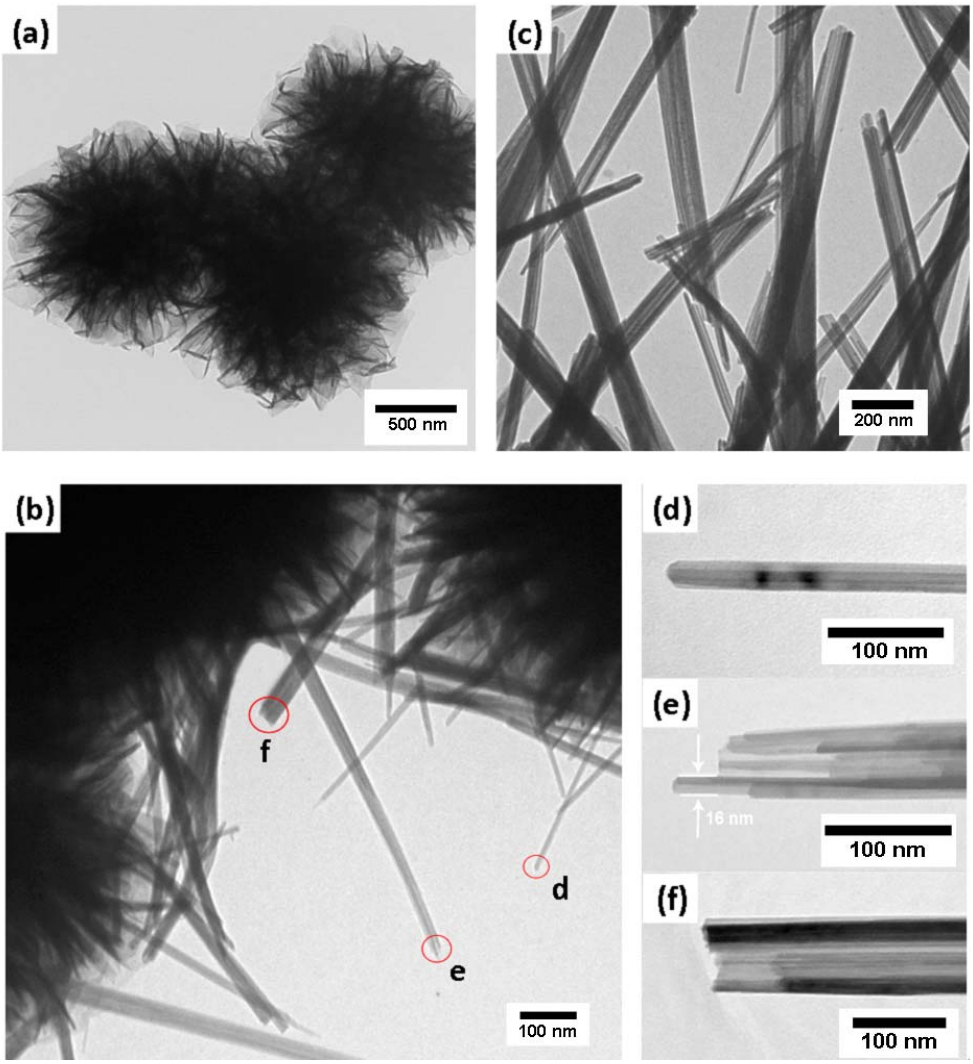

Figure 8.5 TEM images of the products prepared in (a) 5 min, (b, d, e, and f) 15 min, and (c) 25 min at a reaction temperature of 140 °C.

It has been reported that α-MnO_2 naowires/nanorods tended to assemble along lateral surface and form thick nanorods through an "oriented attachment" mechanism under the hydrothermal condition since the formation of bundles could reduce the surface-to-volume ratio and the surface energy [45-48]. The exact mechanism for the formation of tubular nanostructures in our case is still under investigation.

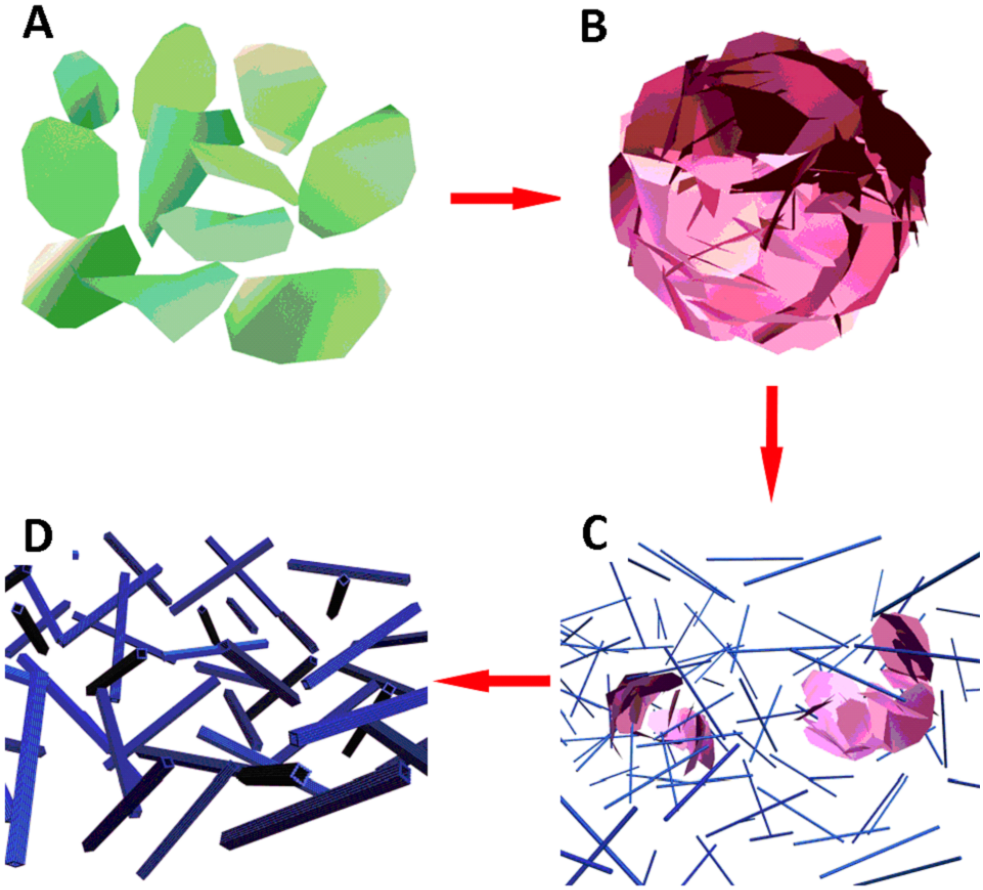

Figure 8.6 Schematic illustration of the formation stages of different shapes of the MnO_2 nanostructures.

But we believe that two mechanisms, as shown in **Figure 8.6**, are responsible for the formation of the nanotubes: (a) a dissolution-crystallization process that converts less ordered precursors into nanorods (from nanosheets to nanorods); (b) an "oriented attachment" process which aggregates nanorods along the lateral faces to form tubular products. The formation process of the MnO_2 nanotubes can be described as follows: At the initial stage, the 3D hierarchical architectures formed as described above; then, nanorods were produced because at higher temperatures (140 °C) thermal energy is enough to overcome the activation energy required for the conversion from nanosheets

to nanorods [49]. Meanwhile, some nanorods tended to assemble along their side surfaces to reduce the surface energy. The small gaps between nanorods were filled rapidly due to coarsening during aging, which led to reconstruction of boundaries and smoothing of the surfaces. That is the reason why the nanotubes show a single crystalline nature. Since the growth along the length direction ([001] direction) was very fast that the mass transport to the growing regions would lead to undersaturation of reaction species in the central portions of the growing faces, {001} planes, and eventually resulted in the formation of tubular structure having hollow interiors. Similar process has been observed in the formation of Te nanotubes [50]. It is necessary to note that the dissolution-crystallization and "oriented attachment" are two simultaneous processes in the crystal growth [51], the separated stages in **Figure 8.6c**, d are illustrated just for the convenience of explanation.

In our experiments, it was found that morphology of the product prepared at 180 °C was different from that prepared at 140 °C, showing a hollow needle-like structure, which was due to the fast growth rate of the nanorods at the external wall of the nanotubes (**Figure 8.7**). This further confirms the proposed growth mechanism.

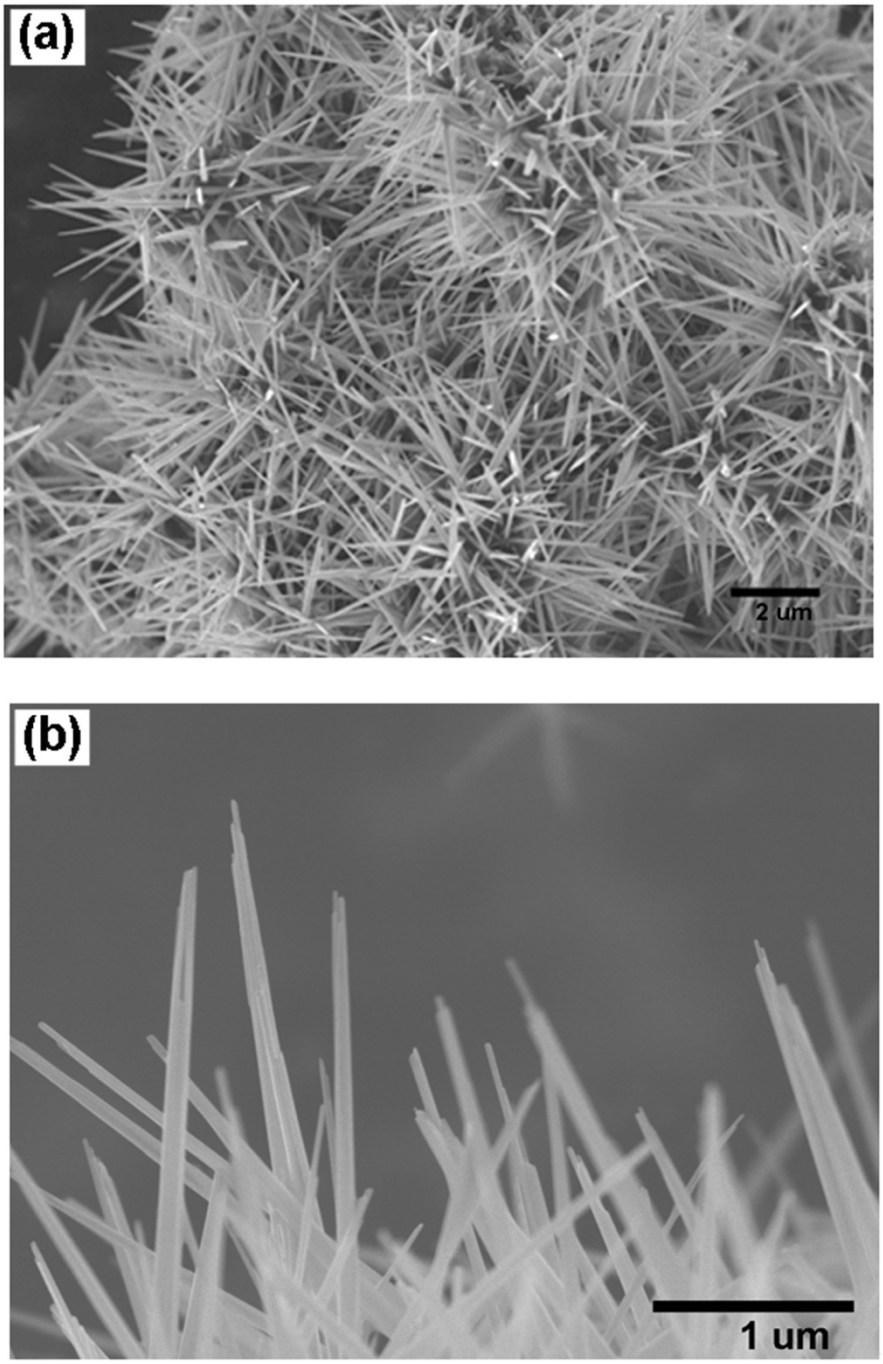

Figure 8.7 SEM images of the product prepared at 180 °C in 25 min.

8.4 Conclusions

In summary, we report a facile microwave-assisted hydrothermal route for synthesis of 3D hierarchical and 1D tubular MnO_2 nanostructures. The crystal phase and morphology can be easily tailed by adjusting reaction temperature. The formation of MnO_2 nanotubes follows the dissolution-crystallization and "oriented attachment" process. Compared to conventional heating methods, the microwave-assisted hydrothermal approach features rapid growth of nanostructured MnO_2 with controlled structure, which is ideal for large-scale production. We believe that this study not only provides a new growth scheme of MnO_2 nanotube formation but also gives a rational strategy in synthesis and design of nanomaterials with complex architecture and novel properties.

Acknowledgement

This research was supported by Natural Sciences and Engineering Research Council of Canada, Canada Research Chair Program, Canada Foundation for Innovation, Ontario Early Researcher Award and the University of Western Ontario. The authors would like to appreciate Mr. Fred Pearson at McMaster University for the fruitful discussion.

References

[1] Z. Li, Y. Ding, Y. Xiong, Y. Xie, Rational growth of various α-MnO_2 hierarchical structures and β-MnO_2 nanorods via a homogeneous catalytic route, *Cryst. Growth Des.*, 2005, **5**, 1953–1958.

[2] G. Ji, S. Tang, B. Xu, B. Gu, Y. Du, Synthesis of $CoFe_2O_4$ nanowire arrays by sol-gel template method, *Chem. Phys. Lett.*, 2003, **379**, 484–489.

[3] S. Chou, C. Zhu, S. Neeleshwar, C. Chen, Y. Chen, C. Chen, Controlled growth and magnetic property of FePt nanostructure: Cuboctahedron, octapod, truncated cube, and cube, *Chem. Mater.*, 2009, **21**, 4955–4961.

[4] T. Almeida, M. Fay, Y. Zhu, P. Brown, Process map for the hydrothermal synthesis of α-Fe_2O_3 nanorods, *J. Phys. Chem. C*, 2009, **113**, 18689–18698.

[5] J. Menéndez, A. Domínguez, M. Inguanzo, J. Pis, Microwave pyrolysis of sewage sludge: analysis of the gas fraction, *J. Anal. Appl. Pyrol.*, 2004, **71**, 657–667.

[6] J. Liu, K. Li, H. Wang, M. Zhu, H. Yan, Rapid formation of hydroxyapatite nanostructures by microwave irradiation, *Chem. Phys. Lett.*, 2004, **396**, 429–432.

[7] M. Nüchter, B. Ondruschka, W. Bonrath, A. Gum, Microwave assisted synthesis – a critical technology overview, *Green. Chem.*, 2004, **6**, 128–141.

[8] S. Naik, T. Jagadale, S. Apte, R. Sonawane, M. Kulkarni, S. Patil, S. Ogale, B. Kale, Rapid phase-controlled microwave synthesis of nanostructured hierarchical tetragonal and cubic β-In_2S_3 dandelion flowers, *Chem. Phys. Lett.*, 2008, **452**, 301–305.

[9] T. Lai, Y. Lai, J. Yu, Y. Shu, C. Wang, Microwave-assisted hydrothermal synthesis of coralloid nanostructured nickel hydroxide hydrate and thermal conversion to nickel oxide, *Mater. Res. Bull.*, 2009, **44**, 2040–2044.

[10] A. Phuruangrat, T. Thongtem, S. Thongtem, Microwave-assisted synthesis of ZnO nanostructure flowers, *Mater. Lett.*, 2009, **63**, 1224–1226.

[11] H. Zhou, R. Yi, J. Li, Y. Su, X. Liu, Microwave-assisted synthesis and characterization of hexagonal Fe_3O_4 nanoplates, *Solid State Sci.*, 2010, **12**, 99–104.

[12] Y. Ma, L. Zhang, X. Cao, X. Chen, Z. Xue, Microwave-assisted solvothermal synthesis and growth mechanism of $WO_3{\cdot}(H_2O)_{0.33}$ hierarchical microstructures, *Cryst. Eng. Comm.*, 2010, **12**, 1153–1158.

[13] W. Li, Microwave-assisted hydrothermal synthesis and optical property of Co_3O_4 nanorods, *Mater. Lett.*, 2008, **62**, 4149–4151.

[14] L. Wang, C. Meng, M. Han, W. Ma, Lithium uptake in fixed-pH solution by ion sieves, *J. Colloid Interface Sci.*, 2008, **325**, 31–40.

[15] R. Kumar, S. Sithambaram, S. Suib, Cyclohexane oxidation catalyzed by manganese oxide octahedral molecular sieves — Effect of acidity of the catalyst, *J. Catal.*, 2009, **262**, 304–313.

[16] A. Lima, N. Bocchi, H. Gomes, M. Teixeira, An electrochemical sensor based on nanostructured hollandite-type manganese oxide for detection of potassium ions, *Sensors*, 2009, **9**, 6613–6625.

[17] F. Cheng, J. Zhao, W. Song, C. Li, H. Ma, J. Chen, P. Shen, Facile controlled synthesis of MnO_2 nanostructures of novel shapes and their application in batteries, *Inorg. Chem.*, 2006, **45**, 2038–2044.

[18] S. Devaraj, N. Munichandraiah, Effect of crystallographic structure of MnO_2 on its electrochemical capacitance properties, *J. Phys. Chem. C*, 2008, **112**, 4406–4417.

[19] D. Zheng, Z. Yin, W. Zhang, X. Tan, S. Sun, Novel branched γ-MnOOH and β-MnO_2 multipod nanostructures, *Cryst. Growth Des.*, 2006, **8**, 1733–1735.

[20] G. Xi, Y. Peng, Y. Zhu, L. Xu, W. Zhang, W. Yu, Y. Qian, Preparation of β-MnO_2 nanorods through a γ-MnOOH precursor route, *Mater. Res. Bull.*, 2004, **39**, 1641–1648.

[21] S. Zhu, H. Zhou, M. Hibino, I. Honma, M. Ichihara, Synthesis of MnO_2 nanoparticles confined in ordered mesoporous carbon using a sonochemical method, *Adv. Funct. Mater.*, 2005, **15**, 381–386.

[22] D. Zheng, S. Sun, W. Fan, H. Yu, C. Fan, G. Cao, Z. Yin, X. Song, One-step preparation of single-crystalline β-MnO_2 nanotubes, *J. Phys. Chem. B*, 2005, **109**, 16439–16443.

[23] J. Liu, Y. Son, J. Cai, X. Shen, S. Suib, M. Aindow, Size control, metal substitution, and catalytic application of cryptomelane nanomaterials prepared using cross-linking reagents, *Chem. Mater.*, 2004, **16**, 276–285.

[24] V. Subramanian, H. Zhu, B. Wei, Alcohol-assisted room temperature synthesis of different nanostructured manganese oxides and their pseudocapacitance properties in neutral electrolyte, *Chem. Phys. Lett.*, 2008, **453**, 242–249.

[25] X. Liu, S. Fu, C. Huang, Synthesis, characterization and magnetic properties of β-MnO_2 nanorods, *Powder Technol.*, 2005, **154**, 120–124.

[26] S. Kim, S. Kim, S. Oh, Preparation of layered MnO_2 via thermal decomposition of $KMnO_4$ and its electrochemical characterizations, *Chem. Mater.*, 1999, **11**, 557–563.

[27] R. Chen, P. Zavalij, M. Whittingham, Hydrothermal synthesis and characterization of $K_xMnO_2 \cdot yH_2O$, *Chem. Mater.*, 1996, **8**, 1275–1280.

[28] X. Wang, Y. Li, Synthesis and formation mechanism of manganese dioxide nanowires/nanorods, *Chem. Eur. J.*, 2003, **9**, 300–306.

[29] Y. Li, X. Li, R. He, J. Zhu, Z. Deng, Artificial lamellar mesostructures to WS_2 nanotubes, *J. Am. Chem. Soc.*, 2002, **124**, 1411–1416.

[30] P. Yu, X. Zhang, D. Wang, L. Wang, Y. Ma, Shape-controlled synthesis of 3D hierarchical MnO_2 nanostructures for electrochemical supercapacitors, *Cryst. Growth Des.*, 2009, **9**, 528–533.

[31] H. Huang, S. Sithambaram, C. Chen, C. Kithongo, L. Xu, A. Iyer, H. Garces, S. Suib, Microwave-assisted hydrothermal synthesis of cryptomelane-type octahedral molecular sieves (OMS-2) and their catalytic studies, *Chem. Mater.*, 2010, **22**, 3664–3669.

[32] D. Portehault, S. Cassaignon, E. Baudrin, J.-P. Jolivet, Structural and morphological control of manganese oxide nanoparticles upon soft aqueous precipitation through MnO^{4-}/Mn^{2+} reaction, *J. Mater. Chem.*, 2009, **19**, 2407–2416.

[33] D. Portehault, S. Cassaignon, N. Nassif, E. Baudrin, J.-P. Jolivet, A core-corona hierarchical manganese oxide and its formation by an aqueous soft chemistry mechanism, *Angew. Chem. Int. Ed.*, 2008, **47**, 441–6444.

[34] C. Julien, M. Massot, C. Poinsignon, Lattice vibrations of manganese oxides: Part I. Periodic structures, *Spectrochim. Acta Part A*, 2004, **60**, 689–700.

[35] W. Xiao, D. Wang, X. Lou, Shape-controlled synthesis of MnO_2 nanostructures with enhanced electrocatalytic activity for oxygen reduction, *J. Phys. Chem. C*, 2010, **114**, 1694–1700.

[36] J. Fernandes, B. Desai, D. Kamat, Studies on chemically precipitated Mn(IV) oxides— I, *Electrochim. Acta*, 1983, **28**, 309–315.

[37] M. Ananth, S. Pethkar, K. Dakshinamurthi, Distortion of MnO_6 octahedra and electrochemical activity of Nstutite-based MnO_2 polymorphs for alkaline electrolytes— an FTIR study, *J. Power Sources*, 1998, **75**, 278–282.

[38] L. Kang, M. Zhang, Z. Liu, K. Ooi, IR spectra of manganese oxides with either layered or tunnel structures, *Spectrochim. Acta Part A*, 2007, **67**, 864–869.

[39] T. Gao, H. Fjellvåg, P. Norby, A comparison study on Raman scattering properties of α- and β-MnO_2, *Anal. Chim. Acta*, 2009, **648**, 235–239.

[40] C. Julien, M. Massot, R. Baddour-Hadjean, S. Franger, S. Bach, J. Pereira-Ramos, Raman spectra of birnessite manganese dioxides, *Solid State Ionics*, 2003, **159**, 345–356.

[41] N. Xu, Z. Liu, X. Ma, S. Qiao, J. Yuan, Controlled synthesis and characterization of layered manganese oxide nanostructures with different morphologies, *J. Nanopart. Res.*, 2009, **11**, 1107–1115.

[42] C. Ye, G. Meng, Z. Jiang, Y. Wang, G. Wang, L. Zhang, Rational growth of Bi_2S_3 nanotubes from quasi-two-dimensional precursors, *J. Am. Chem. Soc.*, 2002, **124**, 15180–15181.

[43] M. Mo, J. Zeng, X. Liu, W. Yu, S. Zhang, Y. Qian, Controlled hydrothermal synthesis of thin single-crystal tellurium nanobelts and nanotubes, *Adv. Mater.*, 2002, **14**, 1658–1662.

[44] J. Luo, H. Zhu, H. Fan, J. Liang, H. Shi, G. Rao, J. Li, Z. Du, Z. Shen, Synthesis of single-crystal tetragonal α-MnO_2 nanotubes, *J. Phys. Chem. C*, 2008, **112**, 12594–12598.

[45] S. Chen, J. Zhu, Q. Han, Z. Zheng, Y. Yang, X. Wang, Shape-controlled synthesis of one-dimensional MnO_2 via a facile quick-precipitation procedure and its electrochemical properties, *Cryst. Growth Des.*, 2009, **9**, 4356–4361.

[46] D. Portehault, S. Cassaignon, E. Baudrin, J.-P. Jolivet, Morphology control of cryptomelane type MnO_2 nanowires by soft chemistry, growth mechanisms in aqueous medium, *Chem. Mater.*, 2007, **19**, 5410–5417.

[47] T. Gao, M. Glerup, F. Krumeich, R. Nesper, H. Fjellvåg, P. Norby, Microstructures and spectroscopic properties of cryptomelane-type manganese dioxide nanofibers, *J. Phys. Chem. C*, 2008, **112**, 13134–13140.

[48] X. Zhang, W. Yang, J. Yang, D. Evans, Synthesis and characterization of α-MnO_2 nanowires: Self-assembly and phase transformation to β-MnO_2 microcrystals, *J. Cryst. Growth*, 2008, **310**, 716–722.

[49] D. Walanda, G. Laurance, S. Donne, Hydrothermal MnO_2: synthesis, structure, morphology and discharge performance, *J. Power Sources*, 2005, **139**, 325–341.

[50] B. Mayers, Y. Xia, Formation of tellurium nanotubes through concentration depletion at the surfaces of seeds, *Adv. Mater.*, 2002, **14**, 279–282.

[51] Y. Li, H. Tan, O. Lebedev, J. Verbeeck, E. Biermans, G. Tendeloo, B. Su, Insight into the growth of multiple branched MnOOH nanorods, *Cryst. Growth Des.*, 2010, **10**, 2969–2976.

Chapter 9

9 Enhanced Performance of Sodium-Oxygen Batteries by Nitrogen-Doped Graphene Cathode Materials*

From the previous chapters, we have shown that the properties of carbon cathode, such as morphology, porosity and defects, etc, have significant impact on the performance of lithium-oxygen battery and we believe that they will also affect the performance of sodium-oxygen battery since the discharge products of the latter is not soluble in the organic electrolyte but deposit on the electrode surface which is similar to the former. Graphene nanosheets (GNSs) have been used as cathode materials for sodium-oxygen battery and it was demonstrated that electrochemical properties of GNSs superior to that of carbon electrode due to the high electrocatalytic activity.

In this chapter, nitrogen-doped graphene nanosheets (N-GNSs) were employed as cathode materials for sodium-oxygen batteries and the battery delivered a discharge capacity of 8600 mAh g^{-1}, which is about two times of that of the pristine GNSs electrode. It was further demonstrated that the electrocatalytic activity of N-GNSs both for oxygen reduction and oxygen evolution reaction is higher than that of GNSs. The excellent electrochemical performance of N-GNSs is attributed to the active sites introduced by nitrogen doping.

---

*A version of this chapter is to be submitted for publishing.

9.1 Introduction

Nonaqueous lithium-oxygen batteries have been intensively studied for past few years because they show extremely high energy density which makes the energy storage system a great candidate for electric vehicles (EVs) and hybrid electric vehicles (HEVs) [1, 2]. Since the discharge products are not soluble in the electrolyte but deposit in the electrode and the battery reaction will be terminated eventually when the oxygen diffusion channels are blocked [3-5]. As a result, it is well accepted that one of the challenges to improve the battery performance is to develop an optimum cathode with appropriate morphology, conductivity, surface area, and porosity, etc. However, large overpotentials are observed for these batteries during the discharge and charge processes, leading to relatively low round-trip energy storage efficiencies. In addition, limited amount of lithium resource inevitably prevents lithium-oxygen batteries from wide applications in EVs and HEVs [6]. Recently, studies on replacing lithium by sodium for lithium-oxygen batteries have been reported and the results are attractive since sodium has high earth abundance, modest cost, and most importantly, the sodium-oxygen batteries can deliver a energy density of about 1600 Wh kg^{-1} which holds the same great promise as lithium-oxygen battery to meet the rapidly growth of energy demands for future automotive applications [7-8]. Similar to lithium-oxygen batteries, the discharge product will also deposit on the electrode surface for sodium-oxygen batteries, therefore, the cathode properties, such as materials, configuration or other factors are very critical for determining the battery performance. For example, Fu et al. demonstrated that graphene nanosheets (GNSs) increased discharge capacity compared to normal carbon film electrode due to the unique chemical and physical properties of GNSs [9].

In our previous studied, we showed that chemical doping with nitrogen atoms to carbon materials can modify the electronic property, provide more active sites, and enhance the interaction between carbon structure and other molecules, thus improves the performance of lithium-oxygen batteries [10, 11]. It is expected that nitrogen

doping into carbon cathode can increase sodium-oxygen battery performance. However, to our best knowledge, there are few reports about heteroatom-doping effect of carbon materials for sodium-oxygen battery system. Here, nitrogen-doped graphene nanosheets (N-GNSs) were synthesized and employed as cathode materials for sodium-oxygen batteries. We found that N-GNSs show excellent electrocatalytic activity for oxygen reduction reaction (ORR), therefore, deliver two times of discharge capacity compared to GNSs. This finding not only shows that N-GNSs are promising electrode materials, but also gives a rational direction to modify other carbon materials for application in sodium-oxygen batteries.

9.2 Experimental

9.2.1 Materials synthesis

GNSs were prepared by the oxidation of graphite powder using the modified Hummers' method, and N-GNSs were prepared by post heating the GNSs under ammonia atmosphere [12].

9.2.2 Physical characterizations

The morphology of the discharge products of GNSs and N-GNSs electrodes were characterized by a Hitachi S-4800 field emission scanning electron microscopy (FESEM). The morphology of GNSs and N-GNSs were characterized by a Hitachi H-7000 transmission electron microscopy (TEM). The XPS spectra were tested by a Kratos Axis Ultra X-ray photoelectron spectrometer with Al Kα as the X-ray source. Raman scattering (RS) spectra were recorded on a HORIBA Scientific LabRAM HR Raman spectrometer system equipped with a 532.4 nm laser. N_2 adsorption/desorption

isotherms were obtained using a Folio Micromeritics TriStar Ⅱ Surface Area and Pore Size Analyser.

9.2.3 Electrochemical measurements

Swagelok type cells were used to test the battery performance. GNSs or N-GNSs and PVDF (Alfa Aesar) with a weight ratio of 9:1 were casted onto a separator (Celgard 3500) as cathode. The electrodes were cut to 3/8 inch in diameter and the loadings of GNSs or N-GNSs were ~ 0.3 mg. The electrolyte was 0.5 mol dm^{-3} $NaSO_3CF_3$ dissolved in diethylene glycol dimethyl ether ($C_6H_{14}O_3$, diglyme, DEGDME). The discharge/charge characteristics were performed using an Arbin BT-2000 battery station in a voltage range of 1.8-3.6 V in a 1 atm oxygen atmosphere at room temperature (25 °C). Cyclic voltammetry (CV) measurements were carried out using a CHI 600c electrochemical work station at a scan rate of 2 mV s^{-1} in a voltage range of 1.8-3.6 V at room temperature (25 ^{o}C). Electrochemical impedance spectra were recorded in the frequency range of 0.01-10^5 Hz using a VMP3 Potentiostat (BioLogic Science Instruments). The resulted spectra were fitted by ZView software.

9.3 Results and Discussion

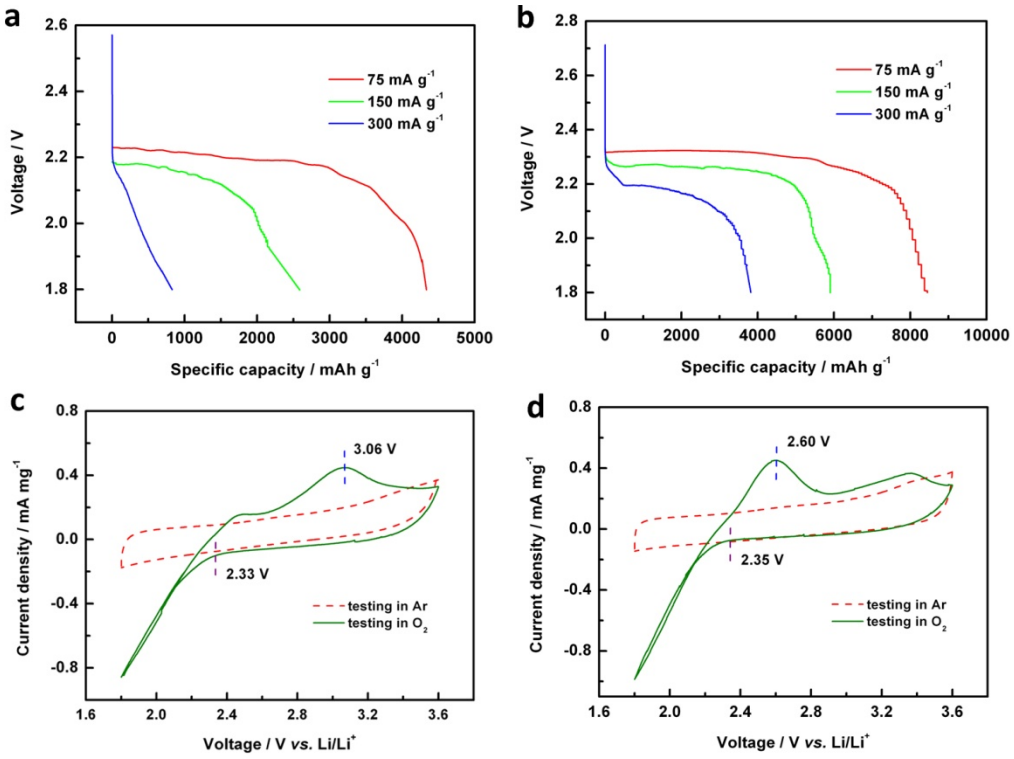

Figure 9.1 The voltage profiles of (a) GNSs and (b) N-GNSs electrodes at various current densities; CV curves of (c) GNSss and (d) N-GNSs electrodes at a scan rate of 2 mV s^{-1} in a voltage range of 1.8-3.6 V.

Figure 9.1a and **9.1b** show the discharge curves of GNSs and N-GNSs electrodes in sodium-oxygen cells at various rates of 75, 150, and 300 mA g^{-1}, respectively. As can be seen, the N-GNSs electrodes deliver higher discharge capacities at all different current densities, for example, the discharge capacity at 75 mA g^{-1} is about 8600 mAh g^{-1}, which is about two times of that for GNSs electrode (4350 mAh g^{-1}). The discharge capacity decreases with increasing current density for both electrode materials. The discharge capacity of N-GNSs electrode decreases to 6000 mAh g^{-1} at

150 mA g^{-1}, and 3980 mAh g^{-1} is obtained at 300 mA g^{-1}. However, they are still higher than that of GNSs, which are 2550 and 990 mAh g^{-1} at 150 and 300 mA g^{-1}, respectively. The average discharge voltages of N-GNSs electrodes are also higher than those of GNSs electrodes at different current densities. Recent studies have shown that the oxygen adsorption is the first step before the first charge transfer process for carbonaceous materials, that the oxygen reduction reaction (ORR) is preferably taken place on the defective sites [13, 14]. As shown in **Figure SI-9.1**, the intensity ratio of D to G bands of GNSs and N-GNSs are 0.96 and 1.10, respectively, confirming that more defects are obtained after nitrogen doping, resulting in an increase in the discharge voltages.

The cyclic voltammetry (CV) curves from the GNSs and N-GNSs electrodes in argon or oxygen atmosphere are shown in **Figure 9.1c** and **9.1d**. There are no obvious cathodic and anodic peaks in the CVs for both samples tested in argon; however, reduction reactions occur after introducing oxygen into the system. As can be seen, the onset potential of ORR for GNSs is at ~ 2.33 V while for N-GNSs, the onset potential of ORR shifted positively to around ~ 2.35 V, indicating a superior electrocatalytic activity of N-GNSs for ORR [15, 16]. It is important to note that the anodic peak, corresponding to the oxidation of discharge product of N-GNSs electrode is at ~ 2.60 V which is ~ 46 mV negative shifted compared to GNSs electrode. The lower oxidation voltage indicates that N-GNSs show better electrocatalytic activity for oxygen evolution reaction (OER) as well.

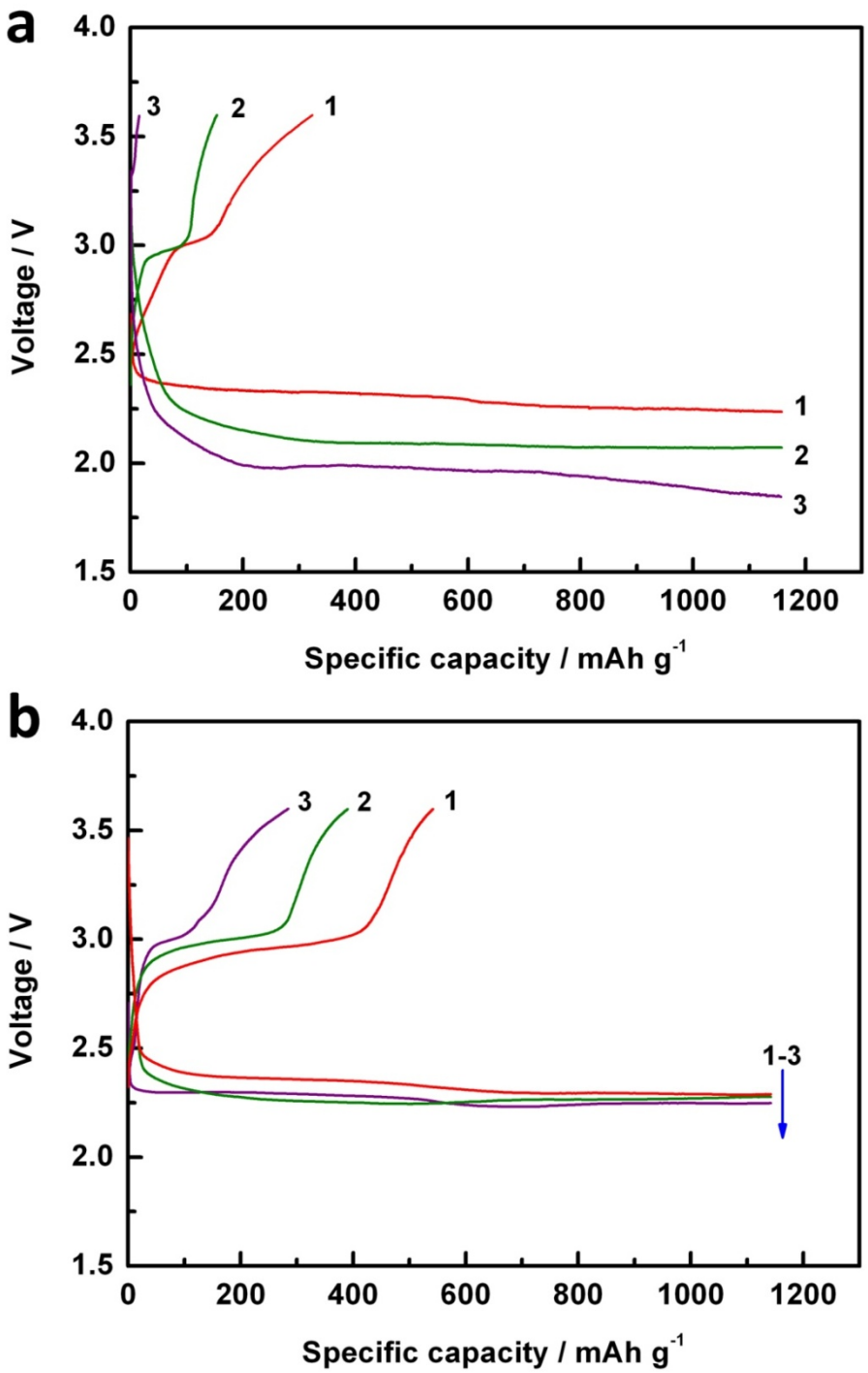

Figure 9.2 Charge/discharge performance of initial 3 cycles of (a) GNS and (b) N-GNSs electrodes at 75 mA g^{-1}.

The cycleability of sodium-oxygen batteries employing GNSs and N-GNSs electrodes were studied by cycling at low depth of discharge (DOD) with a cut-off of 1150 mAh g^{-1} (**Figure 9.2**). It is clearly shown that the discharge plateaus for the first 3 cycles for N-GNSs electrode is slightly decreased while for GNSs electrode, the decreasing is obvious. For the charge processes, the N-GNSs electrode also shows lower charge voltage and higher charge capacity than GNSs electrode. Therefore, the N-GNSs display higher bifunctional electrocatalytic activities for both ORR and OER than that of GNSs.

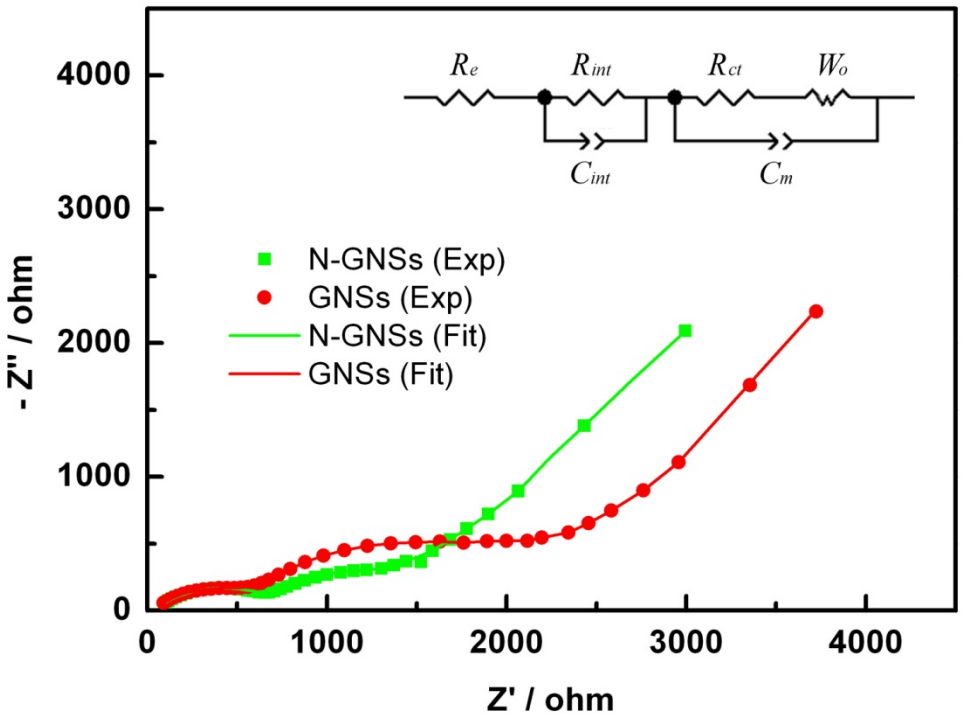

Figure 9.3 Measured and calculated electrochemical impedance spectra of GNSs and N-GNSs electrodes after discharge at 75 mA g^{-1}. The inset is the equivalent circuit used for the analysis of the impedance plots.

In order to further study the electrode polarization of GNSs and N-GNSs electrode, electrochemical impedance spectroscopic (EIS) analysis was conducted. The Nyquist plots for cells employing two samples as electrode materials obtained after the first discharge are shown in **Figure 9.3**. As can be seen, both plots exhibit two semicircles followed by a linear part, which is caused by the dispersion of three different processes with different time constants [17]. The intercept for high frequency at the real Z-axis is corresponded to the total resistance of the circuit including, electrolyte resistance, electronic resistance of current collector and external circuit connecting parts [18]. The first semicircle at high frequency is attributed to the ohmic resistance and film formation within the electrode as well as the intrinsic electronic and contact resistances of the electrode materials while the second semicircle is assigned to the combination of the charge-transfer resistance [19-21]. The EIS spectra are fitted using an equivalent circuit (inset of **Figure 9.3**) and the obtained parameters are listed in **Table 9.1**.

Table 9.1 Dependence of equivalent-circuit parameters for GNSs and N-GNSs electrodes.

	R_e/Ω	R_{int}/F	C_{int}/Ω	R_{ct}/Ω	C_m/F	W_o/Ω
N-GNSs	36.4	655.6	$2.46e^{-6}$	663.7	$47.9e^{-6}$	0.274
GNSs	38.0	517.1	$5.76e^{-6}$	1556.0	$94.4e^{-6}$	0.284

R_e is the ionic resistance of electrolyte; R_{int} and C_{int} are the interfacial resistance and capacitance of film on the interface between electrode/electrolyte, respectively; R_{ct} is the charge-transfer resistance while C_m is the parallel capacitance for the semicircle accordingly, and W_o is the finite length Warburg resistance. It shows that the electrolyte resistance is similar for GNSs and N-GNSs electrodes; however, there are significant differences for other circuit parameters. The interface resistance of N-GNSs electrode is higher than that of GNSs electrode, indicating the formation of more discharge products in the former electrode, which is consistent with the results of the discharge capacities. While for the charge-transfer resistance, R_{ct} which is related to

the conductivity of the discharge products, N-GNSs electrode shows lower value even with more discharge products. The reason for this finding will be discussed in the following section but from the impedance results, it is suggested that the GNSs electrode should have larger electrochemical polarization than N-GNSs electrode due to higher charge-transfer resistance.

Figure 9.4a and **9.4b** show the morphology of the discharge products on GNSs and N-GNSs electrodes, respectively. The particle size on GNSs is 200~300 nm while for N-GNSs is 50 nm. In our previous study on N-GNSs as electrode materials for lithium-oxygen battery, we have found similar results that the particle size decreased after doping nitrogen into GNSs and the reason is the discharge products most likely prefer to nucleate and grow around the defective sites [22]. As can be seen from **Figure 9.4c** and **9.4d**, it is very clear that after 12 h discharge, the discharge products dispersed more uniformly on the N-GNSs surface with smaller particle size 5~10 nm while aggregation of discharge products happened on GNSs (mark by blue circles). The nature and morphology of discharge products, Li_2O_2, significantly affected the charge overpotential of lithium-oxygen battery. It is suggested by the theoretical study that the lithium deficient Li_2O_2 surface would show low charge overpotential and the better interaction between the discharge products and carbon surface would further lower the charge overpotential [23, 24]. There is no information on the electric transport properties of NaO_2 due to sodium vacancy or deficiency and further study is required; however, it is believed that the difference in morphology on GNSs and N-GNSs electrodes as well as the enhanced interaction for the discharge products to N-GNSs surface resulted from the defective sites should be correlated to the lower overpotential/polarization.

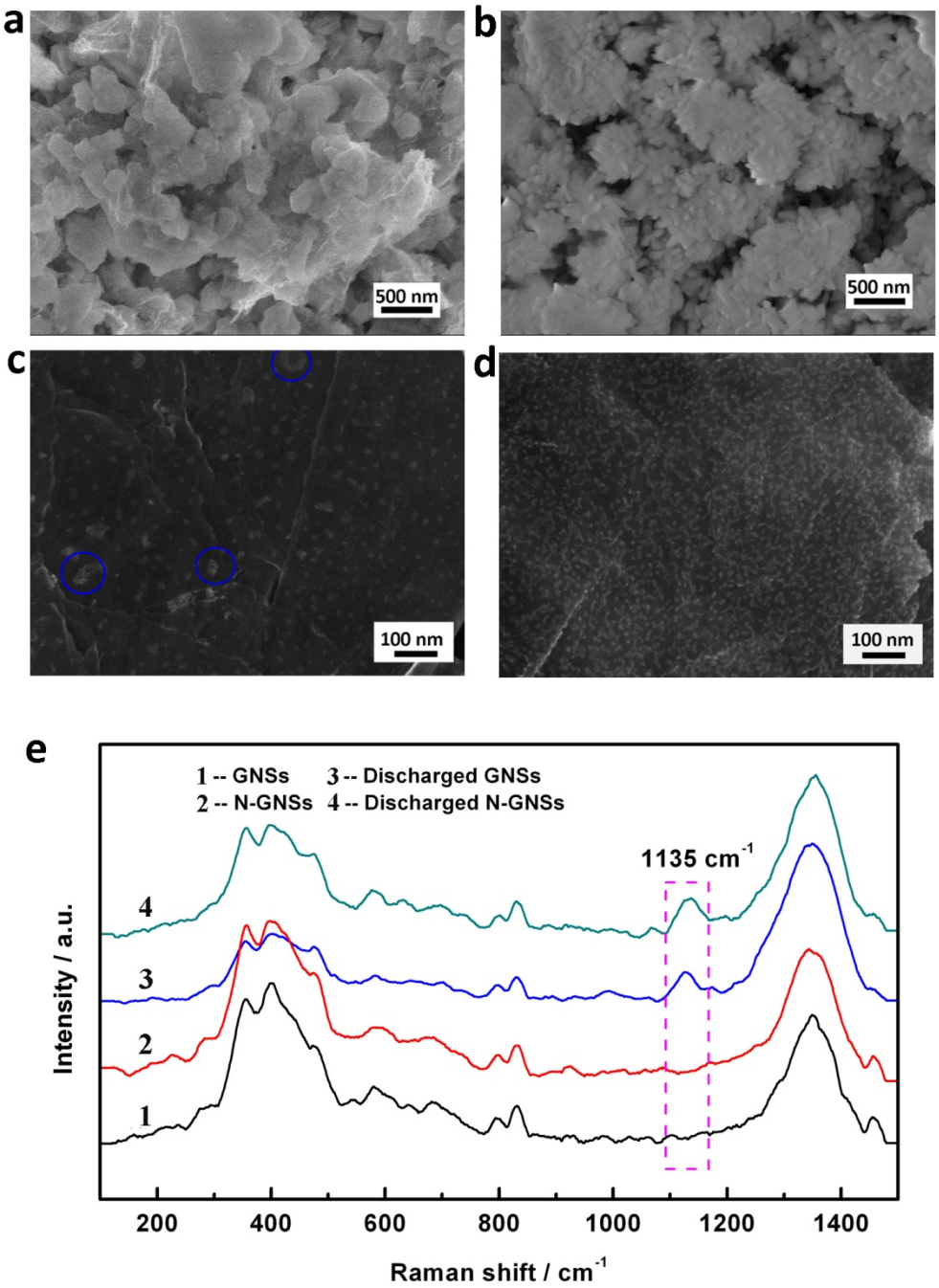

Figure 9.4 SEM images of the fully discharged a, GNSs, b, N-GNSs electrodes and c, GNSs, d, N-GNSs electrodes discharged for 12 h; e, Raman spectra of pristine and discharged GNSs and N-GNSs electrodes.

The composition of the discharge products were identified by Raman spectroscopy and the obtained spectra are shown in **Figure 9.4e**. An addition broad peak corresponding to NaO_2 appears for both GNSs and N-GNSs samples at band of ~ 1135 cm^{-1}, which is shifted to lower frequency compared to the results reported by Adelhelm et al [6]. We believe the band broadening and shift are due to the quantum size confinement effect of the particle size since the discharge product obtained by Adelhelm et al is about 1-50 μm in size which is much bigger than ours [25].

The morphology of discharge products at various current densities were observed by SEM. As shown in **Figure 9.5**, in addition to the particle size with ~ 50 nm in diameter on the carbon surface, larger particle (100-300 nm) also appeared on top of the smaller ones at 150 mA g^{-1}, however, when the current density increases to 300 mA g^{-1}, no obvious particle-shape discharge products could be found but a deposited film. The reaction pathway leading to NaO_2 could be described as the reaction below [26].

$$Na^+ + e^- + O_2^* \rightarrow NaO_2^* \qquad (9.1)$$

where the * refers to a surface adsorbed species. Firstly, NaO_2^* forms on the surface of carbon. If the solubility of NaO_2^* is zero, they will permanently remain on the reaction sites and as the discharge continues, the number of active sites decreases accordingly, leading to a continuous increase in overpotential during discharge [27]. Therefore, the discharge products would re-dissolve into the electrolyte via solvation. It is also clearly demonstrated by the aggregation of particles during discharge, indicating it is not a simple growth mechanism form on the carbon surface.

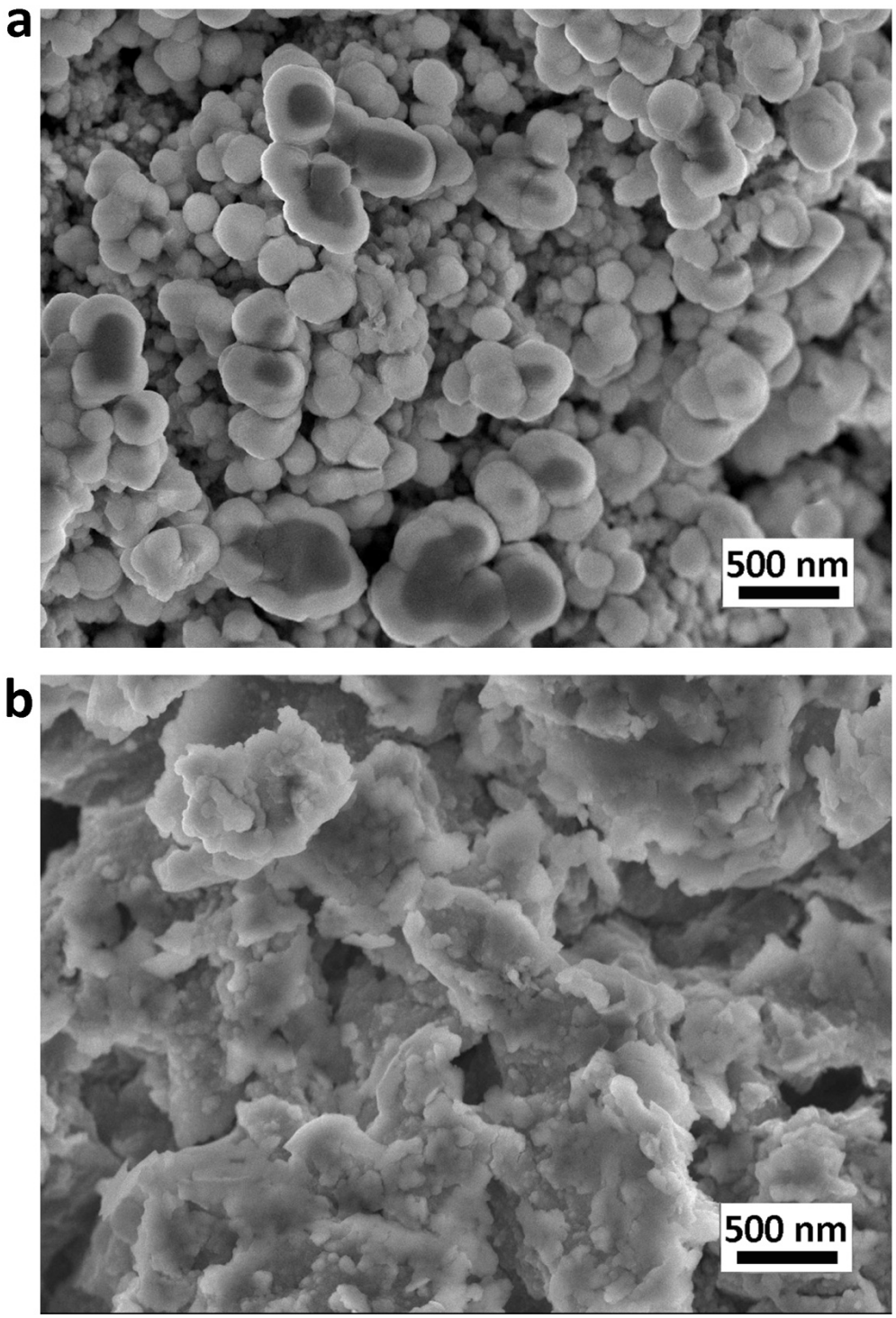

Figure 9.5 SEM images of discharge products on N-GNSs electrodes at (a) 150, and (b) 300 mA g^{-1}.

The growth mechanism for the different morphology of discharge products is proposed and shown in **Figure 9.6**. At low current density, the charge-transfer rate from the surface is slow; the formation rate of NaO_2 is slow as well. When the concentration of the solvated NaO_2 exceeds the solubility limit, they will precipitate on the surface of the carbon materials (**Figure 9.6c**). At high current density, large amount of NaO_2 generates on the surface, which may undergo a surface migration, resulting in the formation of very uniform film (**Figure 9.6d**). For the current densities in the range of low to high, there is competition between the salvation, precipitation and migration. Similar mechanism for the morphology differences of discharge products in lithium-oxygen batteries has been proposed by Nazar et al. [23], however, it is believe that the exact growth of NaO_2 is more complicated and further study is needed.

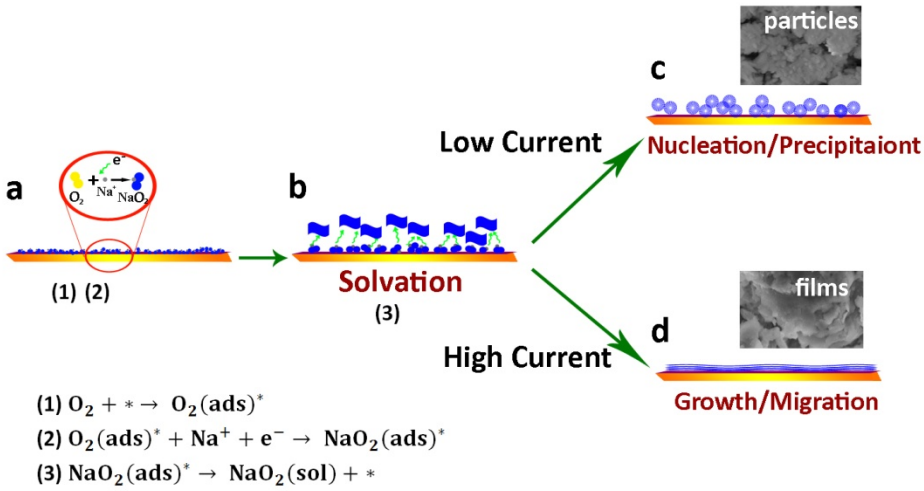

Figure 9.6 Schematic of the growth of discharge product nanostructures on N-GNS electrodes.

9.4 Conclusions

In summary, we reported the superior performance of N-GNSs as cathode materials for sodium-oxygen batteries in comparison to GNSs. It was demonstrated the improvement was due to the defective sites introduced by nitrogen doping. The morphology of the discharge products on N-GNSs electrode is different from those on GNSs electrode, in which product distribution is more uniform and the particle size is smaller. The formation of the discharge products on N-GNSs at different current densities are resulted from various processes, including salvation, precipitation and migration. We believe that heteroatom-doping to carbon cathode is a rational direction to modify other substrate materials for sodium-oxygen batteries.

Acknowledgements

This research was supported by Natural Sciences and Engineering Research Council of Canada, Canada Research Chair Program, Canada Foundation for Innovation, Ontario Early Researcher Award and the University of Western Ontario.

References

[1] K. Abraham, Z. Jiang, A polymer electrolyte-based rechargeable lithium/oxygen battery, *J. Electrochem. Soc.*, 1996, **143**, 1–5.

[2] G. Girishkumar, B. McCloskey, A. Luntz, S. Swanson, W. Wilcke, Lithium-air battery: Promise and challenges, *J. Phys. Chem. Lett.*, 2010, **1**, 2193–2203.

[3] R. Mitchell, B. Gallant, C. Thompson, Y. Shao-Horn, All-carbon-nanofiber electrodes for high-energy rechargeable Li-O_2 batteries, *Energy Environ. Sci.*, 2011, **8**, 2952–2958.

[4] R. Williford, J. Zhang, Air electrode design for sustained high power operation of Li/air batteries, *J. Power Sources*, 2009, **194**, 1164–1170.

[5] J. Xiao, D. Mei, X. Li, W. Xu, D. Wang, G. Graff, W. Bennett, Z. Nie, L. Saraf, I. Aksay, J. Liu, J. Zhang, Hierarchically porous graphene as a lithium-air battery electrode, *Nano Lett.*, 2011, **11**, 5071–5078.

[6] P. Hartmann, C. Bender, M. Vračar, A. Dürr, A. Garsuch, J. Janek, P. Adelhelm, A rechargeable room-temperature sodium superoxide (NaO_2) battery, *Nat. Mater.*, 2013, **12**, 228–232.

[7] J. Kim, H. Lim, H. Gwon, K. Kang, Sodium-oxygen batteries with alkyl-carbonate and ether based electrolytes, *Phys. Chem. Chem. Phys.*, 2013, **15**, 3623–3629.

[8] Q. Sun, Y. Yang, Z. Fu, Electrochemical properties of room temperature sodium-air batteries with non-aqueous electrolyte, *Electrochem. Commun.*, 2012, **16**, 22–25.

[9] W. Liu, Q. Sun, Y. Yang, J. Xie, Z. Fu, An enhanced electrochemical performance of a sodium-air battery with graphene nanosheets as air electrode eatalysts, *Chem. Commun.*, 2013, **49**, 1951–1953.

[10] Y. Li, J. Wang, X. Li, D. Geng, J. Yang, R. Li, X. Sun, Nitrogen-doped carbon nanotubes as cathode for lithium-air batteries, *Electrochem. Commun.*, 2011, **13**, 668–672.

[11] Y. Li, J. Wang, X. Li, D. Geng, M. Banis, R. Li, X. Sun, Nitrogen-doped graphene nanosheets as cathode materials with excellent electrocatalytic activity for high capacity lithium–oxygen batteries, *Electrochem. Commun.*, 2012, **18**, 12–15.

[12] D. Geng, S. Yang, Y. Zhang, J. Yang, J. Liu, R. Li, T.-K. Sham, X. Sun, S. Ye, S. Knights, Nitrogen doping effects on the structure of graphene, *Appl. Surf. Sci.*, 2011, **257**, 9193–9198.

[13] S. Nakanishi, F. Mizuno, T. Abe, H. Iba, Enhancing effect of carbon surface in the non-aqueous Li-O_2 battery cathode, *Electrochemistry*, 2012, **80**, 783–786.

[14] Y. Lu, B. Gallant, D. Kwabi, J. Harding, R. Mitchell, M. Whittingham, Y. Shao-Horn, Lithium-oxygen batteries: bridging mechanistic understanding and battery performance, *Energy Environ. Sci.*, 2013, **6**, 750–768.

[15] C. Rao, C. R. Cabrera, Y. Ishikawa, In search of the active site in nitrogen-doped carbon nanotube electrodes for the oxygen reduction reaction, *J. Phys. Chem. Lett.*, 2010, **1**, 2622–2627.

[16] Y. Lu, H. Gasteiger, E. Crumlin, R. Jr. McGuire, Y. Shao-Horn, Electrocatalytic activity studies of select metal surfaces and implications in Li-air batteries, *J. Electrochem. Soc.*, 2010, **157**, A1016–A1025.

[17] N. Takami, A. Satoh, M. Hara, T. Ohsaki, Structural and kinetic characterization of lithium intercalation into carbon anodes for secondary lithium batteries, *J. Electrochem. Soc.*, 1995, **142**, 371–379.

[18] H. Wang, H. Huang, S. Wunderz, Novel microporous poly(vinylidene fluoride) blend electrolytes for lithium-ion batteries, *J. Electrochem. Soc.*, 2000, **142**, 2853–2861.

[19] X. Yang, Y. Xia, The effect of oxygen pressures on the electrochemical profile of lithium/oxygen battery, *J. Solid State Electrochem.*, 2010, **14**, 109–114.

[20] M. Levi, G. Salitra, B. Markovsky, H. Teller, D. Aurbach, U. Heider, L. Heiderb, Solid-state electrochemical kinetics of Li-ion intercalation into $Li_{1-x}CoO_2$: Simultaneous application of electroanalytical techniques SSCV, PITT, and EIS, *J. Electrochem. Soc.*, 1999, **146**, 1279–1289.

[21] J. Song, H. Lee, Y. Wang, C. Wan, Two- and three-electrode impedance spectroscopy of lithium-ion batteries, *J. Power Sources*, 2002, **111**, 255–267.

[22] J. Xiao, D. Mei, X. Li, W. Xu, D. Wang, G. Graff, W. Bennett, Z. Nie, L. Saraf, I. Aksay, J. Liu, J. Zhang, Hierarchically porous graphene as a lithium-air battery electrode, *Nano Lett.*, 2011, **11**, 5071–5078.

[23] B. Adams, C. Radtke, R. Black, M. Trudeau, K. Zaghib, L. Nazar, Current density dependence of peroxide formation in the Li-O_2 battery and its effect on charge, *Energy Environ. Sci.*, 2013, **6**, 1772–1778.

[24] Y. Mo, S. Ong, G. Ceder, First-principles study of the oxygen evolution reaction of lithium peroxide in the lithium-air battery, *Phys. Rev. B*, 2011, **84**, 205446.

[25] J. Marquina, Raman scattering on ZnO nanocrystals, *Revista Mexicana De Física S*, 2007, **53**, 170–173.

[26] C. Laoire, S. Mukerjee, K. Abraham, Elucidating the mechanism of oxygen reduction for lithium-air battery applications, *J. Phys. Chem. C*, 2009, **113**, 20127–20134.

[27] P. Hartmann, C. Bender, J. Sann, A. Dürr, M. Jansen, J. Janek, P. Adelhelm, A comprehensive study on the cell chemistry of sodium superoxide (NaO_2) battery, *Phys. Chem. Chem. Phys.*, 2013, DOI: 10.1039/c3cp50930c.

Supporting Information

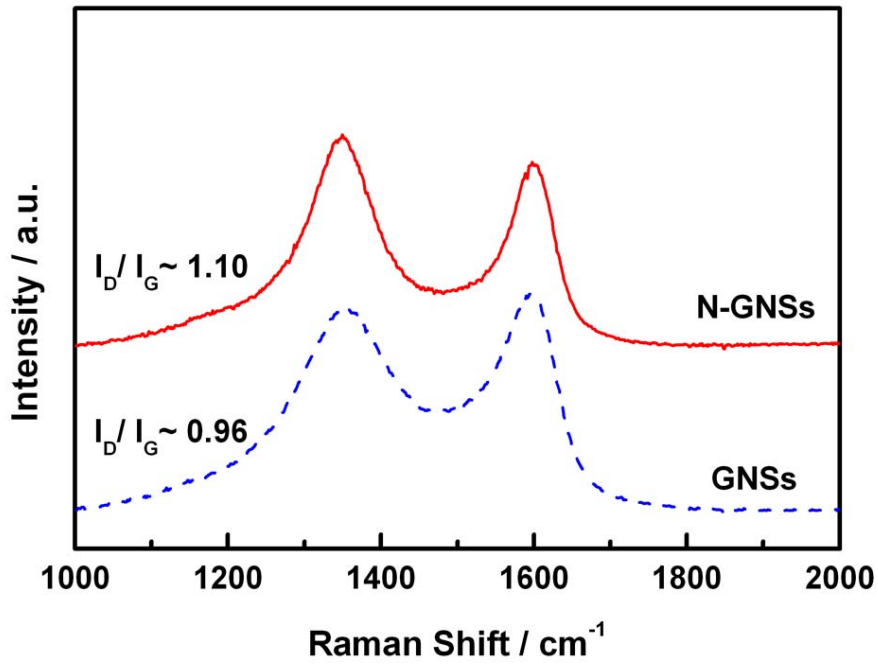

Figure SI-9.1 Raman spectra of GNSs and N-GNSs.

Chapter 10

10 Conclusions and Future Perspective

In this chapter, the results and contributions of the thesis work were summarized and some personal opinions and suggestions for future work are given.

10.1 Conclusions

A series of experiments were conducted in this study to synthesized novel carbon-based nanomaterials as electrode structure and architecture materials for lithium-air and sodium- air batteries. The correlations between the properties of these materials and battery performance were investigated. Besides, the underlying mechanism of discharge product growth and the influence for the battery performance were also explored. In addition, a novel method to synthesize nanomaterials was developed and it is believed this approach is suitable for application in preparing catalysts for lithium-air and sodium-air batteries. In summary, this study mainly worked on three areas: nanomaterials synthesis, characteristics and battery performance.

Carbon blacks with nanoscale size have been heat-treated under different atmospheres (NH_3, CO_2, and CO_2/H_2) for various times. The procedure allowed the properties of carbon materials to be tailored and controlled, such as the surface area, porosity, defects, nitrogen content, and functional group amount. More importantly, all the samples studied as cathode materials for lithium-air batteries were from the same starting material which made this study systematic and the results comparable.The mesopore surface areas increased as the treating time increased while the micropore surface area only increased until the mass loss reached 35% and then decreased. It is suggested that the surface area of mesopores plays an important role for the discharge capacity of lithium-air batteries due to the passivation effect of discharge product film on the carbon surface no matter what gas (NH_3 or CO_2 or $CO_2 + H_2$) is used to obtain porosity in the samples. Nitrogen and oxygen-containing functional groups introduced by the gas treatments or by contact of the pyrolysed product with air, have very little or no influence on the performance of these carbon materials in batteries. However, too large pore size in the mesoporous range leads to a less efficient use of mesopore volumes and the the desired pore size is about 3.5 nm considering the passivation effect.

1D N-CNTs were prepared and employed as cathode materials for lithium-air batteries. This work compared the battery performance based on pristine and doped carbon nanotubes. Both the samples can form 3D opening electrodes which provide good oxygen transportation channels, however, the N-CNT electrode delivered a discharge capacity of 866 mAh g^{-1}, which is about 1.5 times of that for CNT electrode. In addition, the N-CNTs showed much better electrocatalytic activity for Li_2O_2 decomposition, therefore improving the reversibility for lithium air batteries. The performance improvement of N-CNTs results from heteroatom nitrogen doping.

2D GNSs were synthesized by a modified Hummers' method which involves graphite oxidation and thermal exfoliation procedures. The GNSs electrode delivers a capacity of 8705.9 mAh g^{-1}, which is the highest capacity of any carbon-based materials in lithium-air batteries ever reported by then. The unique structures of GNSs provide ideal porosity which is suitable for the electrolyte wetting and the O_2 diffusion, thus improving the efficiency of the catalyst reactions. And the electrode with these structures not only increases the electrochemically accessible site, but also provides a large diffusion path for the O_2 mass transfer, therefore, improving the discharge capacity dramatically. Besides, the pore size distribution as well as the active sites at the edge sites of GNSs also plays important roles in the superior performance.

The lithium-air battery performance made of 2D GNSs as cathode materials were further improved by doping nitrogen to the graphene frameworks. The N-GNSs electrode delivered a discharge capacity of 11660 mAh g^{-1}, which is about 40% higher than that of the pristine GNSs electrode. Furthermore, the electrocatalytic activity of N-GNSs for oxygen reduction in the nonaqueous electrolyte was 2.5 times as that of GNSs. The excellent electrochemical performance of N-GNSs was attributed to the defects and functional groups as active sites introduced by nitrogen doping. Moreover, the distribution of the discharge products was more uniform on N-GNSs, while the product particles aggregated into large clusters on GNSs and some surfaces are free of coverage. This suggested that the presence of the homogeneously distributed nitrogen

species resulting in more active sites (defects and functional groups) of N-GNSs provide more nucleation sites and thus promotes a higher dispersion.

Furthermore, GNSs were doped by sulphur element and it was confirmed and the sulphur distribution in the graphene was relatively uniform (not only in plane but also at the edge of GNSs). The as-prepared sample was applied as cathode material for lithium-air battery. In contrast to nitrogen-doping graphene sample, the S-GNSs electrode showed decreased discharge capacity compared to pristine GNSs electrode. In addition, the morphology of discharge products were also varied, and Li_2O_2 nanorods with a diameter about 100 nm grew on the S-GNSs electrode. From the XANES results, it is suggested the discharge product contained structural defects such as oxygen and/or lithium vacancies resulting in different charge performance. The growth of the discharge products was also studied and the morphology evolution was due to different electrode polarizations.

A facile microwave-assisted hydrothermal route for synthesis of MnO_2 nanostructures with different morphologies (3D hierarchical, 1D tubular) and crystallinities (birnessite-, α-type) was developed. It is found that the crystal phase and morphology can be easily tailed by adjusting reaction temperature. The formation of MnO_2 nanotubes follows the dissolution-crystallization and "oriented attachment" process. And compared to conventional heating methods, the microwave-assisted hydrothermal approach features rapid growth of nanostructured MnO_2 with controlled structure, which is ideal for large-scale production. The finding gives a rational strategy in synthesis and design of nanomaterials with complex architecture and novel properties which can be used as electrocatalysts for lithium- and sodium-air batteries.

The N-GNSs were also employed as cathode materials for nonaqueous sodium-oxygen batteries and it was found that N-GNSs showed higher electrocatalytic activity for oxygen reduction reaction (ORR) and oxygen evolution reaction (OER), resulting in improving discharge and charge performance. It is believed that the excellent electrochemical performance of N-GNSs is attributed to the active sites by nitrogen

doping. Similarly, the morphology of the discharge products, NaO_2, on N-GNSs electrode was different from GNSs, which the dispersion was more uniform and the particle size was smaller. The formation of the discharge products on N-GNSs at different current densities were from different processes, including salvation, precipitation and migration.

10.2 Future Perspective

Despite the advances demonstrated in this thesis, a large number of unsolved challenges still remain. Future work could focus on the following aspects:

- This thesis reported that the surface area of mesopores in carbon black is critical for lithium-air battery performance; however, due to the passivation effect of discharge products, a desired pore size is obtained (~ 3.5 nm). It is expected to modify the procedure and parameters for the heat-treatment that carbon blacks with large amount of desired pore size can be prepared, further optimizing the battery performance.

- This thesis demonstrated that nitrogen doping into CNTs and GNSs can increase the electrocatalytic activity towards electrode reactions, therefore improving the battery performance. However, the study of mechanisms for the nitrogen doping can be deeper. For example, samples with different nitrogen amount or nitrogen types (pyridinic-, pyrrolic-, or graphitic-N) can be synthesized and the correlations between these parameters and battery performance should be investigated.

- The cycleability is another critical issue for the practical application of lithium-air and sodium-air batteries. Therefore, bifunctional electrocatalysts which are both good for ORR and OER should be synthesized and applied in

these systems. And based on the finding that N-CNTs and N-GNSs can form novel 3D porous electrode, it is interesting to combine the electrocatalysts with these air electrode materials to develop high capacity, rechargeable batteries. Another strategy is to apply metal or metal oxides nanowires which process certain catalytic activity for ORR as 3D electrodes in lithium-air and sodium-air batteries. For example, growth of various nanowires (TiO_x, ZrO_2, WO_3, SnO_2, Sn) directly on carbon paper may considerably improve electrical contact with the external electrical circuit and the supported catalysts' utilization.

- The research of sodium-air battery is at the early stage, air electrode materials and structure design as well as electrocatalysts synthesis and optimization should also be considered. More importantly, the understanding of reaction mechanisms is the key for developing this energy system.

Appendices

Appendix I: PERMISSION FROM ELSEVIER FOR PUBLISHED ARTICLE

Published article:

1. Nitrogen-doped Carbon Nanotubes as Cathode for Lithium-Air Batteries, ***Electrochemistry Communications***, 2011, **13**, 668-672.

2. Nitrogen-Doped Graphene Nanosheets as Cathode Materials with Excellent Electrocatalytic Activity for High Capacity Lithium-Oxygen Batteries, ***Electrochemistry Communications***, 2012, **18**, 12-15.

3. Facile Controlled Synthesis and Growth Mechanisms of Flower-Like and Tubular MnO_2 Nanostructres by Microwave-Assisted Hydrothermal Method, ***Journal of Colloid and Interface Science***, 2012, **369**, 123-128.

4. Challenges and Opportunities of Nanostructured Materials for Aprotic Rechargeable Lithium-Oxygen Batteries, ***Nano Energy***, 2013, 2, 443-467.

5. Carbon Black Cathodes for Lithium Oxygen Batteries: Influence of Porosity and Heteroatom-Doping, ***Carbon***, 2013, in press.

Elsevier Copyright Policy:

(*http://www.elsevier.com/journal-authors/author-rights-and-responsibilities#rights*)

As a journal author, you have rights for a large range of uses of your article, including use by your employing institute or company. ***These rights can be exercised without the need to obtain specific permission.***

Authors publishing in Elsevier journals have wide rights to use their works for teaching and scholarly purposes without needing to seek permission.

Table of Authors' Rights

	*Preprint version (with a few exceptions- see below *)*	*Accepted Author Manuscript*	*Published Journal Articles*
Use for classroom teaching by author or author's institution and presentation at a meeting or conference and distributing copies to attendees	*Yes*	*Yes with full acknowledgement of final article*	*Yes with full acknowledgement of final article*
Use for internal training by author's company	*Yes*	*Yes with full acknowledgement of final article*	*Yes with full acknowledgement of final article*
Distribution to colleagues for their research use	*Yes*	*Yes*	*Yes*
Use in a subsequent compilation of the author's works	*Yes*	*Yes with full acknowledgement of final article*	*Yes with full acknowledgement of final article*
Inclusion in a thesis or dissertation	***Yes***	***Yes with full acknowledgement of final article***	***Yes with full acknowledgement of final article***
Reuse of portions or extracts from the article in other works	*Yes*	*Yes with full acknowledgement of final article*	*Yes with full acknowledgement of final article*
Preparation of derivative works (other than for commercial purposes)	*Yes*	*Yes with full acknowledgement of final article*	*Yes with full acknowledgement of final article*
Preprint servers	*Yes*	*Yes with the specific written permission of Elsevier*	*No*

Voluntary posting on open web sites operated by author or author's institution for scholarly purposes	*Yes (author may later add an appropriate bibliographic citation, indicating subsequent publication by Elsevier and journal title)*	*Yes, with appropriate bibliographic citation and a link to the article once published*	*Only with the specific written permission of Elsevier*
Mandated deposit or deposit in or posting to subject-oriented or centralized repositories	*Yes under specific agreement between Elsevier and the repository*	*Yes under specific agreement between Elsevier and the repository***	*Yes under specific agreement between Elsevier and the repository*
Use or posting for commercial gain or to substitute for services provided directly by journal	*Only with the specific written permission of Elsevier*	*Only with the specific written permission of Elsevier*	*Only with the specific written permission of Elsevier*

Appendix II: PERMISSION FROM ROYAL SOCIETY OF CHEMISTRY (RSC) FOR PUBLISHED ARTICLE

Published article:

1. Superior Energy Capacity of Graphene Nanosheets for Nonaqueous Lithium-Oxygen Battery, ***Chemical Communications***, 2011, **47**, 9438-9440.

2. Discharge Product Morphology and Increased Charge Performance of Lithium-Oxygen Batteries with Graphene Nanosheet Electrodes: The Effect of Sulphur Doping, ***Journal of Materials Chemistry***, 2012, **22**, 20170-20174.

RSC Copyright Policy:

(http://www.rsc.org/AboutUs/Copyright/Permissionrequests.asp)

Author Use of Own Material in Theses and Dissertations

Authors of articles in RSC journals or chapters in RSC books do not need to formally request permission to reproduce their article or book chapter in their thesis or dissertation. *For all cases of reproduction the correct acknowledgement should be given in the caption of the reproduced material. The acknowledgement depends on the RSC publication in which the material was published. The form of the acknowledgement to be included in the caption can be found on the page entitled Acknowledgements to be used by RSC authors. Please ensure that your co-authors are aware that you are including the paper in your thesis.*

Curriculum Vitae

Name:	Yongliang Li
Post-secondary Education and Degrees:	The University of Western Ontario London, Ontario, Canada 2009-2013 Ph.D.
	Sun Yat-sen University Guangzhou, Guangdong, China 2005-2008 M.Sc.
	Sun Yat-sen University Guangzhou, Guangdong, China 2001-2005 B.Sc.
Honours and Awards:	Western Engineering Scholarship 2009-2013

Related Work Experience Research & Teaching Assistant

The University of Western Ontario

2009-2013

Publications:

(A) *Peer-reviewed Journal Papers Based on This Thesis* ***(First author)***

1. **Y. L. Li**, J. J. Wang, X. F. Li, D. S. Geng, M. N. Banis, Y. J. Tang, D. N. Wang, R. Y. Li, T.-K. Sham, X. L. Sun. *Discharge Product Morphology and Increased Charge Performance of Lithium-oxygen Batteries with Graphene Nanosheet Electrodes: The Effect of Sulphur Doping.* **J. Mater. Chem.** 22 (2012) 20170-20174. (**Invited aricle**)

2. **Y. L. Li**, J. J. Wang, X. F. Li, D. G. Geng, M. N. Banis, R. Y. Li, X. L. Sun. *Nitrogen-doped Graphene Nanosheets as Cathode Materials with Excellent Electrocatalytic Activity for High Capacity Lithium-oxygen Batteries.* **Electrochem. Commun.** 18 (2012) 12-15.（**Most downloaded article from Apr. to Jun. in 2012**）

3. **Y. L. Li**, J. J. Wang, Y. Zhang, M. N. Banis, J. Liu, D. S. Geng, R. Y. Li, X. L. Sun. *Facile Controlled Synthesis and Growth Mechanisms of Flower-like and Tubular MnO_2 Nanostructures by Microwave-assisted Hydrothermal Method.* **J. Colloid Interface Sci.** 369 (2012) 123-128.

4. **Y. L. Li**, J. J. Wang, X. F. Li, D. S. Geng, R. Y. Li, X. L. Sun. *Superior Energy Capacity of Graphene Nanosheets for Nonaqueous Lithium-oxygen Battery.* **Chem. Commoun.** 47 (2011) 9438-9440.

5. **Y. L. Li**, J. J. Wang, X. F. Li, J. Liu, D. S. Geng, J. L. Yang, R. Y. Li, X. L. Sun. *Nitrogen-doped Carbon Nanotubes as Cathode for Lithium-air Batteries.* **Electrochem. Commun**. 13 (2011) 668-672.（**Most downloaded article from Oct. to Dec. in 2011**）

6. **Y. L. Li**, X. F. Li, D. S. Geng, Y. J. Tang, R. Y. Li, J.-P. Dodelet, M. Lefèvre, X. L. Sun. *Carbon Black Cathodes for Lithium-oxygen Batteries: Influence of Porosity and Heteroatom-doping.* **Carbon** (2013) in press.

7. **Y. L. Li**, X. F. Li, H. Yadegari, Y. J. Tang, B. W. Xiao, R. Y. Li, X. L. Sun, Enhanced Performance of Sodium-oxygen Batteries by Nitrogen-doped Graphene Cathode Materials. To be submitted.

(B) *Peer-reviewed Journal Papers Based on This Thesis (**Coauthor**)*

8. J. J. Wang, **Y. L. Li**, X. L. Sun. *Challenges and Opportunities of Electrode Materials for Aprotic Rechargeable Lithium-oxygen Batteries.* **Nano Energy** 2 (2013) 443-467.

9. J. J. Wang, J. L. Yang, Y. Zhang, **Y. L. Li**, M. N. Banis, X. F. Li, R. Y. Li, X. L. Sun, G. X. Liang, M. Gauthier. *Interaction of Carbon Coating on $LiFePO_4$: Local Visualization Study of the Influence of Impurity Phases.* **Adv. Funct. Mater.** 23 (2013) 806-814.

10. X. F. Li, X. B. Meng, J. Liu, D. S. Geng, Y. Zhang, M. N. Banis, **Y. L. Li**, R. Y. Li, X. L. Sun, M. Cai, M. Verbrugge. *Tin Oxide with Controlled Morphology and Crystallinity by Atomic Layer Deposition onto Graphene Nanosheets for Enhanced Lithium Storage.* **Adv. Funct. Mater.** 22 (2012) 1647-1654.（**Highlighted as Frontispeces, most accessed article from Nov. 2011 to Nov. 2012**）

11. X. F. Li, J. Liu, Y, Zhang, **Y. L. Li**, H. Liu, X. B. Meng, J. L. Yang, D. S. Geng, D. N. Wang, R. Y. Li, X. L. Sun. *High Concentration Nitrogen Doped Carbon Nanotube Anodes with Superior Li^+ Storage Performance for Lithium Rechargeable Battery Application.* **J. Power Sources** 197 (2012) 238-245.

12. J. L. Yang, J. J. Wang, X. F. Li, D. N. Wang, J. Liu, G. X. Liang, M. Gauthier, **Y. L. Li**, D. S. Geng, R. Y. Li, X. L. Sun. *Hierarchically Porous $LiFePO_4$/nitrogen-doped Carbon Nanotubes Composite as a Cathode for Lithium Ion Batteries.* **J. Mater. Chem.** 22 (2012) 7537-7543.

13. D. S. Geng, Y. H. Hu, **Y. L. Li**, R. Y. Li, X. L. Sun. *One-pot Solvothermal Synthesis of Doped Graphene with the Designed Nitrogen Type Used as a Pt Support for Fuel Cells.* **Electrochem. Commun.** 22 (2012) 65-68.

14. J. Liu, X. F. Li, J. L. Yang, D. S. Geng, **Y. L. Li**, D. N. Wang, R. Y. Li, X. L. Sun. *Microwave-assisted Hydrothermal Synthesis of Nanostructured Spinel $Li_4Ti_5O_{12}$ as Anode Materials for Lithium Ion Batteries.* **Electrochim. Acta** 63 (2012) 100-104.

15. X. F. Li, J. J. Yang, Y. H. Hu, J. J. Wang, **Y. L. Li**, M. Cai, R. Y. Li, X. L. Sun. *Novel Approach toward Binder-free and Current Collector-free Anode Configuration: Highly Flexible Nanoporous Carbon Nanotube Electrodes with Excellent Mechanical Strength Harvesting Improved Lithium Storage.* **J. Mater. Chem.** 22 (2012) 18847-18853.

16. D. S. Geng, Y. Chen, Y. G. Chen, **Y. L. Li**, R. Y. Li, X. L. Sun, S. Y. Ye, S. Knights. *High Oxygen-reduction Activity and Durability of Nitrogen-doped Graphene.* **Energy Environ. Sci.** 4 (2011) 760-764.

17. Y. J. Tang, J. J. Wang, J. L. Yang, **Y. L. Li**, B. W. Xiao, X. F. Li, G. X. Liang, R. Y. Li, T.-K. Sham, X. L. Sun, Observation of $LiMn_{0.7}Fe_{0.3}PO_4$ Aging in Electrolyte: Effect of impurity phases. (2013) Submitted.

18. X. F. Li, **Y. L. Li**, J. Liu, Y. Zhang, R. Y. Li, M. Cai, X. L. Sun. *Enhanced Lithium Storage Performance of Hybrid Structured Coaxial Nanoflower-like MnO_2@Nitrogen-doped Carbon Nanotube Composites.*To be submitted.

(C) *Previous Publications*

18. **Y. L. Li**, F. P. Hu, X. Wang, P. K. Shen. *Anchoring Metal Particles on Multiwalled Carbon Nanotubes as Stable Electrocatalysts*. **Electrochem. Commun.** 10 (2008) 1101-1104.

19. J. Y. Liang, **Y. L. Li**, Y. Q. Huang, J. Y. Yang, H. L. Tang, Z. D. Wei, P. K. Shen. *Sodium Borohydride Hydrolysis on Highly Efficient Co-B/Pd Catalysts*. **Int. J. Hydrogen Energ.** 33 (2008) 4048-4054.

20. J. Y. Yang, **Y. L. Li**, Y. Q. Huang, J. Y. Liang, P. K. Shen. *Dynamic Conducting Effect of WO_3/PFSA Membranes on the Performance of Proton Exchange Membrane Fuel Cells*. **J. Power Sources** 177 (2008) 56-60.

21. F. P. Hu, P. K. Shen, **Y. L. Li**, J. Y. Liang, J. Wu, Q. L. Bao, C. M. Li, Z. D. Wei. *Highly Stable Pd-based Catalytic Nanoarchitectures for Low Temperature Fuel Cells*. **Fuel cells** 8 (2008) 429-435.

22. Z. Z. Zhao, X. Fang, **Y. L. Li**, Y. Wang, P. K. Shen, F. Y. Xie, X. Zhang. *The Origin of the High Performance of Tungsten Carbides/carbon Nanotubes Supported Pt Catalysts for Methanol Electrooxidation*. **Electrochem. Commun.** 11 (2008) 290-293.

23. F. P. Hu, Z. Y. Wang, **Y. L. Li**, C. M. Li, X. Zhang, P. K. Shen. *Improved Performance of Pd Electrocatalyst Supported on Ultrahigh Surface Area Hollow Carbon Spheres for Direct Alcohol Fuel Cells*. **J. Power Sources** 177 (2008) 61-66.

24. H. T. Zheng, **Y. L. Li**, J. Y. Liang, P. K. Shen. *Methanol Oxidation on Pd-based Electrocatalysts*. **Acta Phys.-Chim. Sin.** 23 (2007) 993-996.

25. P. K. Shen, S. L. Wang, Z. Y. Hu, **Y. L. Li**, R. Zeng, Y. Q. Huang. *Hydrogen Production by Alcohol Electrolysis*. **Acta Phys.-Chim. Sin.** 23 (2007) 107-110.

26. H. T. Zheng, **Y. L. Li**, S. X. Chen, P. K. Shen. *Effect of Support the Activity of Pd Electrocatalyst for Ethanol Oxidation*. **J. Power Sources** 163 (2006) 371-375.

27. Z. Y. Hu, **Y. L. Li**, P. K. Shen. *Hydrogen Production by Methanol Electrolysis*. **Bimonthly Battery** 36 (2006) 383-384.

28. J. Y. Liang, **Y. L. Li**, P. K. Shen. *Research Progress in the key Components for PEMFC*. **Bimonthly Battery** 36 (2006) 226-228.

(D) *Conference Presentations and Abstracts*

1. **Y. L. Li**, J. J. Wang, X. L. Li, D. S. Geng, R. Y. Li, X. L. Sun. *Heteroatom-doped Graphene as Cathode Materials for Lithium-oxygen Batteries*. The 223rd Electrochemical Society Meeting. 2013, Toronto, Canada.

2. **Y. L. Li**, J. J. Wang, X. F. Li, D. S. Geng, M. N. Banis, R. Y. Li, X. L. Sun. *Graphene and N-doped Graphene as Cathodes for Li-air Batteries*. The 24th Canadian Materials Science Conference. 2012, London, Canada.

3. **Y. L. Li**, J. J. Wang, X. F. Li, D. S. Geng, J. Liu, M. N. Banis, R. Y. Li, X. L. Sun. *Heteroatom-doped Nanocarbon for Nonaqueous Li/O_2 Battery*. The 16th International Meeting on Lithium Batteries. 2012, Jeju, Korea.

4. **Y. L. Li**, J. Liu, X. F. Li, J. J. Wang, R. Y. Li, X. L. Sun. *3-D Air Electrode of MnO_2 Nanoflakes Coated Nitrogen-doped Carbon Nanotubes for Lithium/air Batteries.* The 219th Electrochemical Society Meeting. 2011, Montreal, Canada.

5. **Y. L. Li**, X. F. Li, J. J. Wang, J. Liu, R. Y. Li, X. L. Sun. *Controlled Synthesis of MnO_x Nanowires as Catalysts for Li/O_2 Batteries.* The 15th International Meeting on Lithium Batteries. 2010, Montreal, Canada.

6. **Y. L. Li**, X. F. Li, J. J. Wang, J. Liu, R. Y. Li, X. L. Sun. *Controlled Synthesis of MnO_x Nanowires as Catalysts for Li/O_2 Batteries.* Fall Symposium, Canadian Section, The Electrochemical Society. 2010, London, Canada.

7. X. F. Li, D. S. Geng, X. B. Meng, J. J. Wang, J. Liu, **Y. L. Li**, D. N. Wang, J. L. Yang, R. Y. Li, X. L. Sun. *Graphene and SnO_2/graphene as Anodes of Lithium-ion Batteries*. The 15th International Meeting on Lithium Batteries. 2010, Montreal, Canada.

8. F. P. Hu, **Y. L. Li**, P. K. Shen. *Hollow Carbon Spheres Prepared by a Hydrothermal Template and IMH Method*. The 6th International Conference on Materials Processding for Properties and Performance (MP3). 2007, Beijing, China. （**Invited talk**）

9. P. K. Shen, **Y. L. Li**, J. Y. Liang, M. Wu. *Indirect Borohydride Portable Fuel Cells*. The International Conference on Clean Technology and Fuel Cells. 2006, Yokosuka, Japan.